THE UNIVERSITY OF QUEENSLAND

AUSTRALIA

Quench dynamics and relaxation of one-dimensional Bose gases

Francis A. Bayocboc, Jr.

B.Sc., M.Sc.

0000-0002-7157-6184

A thesis submitted for the degree of Doctor of Philosophy at The University of Queensland in 2021

School of Mathematics and Physics

Abstract

Ultracold atom experiments are a great experimental platform for studying many-body physics due to their isolation and high tunability. In particular, they are excellent candidates for studying many paradigmatic models of quantum many-body physics with a high degree of accuracy. Advances in ultracold atom experiments have enabled the realisation of lower-dimensional systems that have been of theoretical interest historically. Low dimensional systems have several striking differences from their three-dimensional counterparts; most notable is the absence of Bose-Einstein condensation in the thermodynamic limit. In this thesis, we study the nonequilibrium dynamics of quantum many-body interacting ultracold Bose gases. We are particularly interested in quenches of Bose gases in one spatial dimension and their subsequent time-evolution and relaxation dynamics. We present numerical simulations of one-dimensional Bose gases where we incorporate thermal and quantum fluctuations and investigate their effects on the post-quench dynamics of the system.

First, we consider a system of two tunnel-coupled, one-dimensional quasicondensates following a quench of the coupling strength from zero to a fixed finite value. More specifically, starting from two independent quasicondensates in equilibrium, with an initial temperature and chemical potential imbalance, we suddenly switch on the tunnel-coupling and analyse the post-quench equilibration dynamics. We find that after coupling the quasicondensates, the low-energy particles flow predominantly from the colder quasicondensate to the hotter one, whereas the reverse is true for the higher-energy particles. The net energy flow is governed by the surplus (or otherwise) of the overall number of lower energy particles flowing from the initially colder quasicondensate to the initially hotter quasicondensate, compared to the overall number of higher-energy particles flowing in the opposite direction. We also find that the coupled quasicondensates can evolve to a relaxed state with a higher equilibrium temperature than their initial temperature. Surprisingly, we find that, though the final equilibrium temperature is higher, the system can have a higher phase coherence within each quasicondensate.

We also consider the case where the two quasicondensates in the system above contain an equal number of particles with an initial phase difference. The two quasicondensates are obtained from the coherent splitting of a single quasicondensate. After imprinting an initial phase difference, we abruptly turn on the coupling strength between the two and characterise the post-quench dynamics. This is motivated by a recent experiment of Pigneur *et al.*, Phys. Rev. Lett. **120**, 173601 (2018), where the fast relaxation of the system to a phase-locked state cannot be described by the quantum sine-Gordon model that has described their experimental results well in the past. We find that our 1D simulations of the experiment can reproduce the phase-locked steady state but not the fast decay observed in the experiment.

We then investigate the breathing mode oscillations of a one-dimensional Bose gas after a quench of the longitudinal harmonic trap frequency. In particular, after preparing a Bose gas at a chemical potential and temperature, we suddenly change the longitudinal trapping frequency to a lower value and observe the dynamics of the gas. We find that two breathing modes corresponding to two components of the system exist: low-energy particles occupying the bulk and high-energy particles in the tails of

the Bose gas. Each component has its own distinct breathing frequency and damping rate. We find that the low-energy particles in the bulk have dynamical behaviour closer to that of a zero temperature quasicondensate, whereas highly energetic particles in the tails have dynamical behaviour closer to that of an ideal Bose gas. We also find that the damping rate of the quasicondensate is much lower than the rate predicted from one-dimensional Landau damping.

Lastly, we consider the effects of thermal and quantum fluctuations on the dynamics of dispersive quantum shock waves in a one-dimensional Bose gas. Starting with a local density bump on top of a uniform background density, we let the former expand into the latter and observe the formation and dynamics of dispersive shock waves. Here, the oscillatory train that forms after releasing the local density bump results from quantum mechanical self-interference. We find that the amplitude of oscillation decreases with the increase of temperature due to the reduced phase coherence within the Bose gas. Furthermore, we find that vacuum and thermal fluctuations can significantly wash out the amplitude of oscillations due to shot-to-shot fluctuations in the position of interference fringes around the mean.

Declaration by author

This thesis is composed of my original work, and contains no material previously published or written by another person except where due reference has been made in the text. I have clearly stated the contribution by others to jointly-authored works that I have included in my thesis.

I have clearly stated the contribution of others to my thesis as a whole, including statistical assistance, survey design, data analysis, significant technical procedures, professional editorial advice, financial support and any other original research work used or reported in my thesis. The content of my thesis is the result of work I have carried out since the commencement of my higher degree by research candidature and does not include a substantial part of work that has been submitted to qualify for the award of any other degree or diploma in any university or other tertiary institution. I have clearly stated which parts of my thesis, if any, have been submitted to qualify for another award.

I acknowledge that an electronic copy of my thesis must be lodged with the University Library and, subject to the policy and procedures of The University of Queensland, the thesis be made available for research and study in accordance with the Copyright Act 1968 unless a period of embargo has been approved by the Dean of the Graduate School.

I acknowledge that copyright of all material contained in my thesis resides with the copyright holder(s) of that material. Where appropriate I have obtained copyright permission from the copyright holder to reproduce material in this thesis and have sought permission from co-authors for any jointly authored works included in the thesis.

Publications included in this thesis

1. [1] S.A. Simmons, **F.A. Bayocboc, Jr.**, J.C. Pillay, D. Colas, I.P. McCulloch, and K.V. Kheruntsyan, What is a quantum shock wave?, *Phys. Rev. Lett.* **125**, 180401 (2020).
   Some results in this publication have been included in Chapter 6 of this thesis.

Submitted manuscripts included in this thesis

1. [2] **F.A. Bayocboc, Jr.**, M.J. Davis, and K.V. Kheruntsyan, Dynamics of thermalization of two tunnel-coupled one-dimensional quasicondensates, submitted to *Phys. Rev. A* on 30th Aug 2021.

Other publications during candidature

Conference Abstracts

1. **F. A. Bayocboc, Jr.**, M. J. Davis, and K. V. Kheruntsyan, 'Dynamics of thermalisation of two tunnel-coupled quasicondensates', 23rd *Australian Institute of Physics Congress*, Perth, Western Australia, Dec. 2018. – poster presentation

2. **F. A. Bayocboc, Jr.** and K. V. Kheruntsyan, 'Non-equilibrium transport in two tunnel-coupled 1D quasicondensates', *Finite Temperature Nonequilibrium Superfluid Systems (FINESS) 2018*, Wanaka, New Zealand, Feb. 2018. – poster presentation

Contributions by others to the thesis

Karén V. Kheruntsyan provided critical feedback, editing, and supervision throughout my candidature.
Fig. 2.1 reproduced from Phys. Rev. A **88**, 023419 (2009), © APS; reused with permission (License RNP/21/NOV/046518).
Fig. 2.2 reproduced from Science **307**(5711), 860 (2005), ©AAAS; reused with permission (License 5185290320980).

Statement of parts of the thesis submitted to qualify for the award of another degree

No works submitted towards another degree have been included in this thesis.

Research involving human or animal subjects

No animal or human subjects were involved in this research.

Acknowledgments

Pax et bonum!

First and foremost, I would like to express my deep appreciation and gratitude to my thesis supervisor, Prof. Karén Kheruntsyan, for his long-standing patience, guidance, and support. My appreciation also to my thesis co-supervisor, Prof. Matthew Davis, from whom I have learned a lot about computational methods.

I am grateful to the people in the School of Mathematics and Physics of UQ, especially the members, past and present, of the Quantum Many-Body Dynamics group and BEC journal club. These people have provided a good environment to learn physics.

I am also grateful for the support and friendship of the wonderful people I have met during my stay here in Brisbane, particularly the Amor and Venezuela families who have made my past four years enjoyable. I also want to thank Ivy and Klaus for giving me a place to thrive during my studies and for all the great food and friendship over the years. I would also like to thank the wonderful people I met at the UQ Catholic Chaplaincy for the great spiritual companionship in campus.

To K-Pop idols, especially IU, Mamamoo, and Red Velvet, thank you for your beautiful music. They have kept me sane *Through the Night*s of writing when *Words Don't Come Easy* and I have my *Eyes Locked, Hands Locked* on my computer. 매우 감사합니다!

Special thanks also to my long-time friends who have accompanied me virtually through our *e-numans*, especially during the COVID-19 pandemic.

I would like to thank the unwavering support, understanding, and encouragement of my family — Mama, Papa, and Charlene — and Raffee. Thank you for all the love which I could very much feel regardless of the distance.

Finally, greatest thanks to GOD, *Deus meus et omnia*, in whom alone my soul finds rest (*cf.* Psalm 62). *Ad majorem Dei gloriam*.

Financial support

This research was supported by The University of Queensland (UQ Research Training Tuition Fee Offset and UQ Reseach Training Stipend)

Keywords

Bose-Einstein condensation, one-dimensional Bose gases, ultracold quantum gases, nonequilibrium quantum many-body systems, quantum quenches, relaxation

Australian and New Zealand Standard Research Classifications (ANZSRC)

ANZSRC code: 020601, Degenerate Quantum Gases and Atom Optics, 100%

Fields of Research (FoR) Classification

FoR code: 0206, Quantum Physics, 100%

Para sa iyo na nangangarap at nagsusumikap para sa Inang Bayan.

Contents

Abstract ii

Contents **ix**

List of Figures **xi**

List of Abbreviations and Symbols **xiii**

1 Introduction **1**

2 Theoretical Background **7**

2.1 Bose–Einstein condensation 7

2.1.1 Bose–Einstein condensation in a box 8

2.2 Dilute Bose Gas 10

2.2.1 The Gross–Pitaevskii equation 11

2.2.2 Thomas–Fermi limit 13

2.2.3 Hydrodynamic equations 14

2.2.4 Bogoliubov theory of interacting Bose gases 15

2.3 One-dimensional Bose gas 19

2.3.1 Long-range order in lower dimensions 20

2.3.2 One-dimensional Thomas–Fermi approximation 22

2.3.3 One-dimensional hydrodynamic equations 23

2.3.4 Realisation of 1D Bose gases in experiments 23

2.3.5 Uniform 1D Bose gas 27

2.3.6 Regimes of uniform 1D Bose gases 28

2.3.7 Bogoliubov theory of 1D quasicondensates 32

2.3.8 Finite temperature momentum distribution 38

2.4 Stochastic methods for interacting Bose gases 38

2.4.1 Wigner representation 39

2.4.2 The stochastic projected Gross–Pitaevskii equation 44

2.4.3 Dimensionless units 48

2.4.4 Penrose–Onsager criterion 50

3 Thermalisation of tunnel-coupled 1D quasicondensates **53**
3.1 Introduction . . . 53
3.2 System and c-field method . . . 55
3.2.1 The model . . . 55
3.2.2 The c-field method . . . 56
3.3 Results and Discussion . . . 59
3.3.1 Energy and particle exchange . . . 59
3.3.2 Dynamics of particles in momentum space . . . 63
3.3.3 Equilibrium chemical potential and temperature . . . 66
3.3.4 Equilibration and thermal phase coherence . . . 69
3.4 Summary . . . 74

4 Relaxation in a 1D bosonic Josephson junction **75**
4.1 Motivation . . . 75
4.2 Details of the experiment . . . 76
4.2.1 Phenomenological model . . . 76
4.3 Model of the system . . . 77
4.4 Summary . . . 81

5 Damping of breathing mode oscillations in a 1D quasicondensate **83**
5.1 Motivation . . . 83
5.2 Preparation of initial state and quench protocol . . . 85
5.3 Breathing mode frequencies . . . 90
5.4 Damping of breathing mode oscillations . . . 94
5.4.1 Landau damping . . . 95
5.4.2 Damping rate from numerical simulations . . . 97
5.5 Summary . . . 99

6 Role of fluctuations in the propagation of shock waves **101**
6.1 Introduction . . . 101
6.2 Dispersive shock waves . . . 102
6.3 The effects of thermal fluctuations . . . 105
6.4 The effects of vacuum fluctuations . . . 110
6.4.1 Second-order correlation function . . . 115
6.5 Summary . . . 118

7 Conclusion **119**

Bibliography **123**

List of Figures

2.1 Schematic diagram of a 2D optical lattice used to realise an array of 1D Bose gases. . . . 25
2.2 Highly anisotropic harmonic trap created using an atom chip. 26
2.3 Physical regimes of a uniform 1D Bose gas. 29
2.4 Comparison of the polylogarithmic functions $g_{3/2}(z)$ and $g_{1/2}(z)$. 30
2.5 Schematic view of the c-field region and the incoherent region. 45

3.1 The three initial conditions considered in Fig. 3.2. 60
3.2 Evolution of the particle number imbalance and the energy imbalance. 61
3.3 Evolution of the cross- and intra-well components of the momentum distribution currents $dn_j(k,t)/dt$. 64
3.4 Momentum distributions of two initially balanced 1D quasicondensates in a tunnel-coupled setup. 67
3.5 First-order correlation function for two initially independent but number- and temperature-balanced quasicondensates. 70
3.6 Two-point correlation function for two initially independent but number- and temperature-balanced quasicondensates. 72

4.1 Quench protocol: splitting, relative phase imprinting, and recoupling. 77
4.2 Evolution of the particle number imbalance. 79
4.3 Evolution of the phase difference. 80

5.1 Quench protocol: initiating breathing mode oscillations. 85
5.2 Evolution of the density profile and the momentum distribution. 88
5.3 Root-mean-square width of the density profile. 89
5.4 Computed breathing mode frequencies. 91
5.5 Evolution of the momentum distribution at $k_x = 0$ and at $k_x = 13.5/a_{\rm osc}$. 92
5.6 Relative power of the eigenmodes in the breathing mode oscillations. 93
5.7 Condensate fraction of the 1D Bose gas at different values of $\gamma_0^{3/2}\overline{\tau}$. 94
5.8 Landau damping mechanism. 95
5.9 Computed breathing mode damping rates. 97

5.10 Damping rate calculated from 1D Landau damping compared to the damping rates obtained from SPGPE simulations. 98

6.1 Shock waves in a weakly interacting 1D quasicondensate at zero temperature. 104
6.2 Shock waves in a finite-temperature quasicondensate with $N = 2000$ particles. 106
6.3 Normalised first-order correlation function of the bump on the uniform background. . . . 107
6.4 Shock waves in a finite-temperature quasicondensate with $N = 50$ particles. 109
6.5 Normalised second-order correlation function of a Gaussian density bump on top of a uniform background density at finite temperature. 110
6.6 Local second-order correlation function of a Gaussian density bump on top of a uniform background density at finite temperature. 111
6.7 Shock waves in a weakly interacting 1D Bose gas at $T = 0$ temperature with quantum fluctuations. 114
6.8 Normalised first-order correlation function calculated from the centre of the box of the initial Gaussian bump with quantum fluctuations. 115
6.9 Local normalised second-order correlation function of the system with $N = 50$ particles and $\gamma_{bg} = 0.1$. 116
6.10 Local normalised second-order correlation function $g^{(2)}(x, x' = x, t)$ of the system with $N = 2000$ particles and $\gamma_{bg} = 0.01$. 117

List of Abbreviations and Symbols

The following lists are neither exhaustive nor exclusive, but may be helpful.

Abbreviations	
BEC	Bose-Einstein condensate
GPE	Gross-Pitaevskii equation
SPGPE	stochastic projected Gross-Pitaevskii equation
TWA	truncated Wigner approximation
RMS	root-mean-square
HWHM	half-width at half-maximum
1D	one-dimensional
3D	three-dimensional

Symbols	
$\hat{\Psi}$	bosonic field operator
Ψ	mean-field/condensate wavefunction
$\Psi_{\mathbf{C}}$	c-field
$\hat{\rho}$	density operator
$\hat{H}$	many-body Hamiltonian
H	mean-field Hamiltonian
μ	chemical potential
ξ	healing length
a_s	3D s-wave scattering length
g	interparticle interaction parameter
γ	1D Lieb-Liniger (dimensionless) interaction parameter
T_d	temperature of quantum degeneracy
$\overline{\mathcal{T}}$	dimensionless temperature (scaled to T_d)
m	mass
t	time
T	temperature

$\hbar$	Planck's constant
k_{B}	Boltzmann's constant
λ_T	thermal de Broglie wavelength
N	total number of particles
$G^{(1)}$	first-order correlation function
$G^{(2)}$	second-order correlation function
$l^{(\phi)}$	thermal phase coherence length

Chapter 1

Introduction

The discovery of the fully quantum phenomenon known as Bose–Einstein condensation began in 1924 with the work of Satyendra Nath Bose on statistical description of photons [3]. Using this then-new statistics of particles from Bose's paper, now known as Bose–Einstein statistics, Einstein introduced a theory where a system of noninteracting identical particles with integer spin could undergo phase transition [4, 5]. Here, Einstein predicted that a large number of bosons could condense and occupy a single quantum state when the system is cooled below a critical temperature. Once a large number of particles occupy the lowest energy state, the gas of particles acquires a long-range phase coherence absent in the usual ideal gas. However, it proved difficult to achieve the required temperatures and densities for Bose–Einstein condensation to occur because of technological limitations and the fact that regular gases typically condense into liquids or solids above the Bose–Einstein condensate (BEC) critical temperature [6]. The necessary technological advancement required for the experimental realisation of BECs did not emerge until around the 1980s after the development of laser-based techniques such as laser cooling and magneto-optical trapping to cool and trap neutral atoms. Steven Chu, Claude Cohen-Tannoudji, and William D. Phillips developed the necessary methods to cool and trap atoms using laser light. For this development, they won the 1997 Nobel Prize in Physics [7]. The group of Eric Cornell and Carl Wieman at JILA used these new experimental methods to make the first experimental observation of BECs in 1995 using a gas of rubidium-87 atoms [8]. A few months later, a group led by Wolfgang Ketterle at MIT observed a BEC with a much larger number of particles using sodium-23 atoms [9]. The larger number of atoms enabled Ketterle's group to observe important results such as quantum mechanical interference between two different condensates. Cornell, Wieman, and Ketterle were awarded the Nobel Prize in Physics in 2001 for their achievement [10]. Later that same year, when BEC was first observed using the repulsive rubidium and sodium isotopes, evidence of Bose–Einstein condensation was observed using attractive lithium-7 atoms by Randall Hulet's group at Rice University [11] with a definitive proof coming in 1996 [12]. Due to the atoms' attractive interaction, the lithium-7 BEC could only accommodate a smaller number of particles before it destabilises and completely collapses. Since then, BECs in various isotopes have been realised experimentally.

In recent years, both experimental and theoretical efforts have been devoted to advancing the field of ultracold atoms [13, 14]. The advances in ultracold atom experiments have fuelled the growing interest in studying quantum many-body systems far from equilibrium [15] in recent years. The isolation and high tunability of experimental setups of ultracold atomic systems made them an attractive option to realise many paradigmatic models of quantum many-body theory with a high degree of accuracy. Apart from a wide range of tools available for experimental control and tunability of system parameters, the key advantage of using ultra-cold atoms for understanding nonequilibrium physics is that the desired dynamics in these systems occurs over observable timescales – often on the order of seconds. This is in stark contrast to the very fast (on the order of picosecond) timescales of equilibration typical of conventional condensed matter systems.

Nonequilibrium quantum many-body dynamics

Quantum many-body systems in equilibrium can be understood through the techniques of equilibrium quantum statistical mechanics [16]. Statistical mechanics is built upon the fundamental connection between the microscopic and macroscopic properties of an isolated system. When such a system settles into an equilibrium state, all its microstates are equally likely to occur over long periods of time. This key hypothesis is known as the fundamental assumption of statistical mechanics. It provides the basis for introducing the so-called micro-canonical ensemble a nd calculating average macroscopic observables by assuming that time averages in such an equilibrium state can be replaced by (time-independent) ensemble averages. This ergodic hypothesis leads to the introduction of other statistical ensembles, such as the canonical and grand-canonical ensembles, for open systems in thermal or diffusive contact with a reservoir (respectively).

By contrast, there is no similar stepping-stone for formulating foundational principles of nonequilibrium statistical mechanics. Moreover, understanding such principles is hindered by the fact that the out-of-equilibrium dynamics of interacting many-body systems is, by itself, an unsolved problem in quantum physics, with different approaches (approximate or exact) being typically tailored for generic (nonintegrable) and integrable models. Here, a system is said to be integrable if the number of its integrals of motion or conserved quantities equals exactly the number of its degrees of freedom. The presence of a full set of conserved quantities precludes thermalisation of the system. Some of the most significant open questions in out-of-equilibrium many-body physics include [15]: How can we classify nonequilibrium behaviour in closed many-body systems? What is the general relation between integrability and dynamics? What is the dynamical effect of a gradual breaking of integrability?

Among the nonequilibrium many-body systems realised in ultracold atom experiments, studies of relaxation in *isolated* one-dimensional systems are of particular interest [17–21]. Specifically, reaching an understanding of how such systems evolve to a new equilibrium state, if they do indeed thermalise, after bringing the system out of equilibrium.

An effective 1D system can be experimentally realised by trapping a Bose gas in a highly anisotropic 3D potential where the trap frequency in one direction (longitudinal direction) is much lower than

the trap frequency in the other two directions (transverse direction), *e.g.* $\omega_x \ll \omega_y = \omega_z$, given that the chemical potential of the system is lower than the excitation energy of the harmonic trap in the transverse direction. In this configuration, the energy modes in the transverse direction are highly suppressed, and those states tend toward their respective static harmonic oscillator ground state. The Bose gas, effectively, becomes a 1D system. The first experimental realisation of a Bose gas in such configuration was done by the group of Ketterle [22] using highly elongated magnetic traps.

In 3D, a weakly interacting Bose gas undergoes a transition to a true Bose–Einstein condensate (BEC) at sufficiently low temperature, where there is a macroscopic particle occupation of the same quantum state. Here, the system shows off-diagonal long-range order where the one-body density matrix, $\hat{\rho}(\mathbf{r}, \mathbf{r}') = \langle \hat{\psi}^\dagger(\mathbf{r}) \hat{\psi}(\mathbf{r}') \rangle$, gives a finite value in the thermodynamic limit, instead of going to zero even as $|\mathbf{r} - \mathbf{r}'| \to \infty$ [23]. This means that remote parts of the gas exhibit correlated behaviour. However, the Mermin–Wagner–Hohenberg theorem [24, 25] prohibits the existence of off-diagonal long-range order in lower dimensions at finite temperatures. Indeed, long-range order does not occur in a one-dimensional system even at zero temperature. While there is still a macroscopic occupation of the lowest energy quantum state, with interparticle interactions suppressing the fluctuations of the density in the weakly interacting regime [26–28], long-wave fluctuations of the phase result in an algebraic decay of the one-particle density matrix [26–30]. Such a phase is called a *quasicondensate* because it shares certain properties with those of a true BEC (suppressed density fluctuations), but long-range phase coherence is lost even in the thermodynamic limit [31–33].

One way of bringing a quantum system out of equilibrium is the so-called quantum quench [34, 35]. A quantum quench is a nonadiabatic protocol wherein a quantum system is prepared in an eigenstate (in most cases, the ground state) of an initial Hamiltonian $\hat{H}(\lambda_i)$ with some parameter of interest λ_i. Then, at some initial time t_0, the parameter λ_i is suddenly changed (quenched) to another value λ_f, and the system evolves according to the new Hamiltonian $\hat{H}(\lambda_f)$ of the system. The system is now in a nonequilibrium scenario because the initial state of the system is not an eigenstate of the new Hamiltonian. Experimentally, the length of time in which the parameter of interest is changed from λ_i to λ_f should be much less than the relaxation time of the system; otherwise, the system will have time to evolve adiabatically.

Given that an isolated quantum system evolves unitarily in time according to the system's Hamiltonian, that is, $|\psi(t)\rangle = e^{-i\hat{H}t/\hbar}|\psi(0)\rangle$, it follows that we should not observe thermalisation. Information about the initial state of the system is retained in the many-body state $|\psi(t)\rangle$ at all times. However, one- or few-body observables can relax to distributions that appear consistent with the predictions of thermal ensembles [36]. This is because, in an isolated (complex) many-body quantum system, one cannot determine all the quantum numbers of the state [37, 38]. Typical observables or measurable quantum numbers comprise only a subset/subsystem of the total many-body Hilbert space. This subsystem is immersed in a subspace of undetermined quantum numbers, which acts as a thermal bath or reservoir for the subsystem. This scenario is similar to a (grand) canonical ensemble of the subsystem coupled to the reservoir and is expected to give thermal properties to the subsystem.

In generic (non-integrable) isolated quantum systems, thermalisation occurs through a mechanism

known as the eigenstate thermalisation hypothesis (ETH) [39] (for recent reviews, see Refs. [38,40,41]). ETH, which was proposed by Deutsch [42] and Srednicki [43], postulates that thermalisation happens at the level of eigenstates. That is, given an energy eigenstate $|j\rangle$ of the system's Hamiltonian $\hat{H}$ with mean energy $E_j = \langle j|\hat{H}|j\rangle$, the expectation value $\langle j|\hat{\mathcal{O}}|j\rangle$ of a few-body observable $\hat{\mathcal{O}}$ is equal to the thermal average given by a thermal ensemble at mean energy E_j. According to ETH, the equilibrium value of the observable $\hat{\mathcal{O}}$ is encoded in the system from the start and is revealed by the dephasing between different energy eigenstates $|j\rangle$ during the system's evolution.

On the other hand, integrable isolated systems fail to exhibit eigenstate thermalisation [44]. Instead of relaxing to a thermal state described by the conventional ensembles of statistical mechanics, integrable quantum systems were recently shown to generally relax to a non-thermal state described by the so-called generalised Gibbs ensemble (GGE) [45]. This is due to the many conserved quantities $\{\hat{\mathcal{I}}_m\}$ that exist in an integrable system and prohibit its relaxation to a thermal state. In a GGE, the many-body density matrix is given by

$$\hat{\rho} = \frac{\exp[-\sum_m \lambda_m \hat{\mathcal{I}}_m]}{\mathrm{Tr}\{\exp[-\sum_m \lambda_m \hat{\mathcal{I}}_m]\}} \tag{1.1}$$

and incorporates all integrals of motion. Here, each conserved quantity $\hat{\mathcal{I}}_m$ has its own Lagrange multiplier λ_m. For the case of a thermal state described by the canonical ensemble with the system Hamiltonian $\hat{H}$, $\hat{\mathcal{I}}_1 = \hat{H}$ and $\lambda_1 = \beta = 1/k_B T$ is the inverse temperature T. In the grand-canonical ensemble, one has an additional pair – the total number of particles $\hat{\mathcal{I}}_2 = \hat{N}$ and the chemical potential $\lambda_2 = -\beta\mu$.

One of the first experiments on relaxation in an isolated ultracold atomic gas was the realisation of a quantum Newton's cradle by Kinoshita *et al.* [17]. Here, with the use of a strongly interacting (hard-core) 1D Bose gas in a harmonic trap, they realised a quantum Newton's cradle by bringing the system out of equilibrium in a way that split the system into two halves with equal but opposite momenta. After the quench, the system underwent repeated collisions and did not equilibrate even after thousands of collisions. This phenomenon of non-thermalisation was first attributed to the integrability of the Lieb–Liniger model [46, 47] that approximately describes the system. However, Rigol *et al.* showed in Ref. [45] that this system relaxed to a non-thermal state described by a GGE.

Another example of interesting relaxation dynamics in an isolated ultracold quantum gas is the experiment of Hofferberth *et al.* [18]. They studied how dephasing occurs in a coherently split 1D Bose gas. Starting with a 1D Bose gas in equilibrium, they quenched the system by splitting the 1D gas along the longitudinal direction. This splitting process ensured that the two 1D Bose gases had the same initial local phases. They then observed how the two new 1D Bose gases evolved (dephased) independently from each other. Here, they observed that the phase coherence between the two Bose gases followed a subexponential decay [48, 49]. In just an order of milliseconds, the system had already reached a seemingly relaxed state. This is in full contrast with what was observed in the quantum Newton's cradle experiment, although both systems can be described by the same integrable Lieb–Liniger model. In light of the results of Gring *et al.* [19], the fast dephasing in Ref. [18] has been reinterpreted as relaxation to a prethermal state [50] and not to its final thermal state. Subsequent studies on dephasing

dynamics in a coherently split 1D Bose gas also showed that the steady state reached by the system due to prethermalisation could be described by a GGE [21]. Also, they observed that during the evolution to a prethermalised state, thermal phase correlations emerge locally in their final prethermalised form and propagate through the system in a light-cone-like evolution [20, 51]. In a recent study [52], it has been shown that after reaching the prethermal state, the coherently split 1D Bose gas then continues to dephase in a slower second light-cone-like evolution to its final thermal state.

Outline of the thesis

This thesis is organised as follows:

In Chapter 2, we give a review of essential theoretical background on Bose gases, both in 3D and 1D geometries. We also introduce the numerical methods we use for incorporating quantum and thermal fluctuations in numerical simulations of Bose gases.

In Chapter 3, we study the thermalisation of tunnel-coupled one-dimensional quasicondensates. Here, we consider cases where the two initially independent quasicondensates have temperature and chemical potential gradients. We characterise the dynamics after a quench of the coupling parameter and relaxed state of the coupled system.

In Chapter 4, we study the relaxation of an extended Josephson junction to a phase-locked state. Motivated by Ref. [53], we try to reproduce the fast relaxation to a phase-locked state observed in the experiment.

In Chapter 5, we study the breathing mode oscillations of a Bose gas after a quench of the longitudinal harmonic trap frequency. We characterise the breathing mode dynamics and try to understand the underlying mechanism behind the damping of oscillations at finite temperature.

In Chapter 6, we study the propagation of shock waves in a 1D Bose gas. We investigate the effects of thermal and quantum fluctuations on the behaviour of shock waves.

We conclude this thesis in Chapter 7 with a summary of our main results.

Chapter 2

Theoretical Background

In this chapter, we introduce the theoretical models used in this thesis. We start by discussing the phenomenon of Bose–Einstein condensation in three-dimensional (3D) systems. From the 3D Hamiltonian of the system, we derive the mean-field and low-energy effective theories of a Bose gas. We then introduce the one-dimensional (1D) model for a Bose gas in a 1D trap. The different physical regimes of a 1D Bose gas at different interaction strengths and temperatures are introduced, emphasising the quasicondensate regime that is the focus of this thesis. Lastly, we introduce the stochastic methods used to include quantum and thermal fluctuations in numerical simulations of 1D Bose gases.

2.1 Bose–Einstein condensation

In this section, we discuss some of the foundational concepts required for the study of Bose–Einstein condensates. We first consider the ideal system of noninteracting bosons. Let us recall that in the grand canonical ensemble, the probability of realising a configuration with N_k particles in a state k with energy E_k is calculated as

$$P(k) = \frac{1}{\mathcal{Z}} e^{\beta(\mu N_k - E_k)}, \tag{2.1}$$

where $\beta = 1/k_{\mathrm{B}}T$ is the inverse temperature with k_{B} being the Boltzmann constant, and μ is the chemical potential of the reservoir with which the system is in thermal equilibrium. The normalisation constant for the probability $P(k)$ is given by the partition function

$$\mathcal{Z} = \sum_{N_k=0}^{\infty} \sum_{k} e^{-\beta(E_k - \mu N_k)}, \tag{2.2}$$

which is the sum of the Gibbs factors for all states k.

Because the system under consideration is composed of non-interacting particles (ideal gas), it can be described by the independent particle Hamiltonian

$$\hat{H} = \sum_{i} \hat{H}_i^{(1)}, \tag{2.3}$$

where $\hat{H}_i^{(1)}$ is the single particle Hamiltonian with energy eigenvalue ϵ_i. In this case, the total energy of the system is given by $E_k = \sum_i \epsilon_i n_i$, with corresponding total number of particles $N_k = \sum_i n_i$ where n_i is the occupation number for the ith single-particle state. Using these expressions, the grand canonical partition function can be written as

$$\mathcal{Z} = \prod_i \left[\sum_{n_i} e^{-\beta(\epsilon_i - \mu) n_i} \right], \tag{2.4}$$

where the sum $\sum_{n_i}$ extends over the values $n_i = 0, 1, 2, \ldots$. The grand canonical potential is then given by

$$\Omega = -k_\mathrm{B} T \ln \mathcal{Z}, \tag{2.5}$$

$$= k_\mathrm{B} T \ln\left[1 - e^{-\beta(\epsilon_i - \mu)}\right], \tag{2.6}$$

where we have employed the partition function from Eq. (2.4). Using the relation $N = -\partial\Omega/\partial\mu$, the total number of particles for the ideal Bose gas is

$$N = \sum_i \frac{1}{e^{\beta(\epsilon_i - \mu)} - 1} = \sum_i \langle n_i \rangle, \tag{2.7}$$

where the average occupation number

$$\langle n_i \rangle = \frac{1}{e^{\beta(\epsilon_i - \mu)} - 1}, \tag{2.8}$$

is the well known Bose–Einstein distribution. Equation (2.8) gives an important physical constraint $\mu < \epsilon_0$ for the chemical potential of the ideal Bose gas. Here, ϵ_0 is the lowest energy eigenvalue of the single-particle Hamiltonian in Eq. (2.3). Any μ greater than ϵ_0 would result in an unphysical negative occupation number of the states i with energy ϵ_i less than μ. For systems where $\mu \to \epsilon_0$, the occupation number

$$N_0 \equiv \langle n_0 \rangle = \frac{1}{e^{\beta(\epsilon_0 - \mu)} - 1}, \tag{2.9}$$

of the lowest energy state becomes larger, and that state is said to be highly occupied. This mechanism leads to the phenomenon of Bose–Einstein condensation.

2.1.1 Bose–Einstein condensation in a box

Let us now consider the simple case of Bose–Einstein condensation of an ideal Bose gas in a box of volume $V = L^3$ with L being the length of the sides of the box. In this case, the single-particle Hamiltonian is given by

$$H^{(1)} = \frac{p^2}{2m}, \tag{2.10}$$

where $\mathbf{p} = (p_x, p_y, p_z)$ is the momentum of a bosonic particle, and m is its mass. Using periodic boundary conditions: $\phi(x, y, z) = \phi(x + L, y, z) = \phi(x, y + L, z) = \phi(x, y, z + L)$, the solution to the single-particle Hamiltonian is plane waves given by

$$\phi_\mathbf{p} = \frac{1}{\sqrt{V}} e^{i\mathbf{p}\cdot\mathbf{r}/\hbar}, \tag{2.11}$$

with energy $\epsilon = p^2/2m$ and momentum $\mathbf{p} = 2\pi\hbar\mathbf{n}/L$ where $\mathbf{n}$ is a vector whose components n_x, n_y, n_z are $0, \pm1, \pm2, \ldots$.

The total number of particles can be divided into two components:

$$N = N_0 + N_T, \tag{2.12}$$

where N_0 is the number of condensate particles, given in Eq. (2.9), with energy ϵ_0, whereas N_T is the number of non-condensed (thermal) particles:

$$N_T = \sum_{\mathbf{p}\neq 0} \frac{1}{e^{\beta(p^2/2m-\mu)} - 1}. \tag{2.13}$$

To estimate N_T analytically, we make the approximation $\sum_{\mathbf{p}\neq 0} \to V/(2\pi\hbar)^3 \int \mathrm{d}\mathbf{p}$ and make use of the substitution $x = (p^2/2m)/k_\mathrm{B}T$. The number of non-condensed particles is then given by

$$N_T = \frac{V}{(2\pi\hbar)^3} \int_0^\infty \frac{1}{e^{\beta(p^2/2m-\mu)} - 1} 4\pi p^2 \mathrm{d}p, \tag{2.14}$$

$$= \frac{V}{\lambda_T^3} g_{3/2}\left(e^{\beta\mu}\right), \tag{2.15}$$

where

$$\lambda_T = \sqrt{\frac{2\pi\hbar^2}{mk_\mathrm{B}T}}\,, \tag{2.16}$$

is the thermal de Broglie wavelength. The function $g_{3/2}(z)$ is a special case of the more general class of Bose functions

$$g_p(z) = \frac{1}{\Gamma(p)} \int_0^\infty \mathrm{d}x x^{p-1} \frac{1}{z^{-1}e^x - 1} = \sum_{l=1}^\infty \frac{z^l}{l^p}, \tag{2.17}$$

where the Gamma function is defined as

$$\Gamma(s) = \int_0^\infty x^{s-1} e^{-x} \mathrm{d}x. \tag{2.18}$$

For $s = 3/2$, the Gamma function gives $\Gamma(3/2) = \sqrt{\pi}\,/2$. Note that the replacement of the sum with an integral above is justified only if the thermal energy $k_\mathrm{B}T$ is much larger than the energy spacing between single-particle levels, that is, if $k_\mathrm{B}T \gg \hbar^2/2mV^{2/3}$. We see from Eq. (2.15) that the density of thermal particles $n_T = N_T/V$ increases with increasing chemical potential μ. However, from the constraint $\mu < \epsilon_0 = 0$, we see that the number of non-condensed particles saturates at a critical density

$$n_c \equiv \frac{N_c}{V} = \frac{g_{3/2}(1)}{\lambda_T^3} \approx \frac{2.612}{\lambda_T^3}. \tag{2.19}$$

This means that as we add more particles N, they are required to occupy the ground state energy level, and condensation to this state begins. From the critical density given above, we see that the onset of condensation can be understood as the point where the mean interparticle separation is of the order of the de Broglie wavelength: $n^{-1/3} \sim \lambda_T$. Substituting the definition of the de Broglie wavelength from Eq. (2.16) into Eq. (2.19) gives us an expression for the critical temperature of the system

$$k_\mathrm{B}T_c = \frac{2\pi\hbar^2}{mg_{3/2}^{2/3}(1)} \left(\frac{N}{V}\right)^{2/3}, \tag{2.20}$$

below which the condensate appears. Using these expressions, one can show that the number of particles in the condensate at any temperature T_c is given by

$$N_0(T) = N\left[1 - \left(\frac{T}{T_c}\right)^{3/2}\right]. \tag{2.21}$$

2.2 Dilute Bose Gas

Let us now consider an interacting Bose gas, specifically, a dilute Bose gas in a potential trap. In dilute Bose gases, the inter-particle interactions between particles are short ranged compared to the typical inter-particle distance $n^{-1/3}$ between atoms. As a result, dilute Bose gases can be well described by a theory that only considers interactions between pairs of particles (two-body interactions) and neglects all other multi-particle interactions. These two-body interactions are described by a scalar potential that is a function of the relative position of the particles $V_{\text{int}}(|\mathbf{r} - \mathbf{r}'|)$. The second quantised Hamiltonian describing a dilute interacting Bose gas is given by

$$\hat{H} = \int \hat{\Psi}^\dagger(\mathbf{r}, t) H_{\text{sp}} \hat{\Psi}(\mathbf{r}, t) \mathrm{d}\mathbf{r} + \frac{1}{2} \iint \hat{\Psi}^\dagger(\mathbf{r}, t) \hat{\Psi}^\dagger(\mathbf{r}', t) V_{\text{int}}(|\mathbf{r} - \mathbf{r}'|) \hat{\Psi}(\mathbf{r}', t) \hat{\Psi}(\mathbf{r}, t) \mathrm{d}\mathbf{r}' \mathrm{d}\mathbf{r}, \tag{2.22}$$

where the single particle Hamiltonian H_{sp} is given by

$$H_{\text{sp}} = -\frac{\hbar^2}{2m}\nabla^2 + V_{\text{ext}}(\mathbf{r}), \tag{2.23}$$

and $V_{\text{ext}}(\mathbf{r})$ is the external trapping potential. The bosonic field operators $\hat{\Psi}^\dagger(\mathbf{r}, t)$ and $\hat{\Psi}(\mathbf{r}, t)$, which create and annihilate particles, respectively, at the position $\mathbf{r}$ can be expanded in the single-particle eigenbasis $\varphi(\mathbf{r}, t)$ as

$$\hat{\Psi}^\dagger(\mathbf{r}, t) = \sum_i \hat{a}_i^\dagger(t) \varphi_i^*(\mathbf{r}, t), \tag{2.24}$$

$$\hat{\Psi}(\mathbf{r}, t) = \sum_i \hat{a}_i(t) \varphi_i(\mathbf{r}, t). \tag{2.25}$$

These field operators satisfy the equal-time commutation relations

$$\left[\hat{\Psi}(\mathbf{r}, t), \hat{\Psi}^\dagger(\mathbf{r}', t)\right] = \delta(\mathbf{r} - \mathbf{r}'), \tag{2.26}$$

$$\left[\hat{\Psi}(\mathbf{r}, t), \hat{\Psi}(\mathbf{r}', t)\right] = \left[\hat{\Psi}^\dagger(\mathbf{r}, t), \hat{\Psi}^\dagger(\mathbf{r}', t)\right] = 0. \tag{2.27}$$

The creation and annihilation operators $\hat{a}_i^\dagger$ and $\hat{a}_i$, respectively, similarly obey the commutation relations

$$[\hat{a}_i, \hat{a}_{i'}^\dagger] = \delta_{i,i'}, \tag{2.28}$$

$$[\hat{a}_i, \hat{a}_i] = [\hat{a}_i^\dagger, \hat{a}_i^\dagger] = 0, \tag{2.29}$$

while the corresponding single-particle basis function $\varphi_i(\mathbf{r}, t)$ satisfies the orthonormality condition

$$\int \varphi_i^\dagger(\mathbf{r}, t) \varphi_{i'}(\mathbf{r}, t) \mathrm{d}\mathbf{r} = \delta_{i,i'}. \tag{2.30}$$

In principle, the Hamiltonian in Eq. (2.22) provides a complete description of dilute Bose gases. However, solving for the equation of motion that results from this Hamiltonian is difficult in practice due to the inter-particle interaction potential. Fortunately, it can be shown that for low-energy collisions typical at ultra-cold temperatures, the scattering amplitude for two-body interactions is approximately independent of the energy and angle of the scattering event [54]. This is the regime where atomic interactions are dominated by low-energy s-wave collisions, and the scattering is characterised by a single parameter, the s-wave scattering length a_s. We further simplify the description of the dilute Bose gas given in Eq. (2.22) by introducing a computationally convenient effective interaction potential $V_{\text{int}}^{\text{eff}}(|\mathbf{r}-\mathbf{r}'|)$:

$$V_{\text{int}}(|\mathbf{r}-\mathbf{r}'|) \to V_{\text{int}}^{\text{eff}}(|\mathbf{r}-\mathbf{r}'|) = g_{3\text{D}}\delta(\mathbf{r}-\mathbf{r}'), \tag{2.31}$$

where $g_{3\text{D}} = 4\pi\hbar^2 a_s/m$ is the three-dimensional interparticle interaction parameter and is dependent only on the scattering length a_s and the atomic mass m. By invoking the properties of the delta function, the Hamiltonian in Eq. (2.22) can then be written as

$$\hat{H} = \int \hat{\Psi}^\dagger(\mathbf{r},t)H_{\text{sp}}\hat{\Psi}(\mathbf{r},t)\mathrm{d}\mathbf{r} + \frac{g_{3\text{D}}}{2}\int \hat{\Psi}^\dagger(\mathbf{r},t)\hat{\Psi}^\dagger(\mathbf{r},t)\hat{\Psi}(\mathbf{r},t)\hat{\Psi}(\mathbf{r},t)\mathrm{d}\mathbf{r}. \tag{2.32}$$

Using the Heisenberg equation of motion

$$i\hbar\frac{\partial}{\partial t}\hat{\Psi}(\mathbf{r},t) = \left[\hat{\Psi}(\mathbf{r},t), \hat{H}\right], \tag{2.33}$$

the time evolution of the field operator $\hat{\Psi}(\mathbf{r},t)$ is given by

$$i\hbar\frac{\partial}{\partial t}\hat{\Psi}(\mathbf{r},t) = \left[H_{\text{sp}} + g_{3\text{D}}\hat{\Psi}^\dagger(\mathbf{r},t)\hat{\Psi}(\mathbf{r},t)\right]\hat{\Psi}(\mathbf{r},t). \tag{2.34}$$

2.2.1 The Gross–Pitaevskii equation

The Gross–Pitaevskii equation is the central tool used in the theoretical description of Bose–Einstein condensates. This widely employed tool, introduced independently by Eugene P. Gross [55] and Lev Petrovich Pitaevskii [56] in 1961, is a classical mean-field equation that describes the behaviour of Bose–Einstein condensates at zero temperature. This is only possible due to the remarkable feature of Bose–Einstein condensates that, though a purely quantum phenomena, can be described by a classical equation due to macroscopic particle occupation of a single quantum state.

Using the decomposition of the field operator in Eq. (2.25), we single out the lowest energy state and write:

$$\hat{\Psi}(\mathbf{r},t) = \hat{a}_0\varphi_0(\mathbf{r},t) + \sum_{i=1}^{\infty}\hat{a}_i(t)\varphi_i(\mathbf{r},t). \tag{2.35}$$

In order to derive the Gross–Pitaevskii equation, we consider the zero temperature limit of the Bose gas, in which all of the particles occupy the lowest energy state. Thus, all states higher than $i = 0$ are vacant:

$$\hat{\Psi}(\mathbf{r},t) = \hat{a}_0\varphi_0(\mathbf{r},t). \tag{2.36}$$

It should be noted that a theoretical description of the dilute gas that includes the higher-energy states of $\hat{\Psi}(\mathbf{r},t)$ using classical fields can be constructed. We shall consider this in Section 2.2.4.

Assuming that the number of particles in the condensate mode is large, *i.e.* $N_0 \equiv \langle \hat{a}_0^\dagger \hat{a}_0 \rangle \gg 1$, then the commutator $\hat{a}_0 \hat{a}_0^\dagger - \hat{a}_0^\dagger \hat{a}_0 = 1$ is small compared to the operators themselves. This enables us to neglect the non-commutability of the operator $\hat{a}_0$ and write it as an ordinary number [57]:

$$\hat{a}_0 \to a_0 = \sqrt{N_0}\ , \tag{2.37}$$

$$\hat{a}_0^\dagger \to a_0^* = \sqrt{N_0}\ . \tag{2.38}$$

Thus, instead of dealing with the field operator $\hat{\Psi}(\mathbf{r}, t)$, we can now replace it by a c-number given by

$$\hat{\Psi}(\mathbf{r}, t) \to \Psi_0(\mathbf{r}, t) = \sqrt{N_0}\ \varphi_0(\mathbf{r}, t), \tag{2.39}$$

$$\hat{\Psi}^\dagger(\mathbf{r}, t) \to \Psi_0^*(\mathbf{r}, t) = \sqrt{N_0}\ \varphi_0^*(\mathbf{r}, t). \tag{2.40}$$

The classical field Hamiltonian is obtained be substitution of the c-numbers into Eq. (2.32):

$$H = \int \Psi_0^*(\mathbf{r}, t) H_{\text{sp}} \Psi_0(\mathbf{r}, t) \mathrm{d}\mathbf{r} + \frac{g_{3\text{D}}}{2} \int \Psi_0^*(\mathbf{r}, t) \Psi_0^*(\mathbf{r}, t) \Psi_0(\mathbf{r}, t) \Psi_0(\mathbf{r}, t) \mathrm{d}\mathbf{r}. \tag{2.41}$$

Replacing the field operators in Eq. (2.34) leads us to the Gross–Pitaevskii equation:

$$i\hbar \frac{\partial}{\partial t} \Psi_0(\mathbf{r}, t) = \left[-\frac{\hbar^2 \nabla^2}{2m} + V_{\text{ext}}(\mathbf{r}, t) + g_{3\text{D}} |\Psi_0(\mathbf{r}, t)|^2 \right] \Psi_0(\mathbf{r}, t), \tag{2.42}$$

where we use the notation $|\Psi_0(\mathbf{r}, t)|^2 = \Psi_0^*(\mathbf{r}, t) \Psi_0(\mathbf{r}, t)$.

We note that the time-dependence of the condensate mode can be written as

$$\Psi_0(\mathbf{r}, t) = \Psi_0(\mathbf{r}) e^{-i\mu_{3\text{D}} t/\hbar}, \tag{2.43}$$

where $\Psi_0(\mathbf{r})$ is the stationary solution of the GPE and $\mu_{3\text{D}}$ is the three-dimensional chemical potential. Substituting this solution into Eq. (2.42), we get the time-independent Gross–Pitaevskii equation:

$$\mu_{3\text{D}} \Psi_0(\mathbf{r}) = \left[-\frac{\hbar^2 \nabla^2}{2m} + V_{\text{ext}}(\mathbf{r}, t) + g_{3\text{D}} |\Psi_0(\mathbf{r})|^2 \right] \Psi_0(\mathbf{r}). \tag{2.44}$$

One characteristic length scale of Bose–Einstein condensates worth mentioning at this point is the healing length

$$\xi = \frac{1}{\sqrt{4\pi \rho_0 a}} = \frac{\hbar}{\sqrt{m \rho_0 g_{3\text{D}}}} \tag{2.45}$$

where $\rho_0 = |\Psi_0|^2$ is the condensate density. The healing length ξ gives the scale over which the density responds to perturbations. For example, in the case of a condensate in an infinite box potential, this is the length scale at which the density profile changes from zero (at the edge of the box) to its maximum value ρ_0 (away from the edge).

Let us now consider a gas confined in a three-dimensional harmonic trap given by

$$V_{\text{ext}} = \frac{1}{2} m \big(\omega_x^2 x^2 + \omega_y^2 y^2 + \omega_z^2 z^2 \big), \tag{2.46}$$

where ω_i ($i = x, y, z$) is the trapping frequency in the i-direction. For a non-interacting gas ($g_{3\text{D}} = 0$), the Gross–Pitaevskii equation becomes the usual Schrödinger equation and the excitation states

correspond to the usual harmonic oscillator states. For weakly interacting particles ($g_{3\mathrm{D}} \neq 0$) where the kinetic energy dominates the interaction between particles, *i.e.*

$$\frac{E_{\mathrm{int}}}{E_{\mathrm{kin}}} \propto N\frac{|a|}{a_{\mathrm{ho}}} \ll 1, \tag{2.47}$$

the system can be approximated as ideal/non-interacting [58]. Here,

$$a_{\mathrm{ho}} = \sqrt{\frac{\hbar}{m\omega_{\mathrm{ho}}}} \tag{2.48}$$

is the mean harmonic oscillator length of the potential trap with $\omega_{\mathrm{ho}} = (\omega_x\omega_y\omega_z)^{1/3}$. For a gas with attractive interactions ($g_{3\mathrm{D}} < 0$), the particles tend to clump at the state of lowest energy, with density $\rho_0 = |\Psi_0|^2$ at the centre of the trap.

2.2.2 Thomas–Fermi limit

For repulsive inter-particle interactions, $g_{3\mathrm{D}} > 0$, the density profile becomes broad. As the strength of interactions increases, the variation of the density profile becomes smooth with respect to the distance from the centre of the harmonic trap. In this limit, the kinetic energy term $-\hbar^2\nabla^2\Psi_0(\mathbf{r})/(2m)$ can be disregarded in comparison to the interaction term $g_{3\mathrm{D}}|\Psi_0(\mathbf{r})|^2\Psi_0(\mathbf{r})$. This is known as the Thomas–Fermi limit and is valid for

$$N\frac{a_s}{a_{\mathrm{ho}}} \gg 1. \tag{2.49}$$

This quantity is called the Thomas–Fermi parameter. In this limit, the density profile of the condensate, from the time-independent Gross–Pitaevskii equation (Eq. (2.44)), is given by

$$\rho_0(\mathbf{r}) = |\Psi_0(\mathbf{r})|^2 = \frac{1}{g_{3\mathrm{D}}}\big[\mu_{3\mathrm{D}} - V_{\mathrm{ext}}(\mathbf{r})\big], \tag{2.50}$$

for $\mu_{3\mathrm{D}} > V_{\mathrm{ext}}(\mathbf{r})$ and zero elsewhere. For an external harmonic trap like the one given above, the density profile of the condensate in the Thomas–Fermi limit is given by an inverted parabola that vanishes at the turning points defined by the Thomas–Fermi radius along the i-direction ($i = x, y, z$):

$$R_{\mathrm{TF},i} = \sqrt{\frac{2\mu_{3\mathrm{D}}}{m\omega_i^2}}\ , \tag{2.51}$$

Integrating Eq. (2.50) over the unit sphere and using the normalisation condition $\int |\Psi_0(\mathbf{r})|^2 \mathrm{d}\mathbf{r} = N$ leads us to the analytical expression for the chemical potential in the Thomas–Fermi limit:

$$\mu_{3\mathrm{D}} = \frac{\hbar\omega_{\mathrm{ho}}}{2}\left(\frac{15Na}{a_{\mathrm{ho}}}\right)^{2/5}. \tag{2.52}$$

It is useful to write $\rho_0(\mathbf{r})$ in terms of the peak value of the density profile (the density at the centre of the trap) $\rho_0(0)$. To do this, we rewrite Eq. (2.50) in terms of R_i and get

$$\rho_0(\mathbf{r}) = \rho_0(0)\left(1 - \frac{x^2}{R_x^2} - \frac{y^2}{R_y^2} - \frac{z^2}{R_z^2}\right), \tag{2.53}$$

where $\rho_0(0) = \mu_{3\mathrm{D}}/g_{3\mathrm{D}}$. With Eq. (2.52), the relation between the density at the centre of the trap and the total number of particles can easily be obtained and is given by

$$\rho_0(0) = \frac{1}{8\pi a}\frac{1}{a_{\mathrm{ho}}^2}\left(\frac{15Na}{a_{\mathrm{ho}}}\right)^{2/5}. \tag{2.54}$$

2.2.3 Hydrodynamic equations

The Gross–Pitaevskii equation (Eq. (2.42)) can be conveniently represented in terms of classical fluid dynamics by employing the Madelung transformation [59]

$$\Psi_0(\mathbf{r},t) = \sqrt{\rho_0(\mathbf{r},t)}\, e^{i\phi(\mathbf{r},t)}, \tag{2.55}$$

where $\phi(\mathbf{r},t)$ is the macroscopic phase of the condensate. The gradient of the phase defines a velocity field given by

$$\mathbf{v}(\mathbf{r},t) = \frac{\hbar}{m}\nabla\phi(\mathbf{r},t). \tag{2.56}$$

Because the curl of the gradient of any non-singular function vanishes, $\nabla \times \nabla f(\mathbf{r}) = 0$, it follows that the curl of the velocity field $\mathbf{v}$ vanishes:

$$\nabla \times \mathbf{v}(\mathbf{r},t) = 0. \tag{2.57}$$

As a consequence, the velocity field of the condensate is irrotational and the possible motions of the condensate are more restricted than those of a classical fluid [6]. Substitution of Eq. (2.55) into the GPE and equating the real and imaginary parts leads to two coupled equations:

$$\frac{\partial}{\partial t}\rho_0(\mathbf{r},t) = -\nabla\cdot\left[\rho_0(\mathbf{r},t)\mathbf{v}(\mathbf{r},t)\right], \tag{2.58}$$

$$m\frac{\partial}{\partial t}\mathbf{v}(\mathbf{r},t) = -\nabla\left[\frac{1}{2}m\mathbf{v}^2(\mathbf{r},t) + V_{\text{ext}} + g_{3\text{D}}\rho_0(\mathbf{r},t) - \frac{\hbar^2}{2m}\frac{1}{\sqrt{\rho_0(\mathbf{r},t)}}\nabla^2\sqrt{\rho_0(\mathbf{r},t)}\right]. \tag{2.59}$$

Eq. (2.58) is the well-known continuity equation that expresses the conservation of particle number, while Eq. (2.59) describes the evolution of the velocity field $\mathbf{v}(\mathbf{r},t)$. Under stationary conditions and constant phase ($\mathbf{v} = 0$), Eq. (2.59) is exactly the time-independent Gross–Pitaevskii equation (Eq. (2.44)).

The term $g_{3\text{D}}\rho_0(\mathbf{r},t)$ in Eq. (2.59) is the expression for the chemical potential $\mu_{3\text{D}}$ of a uniform Bose gas. At zero temperature, changes in the chemical potential of a system are related to changes in the pressure P via the Gibbs–Duhem thermodynamic relation [6, 23]

$$\rho_0 = \left(\frac{\partial P}{\partial \mu_{3\text{D}}}\right)_{T=0}, \tag{2.60}$$

that enables us to define the pressure

$$P(\mathbf{r},t) = \frac{1}{2}\frac{\mu_{3\text{D}}^2(\mathbf{r},t)}{g_{3\text{D}}} = \frac{1}{2}g_{3\text{D}}\rho_0^2(\mathbf{r},t). \tag{2.61}$$

Thus, after some further manipulations[1], Eq. (2.59) may be rewritten in a more familiar form given by [60, 61]

$$m\rho_0(\mathbf{r},t)\left[\frac{\partial}{\partial t}\mathbf{v}(\mathbf{r},t) + (\mathbf{v}(\mathbf{r},t)\cdot\nabla)\mathbf{v}(\mathbf{r},t)\right] = -\nabla\left[P(\mathbf{r},t) + P_q(\mathbf{r},t)\right] - \rho_0(\mathbf{r},t)\nabla V_{\text{ext}}, \tag{2.62}$$

[1] By using the vector identity $\nabla(\mathbf{A}\cdot\mathbf{B}) = (\mathbf{A}\cdot\nabla)\mathbf{B} + (\mathbf{B}\cdot\nabla)\mathbf{A} + \mathbf{A}\times(\nabla\times\mathbf{B}) + \mathbf{B}\times(\nabla\times\mathbf{A})$ and noting that $\nabla\times\mathbf{v}(\mathbf{r},t) = 0$.

that resembles the classical Euler equation describing an inviscid compressible fluid [62]. The only difference between Eq. (2.62) and its classical counterpart is the inclusion of the quantum pressure

$$P_q(\mathbf{r},t) = -\frac{\hbar^2}{4m}\rho_0(\mathbf{r},t)\nabla^2\left[\ln\rho_0(\mathbf{r},t)\right]. \tag{2.63}$$

This term is equivalent to the last term in Eq. (2.59). The quantum pressure is a pure quantum effect and vanishes if we set the Plank's constant equal to zero. Similar to $-m\nabla\mathbf{v}^2/2$ in Eq. (2.59), the origin of the quantum pressure is the kinetic energy term in the GPE (first term on the right-hand side of Eq. (2.42)). Though the same in origin, the two correspond to different physical effects: the term $-m\nabla\mathbf{v}^2/2$ corresponds to the kinetic energy of motion of particles. In contrast, the quantum pressure corresponds to zero-point motion, which creates a pressure that opposes deformation of the condensate (variation of the complex amplitude $\Psi_0(\mathbf{r},t)$) and does not give rise to particle currents [6, 61].

The quantum pressure is small in regions where the density of the condensate changes slowly in space. The quantum pressure term is negligible in the bulk of a trapped condensate where the density is homogeneous. To show this, let us consider the length scale d for the variation of the magnitude of the wave function. The contribution of the pressure P is on the order of $\sim g_{3\mathrm{D}}\rho_0^2$, while the contribution of the quantum pressure P_q is on the order of $\sim \hbar^2\rho_0/md^2$. Then, $P_q/P \sim \hbar^2/mg_{3\mathrm{D}}\rho_0 d^2$, and hence, the quantum pressure term is negligible $(P_q \ll P)$ if spatial variations of the density occur on length scales d much larger than the system's healing length ξ (Eq. (2.45)) [6, 61, 63]. For example, in the Thomas–Fermi regime where the variation of the condensate density is given by the Thomas–Fermi radius $R = \sqrt{2\mu_{3\mathrm{D}}/(m\omega^2)}$, the ratio between R and ξ is

$$\frac{R}{\xi} = \left(\frac{2\mu_{3\mathrm{D}}/(m\omega^2)}{\hbar^2/(m\mu_{3\mathrm{D}})}\right)^{1/2} = \sqrt{2}\,\frac{\mu_{3\mathrm{D}}}{\hbar\omega} \gg 1. \tag{2.64}$$

Thus, the quantum pressure term is negligible in the Thomas–Fermi regime, and Eq. (2.62) reduces to the classical Euler equation that describes the motion of a classical fluid without viscosity.

2.2.4 Bogoliubov theory of interacting Bose gases

We now consider higher-energy states above the condensate mode $\Psi_0(\mathbf{r},t)$ that we previously ignored from Eq. (2.35). We denote these excited states by $\delta\hat{\psi}(\mathbf{r},t)$, which allows us to write:

$$\hat{\Psi}(\mathbf{r},t) = \hat{a}_0\varphi_0(\mathbf{r},t) + \sum_{i=1}^{\infty}\hat{a}_i(t)\varphi_i(\mathbf{r},t), \tag{2.65}$$

$$= \Psi_0(\mathbf{r},t) + \delta\hat{\psi}(\mathbf{r},t), \tag{2.66}$$

where we have replaced the operator $\hat{a}_0$ by a c-number $\sqrt{N_0}$. Here, it is assumed that the condensate mode is still dominant, and we treat the excited particles in $\delta\hat{\psi}(\mathbf{r},t)$ as small fluctuations around the mean value $\Psi_0(\mathbf{r},t)$. This perturbative approach, proposed by Nikolai Bogoliubov in 1947 [57], allows one to describe the elementary excitations of condensates using a linearised approach. Ignoring the fluctuations $\delta\hat{\psi}(\mathbf{r},t)$ leads us back to the GPE.

Using the stationary solution to the GPE, we rewrite Eq. (2.66) as

$$\hat{\Psi}(\mathbf{r},t) = e^{-i\mu_{3\mathrm{D}}t/\hbar}\big[\Psi_0(\mathbf{r}) + \delta\hat{\psi}(\mathbf{r},t)\big]. \tag{2.67}$$

Substituting this into Eq. (2.34) and ignoring all terms that are not linear in $\delta\hat{\psi}(\mathbf{r},t)$ or $\delta\hat{\psi}^\dagger(\mathbf{r},t)$, we obtain the linearised equations of motion for small fluctuations around the mean:

$$i\hbar\frac{\partial}{\partial t}\delta\hat{\psi}(\mathbf{r},t) = \left(-\frac{\hbar^2}{2m}\nabla^2 + V(\mathbf{r}) + 2g_{3\mathrm{D}}|\Psi_0(\mathbf{r})|^2 - \mu_{3\mathrm{D}}\right)\delta\hat{\psi}(\mathbf{r},t) + g_{3\mathrm{D}}\Psi_0^2(\mathbf{r})\delta\hat{\psi}^\dagger(\mathbf{r},t), \tag{2.68}$$

$$-i\hbar\frac{\partial}{\partial t}\delta\hat{\psi}^\dagger(\mathbf{r},t) = \left(-\frac{\hbar^2}{2m}\nabla^2 + V(\mathbf{r}) + 2g_{3\mathrm{D}}|\Psi_0(\mathbf{r})|^2 - \mu_{3\mathrm{D}}\right)\delta\hat{\psi}^\dagger(\mathbf{r},t) + g_{3\mathrm{D}}[\Psi_0^*(\mathbf{r})]^2\delta\hat{\psi}(\mathbf{r},t). \tag{2.69}$$

To solve these coupled equations, we employ the Bogoliubov transformation given by

$$\delta\hat{\psi}(\mathbf{r},t) = \sum_{i=1}^{\infty}\big(u_i(\mathbf{r})\hat{b}_i e^{-i\epsilon_i t/\hbar} + v_i^*(\mathbf{r})\hat{b}^\dagger e^{i\epsilon_i t/\hbar}\big), \tag{2.70}$$

where $\hat{b}_i$ and $\hat{b}_i^\dagger$ are bosonic operators that annihilate and create, respectively, a quasiparticle of elementary excitation with energy given by the Bogoliubov dispersion ϵ_i, and satisfy the commutation relations

$$\left[\hat{b}_i, \hat{b}_{i'}^\dagger\right] = \delta_{i,i'}, \qquad \left[\hat{b}_i, \hat{b}_i\right] = \left[\hat{b}_i^\dagger, \hat{b}_i^\dagger\right] = 0. \tag{2.71}$$

The average occupation number of the quasiparticles with energy ϵ_i is then given by

$$\langle\hat{b}_i^\dagger\hat{b}_i\rangle = \frac{1}{\exp[\beta\epsilon_i] - 1}. \tag{2.72}$$

The functions $u_i(\mathbf{r})$ and $v_i(\mathbf{r})$, called the Bogoliubov modes, are basis functions of the elementary excitations that are yet to be solved. In order for the fluctuations $\delta\hat{\psi}(\mathbf{r},t)$ to still satisfy the bosonic commutation relations, the Bogoliubov modes $u_i(\mathbf{r})$ and $v_i(\mathbf{r})$ in Eq. (2.70) must obey the following conditions:

$$\int\big[u_i(\mathbf{r})u_j^*(\mathbf{r}) - v_i(\mathbf{r})v_j^*(\mathbf{r})\big]\,\mathrm{d}\mathbf{r} = \delta_{ij}, \tag{2.73}$$

$$\sum_i\big[u_i(\mathbf{r})u_i^*(\mathbf{r}') - v_i(\mathbf{r})v_i^*(\mathbf{r}')\big] = \delta(\mathbf{r}-\mathbf{r}'). \tag{2.74}$$

Substituting Eq. (2.70) into the linearised equations of motion Eqs. (2.68) and (2.69) and equating the terms with coefficients $\hat{b}_i$ and $\hat{b}_i^\dagger$, we get the time-independent Bogoliubov–de Gennes equations

$$\begin{aligned}\left(-\frac{\hbar^2}{2m}\nabla^2 + V(\mathbf{r}) + 2g_{3\mathrm{D}}|\Psi_0(\mathbf{r})|^2 - \mu_{3\mathrm{D}}\right)u_i(\mathbf{r}) + g_{3\mathrm{D}}\Psi_0^2(\mathbf{r})v_i(\mathbf{r}) &= \epsilon_i u_i(\mathbf{r}),\\ \left(-\frac{\hbar^2}{2m}\nabla^2 + V(\mathbf{r}) + 2g_{3\mathrm{D}}|\Psi_0(\mathbf{r})|^2 - \mu_{3\mathrm{D}}\right)v_i(\mathbf{r}) + g_{3\mathrm{D}}[\Psi_0^*(\mathbf{r})]^2u_i(\mathbf{r}) &= -\epsilon_i v_i(\mathbf{r}).\end{aligned} \tag{2.75}$$

This set of coupled equations enable us to calculate the Bogoliubov dispersion ϵ_i and the Bogoliubov modes $u_i(\mathbf{r})$ and $v_i(\mathbf{r})$ for any weakly interacting system.

Substituting Eq. (2.67) into the many-body Hamiltonian Eq. (2.32) and retaining only the terms not higher than quadratic in $\hat{\psi}(\mathbf{r},t)$ we get

$$\hat{H}^{(2)} = \frac{i\hbar}{2}\int\left[\delta\hat{\psi}^{\dagger}(\mathbf{r},t)\frac{\partial\delta\hat{\psi}(\mathbf{r},t)}{\partial t} - \frac{\partial\delta\hat{\psi}^{\dagger}(\mathbf{r},t)}{\partial t}\delta\hat{\psi}(\mathbf{r},t)\right]\mathrm{d}\mathbf{r}. \tag{2.76}$$

Note that the zeroth-order term in $\delta\hat{\psi}(\mathbf{r},t)$ is equivalent to Eq. (2.41), whereas the term that is linear in $\delta\hat{\psi}(\mathbf{r},t)$ vanishes since $\Psi_0(\mathbf{r})$ is the solution of the Gross–Pitaevskii equation for the ground state. The Bogoliubov transformation in Eq. (2.70) brings the Hamiltonian Eq. (2.76) to its diagonal form

$$\hat{H}^{(2)} = \sum_i \epsilon_i\left(\hat{b}_i^{\dagger}\hat{b}_i + \frac{1}{2}\right), \tag{2.77}$$

that describes a gas of independent quasiparticles with energies given by the Bogoliubov dispersion ϵ_i (to be determined from the Bogoliubov-de Gennes equations, Eq. (2.75)).

Time evolution of Bogoliubov modes in the presence of a non-stationary background

The previous discussion provides the dynamics of the small fluctuating fields in the presence of a stationary background $\Psi_0(\mathbf{r})e^{-i\mu_{3\mathrm{D}}t/\hbar}$. We now consider the presence of a non-stationary condensate mode $\Psi_0(\mathbf{r},t)$. In order to calculate the dynamics of the Bogoliubov modes in the presence of $\Psi_0(\mathbf{r},t)$, we can modify the Bogoliubov transformation Eq. (2.70) and choose the time dependence to be contained entirely in the Bogoliubov modes themselves:

$$\delta\hat{\psi}(\mathbf{r},t) = \sum_{i=1}^{\infty}\left[u_i(\mathbf{r},t)\hat{b}_i + v_i^*(\mathbf{r},t)\hat{b}^{\dagger}\right]. \tag{2.78}$$

Substituting this into the linearised equations of motion Eqs. (2.68) and (2.69), and separating the equations associated with $\hat{b}_i$ and $\hat{b}_i^{\dagger}$, we get

$$\begin{aligned} i\hbar\sum_{i=1}^{\infty}\left[\frac{\partial u_i(\mathbf{r},t)}{\partial t}\hat{b}_i\right] &= \left[-\frac{\hbar^2}{2m}\frac{\partial^2}{\partial x^2} + V + 2g_{3\mathrm{D}}|\Psi_0(\mathbf{r},t)|^2 - \mu_{3\mathrm{D}}\right]\sum_{i=1}^{\infty}\left[u_i(\mathbf{r},t)\hat{b}_i\right] \\ &\quad + g_{3\mathrm{D}}\Psi_0^2(\mathbf{r},t)\sum_{i=1}^{\infty}\left[v_i(\mathbf{r},t)\hat{b}_i\right], \end{aligned} \tag{2.79}$$

$$\begin{aligned} i\hbar\sum_{i=1}^{\infty}\left[\frac{\partial v_i^*(\mathbf{r},t)}{\partial t}\hat{b}_i^{\dagger}\right] &= \left[-\frac{\hbar^2}{2m}\frac{\partial^2}{\partial x^2} + V + 2g_{3\mathrm{D}}|\Psi_0(\mathbf{r},t)|^2 - \mu_{3\mathrm{D}}\right]\sum_{i=1}^{\infty}\left[v_i^*(\mathbf{r},t)\hat{b}_i^{\dagger}\right] \\ &\quad + g_{3\mathrm{D}}\Psi_0^2(\mathbf{r},t)\sum_{i=1}^{\infty}\left[u_i^*(\mathbf{r},t)\hat{b}_i^{\dagger}\right], \end{aligned} \tag{2.80}$$

that then gives us the time-dependent Bogoliubov-de Gennes equations

$$\begin{aligned} i\hbar\frac{\partial}{\partial t}u_i(\mathbf{r},t) &= \left(-\frac{\hbar^2}{2m}\nabla^2 + V(\mathbf{r}) + 2g_{3\mathrm{D}}|\Psi_0(\mathbf{r},t)|^2 - \mu_{3\mathrm{D}}\right)u_i(\mathbf{r},t) + g_{3\mathrm{D}}\Psi_0^2(\mathbf{r},t)v_i(\mathbf{r},t), \\ -i\hbar\frac{\partial}{\partial t}v_i(\mathbf{r},t) &= \left(-\frac{\hbar^2}{2m}\nabla^2 + V(\mathbf{r}) + 2g_{3\mathrm{D}}|\Psi_0(\mathbf{r},t)|^2 - \mu_{3\mathrm{D}}\right)v_i(\mathbf{r},t) + g_{3\mathrm{D}}[\Psi_0^*(\mathbf{r},t)]^2u_i(\mathbf{r},t). \end{aligned} \tag{2.81}$$

Here, assuming that the quasiparticle population is much smaller than the condensate population (same as for the time-independent Bogoliubov equations), we neglect the mean-field potential due to the non-condensed particles. Thus, the time evolution of the condensate mode $\Psi_0(\mathbf{r}, t)$ is entirely given by the time-dependent Gross–Pitaevskii equation (Eq. (2.42)). We also neglect the interaction between quasiparticles under the assumption that their time evolution is primarily due to their coupling to the condensate mode.

Elementary excitations in a box

At this point, it is worth describing the quasiparticle excitations of a Bose gas enclosed in a box. We consider a system of N identical interacting bosons enclosed in a container of volume V. In this case, the Bogoliubov modes $u_i(\mathbf{r})$ and $v_i(\mathbf{r})$ are indexed by the momentum $\mathbf{p}$ such that

$$u_{\mathbf{p}}(\mathbf{r}) = u_{\mathbf{p}} e^{i\mathbf{p}\cdot\mathbf{r}}, \tag{2.82}$$

$$v_{\mathbf{p}}(\mathbf{r}) = v_{\mathbf{p}} e^{-i\mathbf{p}\cdot\mathbf{r}}. \tag{2.83}$$

The Bogoliubov–de Gennes equations for a box are given by

$$\left(\frac{|\mathbf{p}|^2}{2m} + 2\rho_0 g_{3\mathrm{D}}\right) u_{\mathbf{p}} + \rho_0 g_{3\mathrm{D}} v_{\mathbf{p}} = -\hbar\omega_{\mathbf{p}} u_{\mathbf{p}}, \tag{2.84}$$

$$\left(\frac{|\mathbf{p}|^2}{2m} + 2\rho_0 g_{3\mathrm{D}}\right) v^*_{\mathbf{p}} + \rho_0 g_{3\mathrm{D}} u^*_{\mathbf{p}} = \hbar\omega_{\mathbf{p}} v^*_{\mathbf{p}}. \tag{2.85}$$

By solving these coupled equations, one finds that the energy of each elementary excitation is given by

$$\epsilon(\mathbf{p}) = \hbar\omega_{\mathbf{p}} = \sqrt{\left(\frac{|\mathbf{p}|^2}{2m}\right)^2 + \frac{|\mathbf{p}|^2}{m}\rho_0 g_{3\mathrm{D}}}\ . \tag{2.86}$$

Equation (2.86) is known as the Bogoliubov dispersion relation. The coefficients $u_{\mathbf{p}}$ and $v_{\mathbf{p}}$ are given by

$$|u_{\mathbf{p}}|^2 = \frac{1}{2\epsilon(\mathbf{p})}\left[\frac{|\mathbf{p}|^2}{2m} + \rho_0 g_{3\mathrm{D}} + \epsilon(\mathbf{p})\right], \qquad |v_{\mathbf{p}}|^2 = \frac{1}{2\epsilon(\mathbf{p})}\left[\frac{|\mathbf{p}|^2}{2m} + \rho_0 g_{3\mathrm{D}} - \epsilon(\mathbf{p})\right] \tag{2.87}$$

and satisfy

$$|u_{\mathbf{p}}|^2 - |v_{\mathbf{p}}|^2 = 1. \tag{2.88}$$

Let us now consider the number of quasiparticles in the gas. The total number of particles can be calculated using the field operator $\hat{\Psi}(\mathbf{r}) = \Psi_0(\mathbf{r}) + \delta\hat{\psi}(\mathbf{r})$:

$$N = \int \left\langle \hat{\Psi}^\dagger(\mathbf{r})\hat{\Psi}(\mathbf{r}) \right\rangle \mathrm{d}\mathbf{r} = N_0 + \sum_{\mathbf{p}\neq 0} n_{\mathbf{p}}, \tag{2.89}$$

where we have used the Bogoliubov transformation Eq. (2.70) together with the Bogoliubov modes for a box Eqs. (2.82) and (2.83). $N_0 = \int |\Psi_0(\mathbf{r})|^2 \mathrm{d}\mathbf{r}$ is the number of condensate particles, while $n_{\mathbf{p}}$ is the average occupation number of particles in the non-condensed state given by

$$n_{\mathbf{p}} = |u_{\mathbf{p}}|^2 + |u_{\mathbf{p}}|^2 \left\langle \hat{b}^\dagger_{\mathbf{p}} \hat{b}_{\mathbf{p}} \right\rangle + |v_{\mathbf{p}}|^2 \left\langle \hat{b}^\dagger_{-\mathbf{p}} \hat{b}_{-\mathbf{p}} \right\rangle, \tag{2.90}$$

where

$$\left\langle \hat{b}^\dagger_{\mathbf{p}} \hat{b}_{\mathbf{p}} \right\rangle = N_{\mathbf{p}} = \frac{1}{\exp[\beta\epsilon(\mathbf{p})] - 1} \tag{2.91}$$

is the average occupation number of quasiparticles with momentum $\mathbf{p}$. Thus, the number of particles in the condensate is given by

$$N_0 = N - \sum_{\mathbf{p}\neq 0} \left[|u_{\mathbf{p}}|^2 + |u_{\mathbf{p}}|^2 \left\langle \hat{b}^\dagger_{\mathbf{p}} \hat{b}_{\mathbf{p}} \right\rangle + |v_{\mathbf{p}}|^2 \left\langle \hat{b}^\dagger_{-\mathbf{p}} \hat{b}_{-\mathbf{p}} \right\rangle \right]. \tag{2.92}$$

As we can see here, the summation above does not vanish, even at zero temperature where $\langle \hat{b}^\dagger_{\mathbf{p}} \hat{b}_{\mathbf{p}} \rangle = \langle \hat{b}^\dagger_{-\mathbf{p}} \hat{b}_{-\mathbf{p}} \rangle = 0$. This means that even in the absence of quasiparticles, there are still a fraction of particles that do not occupy the mean-field ground state Ψ_0 due to interactions in the gas. This outcome is the consequence of quantum fluctuations and is referred to as quantum depletion [6, 54].

2.3 One-dimensional Bose gas

In this thesis, we will consider systems in one spatial dimension. We must use the corresponding equations for the Bose gas in one spatial dimension to describe such systems. To do this, let us consider an anisotropic harmonic trap given by

$$V_{\text{ext}}(x, r_\perp) = \frac{1}{2} m \left[\omega_x^2 x^2 + \omega_\perp^2 r_\perp^2 \right], \tag{2.93}$$

where $\omega_\perp$ is the trap frequency along the radial (transverse) direction in the yz plane, and $|r_\perp| = \sqrt{y^2 + z^2}$ is the distance from the centre of this plane. The potential $V_{\text{ext}}(x, r_\perp)$ is a harmonic trap that has cylindrical symmetry. Thus, instead of the usual rectangular coordinate system, we use the more appropriate cylindrical coordinate system. The Gross–Pitaevskii equation in cylindrical coordinates is given by

$$i\hbar \frac{\partial}{\partial t} \Psi_0(x, r_\perp, t) = \left[-\frac{\hbar^2}{2m} \left(\frac{\partial^2}{\partial x^2} + \nabla^2_{r_\perp} \right) + \frac{1}{2} m \left(\omega_x^2 x^2 + \omega_\perp^2 r_\perp^2 \right) + g_{3\text{D}} \left| \Psi_0(x, r_\perp, t) \right|^2 \right] \Psi_0(x, r_\perp, t). \tag{2.94}$$

where

$$\nabla^2_{r_\perp} = \frac{1}{r_\perp} \frac{\partial}{\partial r_\perp} \left(r_\perp \frac{\partial}{\partial r_\perp} \right). \tag{2.95}$$

Let us now assume a highly anisotropic trap so that

$$\omega_x \ll \omega_\perp. \tag{2.96}$$

Such a trap takes a cigar shape. If the chemical potential $\mu_{3\text{D}}$ of the system is smaller than the excitation energy of the transverse harmonic trap $\hbar\omega_\perp$, it follows that the harmonic oscillator length along the transverse direction is smaller than the system's healing length:

$$a_\perp \equiv \sqrt{\frac{\hbar}{m\omega_\perp}} < \xi. \tag{2.97}$$

Here, the transverse confinement of the condensate is so tight that states along this direction tend to be restricted to the ground state. The dynamics of such cigar-shaped condensates can be considered

as effectively one-dimensional. This allows for reducing the 3D Gross–Pitaevskii equation to a 1D Gross–Pitaevskii equation.

Assuming a 1D setting where the dynamics along the x and $r_\perp$ directions are decoupled, we decompose the three-dimensional wave function into longitudinal and transverse components and write it in a separable form given by [64, 65]

$$\Psi_0(x, r_\perp, t) = \psi_0(x, t)\phi(r_\perp, t), \tag{2.98}$$

where $\phi(r_\perp, t) = \phi_0(r_\perp)\exp(-i\mu_\perp t/\hbar)$ is the stationary solution of the Schrödinger equation for a two-dimensional harmonic oscillator:

$$\mu_\perp \phi_0(r_\perp) = -\frac{\hbar^2}{2m}\nabla^2_{r_\perp}\phi_0(r_\perp) + \frac{1}{2}m\omega_\perp^2 r_\perp^2 \phi_0(r_\perp). \tag{2.99}$$

Because the system is tightly confined along the transverse direction, the energy modes in the transverse direction are highly suppressed, the states tend toward the static harmonic oscillator groundstate

$$\phi_0(r_\perp) = \sqrt{\frac{m\omega_\perp}{\pi\hbar}}\ \exp\left(-\frac{m\omega_\perp r_\perp^2}{2\hbar}\right), \tag{2.100}$$

and the dynamics of the system are constrained to the longitudinal (x) axis. Substituting Eq. (2.98) into the Gross–Pitaevskii equation Eq. (2.94), we obtain

$$\begin{aligned} i\hbar\phi_0(r_\perp)\frac{\partial\psi_0(x,t)}{\partial t} = &-\frac{\hbar^2}{2m}\phi_0(r_\perp)\frac{\partial^2\psi_0(x,t)}{\partial x^2} + \frac{1}{2}m\omega_x^2 x^2\psi_0(x,t)\phi_0(r_\perp) \\ &+ g_{3\mathrm{D}}|\psi_0(x)|^2|\phi_0(r_\perp)|^2\psi_0(x,t)\phi_0(r_\perp), \end{aligned} \tag{2.101}$$

that we multiply with $\phi_0^\dagger(r_\perp)$ and integrate from $r_\perp = 0$ to $r_\perp = \infty$ to get the 1D Gross–Pitaevskii equation

$$i\hbar\frac{\partial}{\partial t}\psi_0(x,t) = \left[-\frac{\hbar^2}{2m}\frac{\partial^2}{\partial x^2} + \frac{m}{2}\omega_x^2 x^2 + g_{1\mathrm{D}}|\psi_0(x,t)|^2\right]\psi_0(x,t), \tag{2.102}$$

where

$$g_{1\mathrm{D}} = \frac{g_{3\mathrm{D}}}{2\pi a_\perp^2} = 2\hbar a\omega_\perp, \tag{2.103}$$

is the one-dimensional interaction parameter. Hereafter, we shall drop the $1\mathrm{D}$ subscript in Eq. (2.103) and denote it by g for simplicity. Similarly, the one-dimensional chemical potential will be denoted by μ.

2.3.1 Long-range order in lower dimensions

In contrast to the 3D case, the Mermin–Wagner–Hohenberg theorem [24, 25] prohibits the existence of off-diagonal long-range order (a property of BECs in 3D) in 1D and 2D systems at finite temperature in the thermodynamic limit. To show this, we follow a derivation of the theorem according to Ref. [66]. We start with the Bogoliubov inequality [67] given by

$$\langle\{\hat{A}, \hat{A}^\dagger\}\rangle\langle[\hat{B}^\dagger, [\hat{H}, \hat{B}]]\rangle \geq 2k_\mathrm{B}T|\langle[\hat{A}, \hat{B}]\rangle|^2, \tag{2.104}$$

where $\hat{A}$ and $\hat{B}$ represent arbitrary operators, $\hat{H}$ is the Hamiltonian of the system, and $\langle\cdot\rangle$ denotes thermal averages. In order to derive the Mermin–Wagner–Hohenberg theorem, we set the operators in Eq. (2.104)

$$\hat{A} = \hat{b}_{\mathbf{p}}, \qquad \hat{B} = \hat{\rho}_{\mathbf{p}} \equiv \sum_{\mathbf{k}} \hat{b}^{\dagger}_{\mathbf{k}} \hat{b}_{\mathbf{k}+\mathbf{p}}, \tag{2.105}$$

where $\hat{b}^{\dagger}_{\mathbf{p}}$ ($\hat{b}_{\mathbf{p}}$) creates (annihilates) a bosonic particle with momenta $\mathbf{p}$, and satisfies the usual bosonic commutation relations Eq. (2.71). With the use of the commutation relations, the averaged anticommutator in Eq. (2.104) gives

$$\langle\{\hat{b}_{\mathbf{p}}, \hat{b}^{\dagger}_{\mathbf{p}}\}\rangle = 2n_{\mathbf{p}} + 1, \tag{2.106}$$

where $n_{\mathbf{p}} = \langle\hat{b}^{\dagger}_{\mathbf{p}}\hat{b}_{\mathbf{p}}\rangle$ is the average number of particles with momenta $\mathbf{p}$. In order to calculate the commutator in Eq. (2.104) that involves the Hamiltonian of the system, we consider the Hamiltonian in momentum representation given by

$$\hat{H} = \sum_{\mathbf{p}} \epsilon_{\mathbf{p}} \hat{b}^{\dagger}_{\mathbf{p}} \hat{b}_{\mathbf{p}} + \frac{1}{2} \sum_{\mathbf{k},\mathbf{p},\mathbf{q}} V_{\mathbf{k}} \hat{b}^{\dagger}_{\mathbf{p}-\mathbf{k}} \hat{b}^{\dagger}_{\mathbf{q}+\mathbf{k}} \hat{b}_{\mathbf{p}} \hat{b}_{\mathbf{q}}, \tag{2.107}$$

where $\epsilon_{\mathbf{p}} = \hbar^2 k^2/2m$ is the single-particle dispersion and $V_{\mathbf{k}}$ is the two-body interaction parameter. Using the commutation relations Eq. (2.71) and the definition of $\hat{\rho}_{\mathbf{p}}$ in Eq. (2.105), the Hamiltonian can be rewritten as

$$\hat{H} = \sum_{\mathbf{p}} \epsilon_{\mathbf{p}} \hat{b}^{\dagger}_{\mathbf{p}} \hat{b}_{\mathbf{p}} + \frac{1}{2} \sum_{\mathbf{k},\mathbf{p},\mathbf{q}} V_{\mathbf{k}} \hat{\rho}^{\dagger}_{\mathbf{k}} \hat{\rho}_{\mathbf{k}} - \frac{1}{2} \hat{N} \sum_{\mathbf{k}} V_{\mathbf{k}}, \tag{2.108}$$

where we have used the total number operator $\hat{N} = \sum_{\mathbf{p}} \hat{b}^{\dagger}_{\mathbf{p}} \hat{b}_{\mathbf{p}}$. In order to calculate the commutator $[\hat{\rho}^{\dagger}_{\mathbf{p}}, [\hat{H}, \hat{\rho}_{\mathbf{p}}]]$, we further apply the commutations

$$[\hat{b}_{\mathbf{p}}, \hat{\rho}_{\mathbf{p}}] = \hat{b}_{\mathbf{p}+\mathbf{k}}, \qquad [\hat{\rho}_{\mathbf{p}}, \hat{b}^{\dagger}_{\mathbf{p}}] = -\hat{b}^{\dagger}_{\mathbf{p}-\mathbf{k}}, \qquad [\hat{\rho}_{\mathbf{p}}, \hat{\rho}_{\mathbf{k}}] = 0, \qquad [\hat{N}, \hat{\rho}_{\mathbf{p}}] = 0. \tag{2.109}$$

Substituting these into $[\hat{\rho}^{\dagger}_{\mathbf{p}}, [\hat{H}, \hat{\rho}_{\mathbf{p}}]]$ gives

$$[\hat{\rho}^{\dagger}_{\mathbf{p}}, [\hat{H}, \hat{\rho}_{\mathbf{p}}]] = \sum_{\mathbf{k}} \big(\epsilon_{\mathbf{k}+\mathbf{p}} - 2\epsilon_{\mathbf{k}} + \epsilon_{\mathbf{k}-\mathbf{p}}\big) \hat{b}^{\dagger}_{\mathbf{k}} \hat{b}_{\mathbf{k}}, \tag{2.110}$$

$$= \frac{\hbar^2 p^2}{m} \hat{N}, \tag{2.111}$$

where we have used the definition of the single-particle dispersion $\epsilon_{\mathbf{k}}$ in the second line. Lastly, the commutator on the right hand side of Eq. (2.104) gives us

$$[\hat{b}^{\dagger}_{\mathbf{p}}, \hat{\rho}_{\mathbf{p}}] = -\hat{b}^{\dagger}_{0}. \tag{2.112}$$

Thus, the Bogoliubov inequality Eq. (2.104) for a homogeneous gas gives us a lower bound for the number of particles with momenta $\mathbf{p}$:

$$n_{\mathbf{p}} \geq \frac{m k_{\mathrm{B}} T |\langle\hat{b}_0\rangle|^2}{N \hbar^2 p^2} - \frac{1}{2}. \tag{2.113}$$

Summing over $\mathbf{p} \neq 0$ gives us the total number of excitations in the system. In the infinite volume limit, we can replace the sum over $\mathbf{k}$ by an integral:

$$N_{\mathbf{p}\neq 0} \geq \frac{mk_{\mathrm{B}}T|\langle \hat{b}_0 \rangle|^2}{N\hbar^2} \int d^D\mathbf{p} \frac{1}{p^2}, \tag{2.114}$$

where D is the number of spatial dimensions of the system. The integral converges for $D > 2$, whereas low momenta modes cause the integral to diverge for $D \leq 2$. Since the integral gives a lower boundary for the number of excitations in the system, this infrared divergence for $D \leq 2$ leads to a contradiction to a finite number of particles in the system. This shows that at any finite temperature T, long wavelength excitations destroys long-range order and we cannot have a BEC in one and two dimensions. Moreover, the one-particle density matrix for a 1D Bose gas was found to decay algebraically even at zero temperature [68–70]:

$$\langle \hat{\psi}^\dagger(x)\hat{\psi}(0)\rangle \simeq \rho \left(\frac{r_1}{x}\right)^{1/(2\pi\rho\xi)}, \qquad x \gg \xi, \tag{2.115}$$

with $r_1 = e^{2-C}\xi/4 \simeq 1.037\xi$ where $C = 0.57721\ldots$ is the Euler's constant, ρ is the 1D density, and $\xi = \hbar/\sqrt{m\mu}$ is the 1D healing length. Thus, long-range order cannot exist in a 1D system even at zero temperature.

This absence of long-range order in lower dimensions can be understood as the effect of the enhanced role of low-energy, long-wavelength excitations as the dimensionality of the system is reduced [71]. Such excitations lead to the appearance of infrared divergences in the equation of state (that prohibit the formation of off-diagonal long-range order) and can be interpreted as fluctuations in the phase of the condensate. Thus, even though there is still macroscopic occupation of the lowest energy state (with interparticle interactions suppressing the fluctuations in the density in the weakly interacting regime [26–28]), fluctuations of the phase result in an algebraic (at $T = 0$) or exponential (at $T > 0$) decay of the first-order correlation [26–30].

2.3.2 One-dimensional Thomas–Fermi approximation

Substituting the time-dependent solution

$$\psi_0(x,t) = \psi_0(x)e^{-i\mu t/\hbar}, \tag{2.116}$$

into Eq. (2.102), we get the time-independent one-dimensional Gross–Pitaevskii equation

$$\mu\psi_0(x) = \left[-\frac{\hbar^2}{2m}\frac{\partial^2}{\partial x^2} + \frac{1}{2}m\omega_x^2 x^2 + g_{1\mathrm{D}}|\psi_0(x)|^2\right]\psi_0(x). \tag{2.117}$$

Here, μ is the one-dimensional chemical potential. Similar to the three-dimensional case, the density of the 1D Bose gas in the Thomas–Fermi approximation is given by

$$\rho_0(x) = |\psi_0(x)|^2 = \frac{1}{g}\left(\mu - \frac{1}{2}m\omega_x^2 x^2\right), \tag{2.118}$$

within the 1D Thomas–Fermi radius, $|x| \leq R_x = \sqrt{2\mu/(m\omega_x^2)}$, and is zero elsewhere. The expression for the chemical potential μ can be obtained by integrating Eq. (2.118) over the whole parabola from

$x = -R_x$ to $x = R_x$ and using the normalisation condition $\int \rho_0(x)\mathrm{d}x = N$. This gives

$$\mu = \left(\frac{9}{32} m N^2 \omega_x^2 g^2\right)^{1/3}. \tag{2.119}$$

Rewriting Eq. (2.118) in terms of the Thomas–Fermi radius R_x gives

$$\rho_0(x) = \rho_0(0)\left(1 - \frac{x^2}{R_x^2}\right), \tag{2.120}$$

where $\rho_0(0) = \mu/g$ is the peak density. Using Eq. (2.119), the expression relating the peak density to the total number of particles is found to be

$$\rho_0(0) = \left(\frac{9 m N^2 \omega_x^2}{32 g}\right)^{1/3}. \tag{2.121}$$

2.3.3 One-dimensional hydrodynamic equations

Like the 3D case, the 1D GPE can be equivalently formulated in terms of super fluid hydrodynamics via the 1D Madelung's transformation to the density and phase variables:

$$\psi_0(x,t) = \sqrt{\rho_0(x,t)}\, e^{i\phi(x,t)}. \tag{2.122}$$

Substituting Eq. (2.122) into Eq. (2.102) and equating the real and imaginary parts, we get the coupled 1D hydrodynamic equations

$$\frac{\partial}{\partial t}\rho_0(x,t) = -\frac{\partial}{\partial x}\big[\rho_0(x,t)v(x,t)\big], \tag{2.123}$$

$$m\frac{\partial}{\partial t}v(x,t) = -\frac{\partial}{\partial x}\left[\frac{1}{2}mv^2(x,t) + V_{\text{ext}} + g\rho_0(x,t) - \frac{\hbar^2}{2m}\frac{1}{\sqrt{\rho_0(x,t)}}\frac{\partial^2}{\partial x^2}\sqrt{\rho_0(x,t)}\,\right], \tag{2.124}$$

where

$$v(x,t) = \frac{\hbar}{m}\frac{\partial}{\partial x}\phi(x,t), \tag{2.125}$$

is the 1D velocity field.

2.3.4 Realisation of 1D Bose gases in experiments

Apart from the highly anisotropic trap frequencies (Eq. (2.96)) needed to produce an effective 1D Bose gas in experiments, all energy scales need to be much smaller than the energy of the first transverse excited state. That is, the 3D chemical potential and temperature should fulfil the following conditions [72–74]:

$$\mu_{3\mathrm{D}} \ll \hbar\omega_\perp, \qquad k_\mathrm{B}T \ll \hbar\omega_\perp. \tag{2.126}$$

These conditions ensure that transverse excitations are 'frozen out', and only the transverse ground state is macroscopically populated. Thus, the dynamics of the particles are restricted in the longitudinal direction where multiple energy states can be occupied by the particles. In experiments, however, the

conditions in Eq. (2.126) are so hard to fulfil that less strict criteria are used, *i.e.* $\mu_{3\mathrm{D}} \leq \hbar\omega_\perp$ and $k_\mathrm{B}T \leq \hbar\omega_\perp$. This is because there is a smooth 1D-3D crossover [75]. Hence, even at temperatures and chemical potentials on the order of the transverse trapping frequency, a Bose gas exhibits 1D-like behaviour.

To date, two established techniques are used to realise Bose gases in 1D geometry. These are the 2D optical lattices [76–83], where a dipole trap is realised using lasers, and micro-traps [84–88], where particles are trapped using magnetic fields. In the following, we overview the concepts behind the techniques used in realising 1D Bose gases in experiments.

2D optical lattices

The concept of optical dipole trapping is used in 2D optical lattice setups. This optical trapping relies on the interaction between an induced dipole moment in an atom and an external electric field [82]. Such a field induces an oscillating dipole moment in the atom while at the same time interacts with this dipole moment to create a trapping potential given by [89]

$$V_\mathrm{dip}(\mathbf{r}) = -\mathrm{Re}(\alpha)|\mathbf{E}(\mathbf{r})|^2, \tag{2.127}$$

where α is the complex polarisability of an atom and $\mathbf{E}(\mathbf{r})$ is the electric field at position $\mathbf{r}$. The laser light producing the electric field is usually tuned far away from the atomic resonance frequency, so resonant excitations can be neglected, and the dipole potential remains conservative. When the dipole is driven below atomic resonance, known as ‘red-detuning’, the interaction energy is negative and results in the atoms being attracted to regions with a high electric field. On the other hand, driving the dipole above atomic resonance, known as ‘blue-detuning’, interaction energy is positive and results in the atoms being repelled from regions with a high electric field.

Both blue-detuned and red-detuned lasers are used to trap a Bose gas in a 1D geometry. The strong transverse confinement is realised by creating a 2D optical lattice using two orthogonal retroreflected lasers blue-detuned from the atomic transitions. This forms a 2D standing wave interference pattern with intensity gradients and creates an array of 1D tubes centred at the intensity minima of the interference pattern. The atoms are trapped in these 1D tubes. The weak longitudinal confinement is then realised by using a crossed dipole trap made up of two red-detuned beams on the same plane as the 2D optical lattice (see Fig. 2.1). The atoms are attracted to the region where the field intensity from the red-detuned crossed dipole trap is highest. The characteristic length of the longitudinal trapping is proportional to the width (waist) of the red-detuned lasers.

This setup presents several advantages [90]. First, it offers the possibility of realising very strong transverse confinements because light intensity is modulated on distances as small as the laser wavelength. Second, cold atoms are loaded into such a lattice in an adiabatic way starting from a 3D BEC, which permits the realisation of very cold 1D gases. Here, a 3D BEC can be produced first by trapping it in the crossed dipole trap. Then, the 2D lattice can be adiabatically turned on to realise an array of very cold 1D Bose gases [76]. Lastly, the magnetic field in such a setup is a free parameter, and it can be tuned to approach Feshbach resonances and thus adjust the interaction strength between

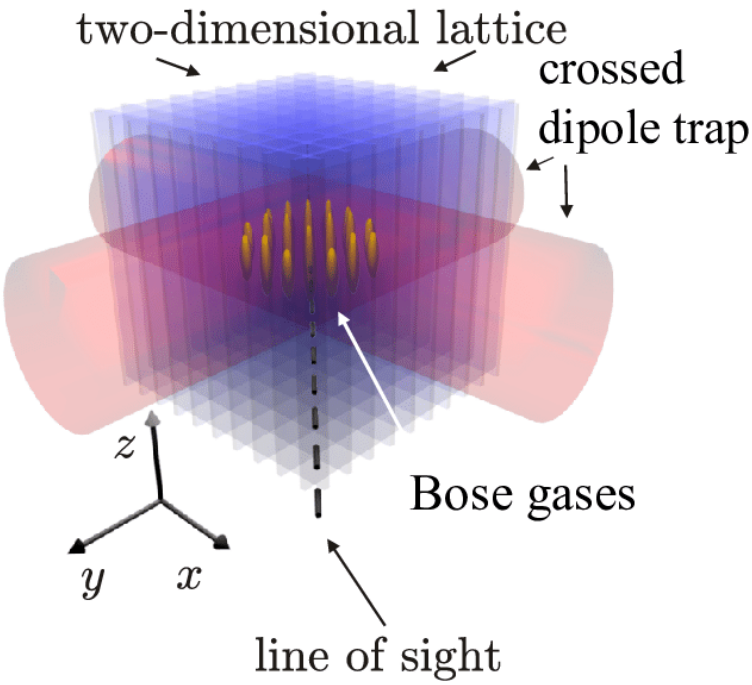

Figure 2.1: Schematic diagram of a 2D optical lattice used to realise an array of 1D Bose gases. Two orthogonal retroreflected blue-detuned lasers form a 2D standing wave interference pattern that tightly confines atoms in 1D tubes. A crossed red-detuned lasers weakly confine the atoms longitudinally. Figure from Li *et al.*, Phys. Rev. A **88**, 023419 (2009). Reprinted with permission from APS.

atoms. However, optical lattices also have some limitations [90]. One of these is that measurements in such a setup are ensemble averages, meaning the value of the measured observable is averaged over several 1D gases. The 1D gas parameters, such as the number of atoms per tube, is inhomogeneous. This inhomogeneity complicates data analysis. Also, this ensemble averaging prevents the investigation of fluctuations and correlation. Another problem is that a 2D optical lattice has a finite length along the direction of the tubes because it is produced using lasers with relatively small waists. This limits the longitudinal extension that the 1D gases can explore.

Atom chips

The other way of realising 1D Bose gases is by magnetic trapping of atoms. Consider an atom with angular momentum $\mathbf{F}$. This atom exhibits a magnetic moment $\boldsymbol{\mu} = -g_F \mu_B \mathbf{F}$, where g_F is the Landé g-factor and μ_B is the Bohr magneton. In the presence of a weak magnetic field $\mathbf{B}(\mathbf{r})$, the hyperfine levels characterised by F are split into equally spaced sublevels labelled by the quantum number $m_F = \{-F \dots F\}$, and the Zeeman effect causes a linear shift of the atomic energy levels given by

$$V(\mathbf{r}) = -\boldsymbol{\mu} \cdot \mathbf{B}(\mathbf{r}) = m_F g_F \mu_B |\mathbf{B}(\mathbf{r})|. \tag{2.128}$$

If the magnitude of the magnetic field varies slowly enough such that

$$\frac{d|\mathbf{B}(\mathbf{r})|}{dt} < \omega_L |\mathbf{B}(\mathbf{r})|, \tag{2.129}$$

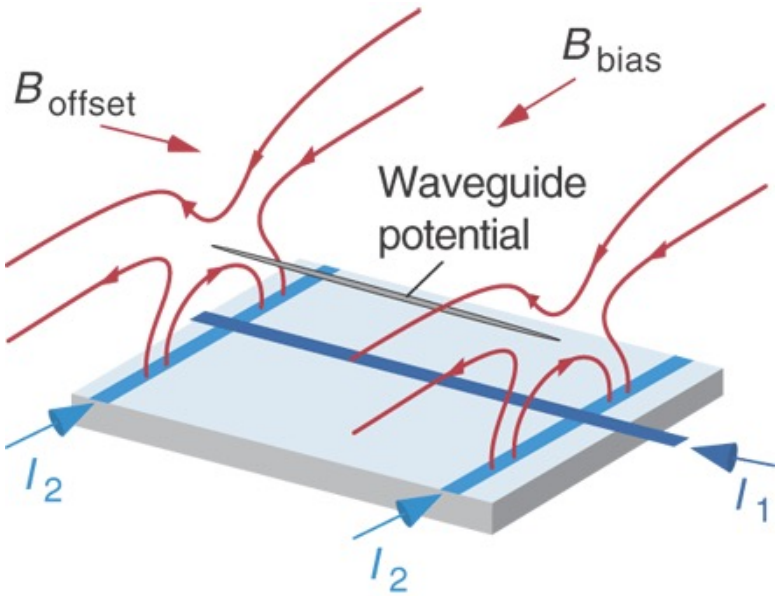

Figure 2.2: Highly anisotropic harmonic trap created using an atom chip. The total magnetic field from the circular magnetic field of the (red) current-carrying wire and the bias magnetic field B_{bias} vanishes on a line parallel to the wire. Atoms that are 'low-field seekers' are trapped in this magnetic field minimum. Confinement along the length of the gas is created with addition of perpendicular currents I_2. Figure from Fortágh and Zimmermann, Science **307**(5711), 860 (2005). Reprinted with permission from AAAS.

the atoms will adiabatically follow the shift of the Zeeman levels. Here, $\omega_L = m_F g_F \mu_B B/\hbar$ is the Larmor frequency of the atoms. Depending on the values of m_F and g_F, atoms can be in a low-field-seeking state ($g_F m_F > 0$) that are attracted to regions of lower magnetic field or in a high-field-seeking state ($g_F m_F < 0$) that are attracted to regions of higher magnetic field. However, only atoms in the low-field-seeking states can be confined in a purely magnetic trap because Maxwell's equations forbid local maxima for static magnetic fields [91].

For regions with a small magnetic field, the precession of the magnetic moment is so slow that the condition for adiabatic approximation, Eq. (2.129), cannot be fulfilled anymore. This leads to atoms undergoing the so-called Majorana spin-flip to an untrapped state [92]. To avoid this loss mechanism due to the spin-flipping of atoms, one can arrange a non-zero magnetic field strength at the potential minimum.

A strong magnetic field gradient can be produced using microwires running an electric current in the so-called atom chip setup [87] to use the above concepts. Consider a current-carrying wire immersed in a homogeneous magnetic field $\mathbf{B}_{\text{bias}}$ perpendicular to the wire (see Fig. 2.2). The bias field cancels the circular magnetic field produced by the current-carrying wire at a distance

$$r_0 = \frac{\mu_0}{2\pi} \frac{I}{|\mathbf{B}_{\text{bias}}|}, \tag{2.130}$$

from the wire, with μ_0 being the magnetic permeability. This cancellation of fields creates a line of zero magnetic field parallel to the wire and attracts atoms that are polarised in a low-field-seeker magnetic state. To avoid the Majorana spin-flip loss mechanism due to vanishing magnetic field in the

trap minima, another homogenous magnetic field $\mathbf{B}_{\text{offset}}$ can be added along the wire axis to create an Ioffe–Pritchard trap [93] setup. This shifts the magnitude of the trap minimum to $|\mathbf{B}_{\text{offset}}|$. The vicinity of the trap minimum then acquires the shape of a harmonic potential.

Longitudinal confinement can then be realised by adding a second set of current-carrying wires perpendicular to the first wire (see Fig. 2.2). If the second set of wires have currents $I_{2,L}$ and $I_{2,R}$ (with L and R denoting left and right, respectively) in opposite directions, a so-called 'U-wire' because the current flow $I_{2,R} \to I_1 \to I_{2,L}$ has a U shape, this results in a quadrupole trap along the length of the Bose gas with a vanishing magnetic field at the trap minimum. However, if the currents $I_{2,L}$ and $I_{2,R}$ flow in the same direction, a so-called 'Z-wire' because the current flow $I_{2,R} \to I_1 \to I_{2,L}$ has a Z shape, this results to an Ioffe–Pritchard trap along the length of the Bose gas.

The advantage of using atom chips is that a single realisation of 1D Bose gases can be prepared and manipulated, which permits the study of fluctuations and their correlations. Also, longer configurations of the 1D geometry can be realised without variations of the transverse confinement along the length of the Bose gas. However, the downside of 1D gases prepared in an atom chip is that atoms are directly prepared and cooled down in the 1D geometry and, therefore, have higher temperatures than those obtained using 2D optical lattices. The physical phenomena limiting the final temperature of the 1D gas in an atom chip is not completely understood, although it has been pointed out that atom losses may have contributed to the limitations of the final temperature [90, 94–96]. Another concern when using atom chips is the nonuniformity of the bottom of the trapping potential due to imperfections in the current-carrying wire that produce the magnetic field [97].

2.3.5 Uniform 1D Bose gas

In the absence of a harmonic potential, $\omega_x = 0$ in Eq. (2.102), the Bose gas is homogeneous with uniform density ρ and can be described by the Lieb–Liniger model [46, 47], whose full many-body Hamiltonian is given by

$$\hat{H} = \int \hat{\psi}^\dagger(x,t) \left[-\frac{\hbar^2}{2m}\frac{\partial^2}{\partial x^2} + V_{\text{ext}}(x) \right] \hat{\psi}(x,t)\mathrm{d}x + \frac{g}{2}\int \hat{\psi}^\dagger(x,t)\hat{\psi}^\dagger(x,t)\hat{\psi}(x,t)\hat{\psi}(x,t)\mathrm{d}x, \quad (2.131)$$

with $V_{\text{ext}}(x) = 0$. The bosonic operator $\hat{\psi}(x,t)$ satisfies the equal time commutation relations

$$[\hat{\psi}(x,t), \hat{\psi}^\dagger(x',t)] = \delta(x-x'), \qquad [\hat{\psi}(x,t), \hat{\psi}(x',t)] = 0, \qquad [\hat{\psi}^\dagger(x,t), \hat{\psi}^\dagger(x',t)] = 0. \quad (2.132)$$

Equivalently, the Hamiltonian Eq. (2.131) can be written in the first quantised form as

$$\hat{H} = -\sum_{i=1}^{N} \frac{\hbar^2}{2m}\frac{\partial^2}{\partial x_i^2} + \frac{g}{2}\sum_{i<j}^{N} \delta(x_j - x_i). \quad (2.133)$$

This Hamiltonian models spinless bosons and has been shown by Girardeau and Lieb and Liniger [46, 47, 98] to be analytically solvable using Bethe ansatz solutions [99]. Moreover, Yang and Yang used this solution to predict properties of the 1D Bose gas at finite temperatures [100, 101]. The exact solution to the Lieb–Liniger model leads to conserved quantities whose existence, in analogy to classical systems, precludes the thermalisation of uniform 1D Bose gases [17, 44].

An important parameter characterising the strength of interactions in a uniform 1D Bose gas is the Lieb–Liniger parameter [46, 47]

$$\gamma = \frac{mg}{\hbar^2 \rho}, \tag{2.134}$$

that is given by the ratio of the interaction energy $\propto g\rho$ to the characteristic kinetic energy per particle $\propto \hbar^2\rho^2/m$ of the gas [102] [2]. For $\gamma \ll 1$, the 1D Bose gas is in the weakly interacting regime where the mean-field and Bogoliubov theories work well. In the strongly interacting limit of $\gamma \gg 1$, the Bose gas approaches the Tonks–Girardeau regime, and as $\gamma, \gamma_0 \to \infty$, one obtains the results for impenetrable bosons [98].

When studying 1D Bose gases at finite temperature, it is intuitive to define a similar dimensionless parameter for the temperature of the system. This dimensionless temperature parameter is defined as [103]

$$\overline{\mathcal{T}} = \frac{T}{T_d} = \frac{2mk_{\mathrm{B}}}{\hbar^2\rho^2}T, \tag{2.135}$$

which is the temperature of the system T scaled by the temperature of quantum degeneracy T_d. At the temperature of quantum deneracy, the thermal de Broglie wavelength $\lambda_T = \hbar/\sqrt{2\pi m k_{\mathrm{B}} T}$ becomes on the order of the mean interparticle separation ρ^{-1}, and quantum effects start to dominate the system. This is in contrast to temperatures well above T_d where the λ_T is much smaller than the mean interparticle distance, and the 1D Bose gas can be considered classical.

2.3.6 Regimes of uniform 1D Bose gases

For a uniform 1D Bose gas, the interplay between the effects due to interparticle interactions and temperature creates distinct physical regimes. In Fig. 2.3, we show these three distinct regimes of a 1D Bose gas in the $(\gamma, \overline{\tau})$ parameter space [103, 104], where $\overline{\tau}$ is a dimensionless temperature defined as

$$\overline{\tau} = \frac{T}{T_d}\frac{1}{\gamma^2} = 2\frac{\hbar^2 k_{\mathrm{B}}}{mg^2}T. \tag{2.136}$$

The region of very low temperature and low density, $\overline{\tau} \ll 1$ and $\gamma \gg 1$, defines a strongly interacting regime (dark grey area) often referred to as the Tonks–Girardeau gas [98, 105, 106]. The region of high temperatures, $\overline{\tau} \gg \max(1, \gamma^{-3/2})$, where thermal effects dominate, defines the nearly ideal gas regime (white area) with its two subregimes: the classical subregime of very high temperatures, $\overline{\tau} \gg \gamma^{-2}$, and the degenerate subregime with temperatures below quantum degeneracy, $\gamma^{-3/2} \ll \overline{\tau} \ll \gamma^{-2}$. Lastly, the region of high density and low temperatures, $\gamma \ll 1$ and $\overline{\tau} \ll \gamma^{-3/2}$, defines the weakly interacting

[2] For the case of a Bose gas in a harmonic potential ($\omega_x \neq 0$), the density is position dependent and the dimensionless interaction parameter γ becomes locally defined:

$$\gamma(x) = \frac{mg}{\hbar^2\rho(x)}.$$

For a given chemical potential μ and temperature T, the density at the centre of the trap $\rho(0)$ can be used to define a dimensionless interaction strength

$$\gamma_0 = \frac{mg}{\hbar^2\rho(0)},$$

that can serve as a global interaction parameter.

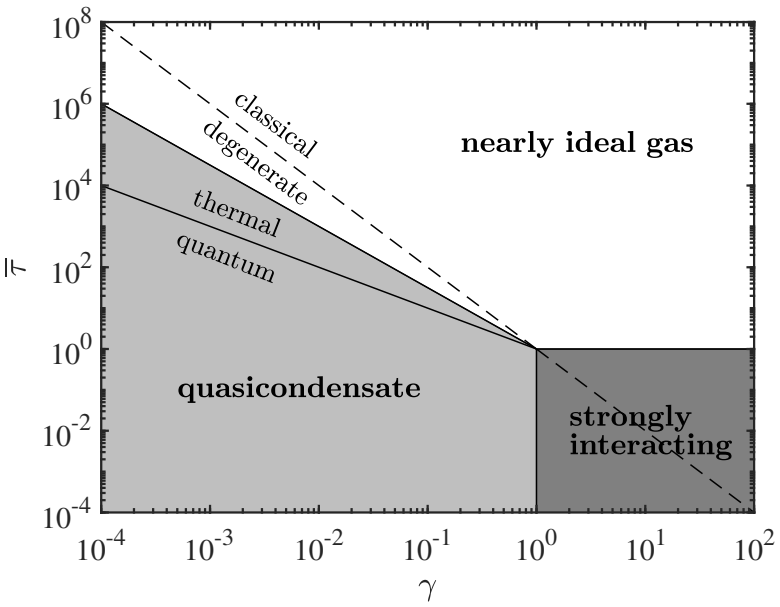

Figure 2.3: Physical regimes of a uniform 1D Bose gas with repulsive contact interactions. In the nearly ideal gas regime (white area), where effects of finite temperature dominates the system and interactions between particles can be neglected, the 1D Bose gas can be well described via a perturbation theory (with respect to g) around the ideal gas. In the quasicondensate regime (light grey area), many of the local properties of a 1D gas look like a true condensate in 3D systems, such as suppressed density fluctuations and a Thomas-Fermi density profile for the bulk of the gas. However, quasicondensates lack global phase coherence due to thermal and quantum fluctuations. In the strongly interacting regime (dark grey area), interactions between particles become dominant. Here, the particles become impenetrable due to strong repulsive interactions. This leads to fermionisation of the bosonic particles. The lines represent smooth crossover rather than phase transitions. Figure adapted from Kheruntsyan *et al.*, Phys. Rev. A **71**, 053615 (2005).

quasicondensate regime (light grey area) with its two subregimes: the thermal subregime defined by $\gamma^{-1} \ll \overline{\tau} \ll \gamma^{-3/2}$ where thermal fluctuations dominate and the quantum subregime defined by $\overline{\tau} \ll \gamma^{-1}$ where quantum fluctuations dominate. We note here that no phase transition occurs in 1D Bose gases and that the boundaries between regimes represent smooth crossovers in behaviour [107].

The nearly ideal Bose gas regime

At sufficiently high temperatures, defined in the $(\gamma, \overline{\tau})$ parameter space as $\overline{\tau} \gg \max(1, \gamma^{-3/2})$, effects of temperature dominate. In this regime, called the (nearly) ideal Bose gas regime, interactions between particles can be neglected, and the gas can be well described as an ideal Bose gas. In thermal equilibrium, the mean occupation of the kth momentum state is given by the Bose–Einstein distribution

$$\langle n_k \rangle = \frac{1}{e^{\beta(\epsilon_k - \mu)} - 1}. \tag{2.137}$$

Each momentum state has energy $\epsilon_k = \hbar^2 k^2 / 2m$ with corresponding wave vector $k = 2\pi n / L$, where L is the length of the 1D Bose gas and $n = 0, 1, 2, \ldots$. Here, the energy scale is chosen such that the ground state has energy $\epsilon_0 = 0$. Given this, the mean occupation of the ground state is

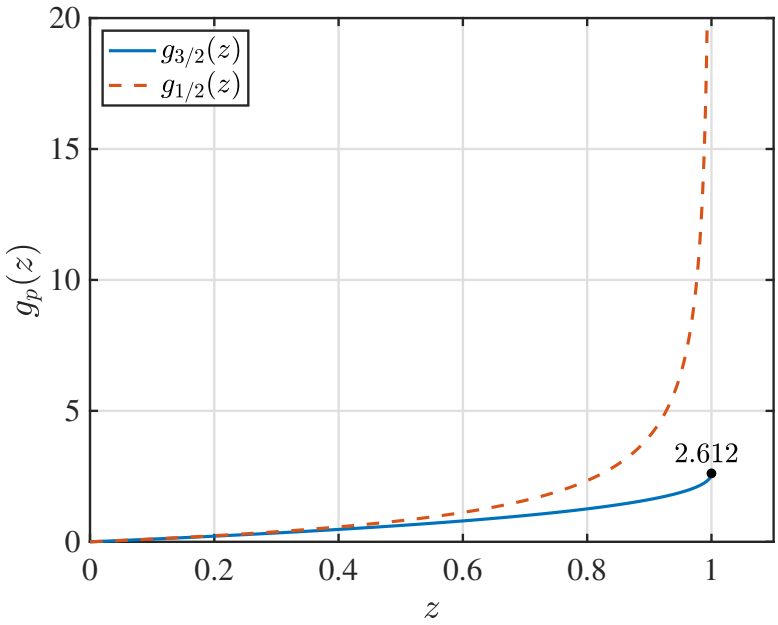

Figure 2.4: Comparison of the polylogarithmic functions $g_{3/2}(z)$ and $g_{1/2}(z)$. Due to the difference in the asymptotic behaviour of the two functions, there is no BEC phase transition in an ideal 1D Bose gas.

$\langle n_0 \rangle = [e^{-\beta\mu} - 1]^{-1}$. This gives a physical constraint $\mu \leq 0$ for the chemical potential so that the occupation number remains physical (positive).

Like the uniform 3D Bose gas, summing $\langle n_k \rangle$ over all $k \neq 0$ momentum states gives us the density of particles in the excited states:

$$n_T \equiv \frac{N_T}{L} = \frac{1}{\lambda_T} g_{1/2}\left(e^{\beta\mu}\right), \tag{2.138}$$

where $g_{1/2}(z)$ is a special case of the more general class of Bose functions given in Eq. (2.17). In subsection 2.1.1, we have seen that for a uniform 3D Bose gas, where $n_{T,3\mathrm{D}} = g_{3/2}\left(e^{\beta\mu_{3\mathrm{D}}}\right)/\lambda_T^3$, the fraction of particles in the excited states saturates due to the behaviour of $g_{3/2}(z)$, *i.e.* $\lim_{z\to 0} g_{3/2}(z) = 2.612$, and the ground state becomes macroscopically occupied. From this behaviour of $g_{3/2}(z)$, one can define a critical density above which the ideal Bose gas transitions to a BEC. However, the behaviour of $g_{1/2}$ is different; *i.e.* $\lim_{z\to 0} g_{1/2}(z) = \infty$ (see Fig. 2.4 for a comparison between the functions). Hence, as the chemical potential is increased, no transition to a true BEC is expected for an ideal 1D Bose gas in the thermodynamic limit, and the gas is described by a thermal gas at any density [107]. This is in agreement with the Mermin–Wagner–Hohenberg theorem [24, 25] that forbids long-range order in 1D (any temperature T) and 2D ($T \neq 0$ temperatures) systems.

In this regime of the 1D Bose gas, two subregimes may be identified: the non-degenerate subregime for which $-\mu \gg k_\mathrm{B}T$ and $\hbar^2\rho^2/m \ll k_\mathrm{B}T$ ($T \gg T_d$), and the degenerate subregime for which $-\mu \ll k_\mathrm{B}T$ and $\hbar^2\rho^2/m \gg k_\mathrm{B}T$ ($T \ll T_d$). These two subregimes are defined by the condition $\overline{\tau} = \gamma^{-2}$ (dashed line in Fig. 2.3). In the non-degenerate subregime, the thermal de Broglie wavelength is much smaller than the mean interparticle distance, $\lambda \ll \rho^{-1}$, and classical statistics apply. Here, the

density of the gas is well approximated by the Maxwell-Boltzmann formula

$$\rho = \frac{1}{\lambda_T} e^{\beta\mu}. \tag{2.139}$$

In the degenerate subregime, the momentum states with energies much smaller than $k_{\mathrm{B}}T$ are highly occupied, and the density of the gas is given by [107]

$$\rho = \frac{k_{\mathrm{B}}T}{\hbar}\sqrt{\frac{m}{-2\mu}}\,. \tag{2.140}$$

Here, the mean interparticle distance becomes much smaller than the thermal de Broglie wavelength: $\lambda_T \gg \rho^{-1}$.

The strongly interacting regime

For low temperatures and low densities, $\overline{\tau} \ll 1$ and $\gamma \gg 1$, the effects of interactions between particles become dominant. We see in this regime a dramatic example of the difference between the physics of 3D Bose gases and of 1D Bose gases. We see here the tendency for a Bose gas to become more strongly interacting as its density decreases [46, 107]. This is in contrast to a 3D Bose gas where the system becomes more non-interacting as the density decreases. The reason for this seemingly paradoxical case is that at temperatures $T \to 0$, the kinetic energy of a particle at the mean interparticle separation is $\propto \rho^2$ and it decreases with decreasing density ρ faster than the interaction energy per particle $\propto \rho$ [108]. With these, the ratio of the interaction energy to kinetic energy, *i.e.* the interaction parameter Eq. (2.134), increases by $\propto 1/\rho$ with decreasing density ρ. In this regime, the particles become impenetrable due to strong repulsive interactions, and the gas is often referred to as a Tonks–Girardeau gas [98, 106]. The strong repulsive interaction leads to fermionisation of the bosonic particles, wherein the wavefunction of two bosonic particles vanishes when they are at the same position. This mimics the Pauli exclusion principle, and the Bose gas acquires some similarities with a gas of noninteracting fermions [107]. More precisely, the available many-body wavefunctions of the 1D Bose gas in this regime are, up to a symmetrisation factor, the wavefunctions of an ideal Fermi gas [98]. The strongly interacting 1D Bose gas and the ideal 1D Fermi gas share the same energy spectrum. However, the momentum distribution of the Bose gas still remains bosonic so that particles do not need to be in different momentum states to be spatially apart [109]. The regime of strongly interacting 1D Bose gas was first realised in optical lattice experiments by adding another lattice potential to increase the effective mass of particles and thereby enhancing the role of interparticle interactions [76, 108].

The quasicondensate regime

For high densities, $\gamma \ll 1$, and low temperatures, $\overline{\tau} \ll \gamma^{-3/2}$, we enter into the regime of weakly interacting quasicondensate regime. 1D Bose gases in this regime are readily accessible in cold atom experiments [107, 110, 111]. In this regime, many of the local properties of a 1D Bose gas look like a true condensate in 3D systems. For example, density fluctuations in a 1D quasicondensate are

suppressed and the density at bulk of the gas takes the form of a Thomas–Fermi parabola. Indeed, it has been shown that the density fluctuations $\delta\hat{\rho}$ in a 1D quasicondensate can be expressed as [31, 70]

$$\frac{\langle \delta\hat{\rho}^2 \rangle}{\rho^2} = \begin{cases} \sqrt{\gamma}\,, & T = 0 \\ \frac{1}{4}\overline{\mathcal{T}}^2\gamma^{-3/2}, & k_{\mathrm{B}}T < \mu \\ \frac{1}{2}\overline{\mathcal{T}}\gamma^{-1/2}, & k_{\mathrm{B}}T > \mu, \end{cases} \tag{2.141}$$

where the dimensionless temperature parameter $\overline{\mathcal{T}}$ is given in Eq. (2.135). For a 1D Bose gas in the quasicondensate regime ($\overline{\mathcal{T}} \ll \sqrt{\gamma}$ or $\overline{\tau}\gamma^{3/2} \ll 1$ with $\gamma \ll 1$), the assumption that density fluctuations are small is justified. The density fluctuations can be used as a tool for ultracold atom thermometry due to their temperature dependence. [75].

However, quasicondensates lack the global coherence that a true condensate exhibits due to phase fluctuations. This phase fluctuation is due to thermal and quantum effects. With this, we can identify two subregimes of the quasicondensate regime. For temperature within the bound $\sqrt{\gamma} \ll \overline{\tau} \ll \gamma^{-3/2}$, thermal effects dominate the system, and it is called the thermal quasicondensate regime. For sufficiently low temperatures, $\overline{\tau} \ll \sqrt{\gamma}$, quantum fluctuations dominate, and the system is in the quantum quasicondensate regime.

2.3.7 Bogoliubov theory of 1D quasicondensates

In Ref. [70], Mora and Castin extended the Bogoliubov theory to 1D quasicondensates (see Sec. 2.2.4 for Bogoliubov theory of 3D Bose gases). In the quasicondensate regime, the fluctuations of density $\hat{\rho}(x) = \hat{\psi}^\dagger(x)\hat{\psi}(x)$ is small in relative values:

$$\mathrm{var}[\hat{\rho}(x)] \equiv \langle \hat{\rho}(x)^2 \rangle - \langle \hat{\rho}(x) \rangle^2 \ll \langle \hat{\rho}(x) \rangle^2. \tag{2.142}$$

However, one finds that the expectation value $\langle \hat{\rho}(x)^2 \rangle$ is infinite at every point x,

$$\langle \hat{\rho}(x)^2 \rangle = \delta(0)\langle \hat{\rho}(x) \rangle + \langle \hat{\psi}^\dagger(x)\hat{\psi}^\dagger(x)\hat{\psi}(x)\hat{\psi}(x) \rangle, \tag{2.143}$$

due to the Dirac delta function $\delta(0)$ that originated from the commutation relations for $\hat{\psi}(x)$, Eq. (2.132). To circumvent this, Mora and Castin discretised space by defining small boxes of equal length l centred at position x, with the length l much greater than the mean interparticle distance:

$$l \gg \frac{1}{\rho(x)}. \tag{2.144}$$

Also, the length l should be small enough so that the energy cut-off

$$E_{\mathrm{cut}} \simeq \frac{\hbar^2}{ml^2}, \tag{2.145}$$

introduced by the grid does not change the physics of the system. This requires that E_{cut} is much larger than the thermal energy $k_{\mathrm{B}}T$ and the chemical potential μ corresponding to the following conditions:

$$l < \xi, \lambda_T, \tag{2.146}$$

where ξ is the healing length, and λ_T is the thermal de Broglie wavelength. These three conditions can be combined as

$$\rho(x)\lambda_T \gg 1, \qquad \rho(x)\xi \gg 1. \tag{2.147}$$

The first one corresponds to the quantum degeneracy regime, while the second condition corresponds to the weakly interacting regime.

In the discretised space, the bosonic operator $\hat{\psi}(x)$ ($\hat{\psi}^\dagger(x)$) annihilates (creates) a particle in the box at position x. The commutation relation in the discretised space is given by

$$\left[\hat{\psi}(x), \hat{\psi}^\dagger(x')\right] = \frac{\delta_{x,x'}}{l}, \tag{2.148}$$

where $\delta_{x,x'}$ is the Kronecker delta. To derive the Bogoliubov theory for quasicondensates, Mora and Castin used the density-phase representation of the field operator

$$\hat{\psi}(x) = e^{i\hat{\phi}(x)}\sqrt{\hat{\rho}(x)}\ , \tag{2.149}$$

where $\hat{\phi}(x)$ represents the phase operator in the box at x. The canonically conjugate operators $\hat{\rho}(x)$ and $\hat{\phi}(x)$ satisfy the commutation relations

$$\left[\hat{\rho}(x), \hat{\phi}(x')\right] = i\frac{\delta_{x,x'}}{l}, \qquad \left[\hat{\rho}(x), \hat{\rho}(x')\right] = 0, \qquad \left[\hat{\phi}(x), \hat{\phi}(x')\right] = 0. \tag{2.150}$$

In the discretised space, the grand canonical Hamiltonian takes the form

$$\hat{H} = \sum_x l\left[-\frac{\hbar^2}{2m}\hat{\psi}^\dagger(x)\nabla^2\hat{\psi}(x) + \left[V_{\text{ext}}(x) - \mu\right]\hat{\psi}^\dagger(x)\hat{\psi}(x) + \frac{g_0}{2}\hat{\psi}^\dagger(x)\hat{\psi}^\dagger(x)\hat{\psi}(x)\hat{\psi}(x)\right], \tag{2.151}$$

where the differential operator ∇^2 is defined in the discrete space as

$$\nabla^2 f(x) = \frac{f(x+l) + f(x-l) - 2f(x)}{l^2}. \tag{2.152}$$

Here, g_0 is different from the one-dimensional interaction parameter g and is given by

$$g_0 = \frac{g}{1 + l/(a_{1\text{D}}\pi^2)}, \tag{2.153}$$

where $a_{1\text{D}} = -2\hbar^2/(mg_{1\text{D}})$ is the one-dimensional scattering length [112, 113]. In the continuum limit, $l \to 0$, we recover $g_0 = g$. To continue with the derivation, the density operator $\hat{\rho}(x)$ is split into a mean density $\rho(x) = \langle\hat{\rho}(x)\rangle$ and fluctuations $\delta\hat{\rho}(x)$ on top of $\rho(x)$:

$$\hat{\rho}(x) = \rho(x) + \delta\hat{\rho}(x). \tag{2.154}$$

The density fluctuation operator $\delta\hat{\rho}(x)$ satisfies the same commutation relations for $\hat{\rho}(x)$ in Eq. (2.150), *i.e.* $\left[\delta\hat{\rho}(x), \hat{\phi}(x')\right] = i\delta_{x,x'}/l$ and $\left[\delta\hat{\rho}(x), \delta\hat{\rho}(x')\right] = 0$. The Hamiltonian Eq. (2.151) is then expanded in terms of the small parameters

$$\epsilon_1 = \frac{|\delta\hat{\rho}(x)|}{\rho_0(x)} \ll 1, \qquad \epsilon_2 = |l\nabla\hat{\phi}(x)| \ll 1, \tag{2.155}$$

where the differential operator ∇ is the discrete gradient defined as

$$\nabla f(x) = \frac{f(x+l) - f(x-l)}{2l}. \tag{2.156}$$

In Eq. (2.155), one assumes that the density fluctuations and phase gradients are small and are of the same order.

The zeroth-order expansion in terms of ϵ_1 and ϵ_2 of the Hamiltonian is given by

$$H^{(0)} = \sum_x l\sqrt{\rho_0(x)}\left[-\frac{\hbar^2}{2m}\nabla^2 + V_{\text{ext}}(x) + \frac{1}{2}g_0\rho_0(x) - \mu\right]\sqrt{\rho_0(x)}\,, \tag{2.157}$$

which is the Gross–Pitaevskii energy functional on the lattice. Minimisation of $H^{(0)}$ gives the time-independent Gross–Pitaevskii equation

$$\left[-\frac{\hbar^2}{2m}\nabla^2 + V_{\text{ext}}(x) + g_0\rho_0(x) - \mu\right]\sqrt{\rho_0(x)} = 0. \tag{2.158}$$

With a density profile fulfilling Eq. (2.158), the first order approximation given by

$$H^{(1)} = \sum_x l\sqrt{\rho_0(x)}\left[-\frac{\hbar^2}{2m\sqrt{\rho_0}}\nabla^2 + V_{\text{ext}}(x) + g_0\rho_0(x) - \mu\right]\delta\hat{\rho}(x), \tag{2.159}$$

vanishes. The leading order contribution of the fluctuations is then given by the second-order expansion to $\hat{H}$:

$$\hat{H}^{(2)} = E_2[\rho_0(x)] + \sum_x l\Bigg[-\frac{\hbar^2}{2m}\frac{\delta\hat{\rho}(x)}{2\sqrt{\rho_0(x)}}\nabla^2\left(\frac{\delta\hat{\rho}(x)}{2\sqrt{\rho_0(x)}}\right) + \frac{\hbar^2\delta\hat{\rho}^2(x)}{8m\rho_0^{3/2}(x)}\nabla^2\sqrt{\rho_0(x)} + \frac{g_0}{2}\delta\hat{\rho}^2(x) + \frac{\hbar^2}{2m}\sqrt{\rho_0(x)\rho_0(x+l)}\,\frac{\left[\hat{\phi}(x+l) - \hat{\phi}(x)\right]^2}{l^2}\Bigg], \tag{2.160}$$

where the energy functional $E_2[\rho_0(x)]$ is given by

$$E[\rho_0(x)] = -\frac{g_0}{2}\sum_x \rho_0(x) - \frac{\hbar^2}{4ml^2}\sum_x\left[\left(\frac{\rho_0(x+l)}{\rho_0(x)}\right)^{1/2} + \left(\frac{\rho_0(x)}{\rho_0(x+l)}\right)^{1/2}\right]. \tag{2.161}$$

This energy functional can be omitted because it does not affect the density fluctuations and phase dynamics. Introducing the bosonic mode operator

$$\hat{B}(x) = \frac{\delta\hat{\rho}(x)}{2\sqrt{\rho_0(x)}} + i\sqrt{\rho_0(x)}\,\hat{\phi}(x), \tag{2.162}$$

that satisfies the commutation relation

$$\left[\hat{B}(x), \hat{B}^\dagger(x')\right] = \frac{\delta_{x,x'}}{l}, \tag{2.163}$$

one can rewrite the second-order Hamiltonian in Eq. (2.160) as

$$\hat{H}^{(2)} = l\sum_x \hat{B}^\dagger\left(-\frac{\hbar^2}{2m}\nabla^2 + V_{\text{ext}}(x) + g_0\rho_0(x) - \mu\right)\hat{B} + g_0\rho_0(x)\left[\hat{B}^\dagger\hat{B} + \frac{1}{2}\left(\hat{B}^2 + \hat{B}^{\dagger 2}\right)\right]. \tag{2.164}$$

This equation has the same structure as the usual Bogoliubov Hamiltonian. One can then use the standard diagonalisation of the Bogoliubov Hamiltonian by using the transformation

$$\hat{B}(x) = \sum_s \hat{b}_s u_s(x) + \hat{b}_s^\dagger v_s^*(x), \tag{2.165}$$

where $\hat{b}_s$ ($\hat{b}_s^\dagger$) is the Bogoliubov quasiparticle annihilation (creation) operator that satisfies the commutation relation $[\hat{b}_s, \hat{b}_{s'}^\dagger] = \delta_{s,s'}$. The Bogoliubov modes $u_s(x)$ and $v_s(x)$ are normalisable as

$$\sum_x l\left[|u_s(x)|^2 - |v_s(x)|^2\right] = 1, \tag{2.166}$$

and are solutions to the Bogoliubov–de Gennes equations

$$\begin{pmatrix} -\frac{\hbar^2}{2m}\nabla^2 + V_{\text{ext}}(x) - \mu + 2g_0\rho_0(x) & g_0\rho_0(x) \\ -g_0\rho_0(x) & \frac{\hbar^2}{2m}\nabla^2 - V_{\text{ext}}(x) + \mu - 2g_0\rho_0(x) \end{pmatrix} \begin{pmatrix} u_s(x) \\ v_s(x) \end{pmatrix} = \epsilon_s \begin{pmatrix} u_s(x) \\ v_s(x) \end{pmatrix}. \tag{2.167}$$

Here, the Bogoliubov dispersion ϵ_s is solved together with the Bogoliubov modes. Combining Eqs. (2.162) and (2.165) leads us to the modal expansion for the density fluctuation operator and phase operator:

$$\delta\hat{\rho}(x) = \sum_s \delta\rho_s(x)\hat{b}_s + \delta\rho_s^*(x)\hat{b}_s^\dagger, \tag{2.168}$$

$$\hat{\phi}(x) = \sum_s \phi_s(x)\hat{b}_s + \phi_s^*(x)\hat{b}_s^\dagger, \tag{2.169}$$

where the coefficients $\delta\rho_s(x)$ and $\phi_s(x)$ are given in terms of $u_s(x)$ and $v_s(x)$ by

$$\delta\rho_s(x) = \sqrt{\rho_0(x)}\,[u_s(x) + v_s(x)], \tag{2.170}$$

$$\phi_s(x) = \frac{u_s(x) - v_s(x)}{2i\sqrt{\rho_0(x)}}. \tag{2.171}$$

The quadratic Hamiltonian in Eq. (2.160) is diagonalised using the modal expansions, Eqs. (2.168) and (2.169), up to a constant term as

$$\hat{H}^{(2)} = \sum_s \epsilon_s \hat{b}_s^\dagger \hat{b}_s + \text{const.}, \tag{2.172}$$

which is a collection of independent harmonic modes with energy ϵ_s.

Luttinger liquid theory

From Eq. (2.160), one can make an approximation where it is assumed that density fluctuations are of short wavelength, *i.e.* the first term inside the summation in Eq. (2.160) can be neglected. This, together with the Thomas–Fermi approximation, leads us to the Luttinger liquid Hamiltonian [32, 69]:

$$\hat{H}_{\text{LL}}^{(2)} = \sum_x l\left[\frac{g}{2}\delta\hat{\rho}^2(x) + \frac{\hbar^2}{2m}\sqrt{\rho(x)\rho(x+l)}\,\frac{\left[\hat{\phi}(x+l) - \hat{\phi}(x)\right]^2}{l^2}\right]. \tag{2.173}$$

In the continuum limit, $l \to 0$, this Hamiltonian is given by

$$\hat{H}^{(2)}_{\mathrm{LL}} = \int \mathrm{d}x \left[\frac{\hbar^2 \rho(x)}{2m} \left(\frac{\partial \hat{\phi}(x)}{\partial x} \right)^2 + \frac{g}{2} \big(\delta\hat{\rho}(x) \big)^2 \right]. \tag{2.174}$$

The operators $\hat{\phi}(x)$ and $\delta\hat{\rho}(x)$ are coarse grained in the sense that they describe physics beyond an energy cutoff [114]. This cutoff is defined in the discrete space by Eqs. (2.145) and (2.146), or in the continuum limit, by the inverse of the healing length and de Broglie wavelength. We now write the density and phase fluctuations in terms of plain waves [114, 115]:

$$\hat{\phi}(x) = \frac{1}{\sqrt{L}} \sum_k e^{ikx} \hat{\phi}_k, \tag{2.175}$$

$$\delta\hat{\rho}(x) = \frac{1}{\sqrt{L}} \sum_k e^{ikx} \delta\hat{\rho}_k, \tag{2.176}$$

where $\hat{\phi}_k$ and $\delta\hat{\rho}_k$ are the Fourier transforms of $\hat{\phi}(x)$ and $\delta\hat{\rho}(x)$, respectively. Here, $k = 2\pi n/L$ with n being nonzero integers. Furthermore, we define the transformations

$$\hat{\phi}_k = -i\sqrt{\frac{mc}{\hbar k \rho}} \left[\hat{b}_k - \hat{b}^\dagger_{-k} \right], \tag{2.177}$$

$$\delta\hat{\rho}_k = \sqrt{\frac{\hbar k \rho}{4mc}} \left[\hat{b}_k + \hat{b}^\dagger_{-k} \right], \tag{2.178}$$

where $\hat{b}_k$ and $\hat{b}^\dagger_k$ are creation and annihilation operators, respectively, of an excitation with momentum $\hbar k$. These operators satisfy the canonical commutation relation $[\hat{b}_k, \hat{b}^\dagger_{k'}] = \delta_{k,k'}$. In this new basis, the Hamiltonian in Eq. (2.174) takes the form

$$\hat{H}^{(2)}_{\mathrm{LL}} = \sum \hbar\omega_k \hat{b}^\dagger_k \hat{b}_k. \tag{2.179}$$

Here, we can see that in the Luttinger liquid approximation, the weakly interacting 1D quasicondensate can be expressed as uncoupled harmonic oscillators. The excitations here are sound waves with energy $\hbar\omega_k = \hbar k c$ and speed of sound $c = \sqrt{\rho g/m}$. Note that we have neglected the $k = 0$ mode because spatial correlations in 1D are determined by excitations with $k \neq 0$ [115].

Phase fluctuations in 1D quasicondensates

The result in Eq. (2.141) implies that a 1D quasicondensate is coherent with respect to the second-order correlation function

$$G^{(2)}(x, x') = \langle \hat{\psi}^\dagger(x) \hat{\psi}^\dagger(x') \hat{\psi}(x') \hat{\psi}(x) \rangle. \tag{2.180}$$

However, the presence of phase fluctuations makes the 1D quasicondensate not coherent in the first-order correlation function

$$G^{(1)}(x, x') = \langle \hat{\psi}^\dagger(x') \hat{\psi}(x) \rangle. \tag{2.181}$$

In the following, we will show how the first-order correlation function decays with distance due to phase fluctuations.

For a uniform 1D system, the first-order correlation function can be defined by the distance between two points: $G^{(1)}(x,x') = G^{(1)}(|x-x'|)$. By setting $x' = 0$ and noting that $\rho(x) = \rho(x') = \rho$ for a uniform system, the first-order correlation function becomes

$$G^{(1)}(x) = \rho \left\langle e^{i\left[\hat{\phi}(x)-\hat{\phi}(0)\right]} \right\rangle, \tag{2.182}$$

where we have used the density-phase representation of $\hat{\psi}^\dagger(x)$, Eq. (2.149). In the quasicondensate regime, $G^{(1)}(x)$ is dominated by long-wavelength excitations whose Hamiltonian reduces to the Luttinger liquid Hamiltonian Eq. (2.174) [32, 69, 107]. The expectation value $\langle e^{i[\hat{\phi}(x)-\hat{\phi}(0)]}\rangle$ can be evaluated by expanding the exponential in powers of $i[\hat{\phi}(x)-\hat{\phi}(0)]$ and using Wick's theorem [116] to evaluate the average of each term in the expansion. Because the Hamiltonian in Eq. (2.174) is quadratic, the terms with odd powers of $i[\hat{\phi}(x)-\hat{\phi}(0)]$ in the expansion will vanish. This leads to $\left\langle e^{i\left[\hat{\phi}(x)-\hat{\phi}(0)\right]} \right\rangle = \exp\left[-\langle(\hat{\phi}(x)-\hat{\phi}(0))^2\rangle/2\right]$. To evaluate $\langle(\hat{\phi}(x)-\hat{\phi}(0))^2\rangle/2$, we follow Ref. [107] and expand the local phase as

$$\hat{\phi}(x) = \sum_{k>0} \sqrt{2}\,\left[\hat{\phi}_{ck}\cos(kx) + \hat{\phi}_{sk}\sin(kx)\right], \tag{2.183}$$

which gives us

$$\frac{1}{2}\langle[\hat{\phi}(x)-\hat{\phi}(0)]^2\rangle = \sum_{k>0}\left[\langle\hat{\phi}_{ck}^2\rangle\big(\cos(kx)-1\big)^2 + \langle\hat{\phi}_{sk}^2\rangle\sin^2(kx)\right]. \tag{2.184}$$

In momentum space, the Hamiltonian Eq. (2.174) is given by

$$\hat{H}_{\mathrm{LL}} = \frac{L}{2\pi}\int \mathrm{d}k\left[\frac{\hbar^2k^2}{2m}\rho\big(\hat{\phi}_k\big)^2 + \frac{g}{2}\big(\delta\hat{\rho}_k\big)^2\right], \tag{2.185}$$

where $\hat{\phi}_k$ and $\delta\hat{\rho}_k$ are Fourier transforms of $\hat{\phi}(x)$ and $\delta\hat{\psi}(x)$, respectively, and L is the length of the uniform Bose gas. For $T \gg \rho g$, the relevant thermal modes contributing to $g^{(1)}(x)$ are large and a classical field picture is sufficient. Thus, via the equipartition theorem, the average energy per quadratic degree of freedom is $k_BT/2$, and we obtain

$$\langle\hat{\phi}_k^2\rangle = \frac{mk_BT}{L\hbar^2k^2\rho}, \tag{2.186}$$

With $\langle\hat{\phi}_{ck}^2\rangle = \langle\hat{\phi}_{sk}^2\rangle = \langle\hat{\phi}_k^2\rangle$, Eq. (2.184) becomes

$$\frac{1}{2}\langle[\hat{\phi}(x)-\hat{\phi}(0)]^2\rangle = 2\sum_{k>0}\frac{mk_BT}{L\hbar^2k^2\rho}\big[1-\cos(kx)\big]. \tag{2.187}$$

Using the approximation $\sum_k \to \frac{L}{2\pi}\int \mathrm{d}k$ and noting that $\int_0^\infty \mathrm{d}k[1-\cos(kx)]/k^2 = |x|\pi/2$, the first-order correlation function becomes

$$G^{(1)}(x) = \rho e^{-\frac{|x|}{2l_\phi}}, \tag{2.188}$$

where

$$l_\phi = \frac{\hbar^2\rho}{mk_BT}, \tag{2.189}$$

is the thermal phase coherence length of the quasicondensate. Like density fluctuations, phase fluctuations can be used to measure the temperature of a quasicondensate by exploiting the temperature dependence of the thermal phase coherence length. Refs. [117–121] have some of the early measurements of phase fluctuations in experiments. Petrov *et al.* showed in Ref. [122] that a similar approach as the above derivation holds for an elongated 3D BEC. The thermal phase coherence length they derived for an elongated 3D BEC has a similar expression as in Eq. (2.189).

2.3.8 Finite temperature momentum distribution

At zero temperature, the momentum distribution of a 1D Bose gas in the weakly interacting regime takes the shape of a Dirac delta function at $k = 0$ momentum. This changes when thermal fluctuations are incorporated into the system. At finite temperatures, the $k = 0$ momentum state still has macroscopic occupation, but a significant number of particles occupy higher momentum states.

The momentum distribution $n(k)$ is given by the Fourier transform of the first-order correlation function $G^{(1)}(x, x') = \langle\hat{\psi}(x)\hat{\psi}(x')\rangle$. For a uniform system in the quasicondensate regime, the first-order correlation function is given in Eq. (2.188). Thus, the momentum distribution $n(k)$ of a uniform 1D quasicondensate is given by the Lorentzian function

$$n(k) = \frac{1}{2\pi}\int G^{(1)}(x)e^{ikx}\mathrm{d}x = \frac{2\rho l_\phi}{\pi\left[1 + (2kl_\phi)^2\right]}. \tag{2.190}$$

For the case of a trapped 1D quasicondensate, we must first consider a slice of the condensate of density $\rho(x) = \langle\hat{\rho}(x)\rangle$ that is constant throughout the region $[x, x + \mathrm{d}x]$. The momentum distribution in the region $[x, x + \mathrm{d}x]$ is the same as Eq. (2.190) . Thus, the total momentum distribution for the whole trapped quasicondensate is given by

$$n(k) = \int \mathrm{d}x n(k, x) = \frac{2}{\pi}\int \mathrm{d}x \frac{\rho(x)l_\phi(x)}{\left[1 + (2kl_\phi(x))^2\right]}. \tag{2.191}$$

Here, the position dependence of $l_\phi(x)$ is due to its dependence on the local density $\rho(x)$.

2.4 Stochastic methods for interacting Bose gases

We employ some well-known stochastic methods: the *c*-field methods and the truncated Wigner method to study the dynamics of a Bose gas beyond mean-field theory. *c*-field methods utilise the fact that Bose condensed systems have significant occupation of some modes of the system at finite temperature. In essence, *c*-field methods approximate the highly occupied modes using a classical field instead of using the full many-body quantum field theory. The truncated Wigner approach incorporates quantum fluctuations by representing them in phase-space by stochastic distributions of *c*-field trajectories. This section will outline the formulation of the truncated Wigner approximation used to model quantum fluctuations and the stochastic projected Gross–Pitaevskii equation used to model thermal fluctuations. Our general procedure follows the outline of a review article by Blakie *et al.* [123].

2.4.1 Wigner representation

The basis of the Wigner representation is the Weyl transformation that provides a one-to-one mapping between quantum mechanical operators and classical functions of phase-space coordinates. For a one-dimensional N-particle system, the Weyl symbol $O_{\mathcal{W}}(x,p)$ corresponding to the quantum mechanical operator $\hat{O}(\hat{x},\hat{p})$ is given by

$$O_{\mathcal{W}}(x,p) = \frac{1}{(2\pi)^N}\int\left\langle x-\frac{\xi}{2}\middle|\hat{O}(\hat{x},\hat{p})\middle|x+\frac{\xi}{2}\right\rangle e^{ip\xi/\hbar}d\xi. \tag{2.192}$$

Of principal interest to us is the Wigner function defined as the Weyl symbol of the density operator $\hat{\rho}(\hat{x},\hat{p})$,

$$W(x,p) = \frac{1}{(2\pi)^N}\int\left\langle x-\frac{\xi}{2}\middle|\hat{\rho}(\hat{x},\hat{p})\middle|x+\frac{\xi}{2}\right\rangle e^{ip\xi/\hbar}d\xi. \tag{2.193}$$

The Wigner function acts like a classical probability function over phase-space variables. One of the main properties of the Wigner function is that its marginals, *i.e.* integration over one set of variables, give the correct probability distribution for the position and momentum

$$P(x) = \int W(x,p)dp, \tag{2.194}$$

$$P(p) = \int W(x,p)dx. \tag{2.195}$$

The Wigner function is always real; however, it must be noted that it is not always non-negative. Thus, an integration of the Wigner function over a subregion of the phase-space may yield a negative result. This negativity in the Wigner function is often suggested as evidence of the non-classicality of the quantum state given by $\hat{\rho}$. Because it is not strictly positive, the Wigner function is called a *quasi-probability* distribution.

So far, we have introduced the Wigner function in the first quantised coordinate representation. However, such representation becomes cumbersome when describing macroscopic systems. A more convenient description of the system is achieved by expanding field operators in terms of coherent states $|\alpha\rangle$, which form a non-orthogonal basis set. Coherent states are advantageous because they are eigenstates of the annihilation operator $\hat{a}$ with complex eigenvalue α: $\hat{a}|\alpha\rangle = \alpha|\alpha\rangle$. The solution to this defining eigenvalue equation that also satisfies $\langle\alpha|\alpha\rangle = 1$ is (up to a phase) [124]

$$|\alpha\rangle = \exp\left(-\frac{1}{2}|\alpha|^2\right)\sum_{n=0}^{\infty}\frac{\alpha^n}{\sqrt{n!}}|n\rangle, \tag{2.196}$$

where $|n\rangle$ are number states which are eigenstates of the number operator $\hat{N} = \hat{a}^\dagger\hat{a}$. Using the action of $\hat{a}$ and $\hat{a}^\dagger$ to the number state, $\hat{a}|n\rangle = \sqrt{n}\,|n-1\rangle$ and $\hat{a}^\dagger|n\rangle = \sqrt{n+1}\,|n+1\rangle$, respectively, it can be shown that the action of these operators to the coherent state $|\alpha\rangle$ are

$$\hat{a}|\alpha\rangle = \alpha|\alpha\rangle, \qquad \hat{a}^\dagger|\alpha\rangle = \left(\alpha^* + \frac{1}{2}\frac{\partial}{\partial\alpha}\right)|\alpha\rangle, \tag{2.197}$$

$$\langle\alpha|\hat{a}^\dagger = \langle\alpha|\alpha^*, \qquad \langle\alpha|\hat{a} = \left(\alpha + \frac{1}{2}\frac{\partial}{\partial\alpha^*}\right)\langle\alpha|. \tag{2.198}$$

(see Section 10.5 of Ref. [124] for other properties of coherent states). In the coherent state representation, the Weyl transformation can be written as [125]

$$O_{\mathcal{W}}(\alpha,\alpha^*) = \frac{1}{(2\pi)^M}\int\int e^{\frac{1}{2}(\lambda^*\alpha-\lambda\alpha^*)}\left\langle \alpha-\frac{\lambda}{2}\middle|\hat{O}(\hat{a}_1\ldots\hat{a}_M,\hat{a}_{1^\dagger}\ldots\hat{a}_M^\dagger)\middle|\alpha+\frac{\lambda}{2}\right\rangle d\lambda d\lambda^*. \quad (2.199)$$

For a multimode quantum state $\hat{\rho}$, the multimode Wigner function in the coherent state phase-space is given by [126, 127]

$$W(\alpha,\alpha^*) = \frac{1}{\pi^{2M}}\int d^2\lambda e^{\lambda^\dagger\alpha-\alpha^\dagger\lambda}\chi_W(\lambda,\lambda^*), \quad (2.200)$$

where

$$\chi_W(\lambda,\lambda^*) = \mathrm{tr}\left[\hat{\rho}\prod_{m=1}^{M} e^{\lambda_m\hat{a}_m^\dagger-\lambda_m^*\hat{a}_m}\right], \quad (2.201)$$

is the symmetrically ordered quantum characteristic function of the density operator $\hat{\rho}$. Here, $\hat{a}_m$ ($\hat{a}_m^\dagger$) are the annihilation (creation) operators of the $m = 1, 2, \ldots, M$ coherent state modes, $\lambda = (\lambda_1, \lambda_2, \ldots, \lambda_M)$ are integration variables, and $\alpha = (\alpha_1, \alpha_2, \ldots, \alpha_M)$ are the coherent state amplitudes. Thus, the Wigner function $W(\alpha,\alpha^*)$ is interpreted as a quasi-probability distribution for the amplitudes α_m.

Because the Wigner function acts like a probability distribution function over the phase-space, one can calculate the expectation value of an operator $\hat{O}$ by calculating the average over the phase-space with weights given by $W(\alpha,\alpha^*)$:

$$\langle\hat{O}\rangle_W = \langle O_{\mathcal{W}}\rangle = \int d^{2M}\alpha O_{\mathcal{W}} W(\alpha,\alpha^*). \quad (2.202)$$

It should be noted that, due to the definition of the Wigner function (with the use of the symmetrically ordered characteristic function), the moments of the Wigner function give symmetrically ordered operator averages

$$\int d\alpha d\alpha^*\alpha^s(\alpha^*)^r W(\alpha,\alpha^*) = \langle\hat{a}^s(\hat{a}^\dagger)^r\rangle_{\mathrm{sym}}. \quad (2.203)$$

For example,

$$\int d\alpha d\alpha^*\alpha_i^*\alpha_i W(\alpha,\alpha^*) = \langle\hat{a}_i^\dagger\hat{a}_i\rangle_{\mathrm{sym}} = \frac{1}{2}\langle\hat{a}_i^\dagger\hat{a}_i + \hat{a}_i\hat{a}_i^\dagger\rangle. \quad (2.204)$$

Truncated Wigner approximation

We now show how the Wigner formalism can be used in practice to calculate the dynamics of different observables. For a quantum system subject to unitary evolution, the dynamics of the density operator is governed by the von Neumann equation

$$i\hbar\frac{\partial\hat{\rho}}{\partial t} = \left[\hat{H},\hat{\rho}\right], \quad (2.205)$$

where $\hat{H}$ is the Hamiltonian of the system. In general, this equation is hard to solve, even numerically, because the size of the Hilbert space increases exponentially with the number of particles in the system. However, by applying phase-space methods, we can transform this equation into an evolution equation for the phase-space distribution, which, in general, can be solved using well-established numerical techniques. The key to phase-space methods is in the quantum to classical correspondence, where

the action of a quantum operator on the density operator is mapped to an equivalent statement of the action of a classical operator on a quasi-probability distribution, which for our case here is the Wigner quasi-probability distribution. The right hand side of the von Neumann equation Eq. (2.205) will be composed of products of operators and the density operator $\hat{\rho}$. By using the characteristic function Eq. (2.201) and the Wigner function Eq. (2.200), it can be shown [123, 124] that the quantum to classical function operator correspondences for the Wigner distribution are given by

$$\hat{\psi}(x)\hat{\rho} \longleftrightarrow \left(\psi_W + \frac{1}{2}\frac{\delta}{\delta\psi_W^*(x)}\right)W, \tag{2.206}$$

$$\hat{\psi}^\dagger(x)\hat{\rho} \longleftrightarrow \left(\psi_W^* - \frac{1}{2}\frac{\delta}{\delta\psi_W(x)}\right)W, \tag{2.207}$$

$$\hat{\rho}\hat{\psi}(x) \longleftrightarrow \left(\psi_W - \frac{1}{2}\frac{\delta}{\delta\psi_W^*(x)}\right)W, \tag{2.208}$$

$$\hat{\rho}\hat{\psi}^\dagger(x) \longleftrightarrow \left(\psi_W^* + \frac{1}{2}\frac{\delta}{\delta\psi_W^*(x)}\right)W, \tag{2.209}$$

where the functional derivatives are defined as

$$\frac{\delta}{\delta\psi_W(x)} = \sum_m \phi_m^*(x)\frac{\partial}{\partial\alpha_m}, \tag{2.210}$$

$$\frac{\delta}{\delta\psi_W^*(x)} = \sum_m \phi_m(x)\frac{\partial}{\partial\alpha_m^*}, \tag{2.211}$$

with

$$\psi_W(x) = \sum_m \alpha_m\phi_m(x), \tag{2.212}$$

where $\phi_m(x)$ are the single-particle eigenstates of the Hamiltonian $\hat{H}$.

Using the previously derived effective Hamiltonian for a weakly-interacting Bose gas (Eq. (2.131)), the von Neumann equation yields

$$\begin{aligned}\frac{\partial W}{\partial t} = \int dx \Bigg\{ &\frac{i}{\hbar}\frac{\delta}{\delta\psi_W(x)}\big[H_{\text{sp}} + g\big(|\psi_W(x)|^2 - \delta(x,x)\big)\psi_W(x)\big] + h.c. \\ &+ \frac{ig}{4\hbar}\frac{\delta}{\delta\psi_W(x)\delta\psi_W^*(x)}\psi_W^*(x)\frac{\delta}{\delta\psi_W(x)} + h.c.\Bigg\}W,\end{aligned} \tag{2.213}$$

where $h.c.$ represents the Hermitian conjugate. This equation is very difficult to solve due to the third-order derivatives that appear in the second line. However, if we are able to neglect these third-order derivatives, then Eq. (2.213) becomes more manageable to solve. This procedure is known as the *truncated Wigner approximation* (TWA) and is valid for a wide range of scenarios (see Section 2.3.9 of Ref. [123] for a discussion of validity conditions for this approximation). In general, this approximation is valid for systems where the modes in question have significant population. In this case, one generally argues that the contribution of third-order derivative terms is negligible, at least for short-time dynamics. As it is, there is no simple mapping of Eq. (2.213) to a stochastic representation [128, 129]. However, by doing the TWA, Eq. (2.213) takes the form of a Fokker–Planck equation with drift (first-order derivatives) but no diffusion (second-order derivatives) terms:

$$\frac{\partial W}{\partial t} = \int dx \Bigg\{\frac{i}{\hbar}\frac{\delta}{\delta\psi_W(x)}\big[H_{\text{sp}} + g\big(|\psi_W(x)|^2 - \delta(x,x)\big)\psi_W(x)\big] + h.c.\Bigg\}W, \tag{2.214}$$

that describes the evolution of the quasi-probability function W in phase-space. The term $\delta(x,x)$ is constant in the Fourier basis and does not affect the evolution of W. Using the method of characteristics, Eq. (2.214) can then be mapped to a stochastic partial differential equation that describes the evolution of a single realisation of the field $\psi_W(x)$:

$$i\hbar\frac{\partial\psi_W(x)}{\partial t} = \left(H_{\rm sp} + g|\psi_W(x)|^2\right)\psi_W(x). \tag{2.215}$$

The absence of diffusion terms in Eq. (2.214) renders Eq. (2.215) deterministic, *i.e.* there is no explicit noise term in the evolution equation. However, the initial conditions $\psi_W(x,t=0)$ are stochastic and are sampled from the initial Wigner function.

Sampling the Wigner distribution

We sample the initial Bogoliubov state by introducing the random variables α_0 and $\{\beta_j\}$ in place of the operators $\hat{a}_0$ and $\{\hat{b}_j\}$, respectively, in the Bogoliubov expansion of the initial state. The initial state is then given by

$$\psi_W(x,0) = \alpha_0\psi_0(x,0) + \sum_{j=1}^{M_B}\left[\beta_j u_j(x) + \beta_j^* v_j^*(x)\right], \tag{2.216}$$

where $\psi_0(x,0)$ is the ground state solution to the GPE (normalised to unity) with the corresponding quantum noise sampled according to the Wigner distribution of the coherent state [124, 130, 131]

$$W_c(\alpha_0,\alpha_0^*) = \frac{2}{\pi}\exp\big(-2\big|\alpha_0 - \sqrt{N_0}\,\big|^2\big), \tag{2.217}$$

that is Gaussian distributed with mean and second moments given by

$$\langle\alpha_0\rangle_{\rm stoch} = \sqrt{N_0}\,, \tag{2.218}$$

$$\langle\alpha_0\alpha_0\rangle_{\rm stoch} = N_0, \tag{2.219}$$

$$\langle\alpha_0^*\alpha_0\rangle_{\rm stoch} = N_0 + \frac{1}{2}. \tag{2.220}$$

Here and hereafter, $\langle\cdot\rangle_{\rm stoch}$ refers to ensemble averaging over a sufficiently large number of stochastic trajectories. The variables $\{\beta_j\}$ represent the quasiparticle modes whose Wigner distribution has the form of a product of uncorrelated Gaussian quasiprobability distributions, given by [123, 132]:

$$W_{\rm qp}(\boldsymbol{\beta},\boldsymbol{\beta}^*) = \prod_{j>0} W_j(\beta_j,\beta_j^*), \tag{2.221}$$

$$W_j(\beta_j,\beta_j^*) = \frac{2}{\pi}\tanh\left(\frac{\epsilon_j}{2k_{\rm B}T}\right)\exp\left[-2|\beta_j|^2\tanh\left(\frac{\epsilon_j}{2k_{\rm B}T}\right)\right]. \tag{2.222}$$

The Gaussian complex random numbers β_j have the properties

$$\langle\beta_j\rangle_{\rm stoch} = \langle\beta_i\beta_j\rangle_{\rm stoch} = 0, \tag{2.223}$$

$$\langle\beta_i^*\beta_j\rangle_{\rm stoch} = \delta_{ij}\left(\bar{n}_j + \frac{1}{2}\right), \tag{2.224}$$

where $\bar{n}_j$ is the Bose occupation number for Bogolibov modes with energies ϵ_j at temperature T:

$$\bar{n}_j = \frac{1}{e^{\epsilon/k_{\mathrm{B}}T} - 1}. \tag{2.225}$$

In practice, the Gaussian noises α_0 and β_j can be generated as

$$\alpha_0 = \sqrt{N_0} + \frac{1}{2}\big(x_0 + iy_0\big), \tag{2.226}$$

$$\beta_j = \sqrt{\bar{n}_j + \frac{1}{2}}\left(\frac{x_j + iy_j}{\sqrt{2}}\right), \tag{2.227}$$

where x_0, y_0, x_j, and y_j are normally distributed random variables with zero mean and unit variance.

One may notice that even in the zero-temperature limit, where $\bar{n}_j = 0$, the random variables $\{\beta_j\}$ have a variance $\langle|\beta_j|^2\rangle = \frac{1}{2}$. That is, each mode of the system has, on average, half an atom of vacuum noise, which is necessary to ensure the symmetrically ordered interpretation of Wigner moments. For example, the density is calculated as an average over many stochastic Wigner trajectories using

$$\rho(x,t) = \langle\psi_W^*(x,t)\psi_W(x,t)\rangle_{\mathrm{stoch}} - \frac{1}{2}\delta_{\mathbf{C}}(x,x), \tag{2.228}$$

where

$$\frac{1}{2}\int \delta_{\mathbf{C}}(x,x)\mathrm{d}x = \frac{M_B}{2} \tag{2.229}$$

represents the half quantum per mode vacuum noise.[3] The second-order correlation function that is given in terms of field operators by

$$G^{(2)}(x,x') = \left\langle \hat{\psi}^\dagger(x)\hat{\psi}^\dagger(x')\hat{\psi}(x')\hat{\psi}(x)\right\rangle, \tag{2.230}$$

has symmetric ordering given by

$$\begin{aligned}
\langle\hat{\psi}^\dagger(x)\hat{\psi}^\dagger(x')\hat{\psi}(x')\hat{\psi}(x)\rangle_{\mathrm{sym}} = \frac{1}{24}\Big[&\langle\hat{\psi}^\dagger(x)\hat{\psi}^\dagger(x')\hat{\psi}(x')\hat{\psi}(x)\rangle + \langle\hat{\psi}^\dagger(x)\hat{\psi}(x')\hat{\psi}^\dagger(x')\hat{\psi}(x)\rangle \\
&+ \langle\hat{\psi}^\dagger(x)\hat{\psi}(x')\hat{\psi}(x)\hat{\psi}^\dagger(x')\rangle + \langle\hat{\psi}(x')\hat{\psi}^\dagger(x)\hat{\psi}^\dagger(x')\hat{\psi}(x)\rangle \\
&+ \langle\hat{\psi}(x')\hat{\psi}(x)\hat{\psi}^\dagger(x)\hat{\psi}^\dagger(x')\rangle + \langle\hat{\psi}(x)\hat{\psi}^\dagger(x)\hat{\psi}(x')\hat{\psi}^\dagger(x')\rangle \\
&+ \langle\hat{\psi}^\dagger(x')\hat{\psi}^\dagger(x)\hat{\psi}(x)\hat{\psi}(x')\rangle + \langle\hat{\psi}^\dagger(x')\hat{\psi}(x)\hat{\psi}^\dagger(x)\hat{\psi}(x')\rangle \\
&+ \langle\hat{\psi}^\dagger(x')\hat{\psi}(x)\hat{\psi}(x')\hat{\psi}^\dagger(x)\rangle + \langle\hat{\psi}(x)\hat{\psi}^\dagger(x')\hat{\psi}^\dagger(x)\hat{\psi}(x')\rangle \\
&+ \langle\hat{\psi}(x)\hat{\psi}(x')\hat{\psi}^\dagger(x')\hat{\psi}^\dagger(x)\rangle + \langle\hat{\psi}(x')\hat{\psi}^\dagger(x')\hat{\psi}(x)\hat{\psi}^\dagger(x)\rangle \\
&+ \langle\hat{\psi}^\dagger(x)\hat{\psi}^\dagger(x')\hat{\psi}(x)\hat{\psi}(x')\rangle + \langle\hat{\psi}^\dagger(x)\hat{\psi}(x)\hat{\psi}^\dagger(x')\hat{\psi}(x')\rangle \\
&+ \langle\hat{\psi}^\dagger(x)\hat{\psi}(x)\hat{\psi}(x')\hat{\psi}^\dagger(x')\rangle + \langle\hat{\psi}(x)\hat{\psi}^\dagger(x)\hat{\psi}^\dagger(x')\hat{\psi}(x')\rangle \\
&+ \langle\hat{\psi}(x)\hat{\psi}(x')\hat{\psi}^\dagger(x)\hat{\psi}^\dagger(x')\rangle + \langle\hat{\psi}(x')\hat{\psi}^\dagger(x)\hat{\psi}(x)\hat{\psi}^\dagger(x')\rangle \\
&+ \langle\hat{\psi}^\dagger(x')\hat{\psi}^\dagger(x)\hat{\psi}(x')\hat{\psi}(x)\rangle + \langle\hat{\psi}^\dagger(x')\hat{\psi}(x')\hat{\psi}^\dagger(x)\hat{\psi}(x)\rangle \\
&+ \langle\hat{\psi}^\dagger(x')\hat{\psi}(x')\hat{\psi}(x)\hat{\psi}^\dagger(x)\rangle + \langle\hat{\psi}(x')\hat{\psi}^\dagger(x')\hat{\psi}^\dagger(x)\hat{\psi}(x)\rangle \\
&+ \langle\hat{\psi}(x')\hat{\psi}(x)\hat{\psi}^\dagger(x')\hat{\psi}^\dagger(x)\rangle + \langle\hat{\psi}(x)\hat{\psi}^\dagger(x')\hat{\psi}(x')\hat{\psi}^\dagger(x)\rangle\Big].
\end{aligned} \tag{2.231}$$

[3]Here, $\delta_{\mathbf{C}}(x,x)$ plays the role of a Dirac-delta function on a computational grid. If the grid spacing is $\Delta x = L/M$, where M is the number of grid points, the delta function is given by $\delta_{\mathbf{C}}(x,x) = M_B/(M\Delta x)$.

After doing the normal ordering of the operators with the use of the Bose commutation rule, we get

$$\begin{aligned} G^{(2)}(x,x') = &\langle \hat{\psi}^\dagger(x)\hat{\psi}^\dagger(x')\hat{\psi}(x')\hat{\psi}(x)\rangle \\ &- \frac{1}{2}\delta(x,x)\left[\langle \hat{\psi}^\dagger(x)\hat{\psi}(x)\rangle + \langle \hat{\psi}^\dagger(x')\hat{\psi}(x')\rangle - \frac{1}{2}\delta(x,x)\right] \\ &- \frac{1}{2}\delta(x,x')\left[\langle \hat{\psi}^\dagger(x)\hat{\psi}(x')\rangle + \langle \hat{\psi}^\dagger(x')\hat{\psi}(x)\rangle - \frac{1}{2}\delta(x,x')\right]. \end{aligned} \tag{2.232}$$

In terms of the classical fields $\psi_W(x)$, this is equivalent to

$$\begin{aligned} G^{(2)}(x,x') = &\langle \psi_W^*(x)\psi_W^*(x')\psi_W(x')\psi_W(x)\rangle_{\text{stoch}} \\ &- \frac{1}{2}\delta_{\mathbf{C}}(x,x)\left[\langle \psi_W^*(x)\psi_W(x)\rangle_{\text{stoch}} + \langle \psi_W^*(x')\psi_W(x')\rangle_{\text{stoch}} - \frac{1}{2}\delta_{\mathbf{C}}(x,x)\right] \\ &- \frac{1}{2}\delta_{\mathbf{C}}(x,x')\left[\langle \psi_W^*(x)\psi_W(x')\rangle_{\text{stoch}} + \langle \psi_W^*(x')\psi_W(x)\rangle_{\text{stoch}} - \frac{1}{2}\delta_{\mathbf{C}}(x,x')\right], \end{aligned} \tag{2.233}$$

and the normalised second-order correlation function is

$$g^{(2)}(x,x') = \frac{G^{(2)}(x,x')}{\rho(x)\rho(x')}, \tag{2.234}$$

with $\rho(x)$ calculated according to Eq. (2.228).

The truncated Wigner approximation is valid when the total number of particles N in the system greatly exceeds the number of relevant Bogoliubov modes M_B. One must be particularly cautious of this criterion in two or three dimensions where physical observables can diverge as a function of the number of modes [133], and the heating of atomic clouds during time evolution can excite many high-energy modes [127]. However, 1D systems are more robust to these effects. In particular, 1D simulations using a static field pre-distributed according to the Bose-Einstein distribution via Eqs. (2.221) and (2.222) do not depend on the total number of quasiparticles modes used, and the observables calculated remain unchanged when the number of modes is varied [130, 131, 133].

2.4.2 The stochastic projected Gross–Pitaevskii equation

We again turn to *c*-field methods [123] to study the dynamics of Bose gases at finite temperature. The formalism we employ utilises the fact that lower energy modes of the Bose gas are highly occupied. When the occupation of an energy mode is larger than one quantum, the system is highly Bose degenerate. The highly occupied modes can be described by a classical field instead of using the full many-body quantum field theory.

C-field methods employ a projector operator that provides a cut-off where the mode occupation is approximately one. Below this cut-off, in the so-called coherent region (**C**), the mode occupation is high and can be treated quantum mechanically using the classical field representation. In contrast, in the region above this cut-off, termed the incoherent region (**I**), modes are treated semi-classically and represent the thermal cloud. There are, however, other approaches to the incoherent region, *e.g.* some do not include the incoherent region (see Ref. [134]) and some add noncondensate atoms using Hartree-Fock calculations (see Refs. [123, 135]).

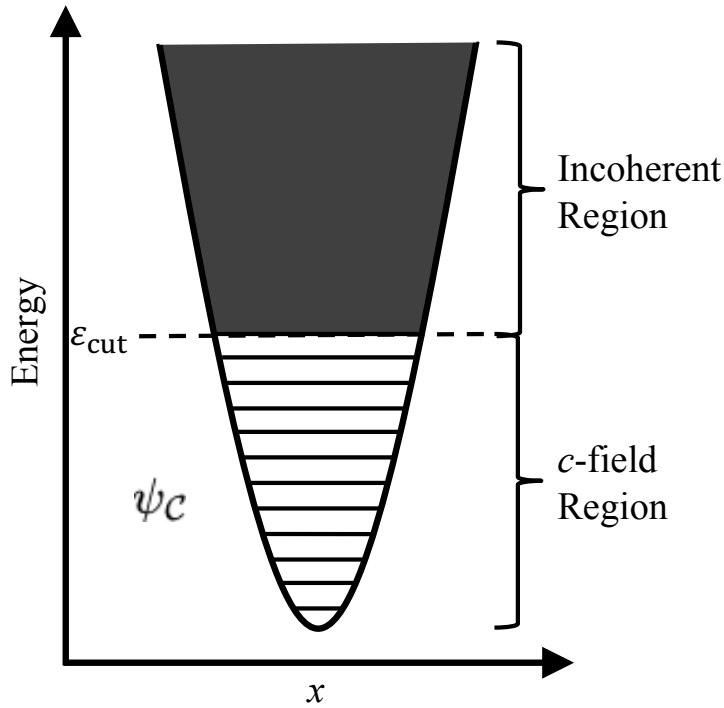

Figure 2.5: Schematic showing the c-field region and the incoherent region, separated by the energy cut-off ϵ_{cut}. In the c-field approach, the energy cut-off ϵ_{cut} is chosen so that all c-field region modes have large occupation. This allows the quantum mechanical treatment of the c-field region in a classical field approximation. The incoherent region acts as a thermal reservoir and is treated semi-classically.

The single particle energy cut-off ϵ_{cut} defines the boundary between the coherent and incoherent regions. The modes in the coherent region have energies $\epsilon \leq \epsilon_{\text{cut}}$, while modes in the incoherent region have energies $\epsilon > \epsilon_{\text{cut}}$.[4] The field operators $F(\mathbf{x})$ describing the system can be restricted to a certain region by employing the projection operators given by

$$\mathcal{P}_{\mathbf{C}}\{F(x\} = \sum_{n\in\mathbf{C}} \phi_n(x) \int \mathrm{d}x' \phi_n^*(x') F(x'), \tag{2.235}$$

$$\mathcal{P}_{\mathbf{I}}\{F(x)\} = \sum_{n\in\mathbf{I}} \phi_n(x) \int \mathrm{d}x' \phi_n^*(x') F(x'), \tag{2.236}$$

where $\mathbf{C} = \{n : \epsilon_n \leq \epsilon_{\text{cut}}\}$ and $\mathbf{I} = \{n : \epsilon_{\text{cut}<\epsilon_n\leq E_{\max}}\}$. The two projectors are orthogonal to each other: $\mathcal{P}_{\mathbf{I}}\mathcal{P}_{\mathbf{C}} = 0$.

[4]It should be noted that for 3D systems, an explicit maximum energy cutoff $E_{\max}$ is needed in the effective field theory, *i.e.* modes in the incoherent region should have energies $\epsilon_{\text{cut}} < \epsilon \leq E_{\max}$. This maximum energy cutoff restricts the effective field theory to low momenta $|\mathbf{k}| \ll 1/a$, with a being the 3D s-wave scattering length, and prevents the ultraviolet divergence in the theory due to the replacement of the actual interaction potential by a delta function potential: $U(\mathbf{x}-\mathbf{x}') \to g_{3\text{D}}\delta(\mathbf{x}-\mathbf{x}')$ [136]. Another approach to this problem of ultraviolet divergence is the ultraviolet renormalisation of the theory where the two-body T-matrix is introduced into the Hamiltonian, resulting in a high-energy cutoff [137]. In 1D calculations, this delta function approximation for the interaction potential does not lead to ultraviolet divergence [31, 63, 105, 138], and therefore does not need the introduction of $E_{\max}$ nor the ultraviolet renormalisation.

The quantum fields in each region are then defined as

$$\hat{\psi}_{\mathbf{C}}(x) \equiv \mathcal{P}_{\mathbf{C}}\{\hat{\psi}(x)\} = \sum_{n\in\mathbf{C}} \hat{a}_n \phi_n(x), \tag{2.237}$$

$$\hat{\psi}_{\mathbf{I}}(x) \equiv \mathcal{P}_{\mathbf{I}}\{\hat{\psi}(x)\} = \sum_{n\in\mathbf{I}} \hat{a}_n \phi_n(x), \tag{2.238}$$

such that the total quantum field is $\hat{\psi}(x) = \hat{\psi}_{\mathbf{C}}(x) + \hat{\psi}_{\mathbf{I}}(x)$. The equal-time commutator of the c-field operator $\hat{\psi}_{\mathbf{C}}(x)$ is given by

$$[\hat{\psi}^{\dagger}_{\mathbf{C}}(x), \hat{\psi}_{\mathbf{C}}(x')] = \delta_{\mathbf{C}}(x, x'), \tag{2.239}$$

where $\delta_{\mathbf{C}}(x, x')$ is called the kernel of the projector $\mathcal{P}_{\mathbf{C}}$:

$$\delta_{\mathbf{C}}(x, x') \equiv \sum_{n\in\mathbf{C}} \phi_n(x)\phi^*_n(x'). \tag{2.240}$$

It is important to note that the function $\delta_{\mathbf{C}}(x, x')$ is not a pure Dirac-delta function due to the imposition of the energy cut-off. However, it still acts like one on any given function within the coherent region, namely

$$\int dx' \delta_{\mathbf{C}}(x, x')\psi_{\mathbf{C}}(x') = \psi_{\mathbf{C}}(x). \tag{2.241}$$

We use the stochastic projected Gross–Pitaevskii equation (SPGPE) to describe the finite-temperature dynamics of a Bose gas. The SPGPE formalism considers the interaction between the coherent region and the incoherent region. Here, the incoherent region is treated as static and fully thermalised, *i.e.* a grand canonical reservoir at a specific temperature and chemical potential.

The whole system (coherent + incoherent regions) is described by a density operator that evolves according to the von Neumann equation

$$i\hbar\frac{\partial\hat{\rho}}{\partial t} = \left[\hat{H}_{\mathbf{C}} + \hat{H}_{\mathbf{I}} + \hat{H}_{\mathbf{I},\mathbf{C}}, \hat{\rho}\right], \tag{2.242}$$

where the $\hat{H}_{\mathbf{C}}$ and $\hat{H}_{\mathbf{I}}$ are the Hamiltonians for the coherent and incoherent regions, respectively. They are simply the Hamiltonian Eq. (2.32) written in terms of the field operators $\hat{\psi}_{\mathbf{C}}$ and $\hat{\psi}_{\mathbf{I}}$. The Hamiltonian $\hat{H}_{\mathbf{I},\mathbf{C}}$ contains the interaction terms between the two regions, *i.e.* nonlinear terms similar to the interaction term in Eq. (2.32) but composed of combinations of $\hat{\psi}_{\mathbf{C}}$ and $\hat{\psi}_{\mathbf{I}}$ [139–142]. The key goal here is to find the master equation for the coherent region density operator $\hat{\rho}_{\mathbf{C}}$ by tracing out the incoherent region. Once the master equation for $\hat{\rho}_{\mathbf{C}}$ is found, it is mapped to an evolution of the Wigner function using the operator correspondences in Eq. (2.206). Like the truncated Wigner approximation above, this process leads to a partial differential equation containing third-order derivatives. By making the truncated Wigner approximation, we obtain a Fokker–Planck equation that can be mapped to a stochastic differential equation. The resulting equation is the full stochastic projected Gross–Pitaevskii equation (SPGPE) :

$$(S)\mathrm{d}\psi_{\mathbf{C}}(x,t) = \mathcal{P}_{\mathbf{C}}\Big\{-\frac{i}{\hbar}\mathcal{L}_{\mathbf{C}}\psi_{\mathbf{C}}(x,t)\mathrm{d}t \tag{2.243a}$$

$$+ \frac{G(x)}{k_{\mathrm{B}}T}\big(\mu - \mathcal{L}_{\mathbf{C}}\big)\psi_{\mathbf{C}}(x,t)\mathrm{d}t + dW_G(x,t) \tag{2.243b}$$

$$+ \int \mathrm{d}x' M(x-x')\frac{i\hbar}{k_{\mathrm{B}}T}\frac{\partial \mathbf{j}_{\mathbf{C}}(x')}{\partial x}\psi_{\mathbf{C}}(x,t)\mathrm{d}t + i\psi_{\mathbf{C}}(x,t)dW_M(x,t)\Big\}, \tag{2.243c}$$

where (S) indicates that the stochastic differential equation is given in Stratonovich form. The first line, Eq. (2.243a), is the projected Gross–Pitaevskii equation (PGPE) that is simply the usual Gross–Pitaevskii equation with the projection operator $\mathcal{P}_{\mathbf{C}}$ applied onto it. The PGPE describes the dynamics of the coherent region without any interaction with the incoherent region. The operator $\mathcal{L}_{\mathbf{C}}$ is a shortcut for the Hamiltonian evolution operator given by

$$\mathcal{L}_{\mathbf{C}}\psi_{\mathbf{C}}(x,t) = \left[-\frac{\hbar^2}{2m}\frac{\partial^2}{\partial x^2} + \frac{1}{2}m\omega^2 x^2 + g|\psi_{\mathbf{C}}(x,t)|^2\right]\psi_{\mathbf{C}}(x,t). \tag{2.244}$$

The second line of the SPGPE, Eq. (2.243b), is responsible for the growth in the coherent region from scattering between two incoherent region particles, with a significant fraction of the collision energy transferred to one of the atoms, with one going into the coherent region. Here, μ and T correspond to the chemical potential and temperature, respectively, of the thermal reservoir of particles in the incoherent region. The growth term $G(x)$ represents the collision rate of particles in the incoherent region. The noise term $dW_G(x,t)$ is the uncorrelated complex white noise associated with the growth process and satisfies

$$\left\langle dW_G^*(x,t)dW_G(x',t)\right\rangle = 2G(x)\delta_{\mathbf{C}}(x,x')\mathrm{d}t, \tag{2.245}$$

$$\left\langle dW_G(x,t)dW_G(x',t)\right\rangle = \left\langle dW_G^*(x,t)dW_G^*(x',t)\right\rangle = 0. \tag{2.246}$$

The third line in the SPGPE, Eq. (2.243c), represents the scattering processes that conserve the number of particles in both the coherent and incoherent regions but provide a mechanism for energy transfer between the two regions. The noise term $dW_M(x,t)$ associated with this scattering process is real and specified by

$$\left\langle dW_M(x,t)dW_M(x',t)\right\rangle = 2M(x-x')\mathrm{d}t, \tag{2.247}$$

where $M(x-x')$ is the scattering rate function. Eq. (2.243c) is significant when the coherent and incoherent regions are far from mutual equilibrium. However, the effect of the Eq. (2.243c) can be small for systems with quasiequilibrium dynamics [143, 144].

Simple growth SPGPE

We see that the scattering processes described by the third line of the SPGPE do not alter the particle population in the coherent region. This is in contrast to the effect of the growth term given by Eq. (2.243b). Thus, it is reasonable to expect that the effect of Eq. (2.243c) is less important than the effect of Eq. (2.243b) in describing the coherent region, especially for systems with quasiequilibrium dynamics [143, 144]. In addition to this, numerical implementation of the scattering term is difficult due to the multiplicative nature of the associated noise [123]. For these reasons, we choose to neglect the scattering term in the full SPGPE. Doing so results in the *simple growth SPGPE*:

$$\mathrm{d}\psi_{\mathbf{C}}(x,t) = \mathcal{P}_{\mathbf{C}}\left\{-\frac{i}{\hbar}\mathcal{L}_{\mathbf{C}}\psi_{\mathbf{C}}(x,t)\mathrm{d}t + \frac{\Gamma}{k_{\mathrm{B}}T}\big(\mu - \mathcal{L}_{\mathbf{C}}\big)\psi_{\mathbf{C}}(x,t)\mathrm{d}t + dW_\Gamma(x,t)\right\}, \tag{2.248}$$

where we choose a spatially constant growth rate $G(x) = \Gamma$. This spatially constant growth rate has been studied and its use is justified [145]. In this thesis, we use Eq. (2.248) to generate the initial

thermal equilibrium configurations of different systems of interest. Thus, from this point on, we shall refer to the simple growth SPGPE as simply the SPGPE.

Integrating each stochastic realisation of the SPGPE, initiated from a random initial noise, for a sufficiently long time (ergodicity assumed), is equivalent to sampling configurations from a canonically distributed Gibbs ensemble. Expectation values of physical observables then correspond to ensemble averages over many stochastic realisations of the SPGPE.

The numerical value of the growth rate Γ in Eq. (2.248) has no consequence for the equilibrium configurations and hence can be chosen for numerical convenience. Furthermore, while the inclusion of an energy cutoff is crucial in higher dimensions to prevent a divergence of the atomic density, its role is less crucial in 1D. This is because the classical field predictions for the atomic density do not diverge in 1D, even in the absence of energy cutoff. For this reason, our simulations were performed without explicitly imposing the projection operator $\mathcal{P}_{\mathrm{C}}$, in which case the cutoff merely determined the size of the computational basis used for the numerical calculations. For a sufficiently large cutoff, our results did not strongly depend on the exact value of this cutoff.

2.4.3 Dimensionless units

When working with experimentally realisable 1D Bose gases, the base SI units are inconvenient because the Bose gases are typically tens of microns in length. We instead choose units that reflect the typical length and energy scales of the system under study. In addition, it is a common practice among theorists to reduce the working equations in a form where the physical constants appearing in the equations are cancelled out. This also helps in doing numerical calculations where we do not have to deal with very small numbers. Here, we introduce two units used in numerical simulations (performed using the XMDS numerical package [146]) in this thesis. We introduce harmonic oscillator units that are convenient when dealing with Bose gases trapped in a harmonic potential and uniform box units that are convenient when examining Bose gases in a uniform box potential.

System in a harmonic potential trap

In many cases, we are interested in Bose gases in a harmonic potential:

$$V_{\mathrm{ext}}(x) = \frac{1}{2} m\omega^2 x^2. \tag{2.249}$$

The natural choice of units for such configuration is given by the harmonic oscillator length a_{osc} and energy quanta $\hbar\omega$ associated with the confining potential:

$$a_{\mathrm{osc}} = \sqrt{\frac{\hbar}{m\omega}}\,, \qquad E_0 = \hbar\omega, \qquad t_0 = \frac{1}{\omega}. \tag{2.250}$$

In terms of the harmonic oscillator units,

$$\bar{x} = \frac{x}{a_{\mathrm{osc}}}, \qquad \bar{E} = \frac{E}{E_0}, \qquad \bar{t} = \frac{t}{t_0}, \tag{2.251}$$

the dimensionless time-dependent GPE is given by

$$i\frac{\partial}{\partial\bar{t}}\bar{\psi}_0(\bar{x},\bar{t}) = \left[-\frac{1}{2}\frac{\partial^2}{\partial\bar{x}^2} + \frac{1}{2}\bar{x}^2 + \bar{g}|\bar{\psi}_0(\bar{x},\bar{t})|^2\right]\bar{\psi}_0(\bar{x},\bar{t}), \tag{2.252}$$

where

$$\bar{\psi}_0(\bar{x},\bar{t}) = \psi_0(x,t)\sqrt{a_{\rm osc}}\ , \qquad \bar{g} = \frac{g}{E_0 a_{\rm osc}}, \tag{2.253}$$

are the dimensionless complex amplitude of the condensate and 1D interaction parameter, respectively. The dimensionless SPGPE then is given by

$$\mathrm{d}\bar{\Psi}_{\mathbf{C}}(\bar{x},\bar{t}) = \mathcal{P}_{\mathbf{C}}\left\{-i\bar{\mathcal{L}}_{\mathbf{C}}\bar{\Psi}_{\mathbf{C}}(\bar{x},\bar{t})\mathrm{d}\bar{t} + \frac{\bar{\Gamma}}{\bar{T}}(\bar{\mu}-\bar{\mathcal{L}}_{\mathbf{C}})\bar{\Psi}_{\mathbf{C}}(\bar{x},\bar{t})\mathrm{d}\bar{t} + d\bar{W}(\bar{x},\bar{t})\right\}, \tag{2.254}$$

where

$$\bar{\mathcal{L}}_{\mathbf{C}} = -\frac{1}{2}\frac{\partial^2}{\partial\bar{x}^2} + \frac{1}{2}\bar{x}^2 + \bar{g}|\bar{\Psi}_{\mathbf{C}}(\bar{x},\bar{t})|^2, \tag{2.255}$$

and

$$\langle d\bar{W}^*(\bar{x},\bar{t})d\bar{W}(\bar{x},\bar{t})\rangle_{\rm stoch} = 2\bar{\Gamma}\delta(\bar{x}-\bar{x}')\mathrm{d}\bar{t}. \tag{2.256}$$

The dimensionless c-field, growth rate, chemical potential, and temperature, respectively, are given by

$$\bar{\Psi}_{\mathbf{C}} = \Psi_{\mathbf{C}}\sqrt{a_{\rm osc}}\ , \qquad \bar{\Gamma} = \Gamma t_0, \qquad \bar{\mu} = \frac{\mu}{E_0}, \qquad \bar{T} = \frac{k_{\rm B}T}{E_0}, \tag{2.257}$$

with $k_{\rm B}$ being the Boltzmann constant.

System in a uniform box potential

In the absence of a confining potential ($V_{\rm ext} = 0$), we have a Bose gas whose ground state is uniform. Suppose that the length of this homogeneous system is L. Then, L is a natural choice of length scale while the time scale and energy scale are given by

$$t_0 = \frac{mL^2}{\hbar}, \qquad E_0 = \frac{\hbar}{t_0} = \frac{\hbar^2}{mL^2}, \tag{2.258}$$

respectively. In terms of the new dimensionless units

$$\bar{x} = \frac{x}{L}, \qquad \bar{E} = \frac{E}{E_0}, \qquad \bar{t} = \frac{t}{t_0}, \tag{2.259}$$

the time-independent GPE for a homogeneous Bose gas is given by

$$i\frac{\partial}{\partial\bar{t}}\bar{\psi}_0(\bar{x},\bar{t}) = \left(-\frac{1}{2}\frac{\partial^2}{\partial\bar{x}^2} + \bar{g}|\bar{\psi}_0(\bar{x},\bar{t})|^2\right)\bar{\psi}_0(\bar{x},\bar{t}). \tag{2.260}$$

The dimensionless complex amplitude of the condensate and 1D interaction parameter are given by

$$\bar{\psi}_0(\bar{x},\bar{t}) = \psi_0(x,t)\sqrt{L}\ , \qquad \bar{g} = \frac{g}{E_0 L}, \tag{2.261}$$

respectively. The dimensionless SPGPE then takes the form

$$\mathrm{d}\bar{\Psi}_{\mathbf{C}}(\bar{x},\bar{t}) = \mathcal{P}_{\mathbf{C}}\left\{-i\bar{\mathcal{L}}_{\mathbf{C}}\bar{\Psi}_{\mathbf{C}}(\bar{x},\bar{t})\mathrm{d}\bar{t} + \frac{\bar{\Gamma}}{\bar{T}}(\bar{\mu}-\bar{\mathcal{L}}_{\mathbf{C}})\bar{\Psi}_{\mathbf{C}}(\bar{x},\bar{t})\mathrm{d}\bar{t} + d\bar{W}_{\bar{\Gamma}}(\bar{x},\bar{t})\right\}, \tag{2.262}$$

where

$$\bar{\mathcal{L}}_{\mathbf{C}} = -\frac{1}{2}\frac{\partial^2}{\partial \bar{x}^2} + \bar{V}(\bar{x}) + \bar{g}|\bar{\Psi}_{\mathbf{C}}(\bar{x},\bar{t})|^2, \tag{2.263}$$

and

$$\langle d\bar{W}^*_{\bar{\Gamma}}(\bar{x},\bar{t}) d\bar{W}_{\bar{\Gamma}}(\bar{x}',\bar{t})\rangle_{\text{stoch}} = 2\bar{\Gamma}\delta(\bar{x}-\bar{x}')\mathrm{d}\bar{t}. \tag{2.264}$$

The dimensionless c-field, growth rate, chemical potential, and temperature, respectively, are given by

$$\bar{\Psi}_{\mathbf{C}} = \Psi_{\mathbf{C}}\sqrt{L}\ , \qquad \bar{\Gamma} = \Gamma t_0, \qquad \bar{\mu} = \frac{\mu}{E_0}, \qquad \bar{T} = \frac{k_{\mathrm{B}}T}{E_0}. \tag{2.265}$$

Take note that we left the dimensionless trap potential $\bar{V}(\bar{x}) = V(x)/E_0$ in the SPGPE instead of setting it to zero. We will use this potential in Chapter 6 to generate the desired initial condition at finite temperature before releasing the system in a uniform potential.

2.4.4 Penrose–Onsager criterion

In the presence of quantum or thermal fluctuations, we expect that a significant number of particles are excited and comprise the non-condensed part of a Bose gas. One way to quantify this is by calculating the condensate fraction using the Penrose–Onsager criterion [147]. In this case, the condensate fraction of a Bose gas is given by the largest eigenvalue of the single-particle density matrix

$$\rho(x,x') = \langle\hat{\psi}^\dagger(x)\hat{\psi}(x')\rangle \tag{2.266}$$

This is equivalent to solving the eigenvalue problem

$$\int \rho(x,x')\varphi_k(x')\mathrm{d}x' = n_k\varphi_k(x), \tag{2.267}$$

where $\varphi_k(x')$ are the eigenfunctions, and n_k are the eigenvalues of $\rho(x,x')$. After determining the largest eigenvalue n_0 of the one-body density operator, the condensate fraction is then given by

$$\frac{N_0}{N} = \frac{n_0}{\mathrm{Tr}(n_k)}, \tag{2.268}$$

where N is the total number of particles, and N_0 is the number of particles in the condensate. In the c-field simulations, calculation of all eigenvalues n_k is equivalent to diagonalising the one-body density matrix obtained from the stochastic averaging of all trajectories.

The following submitted publication has been incorporated as Chapter 3. Some texts and figures have been modified to address the comments of the Thesis Examiners.

1. [2] **F.A. Bayocboc, Jr.**, M.J. Davis, and K.V. Kheruntsyan, Dynamics of thermalization of two tunnel-coupled one-dimensional quasicondensates, arXiv:2108.13095 (2021).

Contributor	Statement of contribution	%
F.A. Bayocboc, Jr.	writing of text	70
	proof-reading	20
	theoretical derivations	70
	numerical calculations	100
	preparation of figures	90
	initial concept	10
M.J. Davis	writing of text	10
	proof-reading	20
	supervision, guidance	20
	theoretical derivations	10
	initial concept	10
K.V. Kheruntsyan	writing of text	20
	proof-reading	60
	supervision, guidance	80
	theoretical derivations	20
	preparation of figures	10
	initial concept	80

Chapter 3

Thermalisation of tunnel-coupled one-dimensional quasicondensates

In this chapter, we present our numerical study of non-equilibrium dynamics of two tunnel-coupled, one-dimensional quasicondensates following a quench of the coupling strength from zero to a fixed finite value, creating an extended bosonic Josephson junction of two quasicondensates. We find that after turning on the coupling between the quasicondensates, the low-energy particles flow predominantly from the colder quasicondensate to the hotter one, whereas the reverse is true for the higher-energy particles. The Josephson frequency of low-energy particles is distinct from the Josephson frequency of high-energy particles. The net energy flow is governed by the surplus (or otherwise) of the overall number of lower-energy particles flowing from the initially colder quasicondensate to the initially hotter quasicondensate, compared to the overall number of higher-energy particles flowing in the opposite direction. We also find that, under certain conditions, the two coupled quasicondensates can evolve to an equilibrium state in which their thermal phase coherence length is larger than the respective initial phase coherence lengths, even though the new equilibrium temperature is higher.

3.1 Introduction

The relaxation of isolated quantum many-body systems has been the subject of intense theoretical and experimental activity in recent years [15]. In particular, much interest has been devoted to the understanding of how quantum many-body systems evolve after a quantum quench (*i.e.* an abrupt, nonadiabatic change in a system parameter). Generic systems have typically been found to relax to a canonically distributed thermal state, while integrable systems relax to a state described by a generalised Gibbs ensemble [39, 45].

An important physical platform that enabled fundamental advances in this research area has been that of ultracold atomic gases. These have allowed for the experimental realisation of some paradigmatic many-body Hamiltonians, in addition to allowing for a high degree of control over system parameters and dynamics [13, 14].

The advances made in this research area are now fostering the growth of intriguing new research frontiers such as nonequilibrium quantum thermodynamics [148, 149]. In traditional thermodynamics, the simplest building block of a thermodynamic process consists of a dynamical system coupled to a large non-dynamical bath. In quantum thermodynamics, on the other hand, one is often concerned with the dynamics of both the system and the bath, with both being treated quantum mechanically and both being not necessarily large. Examples of open questions include how quantum correlations and fluctuations of the bath, as well as the strength of the coupling between the bath and the system, affect the system dynamics and thermodynamics. Thus, a typical setting for quantum thermodynamics can be realised by considering two coupled quantum many-body systems treated dynamically as a combined closed system.

In this chapter, we study a simple example of such a setting—a pair of tunnel-coupled one-dimensional (1D) Bose gases in the quasicondensate regime, which is characterised by suppressed density fluctuations but a fluctuating phase and hence absence of a true long-range order [26, 110, 150]. This system has already been studied extensively, both theoretically [30, 151–156] and experimentally [18–21, 53, 157–159], in the scenario in which an initially single 1D quasicondensate was coherently split into two quasicondensates and allowed to relax through dephasing. (For related studies of elongated three-dimensional Bose-Einstein condensates, see, *e.g.* Refs. [153–155].) In particular, in the experiment of Hofferberth *et al.* [18], the authors observed a fast, subexponential decay of relative coherence in the completely decoupled case [48, 49]; the dephasing between the two quasicondensate occurred on the order of milliseconds. However, in light of subsequent experiments of Ref. [19], this fast dephasing has been reinterpreted as relaxation to a quasistationary prethermal state (that displays equilibrium-like properties [50]), rather than to the final state of a true thermal equilibrium. Furthermore, in Ref. [21], it has been shown that the steady state reached by the system due to prethermalisation is described by the generalised Gibbs ensemble. Related experimental and theoretical studies have also shown that during the evolution to a prethermalised state, thermal correlations emerge locally and propagate through the system in a light-cone-like evolution [20, 51]. After reaching the prethermal state, the system then continues to dephase in a slower second light-cone-like evolution to its final thermal state [52].

Here we consider the opposite dynamical scenario: rather than coherently splitting a single quasicondensate into two, we instead consider two initially independent (uncoupled) quasicondensates that are suddenly tunnel-coupled at time $t = 0$ and then relax to a new common equilibrium state. More specifically, we study two parallel harmonically trapped 1D quasicondensates with an initial imbalance in their equilibrium temperature and chemical potential. The quasicondensates are then driven out of equilibrium by quenching (at time $t = 0$) the tunnelling strength from zero to a finite value J. Using finite-temperature c-field techniques [123], we simulate the subsequent rephasing of the coupled system and characterise its relaxation to the final equilibrium state in terms of real-space density and momentum distributions, energy and particle number imbalances, and phase coherences. The rephasing of such a system at zero temperature has been previously studied in Ref. [160].

This type of a system, where two subsystems are coupled via tunneling, typically gives rise to Josephson oscillations [161]. Josephson oscillations in Bose-Einstein condensates (BECs) have been

studied previously both theoretically [162–170] and experimentally [171–173]. An interesting effect that has been predicted and observed in such tunnel-coupled systems is the phenomenon of macroscopic self-trapping [164, 171]. In phase fluctuating 1D quasicondensates [30, 168, 174, 175], however, such an effect has been predicted to break down [175] due to the absence of true long-range order and the enhanced role of quantum fluctuations as compared to 3D systems. Here, in the finite-temperature version of the system, we also observe the absence of macroscopic self-trapping, as expected, because of the same lack of true long-range order, albeit due to thermal fluctuations in this case.

3.2 System and *c*-field method

3.2.1 The model

A system of two harmonically trapped 1D Bose gases coupled via tunnel-coupling can be described by the following second-quantised Hamiltonian:

$$\hat{H} = \sum_{j=1}^{2} \int dx \left[\frac{\hbar^2}{2m} \frac{\partial \hat{\Psi}_j^\dagger(x,t)}{\partial x} \frac{\partial \hat{\Psi}_j(x,t)}{\partial x} + \frac{1}{2} m\omega^2 x^2 \hat{\Psi}_j^\dagger(x,t)\hat{\Psi}_j(x,t) \right.$$
$$\left. + \frac{g}{2} \hat{\Psi}_j^\dagger(x,t)\hat{\Psi}_j^\dagger(x,t)\hat{\Psi}_j(x,t)\hat{\Psi}_j(x,t) \right] - \hbar J \int dx \left[\hat{\Psi}_1^\dagger(x,t)\hat{\Psi}_2(x,t) + \hat{\Psi}_2^\dagger(x,t)\hat{\Psi}_1(x,t) \right]. \quad (3.1)$$

Here, $\hat{\Psi}_j(x,t)$ is the annihilation operator of the jth ($j = 1, 2$) Bose gas, satisfying equal-time bosonic commutation relations $\left[\hat{\Psi}_i(x,t), \hat{\Psi}_j^\dagger(x',t)\right] = \delta_{ij}\delta(x - x')$, and m is the mass of a single particle. The quantity ω is the longitudinal trap frequency which we assume is the same for both gases, g is the 1D coupling strength (given by $g = 2\hbar\omega_\perp a$ [105] in the absence of confinement induced resonances, assuming the transverse confinement of both gases is also harmonic with frequency $\omega_\perp$, with a being the 3D s-wave scattering length), and $J > 0$ is the strength of the tunnel-coupling between the two gases.

A uniform 1D Bose gas with density ρ_j at temperature T_j can be completely characterised by two dimensionless parameters [46, 100]: the dimensionless interaction strength given by

$$\gamma_j = \frac{mg}{\hbar^2 \rho_j}, \quad (3.2)$$

and the dimensionless temperature given by

$$\overline{\tau}_j = \frac{2\hbar^2 k_\mathrm{B} T_j}{mg^2}. \quad (3.3)$$

In the case of a harmonically trapped 1D Bose gas, the longitudinal trap frequency ω serves as an additional parameter needed to characterise the system. Because the density of the harmonically trapped system becomes position dependent, the dimensionless interaction parameter becomes defined locally as

$$\gamma_j(x) = \frac{mg}{\hbar^2 \rho_j(x)}. \quad (3.4)$$

The dimensionless temperature $\overline{\tau}_j$, however, remains a global parameter for the system. For a given chemical potential μ_j and temperature $\overline{\tau}_j$, the density at the centre of the trap $\rho_{0,j} = \rho_j(0)$ can be used to define a dimensionless interaction strength

$$\gamma_{0,j} = \frac{mg}{\hbar^2 \rho_{0,j}}, \tag{3.5}$$

that we choose to be our global interaction parameter in this case.

In this work, we restrict ourselves to the weakly interacting regime of the coupled 1D Bose gases, which corresponds to the condition $\gamma_{0,j} \ll 1$. Moreover, we are concerned with characteristic temperatures, most readily attainable in current ultracold atom experiments, at which the highly occupied low-energy modes are dominated by thermal rather than vacuum fluctuations (see, *e.g.* Refs. [75, 107, 110, 111]). This corresponds to temperatures where

$$T_j \ll \sqrt{\gamma_{0,j}}\, \frac{\hbar^2 \rho_{0,j}^2}{m k_{\mathrm{B}}}, \tag{3.6}$$

in which case the 1D Bose gas is in the phase-fluctuating quasicondensate regime, where the characteristic thermal phase coherence length is given by

$$l_{0,j}^{(\phi)} = 2 \frac{\hbar^2 \rho_{0,j}}{m k_{\mathrm{B}} T_j}. \tag{3.7}$$

At these temperatures, a single quasicondensate can, in fact, be characterised by a single dimensionless parameter, which is a nontrivial combination of $\overline{\tau}_j$ and $\gamma_{0,j}$ (see Ref. [176] and references therein):

$$\chi_{0,j} = \frac{1}{2} \gamma_{0,j}^{3/2} \overline{\tau}_j \tag{3.8}$$

$$= \frac{k_{\mathrm{B}} T_j}{\hbar \rho_{0,j}} \sqrt{\frac{m}{g \rho_{0,j}}}\,. \tag{3.9}$$

For two tunnel-coupled quasicondensates, each having a characteristic phase coherence length of $l_{0,j}^{(\phi)}$, there is an additional length-scale in the problem associated with the coupling strength J. It is given by [30]

$$l^{(J)} = \sqrt{\frac{\hbar}{4mJ}}\,, \tag{3.10}$$

and represents the typical length-scale at which the tunnel coupling restores spatially constant relative phase [157]

$$\Delta\phi(x,t) = \phi_1(x,t) - \phi_2(x,t); \tag{3.11}$$

in the strong cross-coupling regime, corresponding to $l^{(J)} \ll l_{0,j}^{(\phi)}$, the two quasicondensates are phase locked. This means that the distribution of $\Delta\phi$ peaks around zero while the local phase in each quasicondensate remains fluctuating [168].

3.2.2 The c-field method

To study the dynamics of the coupled quasicondensates, we use the c-field techniques, which is a proven approach to study degenerate Bose gases at finite temperatures [123, 138]. In this method, the

quantum field operator $\hat{\psi}_j(x,t)$ is decomposed into two regions, a coherent region and an incoherent region. The coherent region contains highly occupied low-energy modes and is described by a single classical field $\psi_j^{(\mathbf{C})}(x,t)$ for respective ($j=1,2$) quasicondensates. In contrast, the incoherent region contains sparsely occupied high-energy modes that act as an effective thermal bath, treated as static, with temperature T_j and chemical potential μ_j governing the thermal average number of particles in the coherent region. The boundary between these two regions is defined by an energy cut-off $\varepsilon_j^{(\mathrm{cut})}$. For initially uncoupled ($J=0$) quasicondensates, each classical field $\psi_j^{(\mathbf{C})}(x,t)$ obeys the following stochastic projected Gross–Piteavskii equation (SPGPE) [123] for finding the initial thermal equilibrium configuration:

$$d\psi_j^{(\mathbf{C})}(x,t) = \mathcal{P}^{(\mathbf{C})}\left\{-\frac{i}{\hbar}\mathcal{L}_j^{(\mathbf{C})}\psi_j^{(\mathbf{C})}(x,t)\,dt + \frac{\Gamma_j}{k_B T_j}(\mu_j - \mathcal{L}_j^{(\mathbf{C})})\psi_j^{(\mathbf{C})}(x,t)\,dt + dW_{\Gamma_j}(x,t)\right\}. \quad (3.12)$$

Here, $\mathcal{P}^{(\mathbf{C})}$ is the projection operator that sets up the high-energy cutoff for the classical field region, and $\mathcal{L}_j^{(\mathbf{C})}$ is a shortcut for the Gross–Pitaevskii operator,

$$\mathcal{L}_j^{(\mathbf{C})} = -\frac{\hbar^2}{2m}\frac{\partial^2}{\partial x^2} + V_j(x) + g|\psi_j^{(\mathbf{C})}(x,t)|^2, \quad (3.13)$$

with $V_j(x) = \frac{1}{2}m\omega_j^2 x^2$ being the trapping potential (where $\omega_1 = \omega_2 \equiv \omega$ in this work). In addition, Γ_j is the growth rate, whereas the last term $dW_{\Gamma_j}(x,t)$ is the associated complex white noise, with the following nonzero correlation:

$$\langle dW^*_{\Gamma_j}(x,t) dW_{\Gamma_j}(x',t)\rangle = 2\Gamma_j \delta(x-x')dt. \quad (3.14)$$

Evolution of each stochastic trajectory (initiated from a random initial noise) according to the SPGPE, for a sufficiently long time, corresponds to sampling the canonically distributed Gibbs ensemble, according to the ergodic hypothesis. Calculating expectation values of physical quantities then corresponds to evaluating ensemble averages over a large number of independent SPGPE trajectories.

In Eq. (3.12), the numerical value of the growth rate Γ_j is somewhat arbitrary and can be chosen for numerical convenience as it has no consequence for the final equilibrium configurations [138, 177]. Furthermore, while the inclusion of an energy cutoff through the projection operator $\mathcal{P}^{(\mathbf{C})}$ is important in higher dimensions in order to prevent a divergence of the atomic density, its role is less crucial in 1D. This is because the classical field predictions for the atomic density do not diverge in 1D, even in the absence of energy cutoff. For this reason, our simulations were carried out without imposing the projection operator $\mathcal{P}^{(\mathbf{C})}$, in which case the cutoff is imposed merely by the finite computational basis itself. For a sufficiently large cutoff, our results did not strongly depend on the exact value of this cutoff.

Once the SPGPE is evolved to its final thermal equilibrium configuration, we turn on the tunnel-coupling J and simulate post-quench dynamics by evolving each stochastic realisation of the c-field in real time according to the coupled Gross–Pitaevskii equations (GPEs),

$$\begin{aligned}\frac{\partial\psi_1^{(\mathbf{C})}(x,t)}{\partial t} &= -\frac{i}{\hbar}\mathcal{L}_1^{(\mathbf{C})}\psi_1^{(\mathbf{C})}(x,t) + iJ\psi_2^{(\mathbf{C})}(x,t),\\ \frac{\partial\psi_2^{(\mathbf{C})}(x,t)}{\partial t} &= -\frac{i}{\hbar}\mathcal{L}_2^{(\mathbf{C})}\psi_2^{(\mathbf{C})}(x,t) + iJ\psi_1^{(\mathbf{C})}(x,t).\end{aligned} \quad (3.15)$$

Dimensionless form of SPGPE

In order to arrive at the dimensionless form of the SPGPE, which can be seen to explicitly depend on one of the earlier introduced dimensionless parameter $\chi_{0,j}$, Eq. (3.8), for the jth quasicondensate (see Ref. [176] for further details), we introduce the dimensionless coordinate $\xi = x/x_0$, time $\tau = t/t_0$ and field $\varphi_j(\xi,\tau) = \psi_j^{(\mathbf{C})}(x,t)/\psi_0$ with the corresponding length-, time-, and field-scales in terms of the temperature of the first quasicondensate:

$$x_0 = \left(\frac{\hbar^4}{m^2 g k_{\mathrm{B}} T_1}\right)^{1/3}, \tag{3.16}$$

$$t_0 = \frac{m x_0^2}{\hbar} = \left(\frac{\hbar^5}{m g^2 k_{\mathrm{B}}^2 T_1^2}\right)^{1/3}, \tag{3.17}$$

$$\psi_0 = \left(\frac{m k_{\mathrm{B}}^2 T_1^2}{\hbar^2 g}\right)^{1/6} = \left(\frac{\hbar}{t_0 g}\right)^{1/2}. \tag{3.18}$$

With these scaling factors, and the role of the energy scale taken by $E_0 = \hbar/t_0$, the SPGPE, Eq. (3.12), acquires the following compact form:

$$d\varphi_j = \mathcal{P}^{(\mathbf{C})}\left\{\left[-i\mathcal{L}_j + \tilde{\kappa}_{\mathrm{th}}\left(\tilde{\mu}_j - \mathcal{L}_j\right)\right]\varphi_j d\tau + d\tilde{W}_j\right\}, \tag{3.19}$$

where the dimensionless nonlinear operator $\mathcal{L}_j$ is obtained from Eq. (3.13) via $\mathcal{L}_j = \mathcal{L}_j^{(\mathbf{C})}/E_0$ and is given by

$$\mathcal{L}_j = -\frac{1}{2}\frac{\partial^2}{\partial\xi^2} + \frac{1}{2}\tilde{\omega}^2\xi^2 + |\varphi_j|^2. \tag{3.20}$$

Here, $\tilde{\omega} = \omega t_0$ is the dimensionless trap frequency, whereas $\tilde{\mu}_j = \mu_j/E_0$ is the dimensionless chemical potential of the j-th quasicondensate. In addition, $\tilde{\kappa}_{\mathrm{th}} = \hbar\Gamma_1/k_{\mathrm{B}}T_1$ is the rescaled growth rate, where we have used the freedom of choice of the numerical value of the growth rate Γ_2 to relate it to Γ_1 via $\Gamma_2 = \Gamma_1\alpha$, where $\alpha = T_2/T_1$ is the ratio of temperatures of the two quasicondensates. The terms $d\tilde{W}_1$ and $d\tilde{W}_2 = \sqrt{\alpha}\, d\tilde{W}_1$ are complex white noises satisfying

$$\langle d\tilde{W}_1^*(\xi,\tau) d\tilde{W}_1(\xi',\tau)\rangle = 2\tilde{\kappa}_{\mathrm{th}}\delta(\xi-\xi')d\tau, \tag{3.21}$$

from Eq. (3.14).

The dimensionless form of the coupled GPEs Eq. (3.15), on the other hand, reads as

$$\begin{aligned}\frac{\partial\varphi_1(\xi,\tau)}{\partial\tau} &= -i\mathcal{L}_1\varphi_1(\xi,\tau) + i\tilde{J}\varphi_2(\xi,\tau),\\ \frac{\partial\varphi_2(\xi,\tau)}{\partial\tau} &= -i\mathcal{L}_2\varphi_2(\xi,\tau) + i\tilde{J}\varphi_1(\xi,\tau),\end{aligned} \tag{3.22}$$

where $\tilde{J} = \hbar J/E_0 = J t_0$ is the dimensionless tunnel-coupling. In the above dimensionless form of the SPGPE and GPE, the nonlinearity constant in front of the $|\varphi_j|^2$ term in Eq. (3.20) is always equal to unity (unlike the respective term in Eq. (3.13), proportional to the interaction strength g), and the normalisation condition that gives the total number of particles in the jth quasicondensate reads $N_j = \int\langle|\psi_j^{(\mathbf{C})}(x,t)|^2\rangle dx = \psi_0^2 x_0 \tilde{N}_j$, where $\tilde{N}_j = \int\langle|\varphi_j(\xi,\tau)|^2\rangle d\xi$.

In the Thomas–Fermi (TF) limit of an inverted parabolic density profile, the chemical potential of a harmonically trapped quasicondensate is given by $\mu_j = g\rho_{0,j}$, and thus the dimensionless chemical potential $\tilde{\mu}_1$ can be expressed in terms of the dimensionless parameter $\chi_{0,1}$, Eq. (3.8), as

$$\tilde{\mu}_1 = \frac{1}{\chi_{0,1}^{2/3}}, \tag{3.23}$$

whereas $\tilde{\mu}_2 = \beta\tilde{\mu}_1 = (\alpha/\chi_{0,j})^{2/3}$, where $\beta = \mu_2/\mu_1$. According to this relation, the dimensionless chemical potential $\tilde{\mu}_1$ can be also interchanged with $\chi_{0,1}^{-2/3}$. This implies then that the SPGPE for a single quasicondensate depends on a nontrivial combination of both the dimensionless interaction strength and temperature, rather than on two independent parameters. Given that the full density profile in the TF approximation is given by $\rho_1(x) = (\mu_1 - \frac{1}{2}m\omega^2x^2)/g$, for $|x| < R_1^{(\mathrm{TF})}$ (and $\rho_1(x) =$ otherwise), where $R_1^{(\mathrm{TF})} = \sqrt{2\mu_1/m\omega^2}$ is the TF radius and $\mu_1 = g\rho_{0,1}$ is the global chemical potential, the peak density $\rho_{0,1}$ can be evaluated from the normalisation condition $N_1 = \int_{-R_1^{(\mathrm{TF})}}^{R_1^{(\mathrm{TF})}} \rho_1(x)dx$. This gives $\rho_{0,1} = (9m\omega^2N_1^2/32g)^{1/3}$, and therefore the dimensionless parameter $\chi_{0,1}$ can be explicitly rewritten as $\chi_{0,1} = 4\sqrt{2}\ k_BT_1/(3N_1\hbar\omega)$ [using $N_1 = \psi_0^2x_0\tilde{N}_1$ and $\tilde{N}_1 = 4\sqrt{2}\ \tilde{\mu}_1^{3/2}/(3\tilde{\omega}) = 4\sqrt{2}\ /(3\chi_{0,1}\tilde{\omega})$], and similarly for $\chi_{0,2} = 4\sqrt{2}\ k_BT_2/(3N_2\hbar\omega)$. Beyond the TF limit, the dimensionless chemical potential $\tilde{\mu}_1$ can still be interchanged with $\chi_{0,1}$ as an input parameter, with the understanding that the simple relationship $\mu_1 = g\rho_{0,1}$ between μ_1 and the TF peak density $\rho_{0,1}$ is now only approximate, whereas the exact relationship has to be determined numerically *a posteriori*, using $\rho_1(x) = \langle|\psi_1^{(\mathbf{C})}(x,t)|\rangle$. We note, however, that in all our numerical examples, the equilibrium peak densities were always very close to the TF peak density of $\rho_{0,1} = \mu_1/g$.

Recalling that for two independent condensates, we had to introduce two additional dimensionless parameters for the ratios of the initial temperatures and chemical potentials,

$$\alpha = \frac{T_2}{T_1} \qquad \text{and} \qquad \beta = \frac{\mu_2}{\mu_1}, \tag{3.24}$$

we thus conclude that the initial state of our (uncoupled) system can be completely characterised by just four dimensionless parameters, $\chi_{0,1}$ (or $\tilde{\mu}_1 = 1/\chi_{0,1}^{2/3}$), $\tilde{\omega}$, α, and β. In doing so, we further note that as $\mu_j = g\rho_j(0)$ in the Thomas-Fermi limit, one has $\chi_{0,2} = \left(\alpha/\beta^{3/2}\right)\chi_{0,1}$ (with $\tilde{\mu}_2 = \beta\tilde{\mu}_1$), and therefore the value of $\chi_{0,2}$ is determined by $\chi_{0,1}$, α, and β. Alternatively, the initial state of our system can be characterised in terms of $\chi_{0,1}$, α, and β. The post-quench dynamics of the coupled quasicondensates, on the other hand, requires a fifth parameter—the dimensionless tunnel coupling $\tilde{J}$.

3.3 Results and Discussion

3.3.1 Energy and particle exchange

We now consider a pair of 1D quasicondensates in parameter regimes that can be realised in ultracold atom experiments (see, *e.g.* Ref. [159]). The initially uncoupled ($J = 0$) quasicondensates are prepared independently, with generally different equilibrium temperatures T_j ($j = 1, 2$) and different chemical

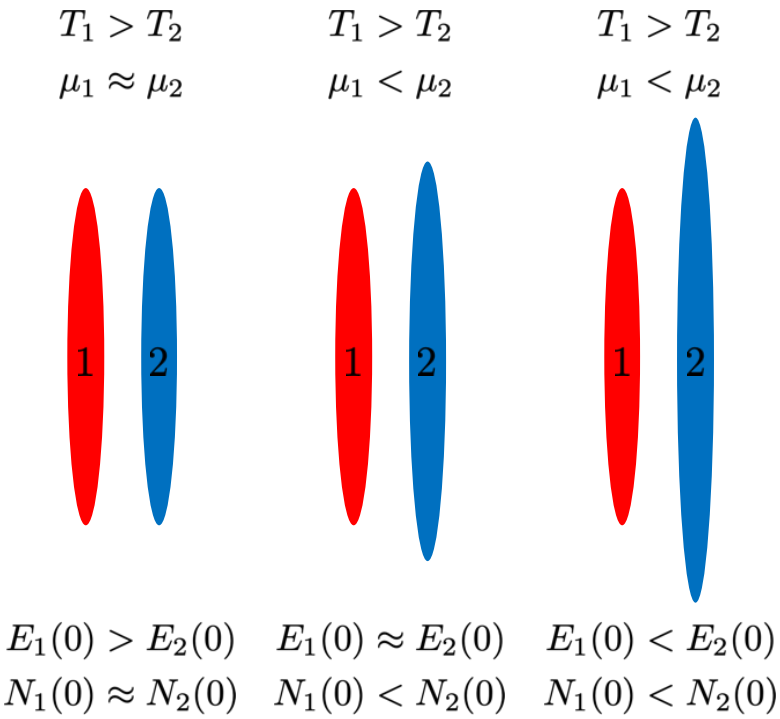

Figure 3.1: The three initial conditions considered in Fig. 3.2.

potentials μ_j, at time $t = 0$. We characterise these initial differences by the respective ratios, as in Eq. (3.24).

At time $t = 0$, the tunnel coupling J is suddenly switched on to a nonzero value $J \neq 0$. This establishes thermal and diffusive contact between the two systems implying that the two systems can now exchange energy and particles while evolving to the new equilibrium state with a new common temperature and chemical potential. We characterise this exchange by the dynamics of the energy and particle number imbalances,

$$E_{\text{imb}}(t) = \frac{E_1(t) - E_2(t)}{E_1(t) + E_2(t)}, \tag{3.25}$$

$$N_{\text{imb}}(t) = \frac{N_1(t) - N_2(t)}{N_1(t) + N_2(t)}, \tag{3.26}$$

where $E_j(t)$ ($j = 1, 2$) are calculated as the stochastic means of the Hamiltonians for each system, in which the quantum mechanical creation and annihilation field operators are replaced by the respective complex c-fields,

$$E_j(t) = \left\langle \hat{H}_j\left(\left[\psi_j^{(\mathbf{C})}(x,t)\right]^*, \psi_j^{(\mathbf{C})}(x,t)\right)\right\rangle, \tag{3.27}$$

and similarly for

$$N_j(t) = \int dx \left\langle \hat{\psi}_j^\dagger(x,t)\hat{\psi}_j(x,t)\right\rangle = \int dx \left\langle |\psi_j^{(\mathbf{C})}(x,t)|^2\right\rangle. \tag{3.28}$$

We recall here that even though the coupled quasicondensates evolve according to the deterministic GPE after the quench of the tunnel coupling, the stochastic averaging here is required because each stochastic realisation (that evolves deterministically according to the GPE) starts off from a random initial condition attained after the SPGPE stage.

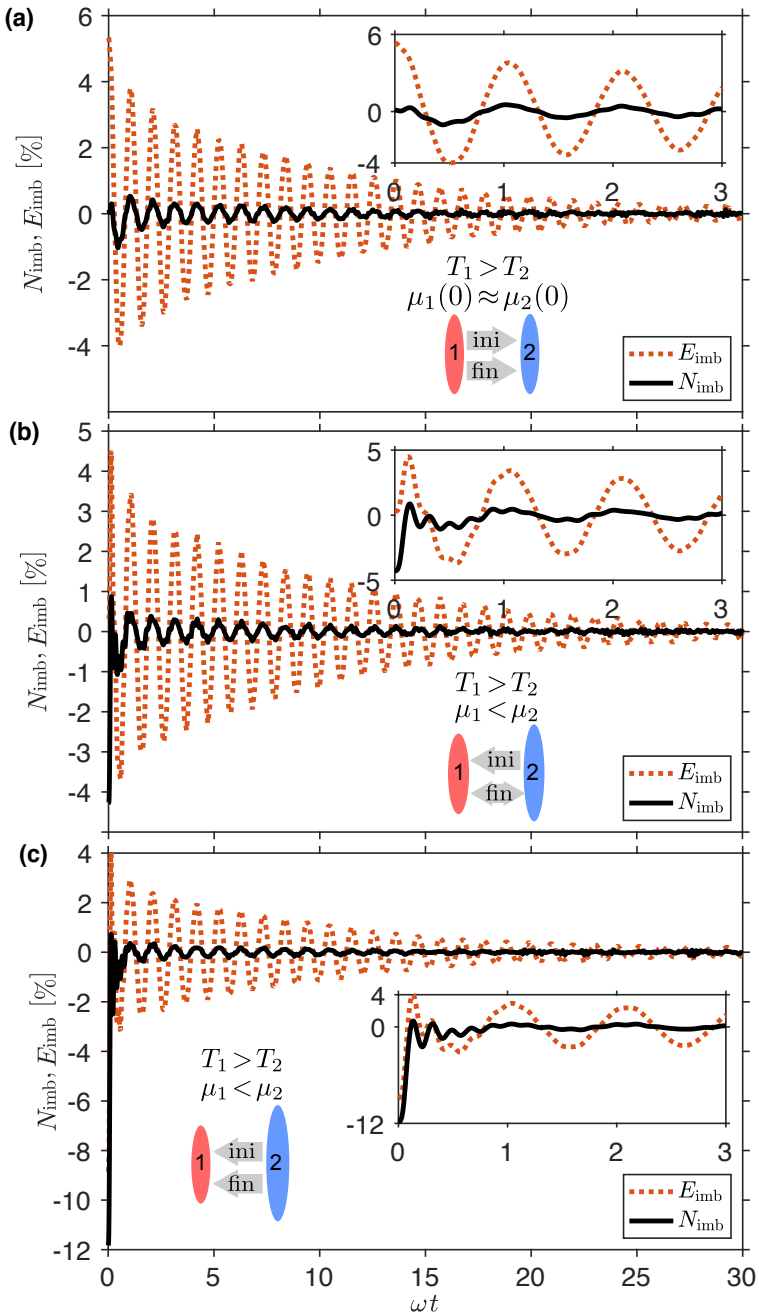

Figure 3.2: Time-evolution of the particle number and energy imbalances between the two quasi-condensates, $N_{\rm imb}(t)$ (full, black line) and $E_{\rm imb}(t)$ (dotted, orange line), after quenching the tunnel coupling from $\tilde{J}=0$ to $\tilde{J}=3\tilde{\omega}$. The initial dimensionless interaction and trap frequency parameters are $\chi_{0,1} \simeq 9.32 \times 10^{-2}$ and $\tilde{\omega} \simeq 4.46 \times 10^{-2}$ in all cases; the initial ratio of the temperatures is $\alpha=0.75$; whereas the ratios of the initial chemical potentials are: (a) $\beta=1.007$, (b) $\beta=1.071$, and (c) $\beta=1.190$. The insets are the zoomed in parts of the curves at early times, showing the initial direction of the energy and particle number transfers (flows), with decreasing imbalances corresponding to transfers from system 1 to system 2, and increasing imbalances corresponding to transfers from 2 to 1. The red and blue ellipses illustrate the quasicondensates 1 and 2 (from Fig. 3.1), where we additionally show the direction of the initial (ini) and net final (fin) flow of energy between the two quasicondensates by grey arrows.

We consider three nontrivial scenarios, illustrated in Fig. 3.1, all of which have $T_1 > T_2$ (with the same ratio of temperatures, $\alpha = T_2/T_1 = 0.75$), whereas the chemical potentials μ_1 and μ_2 vary from being approximately equal to increasingly imbalanced, with $\mu_1 < \mu_2$. In the examples that follow, we use $k_{\rm B}T_1 = 200\hbar\omega$ and $\mu_1 = 109.2\hbar\omega$, with $\omega = 2\pi \times 6.7$ Hz. Moreover, the transverse trapping frequency $\omega_\perp = 2\pi \times 1.4$ kHz, growth rate $\hbar\Gamma_j = 0.01k_{\rm B}T_j$, and maximum momentum $k_{\rm max} = 25/l_{\rm ho}$ are used in all SPGPE and PGPE calculations. The evolution of the energy and particle number imbalances, $E_{\rm imb}(t)$ and $N_{\rm imb}(t)$, for the three scenarios in Fig. 3.1 are shown in Fig. 3.2.

In the example of Fig. 3.2 (a), the initial chemical potentials of the two quasicondensates are approximately the same, $\mu_1 \simeq \mu_2$ This means that the respective initial total number of particles are also approximately the same, $N_1 \simeq N_2$. Indeed, in the quasicondensate regime that we study here the density profiles are well approximated by the Thomas-Fermi inverted parabolas, for which $\mu_j = g\rho_{0,j}$ and the peak densities can be expressed directly through the total atom numbers as N_j using $\rho_{0,j} = (9m\omega^2 N_j^2/32g)^{1/3}$. This means that particle number imbalance is completely determined by the chemical potential imbalance, and therefore for $\mu_1 \simeq \mu_2$, the initial total particle numbers will also be approximately the same so that the initial particle number imballance is zero, $N_{\rm imb}(0) \simeq 0$. This in turn implies that after switching on the tunnel coupling J, the net particle transfer from one system to the other will remain zero, $N_{\rm imb}(t \to \infty) \simeq 0$, in the long time limit, *i.e.* when a new equilibrium is established. However, the initial temperatures and energies are different, with $T_1 > T_2$ and $E_1(0) > E_2(0)$ [$E_{\rm imb}(0)] > 0$], implying that a net energy exchange will occur on the way to the new equilibrium. In this scenario, the only way the two systems can settle into a new thermal equilibrium (at a common new temperature, with $E_{\rm imb}(t \to \infty) = 0$ in the long time limit), while maintaining the net zero particle transfer due to the already equal chemical potentials, is if *high* energy particles predominantly tunnel from hotter system 1 to the colder system 2, whereas the *same* number of *low* energy particles tunnels predominantly in the opposite direction. As we see from Fig. 3.2 (a), this net energy transfer from the initial $E_{\rm imb}(0) > 0$ to final $E_{\rm imb}(t_f) \simeq 0$ (where the final time t_f, in harmonic oscillator units, is $t_f\omega = 30$ here) takes place through transient damped oscillations. Similar transient oscillations are seen in the particle number imbalance, even though both the initial and final imbalances are zero, implying absence of net particle transfer as expected.

In the example of Fig. 3.2 (b), the system 1 is slightly hotter than the system 2 ($T_1 > T_2$), but the chemical potentials satisfy $\mu_1 < \mu_2$ and are chosen is such a way that the energies of the two systems are approximately equal, $E_1(0) \approx E_2(0)$, and the particle number imbalance is negative, $N_{\rm imb}(0) < 0$ ($N_1(0) < N_2(0)$). In this scenario, once the tunnel coupling is switched on, the energy initially flows from the colder system 2 to the hotter system 1, with subsequent transient damped oscillations; however, the net energy flow in the long time limit is approximately zero. The net particle flow, on the other hand, is from system 2 to system 1, as expected from $\mu_1 < \mu_2$. The only way this can happen is if a larger number of low energy particles flows from the colder system 2 to the hotter system 1 compared to the number of high energy particles flowing from the system 1 to system 2, leading to a net particle number flow from system 2 to system 1, while balancing out the net zero energy flow between the two systems.

Finally, in the scenario of Fig. 3.2 (c) the chemical potential imbalance ($\mu_1 < \mu_2$) is larger than in

the previous example, such that there is now an initial energy imbalance too, $E_1(0) < E_2(0)$. In this case, both the initial and long time net energy flow, as well as the particle number flow, is from the cold system 2 to the hot system 1, wherein the energy is carried by a much larger number of low energy particles flowing from system 2 to system 1, compared to the number of high energy particles flowing from system 1 to system 2.

To summarise, in all three examples, the low energy particles flow predominantly from the colder system 2 to the hotter system 1, whereas the reverse is true for the high energy particles. The net energy flow in each example is governed by the surplus of the overall number of low energy particles flowing from system 2 to system 1, compared to the overall number of high energy particles flowing in the opposite direction.

3.3.2 Dynamics of particles in momentum space

To gain further insights into the dynamics of the low- and high-energy particles, we now analyse the local change of the momentum distribution with time, $dn_j(k,t)/dt$, in each quasicondensate ($j = 1, 2$), where

$$n_j(k,t) = \iint \mathrm{d}x\mathrm{d}x' e^{ik(x-x')} \langle \hat{\psi}_j^\dagger(x,t)\hat{\psi}_j(x',t)\rangle. \tag{3.29}$$

(Here and hereafter, we refer to k as the momentum, even though it is in wave-number units, whereas the true momentum is $p = \hbar k$.) As the dynamics of particles in each quasicondensate will generally contain contributions from the internal dynamics and tunnelling of particles from the other quasiondensate, the local rate of change $dn_j(k,t)/dt$ can be further decomposed into intra-well [(i)] and inter- or cross-well [(c)] components,

$$\frac{dn_j(k,t)}{dt} = \frac{dn_j^{(i)}(k,t)}{dt} + \frac{dn_j^{(c)}(k,t)}{dt}, \tag{3.30}$$

with the understanding that the cross-well component due to tunnelling of particles between the two quasicondensates must balance each other, $dn_1^{(c)}(k,t)/dt = -dn_2^{(c)}(k,t)/dt$, due to the particle number conservation. An explicit expression for $dn_j(k,t)/dt$ can be calculated by using the Fourier components of the field operators,

$$\hat{\psi}_j(x,t) = \frac{1}{2\pi}\int \mathrm{d}k\, \hat{a}_j(k,t)e^{ikx}, \tag{3.31}$$

and the equation of motion,

$$i\hbar\frac{\partial\hat{\psi}_j(x,t)}{\partial t} = \left[\hat{\psi}_j(x,t), \hat{H}\right], \tag{3.32}$$

with the Hamiltonian $\hat{H}$ given in Eq. (3.1). From this, the intra-well component is given by

$$\frac{d}{dt}n_j^{(i)}(k,t) = -\frac{\partial}{\partial k}\mathcal{J}_j(k,t) + \frac{1}{4\pi^2}\iint \mathrm{d}\kappa\mathrm{d}\kappa'\mathcal{G}_j(k,\kappa,\kappa',t), \tag{3.33}$$

that takes the form of a continuity equation for $n_j^{(i)}(k,t)$ with a nonvanishing source term (second term on the right-hand side). Here,

$$\mathcal{J}_j(k,t) = \frac{m\omega^2}{\hbar}\mathrm{Im}\left[\left\langle \hat{a}_j^\dagger(k,t)\frac{\partial\hat{a}_j(k,t)}{\partial k}\right\rangle\right], \tag{3.34}$$

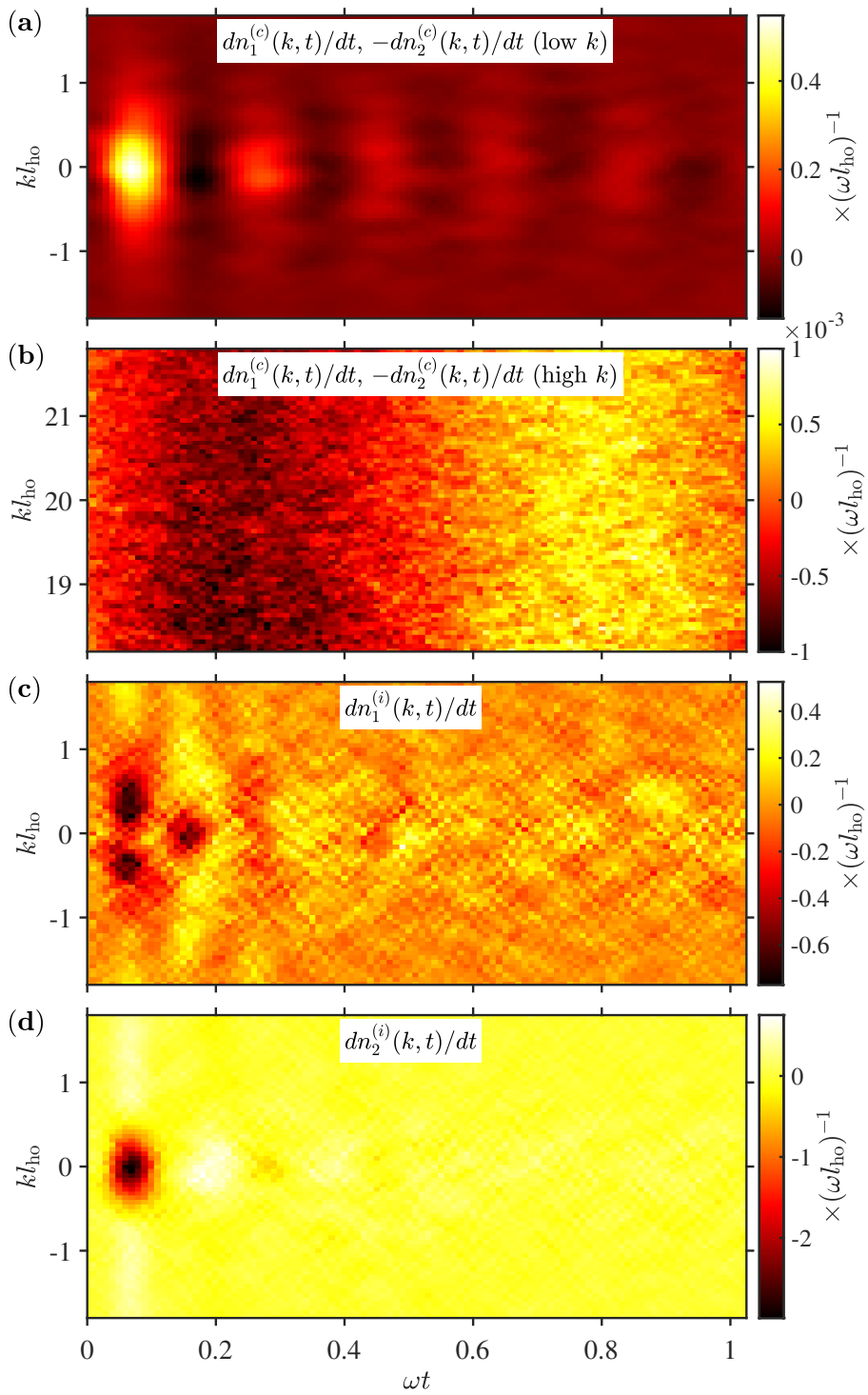

Figure 3.3: Evolution of the cross- and intra-well components of the momentum distribution currents $dn_j(k,t)/dt$ versus dimensionelss momentum $kl_{\rm ho}$ (with $l_{\rm ho}=\sqrt{\hbar/m\omega}$ being the harmonic oscillator length) and dimensionless time ωt: (a) & (b) cross-well component of the current due to tunneling of particles between the two quasicondensates, $dn_1^{(c)}(k,t)/dt=-dn_2^{(c)}(k,t)/dt$, at low and high momenta; (c) intra-well component $dn_1^{(i)}(k,t)/dt$ due to internal dynamics within quasicondensate (1); and (d) intra-well component of $dn_2^{(i)}(k,t)/dt$ due to internal dynamics within quasicondensate (2). Initial parameters are as in Fig. 3.2 (b). Particles oscillate between the two quasicondensates at different frequencies: (a) particles with low momenta oscillate approximately at the Josephson plasma frequency ω_J while (b) particles with high momenta oscillate at the Rabi frequency ω_R (see text).

is the momentum distribution flux at momentum k, whereas

$$\mathcal{G}_j(k,\kappa,\kappa',t) = \frac{2g}{\hbar}\mathrm{Im}\left[\left\langle \hat{a}_j^\dagger(k,t)\hat{a}_j^\dagger(\kappa+\kappa'-k,t)\hat{a}_j(\kappa,t)\hat{a}_j(\kappa',t)\right\rangle\right], \tag{3.35}$$

represents the scattering of two particles with initial momenta κ and κ', and final momenta k and $\kappa+\kappa'-k$. In fluid dynamics, the second term in the right hand side of Eq. (3.33) represents creation of a particle with momentum k, hence the name – the source term. The cross-well components are given by

$$\begin{aligned}\frac{d}{dt}n_1^{(c)}(k,t) &= 2J\mathrm{Im}\left[\left\langle \hat{a}_2^\dagger(k,t)\hat{a}_1(k,t)\right\rangle\right],\\ \frac{d}{dt}n_2^{(c)}(k,t) &= 2J\mathrm{Im}\left[\left\langle \hat{a}_1^\dagger(k,t)\hat{a}_2(k,t)\right\rangle\right],\end{aligned} \tag{3.36}$$

with $dn_1^{(c)}(k,t)/dt = -dn_2^{(c)}(k,t)/dt$, as expected from particle number conservation.

In the c-field approach, the momentum currents defined above are calculated using stochastic averages over the Fourier components of c-field complex amplitudes in place of quantum mechanical expectation values of field operators, just like we did in the calculation of mean energies and particle numbers in Eqs. (3.25) and (3.26).

In Fig. 3.3, we plot the cross- and intra-well components of $dn_j(k,t)/dt$ for two coupled quasicondensates with the same parameters as in Fig. 3.2 (b) [For the parameters of Figs. 3.2 (a) and 3.2 (c), these components have similar features as those shown in Fig. 3.3 and are not plotted.] We can see here that immediately after turning on the coupling between the two quasicondensates particles start to flow across to the other quasicondensate, as well as within the same quasicondensate. Initially, there is a large flow of particles with low momenta from quasicondensate 2 to quasicondensate 1 due to the initial particle difference ($\mu_2 > \mu_1$), as can be seen from the positive valued peak in the cross-well current $dn_1^{(c)}(k,t)/dt$ around $\omega t \simeq 0.05$, in Fig 3.3 (a). At the same time, there is a redistribution of particles within each quasicondensate seen in alternating regions of positive and negative intra-well currents $dn_1^{(i)}(k,t)/dt$ and $dn_1^{(i)}(k,t)/dt$, seen in Figs. 3.3 (c) and (d), which eventually subside to zero currents with time.

The oscillations in $dn_1^{(c)}(k,t)/dt$ and $dn_2^{(c)}(k,t)/dt$) at low momenta, shown in Fig. 3.3 (a), decay quickly—as soon as the particle numbers of the two quasicondensates become close to each other. These oscillations coincide with what we observed in the inset of Fig. 3.2 (b) as high-frequency oscillations in the particle number imbalance, which reside on top of lower frequency oscillations that occur with a significantly larger amplitude. At later times, only the lower frequency oscillations in $dn_1^{(c)}(k,t)/dt$ and $-dn_2^{(c)}(k,t)/dt$ persist; they occur at higher momenta and are shown in Fig. 3.3 (b). This confirms that the low frequency oscillations seen in Fig. 3.2 are mainly due to the high energy particles.

The low momentum range shown Figs. 3.3 (a), (c), and (d) corresponds to particles occupying the bulk of the momentum distribution—as can be seen from the comparison to the full momentum range shown in Fig. 3.4. The distinction between low and high energy particles, or between low and high momenta, can be also identified from an approximate analytic estimate of the widths of the momentum distributions of our quasicondensates. Indeed, for a finite-temperature uniform quasicondensate at

density ρ and temperature T, the bulk of the momentum distribution is well approximated by a Lorentzian of width $\sim 1/l^{(\phi)}$, where $l^{(\phi)} = \hbar^2\rho/mk_BT$ is the phase coherence length [32, 177]. For a harmonically trapped (nonuniform) quasicondensate, the momentum distribution can be calculated as in Ref. [177], and it still has a width on the order of the inverse phase coherence length (up to a numerical factor on the order of one), except evaluated at the peak density. Adopting this result for our quasicondensates, which have peak phase coherence lengths of $l_{0,j}^{(\phi)} = \hbar^2\rho_{0,j}/mk_{\rm B}T_j$ ($j = 1, 2$), we can estimate that the bulk of the respective momentum distributions has the width of $\Delta k_j \sim 1/l_{0,j}^{(\phi)}$. Rewriting this in a dimensionless form $\Delta k_j l_{\rm ho} \sim l_{\rm ho}/l_{0,j}^{(\phi)}$, using the harmonic oscillator length $l_{\rm ho} = \sqrt{\hbar/m\omega}$, one can show that $\Delta k_j l_{\rm ho} \sim \chi_{0,j}^{2/3}$. For $\chi_{0,j} = 9.32 \times 10^{-2}$, as in Figs. 3.2 and 3.3, this gives the dimensionless width on the order of $\Delta k_j l_{\rm ho} \sim 0.2$, which agrees reasonably well with the range of low momentum modes that we identified from the numerical results of Fig. 3.4 below and have shown in Fig. 3.3.

The way the low- and high-energy particles tunnel at different frequencies can be understood by revisiting the theory of a bosonic Josephson junction between two Bose-Einstein condensates [30, 162–168, 171, 172, 174] and extending it to a pair of uniform 1D quasicondensates. Within the linearised theory of modulational instabilities of Josephson oscillations (where there is a small particle imbalance $|N_{\rm imb}(t)| \ll 1$ and a small relative phase $|\Delta\hat{\phi}(x,t)| \equiv |\hat{\phi}_1(x,t) - \hat{\phi}_2(x,t)| \ll 1$), the particles oscillate between the quasicondensates with frequency given by [162]

$$\omega_{\rm lin} = \sqrt{\frac{2g\rho_{0,\rm tot}J}{\hbar} + 4J^2}\ , \tag{3.37}$$

where $\rho_{0,\rm tot} = \rho_{0,1} + \rho_{0,2}$. Here, we can see that if the intra-well interaction energy is sufficiently large such that $g\rho_{0,\rm tot} \gg \hbar J$, particles oscillate between the two quasicondensates at a rate given by the Josephson plasma frequency [30]

$$\omega_{\rm J} = \sqrt{\frac{2Jg\rho_{0,\rm tot}}{\hbar}}\ . \tag{3.38}$$

As this condition in our inhomogeneous quasicondensate is satisfied in the high-density bulk of the system, which is also where the low-energy particles are localised, we do indeed observe that the low-k components in Fig. 3.3 (a) oscillate approximately at the said plasma frequency ω_J, which is the high frequency component. In the opposite limit where interaction between particles is negligible, *i.e.* for high-energy tails of the momentum distribution in our system (Fig. 3.3 (b)), the particles undergo a Rabi-like oscillations with frequency given by [162, 164]

$$\omega_R = 2J, \tag{3.39}$$

which is the low frequency component.

3.3.3 Equilibrium chemical potential and temperature

We now characterise the final relaxed state of the two tunnel-coupled 1D quasicondensates. More specifically, we let the system evolve until it relaxes at some final time $t = t_f$ and compute the final chemical potential and final temperature of both quasicondensates by comparing the momentum

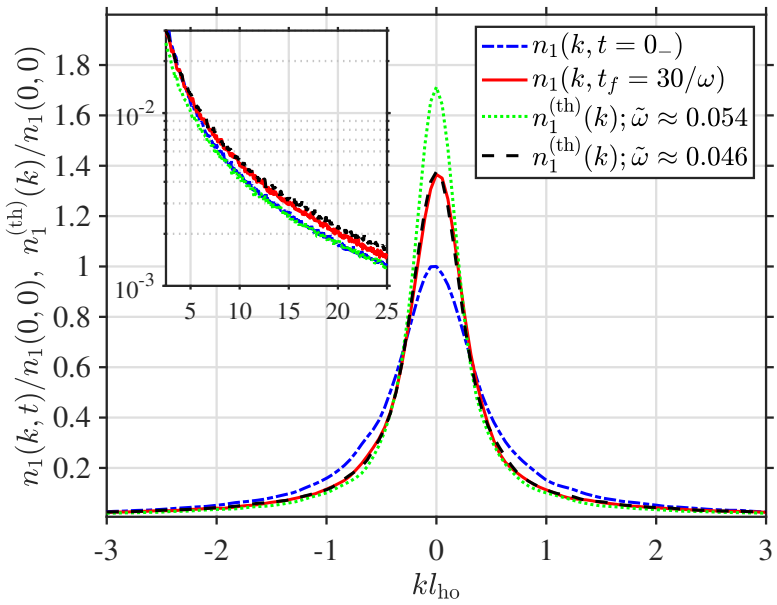

Figure 3.4: Momentum distributions of two initially independent but fully balanced ($\alpha=1$, $\beta=1$) 1D quasicondensate before and after relaxation, for $\tilde{J}=3\tilde{\omega}$. We show only the momentum distribution of the first quasicondensate $n_1(k,t)$, with the understanding that $n_2(k,t)=n_1(k,t)$ in this fully balanced case. The dimensionless momentum kl_{ho} for the horizontal axis is defined as in Fig. 3.3. The initial parameters are $\tilde{\omega}=0.0540$ and $\chi_{0,1}=0.0538$, with the respective dimensionless chemical potentials given by $\tilde{\mu}_1=1/\chi_{0,1}^{2/3}$, according to Eq. (3.23), and $\tilde{\mu}_2=\tilde{\mu}_1$ (for $\beta=1$). The two initially uncoupled quasicondensates [blue, dashed dotted line, with $n_1(k,t=0_-)=n_2(k,t=0_-)$] evolve in a coupled setup and eventually relax into a new equilibrium state, with the respective momentum distribution $n_1(k,t_f=30\omega)=n_2(k,t_f=30/\omega)$ (*i.e.* after 30 oscillation cycles) shown as red full line. The dashed black line is an actual thermal (Gibbs) equilibrium distribution of pre-coupled 1D quasicondensates fitted to the time-evolved and relaxed distribution; the best-fit temperature for this thermal distribution corresponds to $\tilde{\omega}=0.0464$ (recall that $\tilde{\omega}\propto T_1^{-2/3}$), which means that the temperature of the relaxed state is higher than the initial temperature T_1 by a factor of 1.256 [corresponding to $(0.0540/0.0464)^{3/2}$]. The new (relaxed) value of the parameter $\chi_{0,1}$ is also a factor of 1.256 larger than initially, according to $\chi_{0,1}=4\sqrt{2}\,k_BT_1/(3N_1\hbar\omega)$. The threshold for Bhattacharyya distance used here to terminate the search for the best-fit temperature between the relaxed and thermal distributions is $D_B=0.0002$. We also show for comparison (green dotted line) the momentum distribution of a thermal equilibrium state of an initially coupled system, but at the same initial temperature $\tilde{\omega}=0.0540$ as the pre-quenched (lower temperature) uncoupled system; the distribution is narrower than that of the final relaxed state of the quenched system, as expected. The inset is the zoomed in momentum distributions at large momenta k.

distribution of the relaxed state with that of the thermal Gibbs distribution. Given that the initial state of the system (before the coupling J is turned on) is an excited state with respect to the coupled system at $J \neq 0$, we expect the two coupled quasicondensates to relax to a final equilibrium state at a higher temperature.

Given the peak density $\rho_j(x = 0, t_f) \equiv \rho_{0,j}^{(f)}$ of the final relaxed state, the global equilibrium chemical potential of each quasicondensate can be estimated as $\mu_j^{(f)} = g\rho_{0,j}^{(f)}$ in the trap centre, using the Thomas-Fermi approximation. The temperature of the final relaxed state $T_1^{(f)} = T_2^{(f)}$, on the other hand, is obtained by fitting the momentum distributions $n_j(k, t_f)$ of the relaxed state to an equilibrium thermal momentum distributions $n_j^{(\mathrm{th})}(k)$. The thermal momentum distributions $n_j^{(\mathrm{th})}(k)$ are obtained by performing SPGPE simulations of two initially coupled quasicondensates according to Eqs. (3.12) with an added tunnel coupling term as in the GPE (3.15) (*i.e.* by modelling the respective thermal equilibrium state after cooling down two pre-coupled quasicondensates in a transverse double well) with chemical potential $\mu_1^{(f)} = \mu_2^{(f)} = \mu$ and scanning for different values of temperature $T_1^{(f)} = T_2^{(f)} = T_{\mathrm{th}}$ until the obtained equilibrium SPGPE momentum distributions match the momentum distributions of our final (time-evolved) relaxed state.

To quantify the proximity of $n_j^{(\mathrm{th})}(k)$ to the final relaxed momentum distribution, $n_j(k, t_f)$, we calculate the Bhattacharyya statistical distance [178]

$$D_B = -\ln[B(P, P')], \tag{3.40}$$

where $B(P, P')$ is the Bhattacharyya coefficient given by

$$B(P, P') = \sum_{n=0}^{\infty} \sqrt{P(x)P'(x)}\ . \tag{3.41}$$

Here, $P(x)$ and $P'(x)$ are two normalised probability distributions functions of a discrete variable x within the same domain, which are being compared. As $P(x)$ approaches $P'(x)$, the Bhattacharyya coefficient tends to unity, $B(P, P') \rightarrow 1$, which gives a distance of $D_B = 0$ indicating a complete overlap of the two distributions. In our case, the roles of these distribution functions are taken by the normalised momentum distribution of the relaxed state,

$$P_j(k, t_f) = \frac{n_j(k, t_f)}{\sum_{k=-k_{\max}}^{k_{\max}} n_j(k, t_f)}, \tag{3.42}$$

and similarly for the thermal equilibrium state,

$$P_j^{(\mathrm{th})}(k) = \frac{n_j^{(\mathrm{th})}(k)}{\sum_{k=-k_{\max}}^{k_{\max}} n_j^{(\mathrm{th})}(k)}, \tag{3.43}$$

where the summations are over the discrete lattice points in momentum space.

In Fig. 3.4, we plot the momentum distribution $n_1(k, t)$ of the first quasicondensate of a system with two initially uncoupled but fully balanced quasicondensates, *i.e.* with $T_1 = T_2$ ($\alpha = 1$) and $\mu_1 = \mu_2$ ($\beta = 1$), and therefore $N_{\mathrm{imb}}(0) = 0$ and $E_{\mathrm{imb}}(0) = 0$. (The momentum distribution for the second quasicondensate is essentially the same, $n_2(k, t) = n_1(k, t)$, in this balanced case.) The curves

plotted are the momentum distributions before coupling, $n_1(k, t = 0_-)$, and at time $t_f = 30/\omega$, $n_1(k, t_f = 30/\omega)$ when the coupled system has already relaxed. The relaxed distribution (red, full line) is fitted with the momentum distribution at thermal equilibrium of an equivalent pre-coupled system with the same number of particles (black, dashed line), but at a higher temperature than the initial temperature of our system. As we see, the relaxed and best-fit thermal distributions are in excellent agreement with each other (the corresponding Bhattacharyya distance here is $D_B = 0.0002$), implying that the initially uncoupled quasicondensates have relaxed to a higher temperature thermal equilibrium state; the best-fit equilibrium temperature for the relaxed distribution corresponds to $\tilde{\omega} = 0.0464$ (where we recall that $\tilde{\omega} \propto T^{-2/3}$), whereas the initial value of this parameter was $\tilde{\omega} = 0.0540$. We thus conclude that the final relaxed state of the coupled system is described by the thermal Gibbs ensemble, characterised only by the global temperature and the global chemical potential. In addition, we also plot the momentum distribution at thermal equilibrium of a pre-coupled system at the same temperature as the initially uncoupled system. As expected, this distribution is narrower than that of the final relaxed states as it corresponds to a lower temperature thermal equilibrium state.

The increase in temperature of the system can be explained by the redistribution of particles in the system. That is, after introducing the tunnel-coupling J, the two initially independent quasicondensates are suddenly in a double well configuration. Since the ground state energy of the double well system is lower than the combined pre-quench ground state energies of the independent quasicondensates, it opens up more low energy states for the particles in the system. Some high energy particles can now occupy low energy states. Thus, the same pre-quench total energy is now borne by fewer high energy particles. Hence a narrower momentum distribution of the relaxed coupled system at a higher temperature compared to the initial momentum distribution before the coupling J is switched on. We can see this redistribution of particles in Fig. 3.4. The momentum distribution of the relaxed coupled system $n_1(k, t_f = 30/\omega)$ has larger values around $k = 0$ compared to $n_1(k, t = 0_-)$ due to higher occupancy of the low-momentum modes. Moreover, we see higher tails of $n_1(k, t_f = 30/\omega)$ compared to $n_1(k, t = 0_-)$ in the inset of Fig. 3.4 since the total energy is now borne by less high energy particles.

3.3.4 Equilibration and thermal phase coherence

In this subsection we characterise the coherence properties of the coupled quasicondensates before and after relaxation. As we saw in Fig. 3.4, the final relaxed state of each quasicondensate is characterised by the momentum distributions that is narrower and has a higher population of the low-momentum modes around $k = 0$ than the respective initial momentum distribution before the coupling J is switched on. This observation suggests that the condensate fraction (as per Penrose-Onsager criterion [147]), and hence the phase coherence of both quasicondensates, increase despite the fact that the quasicondensates have relaxed to a thermal equilibrium state at a higher, rather than lower, temperature. To confirm this, we compute the normalised first-order correlation function for each quasicondensate,

$$g_j^{(1)}(x, x', t) \equiv \frac{\langle \hat{\psi}_j^\dagger(x, t)\hat{\psi}_j(x', t)\rangle}{\sqrt{\rho_j(x, t)\rho_j(x', t)}}, \tag{3.44}$$

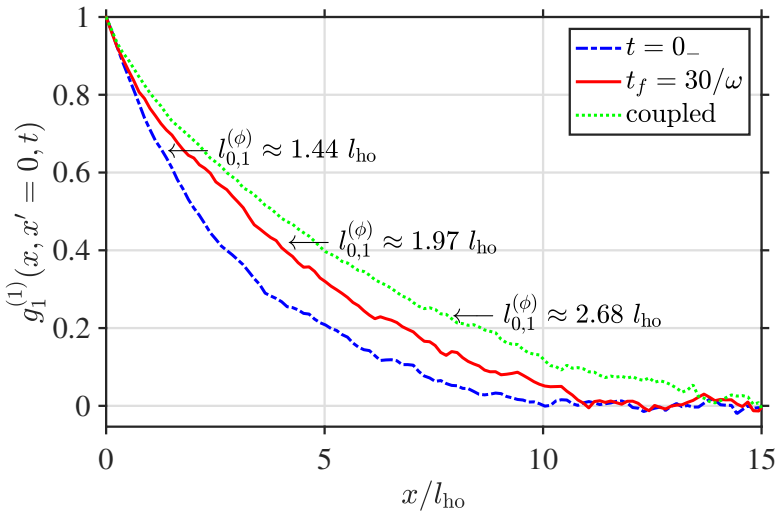

Figure 3.5: First-order correlation function $g_1^{(1)}(x, x' = 0, t)$, Eq. (3.44), before ($t = 0_-$, $\tilde{J} = 0$, blue dash-dotted line) and after ($t = t_f$, $\tilde{J} = 3\tilde{\omega}$, red full line) relaxation, for two initially independent but fully balanced quasicondensates. All parameters are the same as in Fig. 3.4. We also show (by the green dotted line) the thermal equilibrium correlation function $g_1^{(1)}(x, x' = 0)$ for an initially coupled system if it were prepared (cooled down in a transverse double well) at the same temperature as the two initially independent 1D quasicondensates.

and check whether the phase coherence length indeed increases after relaxation.

As a guide to evaluating the phase coherence length, we note that within the Luttinger liquid approach for a uniform system [32, 69, 70, 179] (which treats only the long wavelength excitations, for relative distances much larger than the healing length

$$l_j^{(h)} = \frac{\hbar}{\sqrt{mg\rho_j}}, \tag{3.45}$$

and ignores density fluctuations), the equilibrium first-order correlation function in the quasicondensate regime is expected to decay exponentially as a function of the relative distance (see, *e.g.* [179] for further details),

$$g_j^{(1)}(x, x') = e^{-|x-x'|/2l_j^{(\phi)}}, \qquad |x - x'| \gg l_j^{(h)}, \tag{3.46}$$

where

$$l_j^{(\phi)} = \frac{\hbar^2 \rho_j}{m k_{\rm B} T_j} \tag{3.47}$$

is the thermal phase coherence length of the jth quasicondensate at density ρ_j and temperature T_j.

Adopting this result for our nonuniform system within the local density approximation and evaluating $g_j^{(1)}(x, x', t)$ in the trap centre, *i.e.* at $x' = 0$ and as a function of x, we expect to observe exponentially decaying correlation functions, with the phase coherence length $l_{0,j}^{(\phi)}$ evaluated at the peak density $\rho_{0,j}$ and the respective temperature of the system T_j. More specifically, we calculate $g_j^{(1)}(x, x' = 0, t)$ at time $t = 0_-$ and at $t = t_f$ once the system has relaxed. The results of SPGPE simulations for the initial correlation $g_j^{(1)}(x, x' = 0, t = 0_-)$, and SPGPE plus GPE simulations for the final $g_j^{(1)}(x, x' = 0, t = t_f)$ correlation, are shown in Fig. 3.5 for the same initially fully balanced quasicondensates and same parameters as in Fig. 3.4. [The first-order correlation function for the

second quasicondensate, $g_2^{(1)}(x, x' = 0, t)$, is essentially the same in this balanced case, within the statistical noise, and is not plotted for clarity.] We observe a notable increase of the thermal phase coherence length of the quasicondensates after relaxation (red, full line) compared to that of the initial lower temperature state (blue, dash-dotted line). The numerical values for $l_{0,1}^{(\phi)} = l_{0,2}^{(\phi)}$ shown on the figure are extracted from exponential fits, Eq. (3.46), to the respective curves. For comparison, we also plot (green, dotted line) the thermal equilibrium first-order correlation function of initially pre-coupled quasicondensates at the same temperature as the initially uncoupled system, calculated in the same manner as the thermal momentum distribution $n_j^{(\mathrm{th})}(k)$ in Fig. 3.4, *i.e.* using tunnel coupled SPGPEs. The coherence length of such a system is larger than that of the relaxed state of the post-quench coupled system, reflecting the fact that the post-quench state, immediately after turning on the tunnel coupling J, is an excited state of the transverse double well potential, which relaxes to a new higher temperature equilibrium state of that potential.

The increase in the phase coherence length after relaxation of the coupled system to a new thermal equilibrium state at a higher temperature can be explained by the fact that the tunnel coupling between the condensates is equivalent to an introduction of an effective additional degree of freedom per particle, which generally favours establishment of long range order. This in turn is similar to the general trend that mean-field theories perform better when going from lower to higher dimensional systems or when increasing the coordination number in a many-body system.

From the microscopic dynamical viewpoint, the increase in the phase coherence within each relaxed quasicondensate can be attributed to the phase correlation established between the quasicondensates by the tunnel coupling. A quantitative measure of such a cross-correlation, namely between the phases of the two quasicondensates, is given by the following two-point second-order correlation function [21, 151]:

$$C(x, x', t) = \frac{\langle \hat{\psi}_1(x,t)\hat{\psi}_2^\dagger(x,t)\hat{\psi}_1^\dagger(x',t)\hat{\psi}_2(x',t)\rangle}{\rho_1(x,t)\rho_2(x',t)}. \tag{3.48}$$

The cross-correlation $C(x, x', t)$ characterises the degree of correlation between the complex-valued Bose fields $\hat{\psi}_1(x, t)$ and $\hat{\psi}_2(x, t)$ at two arbitrary points x and x' along the length of the quasicondensates, and is experimentally measurable [21]. In the quasicondensate regime considered throughout this chapter, wherein the density fluctuations are suppressed and can be neglected, the two-point correlation function $C(x, x', t)$ simplifies to

$$C(x, x', t) \approx \langle \exp[i\Delta\hat{\phi}(x,t) - i\Delta\hat{\phi}(x',t)]\rangle, \tag{3.49}$$

where

$$\Delta\hat{\phi}(x,t) = \hat{\phi}_1(x,t) - \hat{\phi}_2(x,t) \tag{3.50}$$

is the relative phase between the two quasicondensates. As such, it quantifies the degree of correlation between the local relative phases of the two quasicondensates at two arbitrary points x and x' [20,30,157]. For all example systems treated in this work, both Eq. (3.48) and Eq. (3.49) gave quantitatively very similar results, confirming that the density fluctuations in our systems are indeed negligible and hence implying that the presence of any correlation in Eq. (3.48) can be attributed purely to phase correlation or phase locking due to the tunnel coupling.

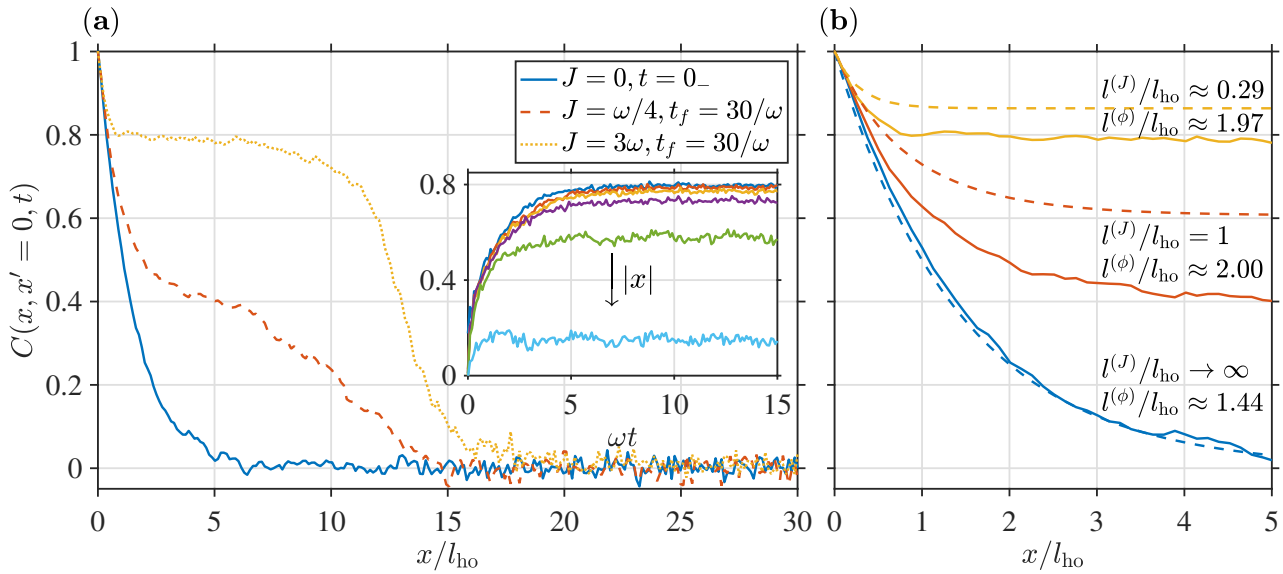

Figure 3.6: (a) Two-point correlation function $C(x, x' = 0, t)$ as a function of distance x from the trap center ($x' = 0$), for two initially independent but fully balanced quasicondensates, and the same parameters as in Fig. 3.4). The different curves correspond to different time instances—before the switching on the tunnel coupling (blue solid line, $t = 0_-$) and after the coupled system has relaxed (dashed red and dottted yellow lines, $t = t_f$), for two different coupling strengths as indicated by the labels. The inset shows the evolution of $C(x, x' = 0, t)$ with dimensionless time ωt (for $\tilde{J} = 3\tilde{\omega}$) at several fixed points x, starting from $x = 2.4 l_{\rm ho}$ (topmost curve) to $x = 14.4 l_{\rm ho}$ (bottommost curve) with an increment of $\Delta x = 2.4 l_{\rm ho}$. (b) Comparison of $C(x, x' = 0, t)$ in (a) to the two-point correlation function for two uniform tunnel-coupled 1D quasicondensates, Eq. (3.51), at short distances. The solid lines are the curves in (a) of the same colors, whereas the dashed lines are plots of Eq. (3.51) using the shown values of $l^{(J)}$ and $l^{(\phi)}$. The phase coherence lengths $l^{(\phi)}$ are obtained by implementing the same procedure as in Fig. 3.5.

In Fig. 3.6 (a), we plot the initial equilibrium ($t = 0_-$) and final relaxed ($t = t_f$) correlation functions $C(x, x' = 0, t)$, for initially fully balanced quasicondensates (*i.e.* the same initial parameters as in Fig. 3.4) and for two different values of the tunnel-coupling strength J: one corresponding to a strong cross-coupling regime with $J = 3\omega$ satisfying $l^{(J)} \equiv \sqrt{\hbar/4mJ} \ll l_j^{(\phi)}$ (dotted yellow line) and the other to an intermediate cross-coupling regime with $J = \omega/4$ (dashed red line). We recall that the lengthscale $l^{(J)} = \sqrt{\hbar/(4mJ)}$, associated with the coupling strength J, represents the characteristic distance over which the tunnel coupling restores a spatially constant relative phase $\Delta\phi(x, t) = \phi_1(x, t) - \phi_2(x, t)$. As we see from the figure, the tunnel coupling establishes stronger correlation between the relative phases of the two relaxed quasicondensates at time $t_f = 30/\omega$, which can be referred to as phase locking, $\Delta\phi = 0$ [157, 159]. The correlation has larger amplitude on a longer range for stronger tunnel-coupling as expected.

We also see in Fig. 3.6 (a) an interesting behaviour of the correlation $C(x, x' = 0, t)$. The curves for $J = 3\omega$ and $J = \omega/4$ decay at short distances from the trap centre $x' = 0$. They then plateau at some intermediate distance before decaying to zero far away from the trap centre. To get an insight on this behaviour of $C(x, x' = 0, t)$, we consider two uniform tunnel-coupled 1D quasicondensates with uniform densities $\rho_1 = \rho_2 = \rho$ and temperatures $T_1 = T_2 = T$. For this case, the equilibrium two-point

correlation function in the harmonic approximation can be expressed as [30, 168]

$$C(x,x') \approx \left\langle \exp\left[i\Delta\hat{\phi}(x) - i\Delta\hat{\phi}(x')\right]\right\rangle = \exp\left[-\frac{l^{(J)}}{l^{(\phi)}}(1 - e^{-|x-x'|/l^{(J)}})\right]. \tag{3.51}$$

In Fig. 3.6 (b), we plot Eq. (3.51) for two uniform quasicondensates (dashed lines) with the same $l^{(\phi)}$ and $l^{(J)}$ as the harmonically trapped quasicondensates in Fig. 3.6 (a). (The phase coherence lengths $l^{(\phi)}$ are obtained by implementing the same procedure as in Fig. 3.5 for $J = 3\omega$ and $J = \omega/4$.) To obtain the characteristic length scales of the decay of $C(x,x')$ in Fig. 3.6 (b), we expand the inner exponential in Eq. (3.51) using the Taylor series expansion $e^z = 1 + z + z^2/2! + z^3/3! + \ldots$:

$$C(x,x') = \exp\left\{-\frac{l^{(J)}}{l^{(\phi)}}\left[\frac{|x-x'|}{l^{(J)}} - \frac{1}{2}\left(\frac{|x-x'|}{l^{(J)}}\right)^2 + \frac{1}{6}\left(\frac{|x-x'|}{l^{(J)}}\right)^3 + \ldots\right]\right\}. \tag{3.52}$$

We immediately see here that at short distances $|x - x'| \ll l^{(J)}$, the leading term in the expansion dominates and the correlation $C(x,x')$ decays as

$$C(x,x') = e^{-|x-x'|/l^{(\phi)}}, \tag{3.53}$$

with a characteristic length given by the thermal phase coherence length $l^{(\phi)}$. Then, at distances $|x - x'| \sim l^{(J)}$, other terms in the expansion become significant and the length scale $l^{(J)}$ takes over as the characteristic length of decay. After this decay, at distances $|x - x'| \gg l^{(J)}$, the correlation function $C(x,x')$ plateaus at

$$C(x,x') = e^{-l^{(J)}/l^{(\phi)}}, \tag{3.54}$$

and does not decrease to zero even as $|x - x'| \to \infty$. For the limiting case $J \to 0$, Eq. (3.51) reduces also to Eq. (3.53). This exponential decay for $J \to 0$ is to be expected since the two-point correlation function, Eq. (3.48), for two uncoupled quasicondensates reduces to a product of their first-order correlation functions, Eq. (3.44).

We see the same behaviour of Eq. (3.51) in the correlation functions $C(x, x' = 0, t)$ for our trapped system (see Fig. 3.6 (b) for a comparison of Eq. (3.51) (dashed lines) to the curves of $C(x, x' = 0, t)$ from Fig. 3.6 (a) (solid lines)). The correlation for the independent ($J = 0$) but fully balanced quasicondensates $C(x, x' = 0, t = 0_-)$ (blue solid line) and Eq. (3.53) (blue dashed line) are in excellent agreement with each other, with characteristic length of decay $l^{(\phi)} \approx 1.44 l_{\rm ho}$. For the relaxed coupled system, the correlation $C(x, x' = 0, t = t_f)$ both for $J = 3\omega$ (yellow solid line) and $J = \omega/4$ (red solid line) overlap at distances $|x| \ll 0.29 l_{\rm ho}$ ($l^{(J)} \approx 0.29 l_{\rm ho}$ for $J = 3\omega$). This is due to the fact that the phase coherence lengths of both relaxed coupled systems are approximately the same ($l^{(\phi)} \approx 1.97 l_{\rm ho}$ for $J = 3\omega$ and $l^{(\phi)} \approx 2.00 l_{\rm ho}$ for $J = \omega/4$). As $|x| \sim l^{(J)}$, the correlation $C(x, x' = 0, t = t_f)$ for both tunnel-coupling strengths deviate from each other and each curve now has a characteristic length scale $l^{(J)}$, with $l^{(J)}$ evaluated at each corresponding J. Then, for distances $|x| \gg l^{(J)}$, we see that $C(x, x' = 0, t = t_f)$ for both tunnel-coupling strengths plateau near the value given by Eq. (3.54) for each J. The discrepancy between $C(x, x' = 0, t = t_f)$ from our simulations and the plots of Eq. (3.51) for both tunnel-coupling strengths in Fig. 3.6 (b) is due to the nonuniformity of our trapped system. Indeed, the correlation $C(x, x' = 0, t = t_f)$ does not stay constant at longer distances. The correlation

$C(x, x' = 0, t = t_f)$ in Fig. 3.6 starts to decay to zero as $|x|$ approaches the Thomas-Fermi radius $R_{\rm TF} \approx 16.03 l_{\rm ho}$ of the trapped quasicondensates. The local relative phases around this area of the nonuniform quasicondensates are less correlated to the local relative phase at the centre of the harmonic trap due to increased phase fluctuations in this region. Then, $C(x, x' = 0, t)$ becomes zero at distances $|x| \gtrsim R_{\rm TF}$ due to further increase in phase fluctuations in the tails of the quasicondensates.

Returning to the phase coherence length within the relaxed quasicondensates, we point out that an increasingly stronger tunnel-coupling does not necessarily lead to an increasingly longer phase coherence length within each quasicondensate (see values of $l^{(\phi)}$ in Fig. 3.6 (b)). This is because of the simultaneous increase in the temperature of the relaxed coupled system: higher temperatures would generally reduce the phase coherence length, however, in the coupled setup such a reduction competes with the increase of phase coherence length due to phase locking so that the overall effect will depend on system parameters.

As a final note, in the inset of Fig. 3.6 we plot the dynamics of the relative phase correlation function $C(x, x' = 0, t)$, monitoring it within the bulk of the quasicondensates at six different fixed points x from the trap center, starting from $x = 2.4 l_{\rm ho}$ (topmost curve) to $x = 14.4 l_{\rm ho}$ (bottommost curve). The correlation functions $C(x, x' = 0, t)$ in the bulk reach their equilibrium value as early as by $t \simeq 7/\omega$. This further confirms our earlier observation that any residual dynamics seen in $E_{\rm imb}(t)$ and $N_{\rm imb}(t)$ past this time (as in Fig. 3.2) is due to the high-energy particles that occupy the tails of the quasicondensates, rather than the bulk.

3.4 Summary

In conclusion, we have studied the relaxation dynamics of two initially independent (uncoupled) 1D quasicondensates following a sudden quench of the strength of tunnel coupling between the quasiocndensates from zero to a constant finite final value. We observe that the coupled quasicondsates relax to a final higher-temperature equilibrium state described by a thermal Gibbs ensemble.

The dynamics of the particle number imbalance between the quasicondensates is characterised by the flow of low energy particles from the colder to the hotter quasicondensate, whereas the reverse is true for the high energy particles. Accordingly, the net energy flow is governed by the surplus of the overall number of low energy particles flowing from the colder system to the hotter system, compared to the overall number of high energy particles flowing in the opposite direction.

We also analysed the phase coherence properties of the coupled quasicondensates and found that, even though the final temperature of the system is higher (which for the same independent quasicondensates would imply a shorter thermal phase coherence length within each quasicondensate), the coherence length of the relaxed coupled quasicondensates can become larger than the initial coherence length. This is explained by the fact that the tunnel coupling acts a phase locking mechanism and is equivalent to an additional degree of freedom in the system, which generally favours establishment of phase coherence over a longer range. The effect is, however, in competition with the trend of reduction of phase coherence length with temperature.

Chapter 4

Relaxation in a bosonic Josephson junction with one-dimensional quasicondensates

Continuing from the previous chapter, we present in this chapter a study of relaxation to phase-locked state in a one-dimensional (1D) bosonic Josephson junction. In a recent experiment [53], Pigneur et al. showed that an extended Josephson junction of 1D Bose gases relaxes to a phase-locked state from a state with an initial phase difference between the two Bose gases. However, this observation cannot be explained by the quantum sine-Gordon model, which effectively describes their previous experiments. Using c-field methods, we try to replicate their experiment. We find that our 1D simulations can reproduce the relaxation of the system to a phase-locked state. However, we could not replicate the fast decay to this final state.

4.1 Motivation

In the previous chapter, we have considered the dynamics of an extended one-dimensional bosonic Josephson junction composed of two tunnel-coupled 1D quasicondensates. It has been proposed in Ref. [180] that such a system can be used to simulate the quantum sine-Gordon model that plays an important model in many fundamental physics questions [174, 180–182]. Indeed, this proposal has been confirmed in recent experiments done in Refs. [159, 183], where the measured thermal correlations agree well with the prediction of the model.

However, in a recent experiment [53], the authors observed a fast decay (after only a few periods of oscillations) of the Josephson oscillations (of the number difference and the global phase difference). The relaxation led to a phase-locked state, and its decay is much faster than predicted in Refs. [151, 152, 160]. Moreover, the authors attempted various theoretical approaches such as quenches in the sine-Gordon model using exact solutions in the single-mode approximations, truncated Wigner approximation, and variational Gaussian approach, but none of these reproduced the fast and complete phase locking they observed. Even succeeding studies of the sine-Gordon model [184, 185] have not described the fast relaxation to a phase-locked state.

In this chapter, we try to reproduce the results of Pigneur *et al.* [53] by doing 1D simulations of the experiment using c-field methods. Specifically, we use the stochastic projected Gross–Pitaevskii equation (SPGPE) to simulate their experiment.

4.2 Details of the experiment

In Ref. [53], they prepared $N = 750 - 4500$ $^{87}\mathrm{Rb}$ atoms in a 3D harmonic potential with longitudinal trapping frequency $\omega_z = 2\pi \times 22$ Hz and transverse trapping frequency $\omega_\perp = 2\pi \times 3$ kHz. The largest chemical potential of their system is $\mu/\hbar = 2.4$ kHz. From Yang–Yang thermometry [186], the estimated initial temperature of their system is $T = 18(3)$ nK. These experimental parameters, where $\omega_x \ll \omega_\perp$, $\mu < \hbar\omega_\perp$, and $k_\mathrm{B}T < \hbar\omega_\perp$, ensure that the system is effectively a 1D BEC [48, 187]. Then, using radio-frequency dressing [188, 189], they deformed the trap by continuously raising a barrier to obtain a symmetric double well potential along the z-axis. This barrier is high enough that tunnelling can be neglected, *i.e.* the two new 1D BECs are considered decoupled. They then imprint an initial relative phase ϕ_0 by shifting the one well of the double well potential along the vertical y-axis. This shift introduces a relative phase due to the energy difference between the two wells: $\phi(t) = \epsilon t/\hbar$. They then re-established the trap symmetry. Finally, the barrier between the two wells is lowered to initiate tunnelling dynamics between the two wells. The quantities of interest that they measured during the tunnelling dynamics are the relative phase between the two Bose gases,

$$\phi(t) = \phi_L(t) - \phi_R(t), \tag{4.1}$$

and its conjugate variable the particle imbalance,

$$n(t) = \frac{N_L(t) - N_R(t)}{N_L(t) + N_R(t)}. \tag{4.2}$$

Here, $\phi_{L(R)}(t)$ and $N_{L(R)}(t)$ are the global phase and particle number of the left (right) 1D Bose gas.

4.2.1 Phenomenological model

To analyse the damped oscillations observed in the experiment, Pigneur *et al.* [53] developed a phenomenological model adapted from the mean-field two-mode Bose–Hubbard model [190]. The undamped dynamics of the particle imbalance and the relative phase between two symmetric traps are given by

$$\dot{n}(t) \approx -\frac{2\mathcal{J}}{\hbar}\sqrt{1 - n^2(t)}\ \sin[\phi(t)], \tag{4.3}$$

$$\dot{\phi}(t) \approx \frac{NU}{\hbar}n(t) + \frac{2\mathcal{J}}{\hbar}\frac{n(t)}{\sqrt{1 - n^2(t)}}\cos[\phi(t)], \tag{4.4}$$

where $\mathcal{J}$ is the single particle tunnel-coupling energy, $N = N_L + N_R$ is the total number of particles, and U is the on-site interaction energy. The Josephson regime is achieved if the ratio $NU/2\mathcal{J} \gg 1$ is satisfied [191]. This experiment is well within the Josephson regime with $NU/2\mathcal{J}$ of the order of

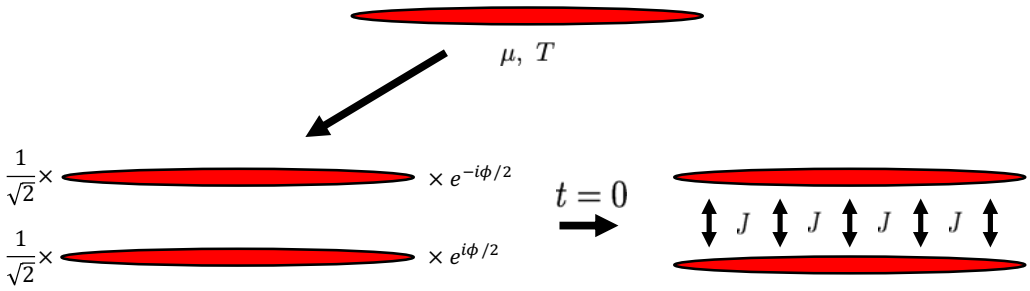

Figure 4.1: Quench protocol: Starting from an initial state with chemical potential μ and temperature T prepared in a harmonic trap with longitudinal trapping frequency ω_0, we split the condensate into two and imprint a relative phase ϕ between the two. Then, we quench the system by turning on the coupling between them at time $t = 0$.

100. Within this regime, the frequency of Josephson oscillations is given by the Josephson plasma frequency

$$\omega_p \approx \frac{1}{\hbar}\sqrt{NU2\mathcal{J}}\ . \tag{4.5}$$

To account for the damping of the oscillations, they added a dissipative term to Eq. (4.3) [53, 165]:

$$\dot{n}(t) \approx -\frac{2\mathcal{J}}{\hbar}\sqrt{1-n^2(t)}\ \sin[\phi(t)] - \frac{\eta}{N}\dot{\phi}(t), \tag{4.6}$$

where η is an empirical dimensionless viscosity. This viscosity results in an exponential decay with characteristic time τ, which, in the harmonic regime and in the limit $NU \gg 2\mathcal{J}$, is given by

$$\tau(U) \approx \frac{2\hbar}{U\eta}. \tag{4.7}$$

Using Eqs. (4.4) and (4.6) on the experimental data presented in their Fig. 2 [53], they obtained the following fit results: $\tau = 9.8(2)$ ms, $U/h = 0.71(15)$ Hz, and $\mathcal{J}/h = 8(2)$ Hz. Since the fit of the phenomenological model to the experimental data in Fig. 2 of Ref. [53] gives an excellent agreement, we shall compare our 1D simulations to the phenomenological model with the aforementioned parameters instead of the actual experimental data points.

4.3 Model of the system

In this section, we outline the 1D model we used to simulate the experiment. We approximate the experimental system as a one-dimensional Bose gas and simulate the experiment using the 1D SPGPE. Our simulation starts by first preparing a single quasicondensate with N_{tot} particles at temperature T. To generate the finite temperature initial state, we solve the one-dimensional SPGPE that, for a single quasicondensate, takes the form

$$\mathrm{d}\Psi^{(\mathbf{C})}(x,t) = \mathcal{P}^{(\mathbf{C})}\left\{-\frac{i}{\hbar}\mathcal{L}^{(\mathbf{C})}\Psi^{(\mathbf{C})}(x,t)\,\mathrm{d}t + \frac{\Gamma}{k_BT}(\mu-\mathcal{L}^{(\mathbf{C})})\Psi^{(\mathbf{C})}(x,t)\,\mathrm{d}t + dW_\Gamma(x,t)\right\}, \tag{4.8}$$

with $\mathcal{L}^{(\mathbf{C})}$ being the Gross–Pitaevskii evolution operator

$$\mathcal{L}^{(\mathbf{C})} = -\frac{\hbar^2}{2m}\frac{\partial^2}{\partial x^2} + \frac{1}{2}m\omega^2x^2 + g|\Psi^{(\mathbf{C})}(x,t)|^2. \tag{4.9}$$

Here, m is the mass of a single particle, ω is the longitudinal trapping frequency, and $g = 2\hbar\omega_\perp a$ is the inter-particle interaction strength with a being the three-dimensional s-wave scattering length and $\omega_\perp$ being the transverse trapping frequency. In Eq. (4.8), $\mathcal{P}^{(\mathbf{C})}\{\cdot\}$ is the projection onto the c-field region while the chemical potential μ of the reservoir controls the number of particles in the c-field region. In addition, Γ is the growth rate, whereas the last term $dW_\Gamma(x,t)$ is the associated complex Gaussian white noise with nonzero correlation given by

$$\langle dW_\Gamma^*(x,t) dW_\Gamma(x',t)\rangle = 2\Gamma\delta(x-x')\mathrm{d}t. \tag{4.10}$$

Once the SPGPE is fully solved to its final thermal equilibrium configuration, we quench the system by first splitting the c-field $\Psi^{(\mathbf{C})}$ into two new c-fields. This procedure models the coherent splitting of the quasicondensate in the experiment. Then, as in the experiment, we imprint a relative phase between the two new quasicondensates. The two new quasicondensates are given by

$$\psi_1^{(\mathbf{C})}(x,t=0) = \frac{1}{\sqrt{2}}\Psi^{(\mathbf{C})}e^{-i\phi(0)/2}, \tag{4.11}$$

$$\psi_2^{(\mathbf{C})}(x,t=0) = \frac{1}{\sqrt{2}}\Psi^{(\mathbf{C})}e^{i\phi(0)/2}, \tag{4.12}$$

where $\phi(0) = \phi_1(0) - \phi_2(0)$ is the relative phase between the two quasicondensates. We initiate the dynamics of the system by turning on the coupling between the two quasicondensates. Due to the imprinted relative phase ϕ, particles will start to oscillate back and forth between the two quasicondensates. We simulate the post-quench dynamics of the system by evolving each stochastic realisation of the two c-fields $\psi_1^{(\mathbf{C})}$ and $\psi_2^{(\mathbf{C})}$ in real time according to the tunnel-coupled Gross–Pitaevskii equation (GPE)

$$i\hbar\frac{\partial}{\partial t}\psi_1^{(\mathbf{C})}(x,t) = \left[-\frac{\hbar^2}{2m}\frac{\partial^2}{\partial x^2} + \frac{1}{2}m\omega^2x^2 + g\left|\psi_1^{(\mathbf{C})}(x,t)\right|^2\right]\psi_1^{(\mathbf{C})}(x,t) - \hbar J\psi_2^{(\mathbf{C})}(x,t), \tag{4.13}$$

$$i\hbar\frac{\partial}{\partial t}\psi_2^{(\mathbf{C})}(x,t) = \left[-\frac{\hbar^2}{2m}\frac{\partial^2}{\partial x^2} + \frac{1}{2}m\omega^2x^2 + g\left|\psi_2^{(\mathbf{C})}(x,t)\right|^2\right]\psi_1^{(\mathbf{C})}(x,t) - \hbar J\psi_1^{(\mathbf{C})}(x,t), \tag{4.14}$$

where J is the strength of coupling between the two quasicondensates. The single particle tunnel-coupling energy $\mathcal{J}$ introduced in the phenomenological model above is related to J by: $\mathcal{J} = \hbar J$.

It should be noted, however, that the new quasicondensates $\psi_1^{(\mathbf{C})}(x,t=0)$ and $\psi_2^{(\mathbf{C})}(x,t=0)$ are not ground states of the potential trap $V_{\text{trap}} = \frac{1}{2}m\omega^2x^2$. Thus, we expect some breathing oscillations in addition to the Josephson oscillations that we are interested in. However, the timescale at which the Josephson oscillations decay is much shorter than the timescale at which the breathing oscillations occur and thus will not affect our observation of the Josephson dynamics.

We also note that, as we have observed in Chapter 3, the dynamics of system has position dependence. Thus, instead of a uniform evolution of the relative phase along the x-axis, we have local relative phase $\phi(x,t)$ whose evolution depends on its position along the x-axis (see Fig.4.3 (a)). To calculate the global phase difference, we calculate the phase of the overlap of the c-fields of the two quasicondensates:

$$\phi(t) = \arg\left\{\int \mathrm{d}x\left[\psi_1^{(\mathbf{C})}(x,t)\right]^*\psi_2^{(\mathbf{C})}(x,t)\right\}. \tag{4.15}$$

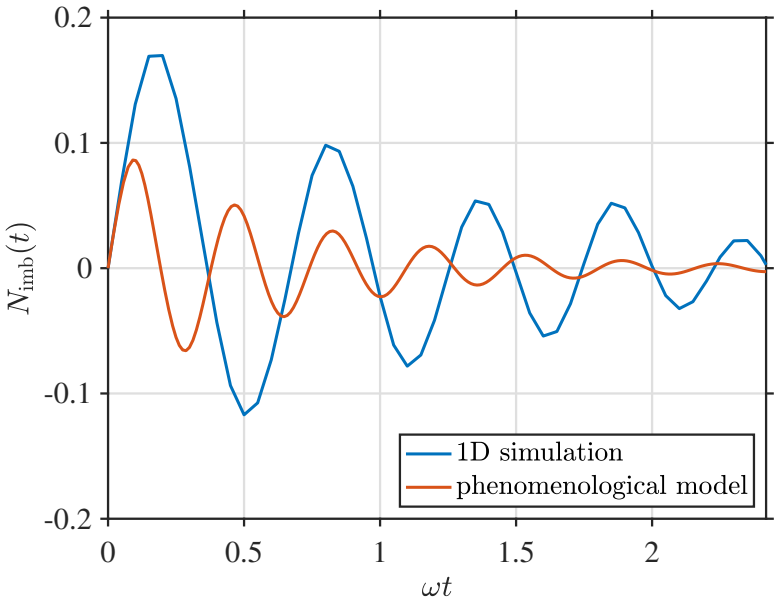

Figure 4.2: Evolution of the particle number imbalance $N_{\mathrm{imb}}(t)$ between the two quasicondensates at finite temperature. The two quasicondensates are initially balanced $N_{\mathrm{imb}}(t=0)=0$. The imprinted initial phase difference of $\phi(t=0)=-1.3$ initiates the Josephson oscillation of particles between the two quasicondensates. The two quasicondensates then evolve to a phase locked state where the phase difference is zero and the particle numbers of the two quasicondensates are balanced. Also shown here is the phenomenological model from Pigneur *et al.*, Phys. Rev. Lett. **120**, 173601 (2018) that represents the experimental data. The two dynamics differ by the rate of damping and the frequency of the Josephson dynamics.

In Figs. 4.2 and 4.3, we plot the particle imbalance and the global relative phase, respectively, between the two one-dimensional quasicondensates, calculated from our simulation. The number of particles in our simulation is the same as the total number of particles reported in Fig. 2 of Ref. [53], *i.e.* $N = 3300(600)$ atoms. Moreover, the growth rate $\hbar\Gamma = 0.01 k_{\mathrm{B}}T$ and maximum momentum $k_{\mathrm{max}} \approx 26/a_{\mathrm{osc}}$ are used in the simulation. The particle imbalance and the global relative phase are compared to the curves obtained from the phenomenological model (Eqs. (4.4) and (4.6)) using the values of τ, U, and $\mathcal{J}$ reported in Fig. 2 of Ref. [53]. It can be seen in Fig. 4.2 that the evolution of both $N_{\mathrm{imb}}(t)$ and $\phi(t)$ does not reflect the evolution of $n(t)$ and $\phi(t)$ in the experiment based on the fit of phenomenological model to experimental data. First, the frequency of oscillations of the curve from the phenomenological order is higher than what we have from our simulations. Given their fit results of $U/\hbar = 0.71(15)$ Hz and $\mathcal{J}/\hbar = 8(2)$ Hz, the frequency of oscillations in their experiment is $\omega_p \approx 2\pi \times 193.62$ Hz, whereas the frequency from our 1D simulation is $\omega_{\mathrm{sim}} \approx 2\pi \times 121.99$ Hz, almost twice as low as what they observed. Second, the characteristic damping time reported in [53], $\tau = 9.8(2)$ ms, is also much lower than the damping time we have in our simulations, which is $\tau_{\mathrm{sim}} \approx 22.7$ ms. We also note that, similar to what we have observed in Chapter 3, the damping time τ is not affected by magnitude of the coupling J.

We note that the quenches we did here are instantaneous compared to the quenches done in the experiment of Ref. [53] where the coherent splitting and imprinting of initial phase difference took a

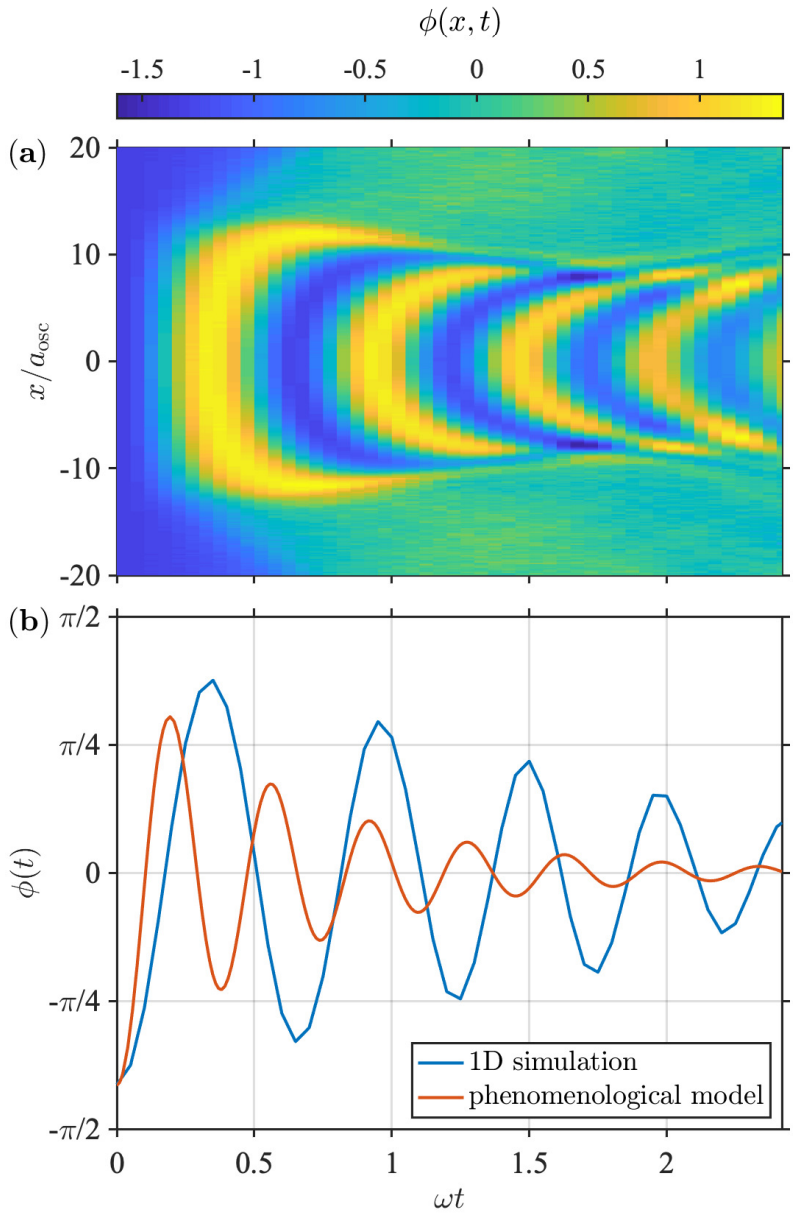

Figure 4.3: Evolution of the phase difference $\phi(t)$ between the two quasicondensates at finite temperature. The initial phase difference of $\phi(t = 0) = -1.3$ initiates Josephson dynamics with the two quasicondensates exchanging particles. The two quasicondensates then evolve to a phase-locked state where the phase difference is zero and the particle numbers of the two quasicondensates are balanced. (a) Some parts of the Bose gas behave differently from other parts due to differences in the local frequencies of oscillations. (b) Global phase difference between the two quasicondensates calculated using Eq. (4.15). Also shown here is the phenomenological model from Pigneur *et al.*, Phys. Rev. Lett. **120**, 173601 (2018) that represents the experimental data. The two dynamics differ by the rate of damping and the frequency of the Josephson dynamics. The damping rate from our simulation is $\tau_{\rm sim} \approx 22.7$ ms, in contrast to the measured damping rate of $\tau_{exp} \approx 9.8$ ms in the experiment of Pigneur *et al.*

short but finite amount of time. However, doing such a non-instantaneous quench in our simulation only delayed the start of Josephson dynamics in our 1D system and did not significantly affect the damping rate and oscillation frequency of our results.

As we can see, our 1D simulations using SPGPE could not replicate the fast decay observed in the experiment of Ref. [53]. A three-dimensional simulation of the experiment might be needed to reproduce the fast decay to a phase-locked state observed in the experiment. As of the writing of this thesis, a pre-print appeared on arXiv (later published on Physical Review Research [192]) where the authors were able to reproduce the fast decay of two quasicondensates to a phase-locked state. Here, they numerically simulated the experiment using a 3D stochastic GPE with an adiabatic radiofrequency potential presented in [188]. They explained that the relaxation to a phase-locked state happens in two stages. The short time dynamics is fully described by multimode dephasing that leads to a local damping of the Josephson oscillations. At longer times, they showed that nonlinear dynamics beyond the sine-Gordon model causes the relaxation of the system to the observed phase-locked state. This work highlights the breakdown of describing the harmonically confined system by a linear model such as the sine-Gordon model.

4.4 Summary

In summary, we have studied the relaxation of two 1D quasicondensates to a phase-locked state. In the experiment of Ref. [53], a fast relaxation to a phase-locked state of two 1D Bose gases was observed. However, this could not be described using the quantum sine-Gordon model that described the authors' previous experiments. This opened the question of the applicability of the model to describe such a quantum system. In our 1D numerical simulations, we observed the same relaxation to a phase-locked state. However, we could not reproduce the fast decay of oscillations observed in the experiment. Full 3D simulations of the experiment might be needed to incorporate the effects of the 3D geometry of the experiment and reproduce the fast relaxation. This is indeed the case in a very recent publication [192] that addressed the same problem. Here, they could reproduce the fast relaxation and explain the relaxation to a phase-locked state through the breakdown of the sine-Gordon model description for harmonic confinements.

Chapter 5

Damping of breathing mode oscillations in a one-dimensional quasicondensate

In this chapter, we study the damping of breathing mode oscillations in a one-dimensional Bose gas that is quenched by changing the harmonic trapping frequency. Using c-field methods, we consider different points in the parameter space of the system, starting from deep in the quasicondensate regime up to the crossover to the nearly ideal gas regime. We find that two breathing modes exist corresponding to two components of the gas: low-energy particles and high-energy particles. Each component has its own distinct breathing frequency and damping rate. We then state the possible mechanism behind the damping of the breathing mode oscillations.

5.1 Motivation

The advances in ultracold atom experiments [13, 14] have renewed interest in the fundamental properties of elementary excitations in interacting Bose gases. Low-energy excitations of a three-dimensional (3D) Bose gas have been studied extensively, both experimentally [193–198] and theoretically [198–214], since the first demonstration of Bose–Einstein condensation in dilute gases [8, 9]. In particular, the temperature dependence of the frequency of collective oscillations and the subsequent damping of excitations have been investigated. Damping of collective oscillations in 3D has been explained either via collisional damping [206, 215] where two parts of the Bose gas (condensate and thermal cloud) exchange energy and particles, or via mean-field effects that lead to Landau damping [199, 200, 204, 209] or Beliaev damping [216]. Here, the lifetime of collective oscillations is usually on the order of milliseconds [194, 199].

In contrast to 3D systems, relaxation in weakly interacting one-dimensional (1D) Bose systems takes a longer time. Due to the integrability of the underlying model describing a 1D system, the Lieb–Liniger model [46, 47], 1D Bose gases retain information of their initial state, which precludes relaxation to a thermal equilibrium state [217]. However, 1D Bose gases realised in experiments are weakly confined in one direction. The longitudinal confinement slightly breaks the integrability of

the system. From a purely mathematical point of view, this can be explained by the impossibility to construct a Bethe-ansatz solution [99] using the eigenfunctions of the longitudinal trapping potential. A physical explanation was also put forward in Ref. [218] for the breaking of integrability in a trapped 1D gas. Here, they argued that the longitudinal confinement introduces finite delay time associated with penetration of quantum particles through each other in the course of a pairwise collision. That is, two particles become a compound particle due to the finite delay time during their collision. Although the total energy of the compound particle is conserved, the single-atom energies are not. This leads to the single-atom energy redistribution after the disintegration of the compound particle and provides a mechanism for relaxation to thermal equilibrium. However, this damping is small enough to be neglected in experiments. Thus, it has been argued that thermalisation in a quasi-1D system is mainly due to virtual excitations of transversal degrees of freedom that give rise to effective velocity-changing three-body elastic collisions [187, 219, 220]. As we will see in this chapter, we still observe damping in simulations of purely 1D systems with no virtual radial excitations.

In this chapter, we study the breathing mode dynamics of a 1D Bose gas after a sudden change of the external trapping potential. As a result of such quench, the system oscillates coherently in a breathing-like fashion governed by the collective excitations of the Bose gas. Measurement of the collective oscillations can serve as a tool to identify which regime the parameters of the Bose gas are in [74, 79, 221–223].

In Ref. [221], the authors experimentally studied a confinement quench of a finite temperature 1D Bose gas. Here, the position-space breathing dynamics have sinusoidal width oscillations whose frequency varies continuously through the quasicondensate to nearly ideal Bose gas crossover. They showed the first observation of the phenomenon of frequency doubling in the oscillations of the momentum distribution relative to the breathing-mode oscillations of the position-space density profile. For experimental parameters set deep in the quasicondensate regime, a periodic narrowing of the momentum distribution occurred at twice the frequency of the breathing oscillations of the density profile. Though the system is at finite temperature, and finite-temperature effects are crucial in describing the momentum-space properties of equilibrium quasicondensates [18, 26, 110, 111], the experimental data for the dynamics were well described by a simple zero-temperature classical hydrodynamic approach, wherein the doubling was interpreted as a result of a self-reflection mechanism due to the mean-field interaction energy barrier. This frequency doubling smoothly disappears as the system goes through the crossover to the nearly ideal Bose gas regime, as expected for a noninteracting gas. This smooth crossover from the regime of frequency doubling to no doubling was explained in Ref. [177] within the hydrodynamic approach. Here, they showed that this crossover results from the competition between the hydrodynamic velocity field (that always displays doubling) and the narrowing and broadening of the thermal component (that does not exhibit doubling) of the gas due to adiabatic compression and decompression.

Interestingly, Ref. [221] observed that the lifetime of the breathing mode dynamics is on the order of seconds. This is in stark contrast to breathing mode dynamics in 3D, where the lifetime of such dynamics is on the order of milliseconds and mainly occurs via the Landau damping mechanism [194, 199]. This

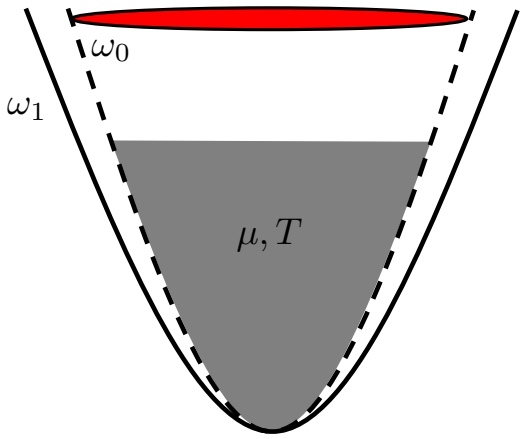

Figure 5.1: Quench protocol: Starting from an initial state with chemical potential μ and temperature T prepared in a harmonic trap with longitudinal trapping frequency ω_0, the system is quenched by changing the longitudinal trapping frequency from ω_0 to ω_1 with quench strength given by ϵ at time $t = 0$.

long lifetime of the breathing mode in 1D has been thought to be related to the integrability of the underlying Lieb–Liniger model [46, 47] of 1D bosons. However, the theoretical explanation of this damping is still lacking.

This chapter delves deeper into the dynamics of breathing mode oscillations in a 1D Bose gas at finite temperature. We characterise the dynamics of the system and try to understand the underlying mechanism behind the damping of oscillations at finite temperature.

5.2 Preparation of initial state and quench protocol

A 1D Bose gas in a harmonic trap is described by the second-quantised Hamiltonian

$$\hat{H} = \int \mathrm{d}x \left[\frac{\hbar^2}{2m} \frac{\partial \hat{\Psi}^\dagger(x,t)}{\partial x} \frac{\partial \hat{\Psi}(x,t)}{\partial x} + \frac{1}{2} m\omega_0^2 x^2 \hat{\Psi}^\dagger(x,t)\hat{\Psi}(x,t) + \frac{g}{2} \hat{\Psi}^\dagger(x,t)\hat{\Psi}^\dagger(x,t)\hat{\Psi}(x,t)\hat{\Psi}(x,t) \right], \tag{5.1}$$

where $\hat{\Psi}(x,t)$ $\left(\hat{\Psi}^\dagger(x,t)\right)$ is the bosonic annihilation (creation) operator that satisfies the equal-time bosonic commutation relation

$$\left[\hat{\Psi}(x,t), \hat{\Psi}^\dagger(x',t)\right] = \delta(x - x'). \tag{5.2}$$

Here, m is the mass of a single particle, ω_0 is the longitudinal trap frequency, and $g = 2\hbar\omega_\perp a_s$ is the 1D coupling strength, with $\omega_\perp \gg \omega_0$ being the transverse confinement frequency and a_s being the 3D s-wave scattering length.

A uniform 1D Bose gas with linear density ρ at temperature T can be completely characterised by two dimensionless parameters [46, 100]: the dimensionless interaction strength given by

$$\gamma = \frac{mg}{\hbar^2 \rho}, \tag{5.3}$$

and the dimensionless temperature given by

$$\overline{\tau} = \frac{2\hbar^2 k_\mathrm{B} T}{mg^2}. \tag{5.4}$$

For the case of a harmonically trapped 1D Bose gas such as one considered in this chapter, the longitudinal trap frequency ω_0 serves as an additional parameter needed to characterise the system. Because the density of the harmonically trapped system becomes position dependent, the dimensionless interaction parameter γ becomes locally defined:

$$\gamma(x) = \frac{mg}{\hbar^2 \rho(x)}. \tag{5.5}$$

In contrast, the dimensionless temperature $\overline{\tau}$ remains a global parameter for the system. For a given chemical potential μ and temperature T, the density at the centre of the trap $\rho(0)$ can be used to define a dimensionless interaction strength

$$\gamma_0 = \frac{mg}{\hbar^2 \rho(0)}, \tag{5.6}$$

that can then serve as a global interaction parameter.

To study the effect of temperature on the damping of breathing mode oscillation, we consider the finite temperature quasicondensate regime of the 1D Bose gas. This regime corresponds to weak interactions $\gamma_0 \ll 1$, and we focus on temperatures of the initial state within the range

$$\gamma_0 \leq \overline{\mathcal{T}} \leq \sqrt{\gamma_0}\,, \tag{5.7}$$

where

$$\overline{\mathcal{T}} = \frac{T}{T_d} = \frac{2mk_{\mathrm{B}}}{\hbar^2 \rho^2(0)} T, \tag{5.8}$$

with T_d being the temperature of quantum degeneracy of the gas at density $\rho(0)$. In this particular range of temperature, which is well within current experimental capabilities [107, 110, 111], the highly occupied, low-energy modes are dominated by thermal fluctuations rather than vacuum fluctuations. In terms of the dimensionless temperature $\overline{\tau}$, Eq. (5.7) is equivalent to

$$\sqrt{\gamma_0} \leq \gamma_0^{3/2} \overline{\tau} \leq 1. \tag{5.9}$$

Thus, instead of using the parameters γ_0 and $\overline{\tau}$ (together with the longitudinal trapping frequency ω_0), we can instead use the product $\gamma_0^{3/2}\overline{\tau}$ to characterise the harmonically trapped 1D Bose gas at finite temperature.

To numerically simulate the dynamics of a 1D quasicondensate at finite temperature, we use c-field methods, which is a proven method to study degenerate Bose gases at finite temperatures [123, 138]. The essence of this method is to treat the highly occupied modes of the quantum Bose field $\hat{\Psi}(x,t)$ as a classical field $\Psi_{\mathbf{C}}(x,t)$. For an observable of interest that is given in terms of the quantum Bose fields $\hat{\mathcal{O}}[\hat{\Psi}(x,t), \hat{\Psi}^\dagger(x,t)]$, calculation of its expectation value $\langle \hat{\mathcal{O}} \rangle$ is equivalent to doing ensemble averaging over many stochastic trajectories $\langle \mathcal{O} \rangle_{\mathrm{stoch}}$ of its corresponding quantity written in terms of the classical fields $\mathcal{O}[\Psi_{\mathbf{C}}(x,t), \Psi^*_{\mathbf{C}}(x,t)]$. For example, calculating the expectation value of the position-space density $\langle \hat{\rho}(x,t) \rangle = \langle \hat{\Psi}^\dagger(x,t)\hat{\Psi}(x,t) \rangle$ is equivalent to calculating the stochastic average $\langle \rho(x,t) \rangle_{\mathrm{stoch}} = \langle \Psi^*_{\mathbf{C}}(x,t)\Psi_{\mathbf{C}}(x,t) \rangle_{\mathrm{stoch}}$.

To generate the initial thermal equilibrium configuration of the system, we numerically solve the simple growth stochastic projected Gross–Pitaevskii equation (SPGPE) given by

$$\mathrm{d}\Psi_{\mathbf{C}}(x,t) = \mathcal{P}^{(\mathbf{C})} \left\{ -\frac{i}{\hbar} \mathcal{L}_0^{(\mathbf{C})} \Psi_{\mathbf{C}}(x,t)\,\mathrm{d}t + \frac{\Gamma}{k_{\mathrm{B}}T} (\mu - \mathcal{L}_0^{(\mathbf{C})}) \Psi_{\mathbf{C}}(x,t)\,\mathrm{d}t + dW_\Gamma(x,t) \right\}. \tag{5.10}$$

Here, the projection operator $\mathcal{P}^{(\mathbf{C})}\{\cdot\}$ sets up the high-energy cutoff for the c-field region, Γ is the growth rate, T is the temperature of the reservoir to which the system is coupled, μ is the chemical potential of the reservoir that controls the number of particles in the c-field region, and $\mathcal{L}_0^{(\mathbf{C})}$ is the Gross–Pitaevskii operator defined by

$$\mathcal{L}_0^{(\mathbf{C})}\Psi_{\mathbf{C}}(x,t) = \left[-\frac{\hbar^2}{2m}\frac{\partial^2}{\partial x^2} + \frac{1}{2}m\omega_0^2 x^2 + g|\Psi_{\mathbf{C}}(x,t)|^2\right]\Psi_{\mathbf{C}}(x,t). \tag{5.11}$$

The last term $dW_\Gamma(x,t)$ in Eq. (5.10) is the associated complex white noise satisfying with the following nonzero correlation:

$$\langle dW_\Gamma^*(x,t)dW_\Gamma(x',t)\rangle = 2\Gamma\delta(x-x')\mathrm{d}t. \tag{5.12}$$

The finite-temperature equilibrium temperature configurations are sampled by integrating the Eq. (5.10) for a sufficiently long time that the memory of the initial trial state is lost.

Once the SPGPE is fully evolved to its final thermal equilibrium configuration, we quench the longitudinal trapping frequency from its initial value ω_0 to a new value ω_1, with the strength of the quench denoted by

$$\epsilon = \left(\frac{\omega_0}{\omega_1}\right)^2 - 1. \tag{5.13}$$

This quench protocol is illustrated in Fig. 5.1. We simulate the post-quench dynamics of the system in its new potential trap by evolving each stochastic realisation of the c-field in real time according to the Gross–Pitaevskii equation (GPE):

$$i\hbar\frac{\partial}{\partial t}\Psi_{\mathbf{C}}(x,t) = \left(-\frac{\hbar^2}{2m}\frac{\partial^2}{\partial x^2} + \frac{1}{2}m\omega_1^2 x^2 + g|\Psi_{\mathbf{C}}(x,t)|^2\right)\Psi_{\mathbf{C}}(x,t). \tag{5.14}$$

In the examples that follow, we use $k_{\mathrm{B}}T = 25\hbar\omega_0$, with $\omega_0 = 2\pi \times 10$ Hz, and vary the chemical potential μ to explore the range of parameters given in Eq. (5.9). Moreover, the transverse trapping frequency $\omega_\perp = 2\pi \times 2$ kHz, the growth rate $\hbar\Gamma = 0.01k_{\mathrm{B}}T$, and the energy cut $\epsilon_{\mathrm{cut}} = 223\hbar\omega_0$ ($k_{\max} \approx 21.12/a_{\mathrm{osc}}$) are used in all SPGPE calculations.

In Figure 5.2, we show a typical evolution of the density profile $\rho(x,t)$ and the momentum distribution $n(k_x,t)$ of a quasicondensate after a quench of the longitudinal trapping frequency. In this example, the initial state is characterised by $\gamma_0^{3/2}\overline{\tau} \approx 0.1$, and the strength of the external trapping potential quench is $\epsilon = 0.2346$. We see here that both $\rho(x,t)$ and $n(k_x,t)$ breathe after the quench, with $n(k_x,t)$ breathing with twice the breathing frequency of $\rho(x,t)$. This phenomenon is known as frequency doubling and can be interpreted, via a simple zero-temperature classical hydrodynamic approach, as a result of a self-reflection mechanism due to the mean-field interaction energy barrier [177]. Based on the results of Ref. [177], we observe it in this finite temperature example because the system (with $\gamma_0^{3/2}\overline{\tau} \approx 0.1$ and $\epsilon = 0.2346$) is in the regime where the contribution of the hydrodynamic velocity field dominates the contribution of the thermal velocities (no frequency doubling) to the breathing dynamics of the momentum distribution. At later times, both density and momentum distribution can be seen to damp, with the damping more apparent in the momentum distribution at this regime.

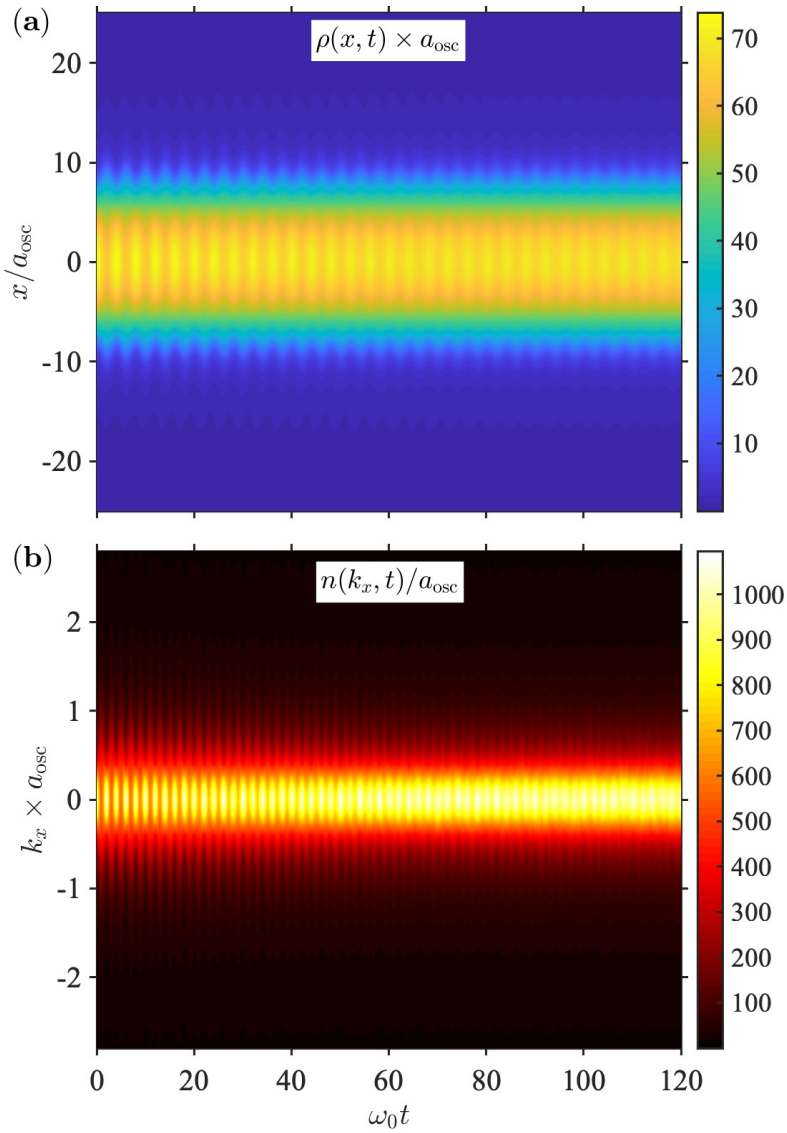

Figure 5.2: Evolution of the density profile $\rho(x,t)$ and the momentum distribution $n(k_x,t)$ of a quasicondensate after a quench of the longitudinal trapping potential $\omega_0 \to \omega_1$ with quench strength $\epsilon = 0.2346$. The initial condition of the system is given by $\gamma_0^{3/2}\overline{\tau} \approx 0.1$.

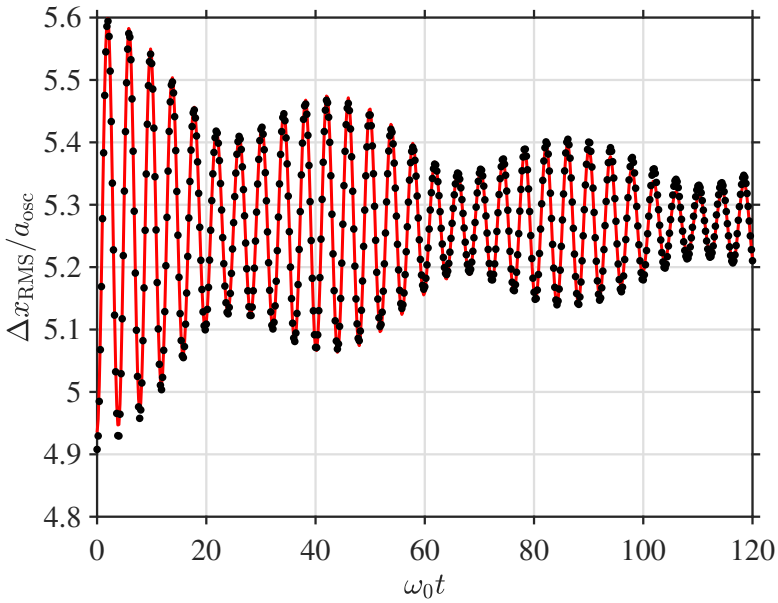

Figure 5.3: Root-mean-square width of the density profile $\rho(x,t)$ shown in Figure 5.2. The black dots are data points from SPGPE simulations while the red line is a fit using Equation (5.16).

To characterise the dynamics of the breathing mode oscillations, we calculate the root-mean-square (RMS) width of the density profile given by

$$\Delta x_{\mathrm{RMS}}(t) = \frac{1}{\sqrt{N}} \left[\int \mathrm{d}x \rho(x,t) x^2 - \left(\int \mathrm{d}x \rho(x,t) x \right)^2 \right]^{1/2}, \tag{5.15}$$

where $N = \int \mathrm{d}x \rho(x)$ is the total number of particles. In Figure 5.3, we show the calculated RMS width Δx_{RMS} of the density profile $\rho(x,t)$ shown in Figure 5.2. A distinct feature of the RMS width in Fig. 5.3 is the presence of beating in the evolution of the RMS width Δx_{RMS}, which is not easily seen in the dynamics of the density profile in Fig. 5.2. This beating of the RMS width suggests that the quasicondensate does not have only one single mode that breathes after the quench of the trapping potential. This beating of the RMS width has been observed in 3D systems, where the effect was called 'collapses' and 'revivals' of the RMS width [198].

To characterise the RMS width of the density profile, we fit a sum of two cosine function, each with its own damping term:

$$\Delta x_{\mathrm{RMS}} = A_1 \cos(\omega_{\mathrm{B1}} t + \phi_1) e^{-\Gamma_1 t} + A_2 \cos(\omega_{\mathrm{B2}} t + \phi_2) e^{-\Gamma_2 t} + C. \tag{5.16}$$

Here, ω_{B1} and ω_{B2} are the two breathing mode frequencies, Γ_1 and Γ_2 are the damping rates of each breathing mode, ϕ_1 and ϕ_2 are the phases of each breathing mode, and the last term C is a constant. As shown in Fig. 5.3, Eq. (5.16) fits well to the RMS width Δx_{RMS} calculated from our *c*-field simulations. The beating of the RMS width Δx_{RMS} that we see in Fig. 5.3 is clearly a result of two components of the 1D Bose gas breathing at two distinct breathing mode frequencies ω_{B1} and ω_{B2}.

5.3 Breathing mode frequencies

We look at quenches of a 1D Bose gas at the limiting regimes considered here for more insight into the breathing frequencies. Depending on the value of the parameter $\gamma_0^{3/2}\overline{\tau}$ (the regime of the 1D Bose gas), a 1D Bose gas can have different values of breathing mode frequencies. For our interest, we shall look at the limiting cases of $\gamma_0, \gamma_0^{3/2}\overline{\tau} \ll 1$ (deep in the quasicondensate regime) and of $\overline{\tau}, \gamma_0^{3/2}\overline{\tau} \gg 1$ (ideal gas regime).

the collective mode frequencies of a 1D Bose gas in a harmonic trap can be estimated using hydrodynamic approach. For this, we follow Ref. [177]. The hydrodynamic description of a 1D Bose gas is given by

$$\frac{\partial}{\partial t}\rho(x,t) + \frac{\partial}{\partial x}\big[\rho(x,t)v(x,t)\big] = 0, \tag{5.17}$$

$$\frac{\partial}{\partial t}v(x,t) + v(x,t)\frac{\partial}{\partial x}v(x,t) = -\frac{1}{m}\frac{\partial}{\partial x}V(x,t) - \frac{1}{m\rho(x,t)}\frac{\partial}{\partial x}P(x,t), \tag{5.18}$$

$$\frac{\partial}{\partial t}s(x,t) + v(x,t)\frac{\partial}{\partial x}s(x,t) = 0, \tag{5.19}$$

where $\rho(x,t)$ is the local 1D density at x, $v(x,t)$ is the corresponding hydrodynamic velocity of that slice, $s(x,t)$ is the entropy per particle, $P(x,t)$ is the pressure, and $V(x,t) = \frac{1}{2}m\omega(t)^2x^2$ is the external harmonic trapping potential. The solutions of the above hydrodynamic equations after a quench of the external trap from ω_0 to ω_1 reduce to the scaling equations of the form

$$\rho(x,t) = \frac{1}{\lambda(t)}\rho_0\left[\frac{x}{\lambda(t)}\right], \tag{5.20}$$

$$v(x,t) = \frac{x}{\lambda(t)}\frac{\mathrm{d}}{\mathrm{d}t}\lambda(t), \tag{5.21}$$

where the scaling parameter $\lambda(t)$ is a solution of the differential equation

$$\frac{\mathrm{d}^2}{\mathrm{d}t^2}\lambda(t) = -\omega_1^2\lambda(t) + \frac{\omega_0^2}{\lambda(t)^{2\nu+1}}. \tag{5.22}$$

This equation satisfies the initial boundary conditions $\lambda(0) = 1$ and $\mathrm{d}\lambda(0)/\mathrm{d}t = 0$. The value of ν depends on the particular regime of the system. For a 1D Bose gas in the nearly ideal gas regime ($\overline{\tau}, \gamma_0^{3/2}\overline{\tau} \gg 1$), we have $\nu = 1$ and Eq. (5.22) can be written as

$$\frac{\mathrm{d}^2}{\mathrm{d}t^2}\lambda(t) = \omega_1^2\left[-\lambda(t) + \frac{\epsilon+1}{\lambda(t)^3}\right]. \tag{5.23}$$

This differential equation has the solution

$$\lambda(t) = \sqrt{1 + \epsilon\sin^2(\omega_1 t)}\ , \tag{5.24}$$

that oscillates with a frequency of $2\omega_1$. Substituting Eq. (5.24) into the scaling equation (Eq. (5.20)) gives us an oscillating density profile where the RMS width is oscillating with a breathing frequency of $\omega_B = 2\omega_1$.

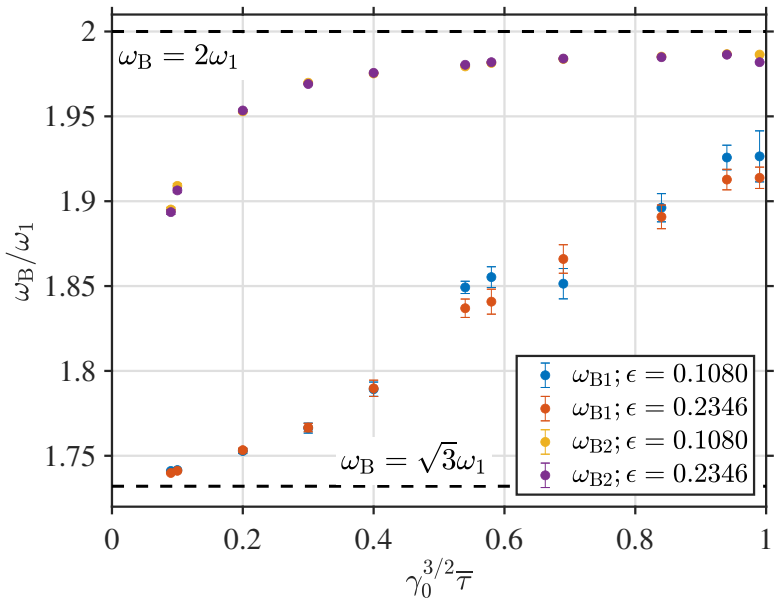

Figure 5.4: Computed breathing mode frequencies ω_{B1} and ω_{B2} using the fitting equation Eq. (5.16). The error bars account for fitting error only, which indicates a 95% confidence interval. For both plots, each colour corresponds to a certain quench strength ϵ. The breathing frequencies of both components approach $\omega_B = \sqrt{3}\,\omega_1$ as the system approach the quasicondensate regime. On the opposite end, both approach $\omega_B = 2\omega_1$ as the system approaches the nearly ideal gas regime.

For the opposite limiting case where a 1D Bose gas is deep in the quasicondensate regime ($\gamma_0, \gamma_0^{3/2}\overline{\tau} \ll 1$), we have $\nu = \frac{1}{2}$:

$$\frac{\mathrm{d}^2}{\mathrm{d}t^2}\lambda(t) = \omega_1^2\left[-\lambda(t) + \frac{\epsilon+1}{\lambda(t)^2}\right]. \tag{5.25}$$

In this regime, Eq. (5.25) can be solved using the method of linearisation for small-amplitude quenches of the external trapping potential, $\epsilon \ll 1$. To do this, we expand the scaling parameter as $\lambda(t) = 1 + \delta\lambda(t)$, with $\delta\lambda(t) \ll \lambda(t)$. By using the approximations $\delta\lambda(t)^2 \approx 0$ and $\epsilon\delta\lambda(t) \approx 0$, and the binomial approximation $(1+x)^\alpha \approx 1 + \alpha x$, Eq. (5.25) can be written as

$$\frac{\mathrm{d}^2}{\mathrm{d}t^2}\delta\lambda(t) = \omega_1^2\left[-3\delta\lambda(t) + \epsilon\right], \tag{5.26}$$

with initial boundary conditions $\delta\lambda(0) = 0$ and $\mathrm{d}\delta\lambda(0)/\mathrm{d}t = 0$ (*cf.* boundary conditions of Eq. (5.22)). This linear differential equation has the solution

$$\delta\lambda(t) = \frac{\epsilon}{3} - \frac{\epsilon}{3}\cos\left(\sqrt{3}\,\omega_1 t\right). \tag{5.27}$$

Thus, the scaling parameter $\lambda(t)$ for the quasicondensate regime is given by

$$\lambda(t) \simeq 1 + \frac{\epsilon}{3} - \frac{\epsilon}{3}\cos\left(\sqrt{3}\,\omega_1 t\right), \tag{5.28}$$

that, after substituting into Eq. (5.20), gives a density profile that breathes with frequency $\omega_B \simeq \sqrt{3}\,\omega_1$.

In Fig. 5.4, we show the two breathing frequencies for a Bose gas deep in the quasicondensate regime ($\omega_B \simeq \sqrt{3}\,\omega_1$) and in the nearly ideal gas regime ($\omega_B = 2\omega_1$), together with the breathing mode

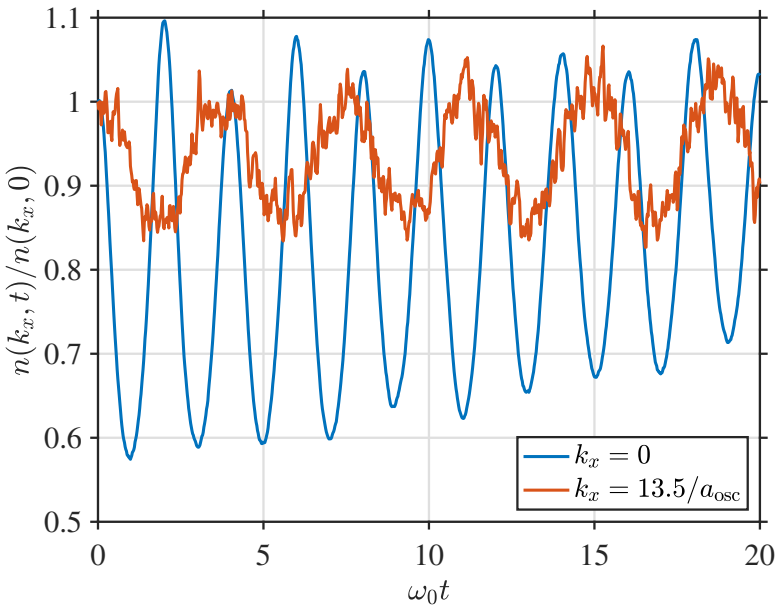

Figure 5.5: Evolution of the momentum distribution at $k_x = 0$ and at $k_x = 13.5/a_{\rm osc}$. The momentum distribution at $k_x = 0$ displays frequency doubling that is a characteristic of a system deep in the quasicondensate regime. On the other hand, the momentum distribution at $k_x = 13.5/a_{\rm osc}$ does not display frequency doubling. A sinusoidal fit to both $n(k_x = 0, t)$ and $n(k_x = 13.5/a_{\rm osc}, t)$ gives $2\omega_{B1} \approx 3.4866\omega_1$ (frequency doubling) and $\omega_{B2} \approx 1.87\omega_1$, respectively.

frequencies obtained from fitting of Eq. (5.16) to the RMS widths at different values of $\gamma_0^{3/2}\overline{\tau}$. We see here that one of the components has a breathing mode frequency ω_{B1} that is close to $\omega_B = \sqrt{3}\,\omega_1$, especially at lower values of $\gamma_0^{3/2}\overline{\tau}$ where the system goes deeper in the quasicondensate regime. The other component has a breathing mode frequency ω_{B2} that is close to $\omega_B = 2\omega_1$, especially as $\gamma_0^{3/2}\overline{\tau} \to 1$, which is the crossover to the nearly ideal gas regime.

The presence of two breathing mode oscillations during the post-quench dynamics is due to particles occupying different energy modes – the high-occupancy, low-energy modes (bulk of the quasicondensate) and the low-occupancy, high-energy modes (tails of the quasicondensate). Particles occupying the bulk of the system, where locally $[\gamma(x)]^{3/2}\overline{\tau} < 1$, thus have breathing frequency close to $\omega_B \simeq \sqrt{3}\,\omega_1$. In contrast, particles that populate the tails locally have $[\gamma(x)]^{3/2}\overline{\tau} \gtrsim 1$ and can be approximated as noninteracting particles (ideal gas). This can be seen if we look at the momentum distribution of the 1D Bose gas. In Fig. 5.5, we can see the difference in behaviour of the momentum distribution $n(k_x, t)$ at $k_x = 0$ and at $k_x = 13.5/a_{\rm osc}$. While the momentum distribution at $k_x = 0$ displays frequency doubling, a property of a Bose gas within the quasicondensate regime, the momentum distribution at $k_x = 13.5/a_{\rm osc}$ does not. In addition, a fit of a sinusoidal function to both curves in Fig. 5.5 yields breathing frequency of $\omega_{B1} \approx 1.7433\omega_1$ for $n(k_x = 0, t)$ and $\omega_{B2} \approx 1.87\omega_1$ for $n(k_x = 13.5/a_{\rm osc}, t)$. These frequencies are close to the breathing mode frequencies we have in Fig. 5.4 for $\gamma_0^{3/2}\overline{\tau} \approx 0.1$. Thus, from this point onwards, we shall call the component with breathing frequency ω_{B1} the *bulk part* while the component with breathing frequency ω_{B2} shall be called the *tail part*.

In addition to the above observation, both breathing mode frequencies appear to approach $\omega_{\rm B} = \sqrt{3}\,\omega_1$ if one goes deeper into the quasicondensate regime. The same is true in the opposite limit:

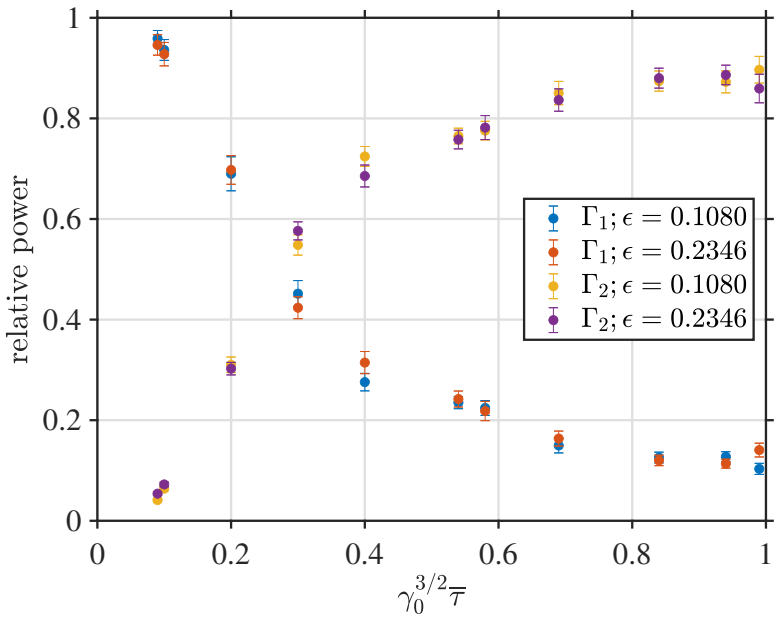

Figure 5.6: Relative power of the eigenmodes in the breathing mode oscillations. The error bars account for fitting error only, which indicates a 95% confidence interval.

both breathing mode frequencies appear to approach the ideal gas frequency $\omega_{\mathrm{B}} = 2\omega_1$ as the system goes beyond $\gamma_0^{3/2}\overline{\tau} = 1$. There is also a smooth crossover of the breathing mode frequencies from one regime to the other like the crossover observed in Ref. [221]. The change from one breathing frequency to two frequencies and then back to one can be explained by considering how particles occupy different energy modes at different values of $\gamma_0^{3/2}\overline{\tau}$. For system parameters deep in the quasicondensate regime ($\gamma_0^{3/2}\overline{\tau} < \sqrt{\gamma_0}$), all particles occupy the low-energy states, and the whole system exhibits breathing oscillations with behaviour close to the zero-temperature limit of the quasicondensate. As we go to higher values of $\gamma_0^{3/2}\overline{\tau}$ (by increasing the temperature or lowering the chemical potential), some particles begin to occupy the higher-energy modes, and a second breathing mode with behaviour closer to that of an ideal gas appears. Then, as we reach the nearly ideal gas regime ($\gamma_0^{3/2}\overline{\tau} \gtrsim 1$), almost all of the particles occupy high-energy modes. The breathing mode associated with low-energy particles begin to disappear – the system starts to exhibit again breathing oscillations with single frequency characteristics similar to that of an ideal gas.

We can quantify this by looking at the relative contribution of each part to the total breathing oscillations of the quasicodensate. To do this, we define the relative power

$$K = \frac{A_2^2}{A_1^2 + A_2^2} \tag{5.29}$$

that quantifies the relative contribution of the tail part to the total breathing oscillations of the RMS width Δx_{RMS}. The relative contribution of the bulk part to the total breathing mode is then given by $1 - K$. Using the relative power K, Eq. (5.16) can be written as

$$\Delta x_{\mathrm{RMS}} = A\left[\sqrt{1-K}\ \cos(\omega_{\mathrm{B}1}t + \phi_1)e^{-\Gamma_1 t} + \sqrt{K}\ \cos(\omega_{\mathrm{B}2}t + \phi_2)e^{-\Gamma_2 t}\right] + C, \tag{5.30}$$

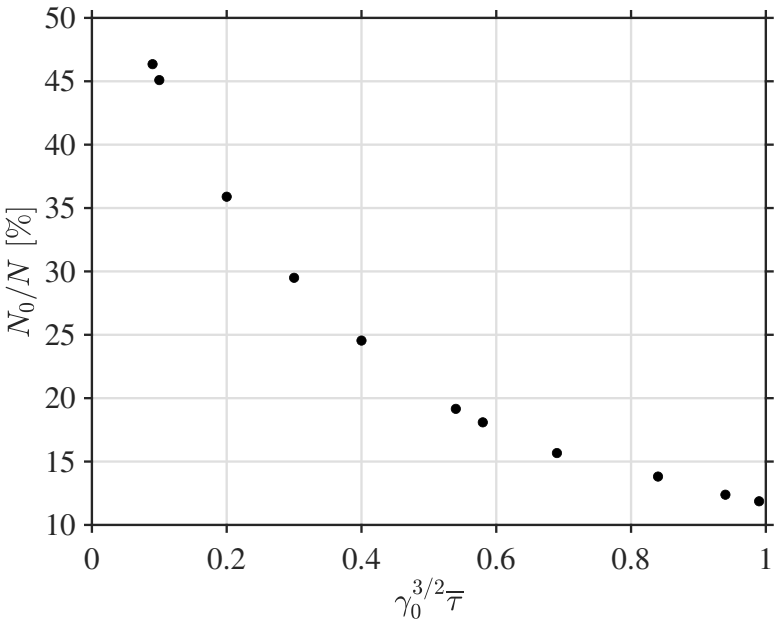

Figure 5.7: Computed condensate fraction of the initial state of the 1D Bose gas at different values of $\gamma_0^{3/2}\overline{\tau}$ using the Penrose–Onsager criterion.

where $A = \sqrt{A_1^2 + A_2^2}$. In Fig. 5.6, we plot the relative power for both quench strengths $\epsilon = 0.1080$ and $\epsilon = 0.2346$. As we can see here, the contribution of the bulk part to the breathing mode oscillation decreases while the contribution of the tail part increases as we go from $\gamma_0^{3/2}\overline{\tau} \approx \sqrt{\gamma_0}$ to $\gamma_0^{3/2}\overline{\tau} \approx 1$. From the preceding paragraph, this is because as we go to higher values of $\gamma_0^{3/2}\overline{\tau}$, the bulk part becomes less populated due to decrease in condensate particles (see Fig. 5.7) and low-energy noncondensed particles. At higher values of $\gamma_0^{3/2}\overline{\tau}$, the tail part starts to dominate the post-quench dynamics of the system.

We note, however, that the intersection of the data points of K and $1 - K$ in Fig. 5.6 is highly dependent on the chosen energy cutoff ϵ_{cut} in the SPGPE during the preparation of the system. That is, the value of ϵ_{cut} dictates how many high-energy particles we include in our system. Choosing a higher-energy cutoff will increase the contribution of the tail part, thus shifting the value of $\gamma_0^{3/2}\overline{\tau}$ at which the data points intersect to a lower value. The opposite is true if we choose a lower energy cutoff.

In Fig. 5.7, we plot the condensate fraction of the system computed using the Penrose–Onsager criterion [147]. For the parameters we considered here, the maximum condensate fraction we have is 46.35% at the lowest $\gamma_0^{3/2}\overline{\tau}$, while the minimum condensate fraction is 19.16% at the maximum $\gamma_0^{3/2}\overline{\tau}$. After comparing this with Fig. 5.6, we see that the collective mode oscillations with mode frequency ω_{B1} are indeed not entirely composed of condensate particles, but also of low-energy noncondensate particles, consistent with our earlier claim.

5.4 Damping of breathing mode oscillations

In this section, we shall look at the damping of breathing mode oscillation that we observed in Fig. 5.3.

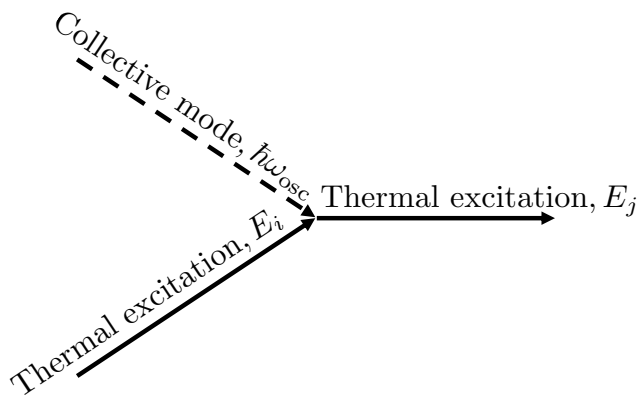

Figure 5.8: Landau damping mechanism: A collective mode with energy $\hbar\omega_{\rm osc}$ interacts with a thermal excitation of energy E_i and produces another thermal excitation with energy $E_j = \hbar\omega_{\rm osc} + E_i$.

Damping of collective mode oscillations is usually attributed to three different mechanisms. First, for collisions that exchange energy and particles between the condensate and the noncondensate, the damping is due to collisional damping [206, 215]. This damping mechanism is present in numerical simulations using the Zaremba–Nikuni–Griffin (ZNG) equations [215, 224] where the condensate part of the system is described by the generalised Gross–Pitaevskii equation, while the noncondensate part is described by the quantum Boltzmann equation. On the other hand, mean-field effects lead to the Landau [199, 200, 204, 209] and Beliaev [216] damping. In the Landau damping mechanism, the collective mode decays due to its interaction with a thermal distribution of excitations where the collective mode absorbs energy, becoming a thermal excitation itself. In the Beliaev damping mechanism, a collective mode decays due to its splitting into two lower-energy excitations. For lowest-energy collective modes in a trapped gas, such as the breathing/monopole mode, the Beliaev damping is absent due to discretisation of energy levels. In the following, we introduce the Landau damping mechanism.

5.4.1 Landau damping

Suppose a collective mode that has been excited by, say, a parameter quench or a periodic driving and oscillates with frequency $\omega_{\rm osc}$. In addition, suppose a collection of thermal excited states with energies E_i and E_j. Due to mean-field interaction effects, the thermal excitations can either absorb or emit a quantum $\hbar\omega_{\rm osc}$ of the collective mode and cause a decay of the collective mode. Here, the quantum $\hbar\omega_{\rm osc}$ of the collective mode is annihilated, and the thermal excitation of energy E_i is transformed into a thermal excitation with energy $E_j = E_i + \hbar\omega_{\rm osc}$ (see Fig. 5.8). This damping mechanism is called the Landau damping.

Within perturbation theory, the decay rate due to Landau damping in a 3D system is given by [200, 204, 209, 210]:

$$\Gamma_{L,\rm 3D} = \frac{\pi}{\hbar}\sum_{ij}|A_{ij}|^2\big[f(E_i) - f(E_j)\big]\delta(E_j - E_i - \hbar\omega_{\rm osc}), \tag{5.31}$$

where

$$f(E_i) = \frac{1}{e^{E_i/k_\mathrm{B}T} - 1} \tag{5.32}$$

is the Bose–Einstein distribution for the thermal excitation with energy E_i at temperature T, and

$$A_{ij} = 2g_{3\mathrm{D}} \int \mathrm{d}\mathbf{r}\Psi_0(\mathbf{r})\big[\big(u_i(\mathbf{r})u_j^*(\mathbf{r}) - v_i(\mathbf{r})u_j^*(\mathbf{r}) + v_i(\mathbf{r})v_j^*(\mathbf{r})\big)u_\mathrm{osc}(\mathbf{r}) \\ - \big(u_i(\mathbf{r})u_j^*(\mathbf{r}) - u_i(\mathbf{r})v_j^*(\mathbf{r}) + v_i(\mathbf{r})v_j^*(\mathbf{r})\big)v_\mathrm{osc}(\mathbf{r})\big] \tag{5.33}$$

is the transition matrix that couples the collective mode with the thermal excitations, with $\Psi_0(\mathbf{r})$ being the condensate complex amplitude and $g_{3\mathrm{D}}$ being the 3D interaction strength parameter. Here, the collective modes $u_\mathrm{osc}(\mathbf{r})$ and $v_\mathrm{osc}(\mathbf{r})$, and the thermally excited modes $u_i(\mathbf{r})$, $u_j(\mathbf{r})$, $v_i(\mathbf{r})$, and $v_j(\mathbf{r})$ are obtained by solving the Bogoliubov–de Gennes equations:

$$\left(-\frac{\hbar^2}{2m}\nabla^2 + V_\mathrm{ext}(\mathbf{r}) + 2g_{3\mathrm{D}}|\Psi_0(\mathbf{r})|^2 - \mu_{3\mathrm{D}}\right)u_i(\mathbf{r}) - g_{3\mathrm{D}}\Psi_0^2(\mathbf{r})v_i(\mathbf{r}) = E_i u_i(\mathbf{r}), \tag{5.34}$$

$$\left(-\frac{\hbar^2}{2m}\nabla^2 + V_\mathrm{ext}(\mathbf{r}) + 2g_{3\mathrm{D}}|\Psi_0(\mathbf{r})|^2 - \mu_{3\mathrm{D}}\right)v_i(\mathbf{r}) - g_{3\mathrm{D}}[\Psi_0^*(\mathbf{r})]^2 u_i(\mathbf{r}) = -E_i v_i(\mathbf{r}). \tag{5.35}$$

In 3D systems, the delta function $\delta(E_j - E_i - \hbar\omega_\mathrm{osc})$ in Eq. (5.31) is replaced by a Lorentzian function with width Δ:

$$\delta(\omega_{ij} - \omega_\mathrm{osc}) \to \frac{\Delta}{2\pi\left[(\omega_{ij} - \omega_\mathrm{osc})^2 + \frac{\Delta^2}{4}\right]}, \tag{5.36}$$

where $\omega_{ij} = (E_j - E_i)/\hbar$ is the frequency difference of the thermally excited states. The width Δ is somewhat arbitrary. In calculations of the damping rate $\Gamma_{L,3\mathrm{D}}$, a range of Δ is chosen such that the variation of $\Gamma_{L,3\mathrm{D}}$ with Δ is very weak. Then, a straight line is fitted to the values of $\Gamma_{L,3\mathrm{D}}$ and is extrapolated back to $\Delta = 0$ to obtain an estimate for the Landau damping rate.

Landau damping for 1D systems

In one-dimensional systems, the region where the Lorentzian changes slowly with the width Δ does not exist. Ref. [225] obtained a similar expression to Eq. (5.31) with Eq. (5.36) for 1D systems by introducing damping terms to the energies $\hbar\omega_\mathrm{osc}$, E_i, and E_j: $\hbar\omega_\mathrm{osc} + i\Gamma_\mathrm{osc}$, $E_i + i\Gamma_i$, and $E_j + i\Gamma_j$. Then, the authors made the approximation $\Gamma_L = \Gamma_\mathrm{osc} = \Gamma_i = \Gamma_j$ and obtained

$$\Gamma_L = \frac{1}{\hbar^2}\sum_{ij}|A_{ij}|^2(f_i - f_j)\frac{3\Gamma_L}{(\omega_{ij} - \omega_\mathrm{osc})^2 + (3\Gamma_L)^2}, \tag{5.37}$$

where A_{ij} is given in Eq. (5.33) (with the replacement of 3D quantities by the corresponding 1D quantities). Here, they interpreted the width Δ in the 3D Landau damping as the relaxation of the elementary excitations in 1D systems. The Landau damping rate for a 1D system can then be estimated by iteratively solving Eq. (5.37). Alternatively, the damping rate can be estimated by plotting the right-hand side of Eq. (5.37) and computing for the point where it intersects with the line $\Gamma_L = \Gamma_L$.

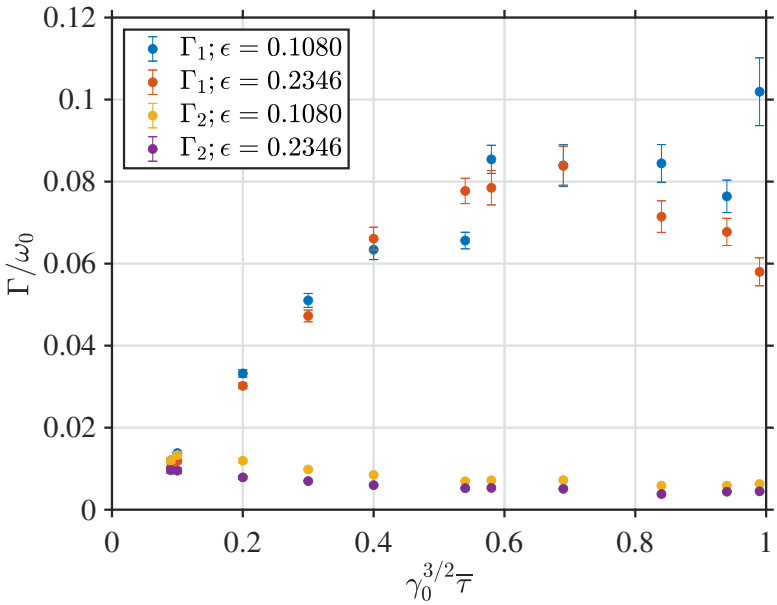

Figure 5.9: Computed damping rates Γ_1 and Γ_2 using the fitting equation Eq. (5.16). The error bars account for fitting error only, which indicates a 95% confidence interval. The component with higher breathing mode frequency has very small damping rates compared to the other one. The component with lower frequency is highly damped compared to the other one.

5.4.2 Damping rate from numerical simulations

We now look at the damping observed in our simulations of 1D Bose gases. In Fig. 5.9, we show the damping rates Γ_1 and Γ_2 associated with the components with the breathing mode frequencies ω_{B1} and ω_{B2} in Fig. 5.4, respectively, obtained using the fitting equation Eq. (5.16). Here, it can easily be seen that the two components of the quasicondensate have distinct damping rates, and the damping rates are independent of the quench strengths considered. The tail part (frequency ω_{B2} and damping rate Γ_2) has a much lower damping rate than the bulk part (frequency ω_{B1} and damping rate Γ_1). This very low damping of the tail part is consistent with our previous observation that the particles that comprise this component are highly energetic particles, and their kinetic energy dominates their interaction energy. Thus, the tail part behaves almost like an ideal gas with no damping.

The bulk part has an increasing damping rate as we go from the lowest considered $\gamma_0^{3/2}\overline{\tau}$ until we reach the value around $\gamma_0^{3/2}\overline{\tau} \approx 0.5$ where the damping rate starts to saturate around $\Gamma_1 \sim 0.8$. The increasing damping rate Γ_1 of the bulk part that we see here can be understood if we treat the tail part as a reservoir that damps the oscillation of the bulk part. We see the lowest damping rate of the bulk part at the lowest value of $\gamma_0^{3/2}\overline{\tau}$ considered here because the system is almost in the Thomas–Fermi regime. The presence of the tail is very minimal, as we can see in its relative power K in Fig. 5.6. As we increase the value of $\gamma_0^{3/2}\overline{\tau}$, the number of particles populating the bulk part decreases relative to the number in the tail part. From the perspective of the bulk part, the reservoir (the tail) is increasing in size, and the more the relative size of the bulk decreases, the faster the reservoir (the tail) can absorb energy from the oscillating bulk part. This then induces more damping of the oscillating bulk part.

At much higher values of $\gamma_0^{3/2}\overline{\tau}$, beyond $\gamma_0^{3/2}\overline{\tau} \approx 0.9$, the damping rate Γ_1 then starts to decline.

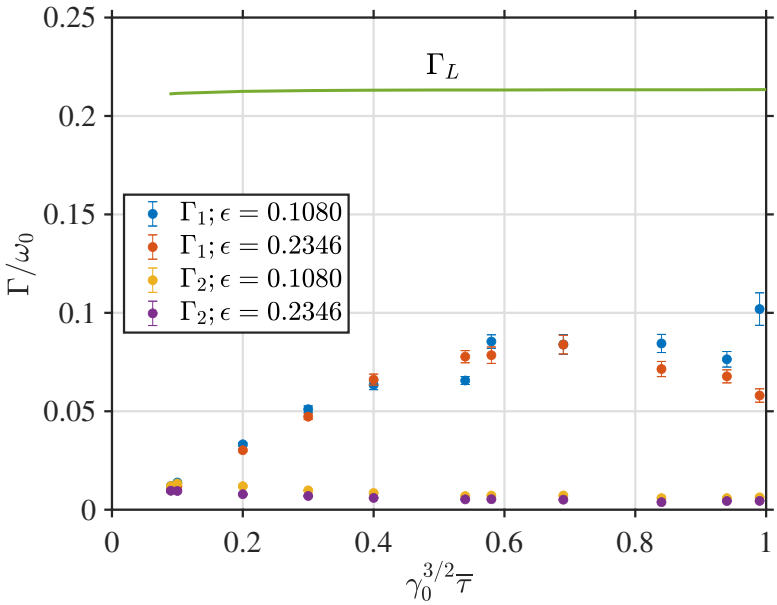

Figure 5.10: Damping rate Γ_L calculated from 1D Landau damping (Eq. (5.37)) compared to the damping rates obtained from SPGPE simulations (dots). The 1D Landau damping rate Γ_L is more than twice larger than the observed damping rates in our simulations.

This downward trend is to be expected as the system now crosses to the nearly ideal gas regime defined by $\gamma_0^{3/2}\overline{\tau} > 1$ (with either high temperature or very low particle density). That is, in this limit, the condensate and low-energy particles of the 1D Bose gas start becoming negligible (see Fig. 5.7), and the system becomes mostly composed of high-energy particles.

The breathing mode oscillations we observe in our simulations have a lifetime on the order of seconds, like those observed in the experiment done in Ref. [221]. However, the damping rates we observe in our numerical simulations are much lower than what Eq. (5.37) predicts for our system (see Fig. 5.10), at least twice as small. To understand this difference in the damping rates, we note that calculations of Landau damping conventionally assume that the thermal excitations are always in thermal equilibrium. However, this does not apply to our system because quenching the longitudinal trapping frequency also initiates the breathing oscillation of the tail part, which acts as the bath of thermal excitations in our system. In this case, the oscillating tail part may also drive the bulk part at its own resonant frequency and affect the damping rate, especially at values of $\gamma_0^{3/2}\overline{\tau}$ where the two mode frequencies are close to each other.

A possible way to explain the damping of breathing mode oscillations in a 1D quasicondensate is the increase of entropy in the system via diffusion. Recently, authors of Ref. [226] argued that thermalisation occurs in a trapped 1D Bose gas due to the entropy production brought by diffusion. Here, they used generalised hydrodynamics (GHD) theory [227, 228] and showed that the diffusion term in the GHD equation makes the dynamics of a trapped system irreversible due to diffusion spreading that redistributes quasiparticle momenta and increases the local thermodynamic entropy. Doing similar calculations for the breathing mode oscillations might give damping rates closer to the observed damping rates in our simulations.

5.5 Summary

In summary, we have studied the breathing oscillations of a 1D Bose gas after a quench of its longitudinal harmonic trap. We observe two breathing modes oscillating with two distinct frequencies, each with its own damping rate. The presence of two breathing modes is due to low-energy particles in the bulk of the system and high-energy particles in the tails of the Bose gas. Particles with low energy and high local chemical potential (bulk part) breathe with a frequency closer to the expected breathing frequency for a quasicondensate at zero temperature. On the other hand, particles with higher energies and low local chemical potential (tail part) breathe with a frequency closer to the breathing frequency expected for a noninteracting (ideal) gas. The calculated damping rate from Landau damping for 1D Bose gases is at least twice larger than the observed damping rates in our simulations. This could be the case because Landau damping assumes that thermal excitations are in thermal equilibrium. However, in our simulations, the high-energy particles in the tails of the Bose gas are also brought out of equilibrium after the quench of the longitudinal trap potential frequency. Instead of rapidly damping the oscillation of the bulk part, the tail part could also drive the bulk at its own breathing frequency, thus lowering the observed damping rate. A possible way of calculating the damping rate for breathing mode oscillations is applying the GHD theory to quenches of 1D quasicondensates .

Some results presented in the following chapter have been published in

1. [1] S.A. Simmons, **F.A. Bayocboc, Jr.**, J.C. Pillay, D. Colas, I.P. McCulloch, and K.V. Kheruntsyan, What is a quantum shock wave?, *Phys. Rev. Lett.* **125**, 180401 (2020).

Contributor	Statement of contribution	%
S.A. Simmons	writing of text	40
	proof-reading	25
	theoretical derivations	60
	numerical calculations	20
	preparation of figures	30
F.A. Bayocboc, Jr.	writing of text	10
	proof-reading	5
	numerical calculations	25
	preparation of figures	20
J.C. Pillay	writing of text	10
	proof-reading	10
	numerical calculations	25
	preparation of figures	10
D. Colas	writing of text	15
	proof-reading	10
	numerical calculations	25
	preparation of figures	30
I.P. McCulloch	proof-reading	20
	supervision, guidance	30
K.V. Kheruntsyan	writing of text	25
	proof-reading	30
	supervision, guidance	70
	theoretical derivations	40
	numerical calculations	5
	preparation of figures	10
	initial concept	100

Chapter 6

Role of thermal fluctuations and phase coherence in the propagation of shock waves in a one-dimensional quasicondensate

In this chapter, we study the formation and propagation of dispersive quantum shock waves in a one-dimensional Bose gas. Starting with a local perturbation on top of a uniform background density, the former is released and allowed to expand into the latter. The formation of oscillatory trains afterwards is a result of quantum mechanical self-interference. Using the stochastic projected Gross–Pitaevskii equation and the truncated Wigner method, we study the effects of thermal and quantum fluctuation in the propagation of dispersive shock waves. We find that the amplitude of the oscillatory train decreases as the phase coherence of the Bose gas is reduced. Furthermore, thermal and quantum fluctuations can significantly wash out the amplitude of these oscillatory trains.

6.1 Introduction

The advances in the field of ultracold atomic gases [13, 14] have opened unique possibilities for controlled studies of far-from-equilibrium phenomena due to the high level of experimental control over the system parameters and dynamics. An example of such a far-from-equilibrium scenario that has been attracting attention in recent years is the propagation of dispersive shock waves in superfluids, such as dilute Bose–Einstein condensates (BECs) [229–238]. Shock waves occur when the wave front propagates faster than the local speed of sound in a medium. This results in an abrupt, nearly discontinuous change in pressure, temperature and density of the medium. On the one hand, dispersive shock waves in fluid dynamics are characterised by an expanding collection of large amplitude oscillatory waves in a dissipationless medium. Dissipative shock waves, on the other hand, take the form of a travelling wave with a smooth but steep change in the density [229, 239, 240]. The effects of dispersion or dissipation, in either case, prevent the unphysical hydrodynamic gradient catastrophe by means of energy transfer from large to small length scales or through the release of the excess energy

via damping.

While dissipative shock waves involve irreversible processes that can be well described within classical hydrodynamics, dispersive shock waves in BECs require quantum or superfluid hydrodynamics for their description. Quantum hydrodynamics for superfluids can be derived from and is equivalent to the mean-field description of weakly interacting Bose–Einstein condensates via the Gross–Pitaevskii equation (GPE) [6, 54, 58]. The effect of dispersion is represented here by the so-called quantum pressure term; hence the use of an alternative term for dispersive shock waves – quantum shock waves [230]. In this case, the nonlinear inter-particle interaction present in the GPE has been used to interpret dispersive shock waves as a train of grey solitons [234, 241]. However, in Ref. [1], we have shown that qualitatively similar density modulations can form in a noninteracting case that does not support solitons. Here, we have argued that the mechanism behind the formation of quantum shock wave trains in a 1D Bose gas is quantum interference, wherein the local perturbation self-interferes with its own background upon expanding into it.

In this chapter, we consider the effects of thermal and quantum fluctuations on the behaviour of quantum shock waves in a quasicondensate using the stochastic projected Gross–Pitaevskii equation and the truncated Wigner approach.

6.2 Dispersive shock waves

In Ref. [1], we showed that the mechanism of formation of dispersive shock wave trains in a one-dimensional Bose gas is quantum interference: the local perturbation self-interferes with its own background upon expanding into it. Here, the local perturbation is a Gaussian bump with width σ and amplitude β above a (real) constant background. Its initial wavefunction is given by

$$\Psi(x,0) = \psi_{\rm bg}(1 + \beta e^{-x^2/2\sigma^2}), \tag{6.1}$$

where $\psi_{\rm bg}$ is a real constant background. This initial wavefunction is then released in a uniform potential of length L. The constant background $\psi_{\rm bg}$ fixes the normalisation of the wavefunction $\Psi(x,0)$ into the total number of particles $N = \int \mathrm{d}x |\Psi(x,0)|^2$ in the system. In terms of the number of particles in the background $N_{\rm bg} = |\psi_{\rm bg}|^2 L$, the total number of particles in the system is given by

$$N = N_{\rm bg}\left\{1 + \frac{\sqrt{\pi}\,\beta\sigma}{L} + \left[\beta \mathrm{erf}\left(\frac{L}{2\sigma}\right) + 2\sqrt{2}\,\mathrm{erf}\left(\frac{L}{2\sqrt{2}\,\sigma}\right)\right]\right\}, \tag{6.2}$$

where $\mathrm{erf}(\cdot)$ is the error function. For an ideal gas, the wavefunction in Eq. (6.1) evolves according to the time-dependent Schrödinger equation for a free particle,

$$i\hbar\frac{\partial}{\partial t}\Psi(x,t) = -\frac{\hbar^2}{2m}\frac{\partial^2}{\partial x^2}\Psi(x,t), \tag{6.3}$$

whose solution can be written as

$$\Psi(x,t) = \psi_{\rm bg}\left[1 + \frac{\beta\sigma}{\sqrt{\sigma^2 + i\hbar t/m}} e^{-x^2/2(\sigma^2 + i\hbar t/m)}\right]. \tag{6.4}$$

To obtain the characteristics of this wavefunction, the solution can be rewritten as

$$\Psi(x,t) = \psi_{\rm bg}\left[1 + B(x,t)e^{i\phi(x,t)}\right], \tag{6.5}$$

so that the density of the perturbation acquires a textbook form of quantum interference,

$$\rho(x,t) = \psi_{\rm bg}^2\left[1 + B(x,t)^2 + 2B(x,t)\cos\phi(x,t)\right], \tag{6.6}$$

with the amplitude

$$B(x,t) = \frac{\beta\sigma}{\left(\sigma^4 + \hbar^2t^2/m^2\right)^{1/4}} e^{-x^2\sigma^2/2\left(\sigma^4+\hbar^2t^2/m^2\right)} \tag{6.7}$$

and phase

$$\phi(x,t) = \frac{\hbar t x^2}{2m\left(\sigma^4 + \hbar^2t^2/m^2\right)} - \frac{1}{2}\arctan\left(\frac{\hbar^2t^2}{m^2\sigma^4}\right). \tag{6.8}$$

From these, the characteristic period of oscillation in the bulk of the shock train is approximately 2σ, while the amplitude scales as $\propto \beta\sigma/\sqrt{t}$.

Let us now consider an interacting Bose gas with repulsive pairwise delta function interactions. In the weakly interacting regime, a uniform 1D Bose gas described by the Lieb–Liniger model [46, 47] can be characterised by a dimensionless interaction parameter given by

$$\gamma = \frac{mg}{\hbar^2\rho}, \tag{6.9}$$

where ρ is the density of the gas, m is the mass of a particle, and g is the 1D inter-particle interaction strength. For a nonuniform gas with a local density bump, we have instead a local interaction parameter

$$\gamma(x) = \frac{mg}{\hbar^2\rho(x)}. \tag{6.10}$$

Thus, one can instead use the background density $\rho_{\rm bg}$ to define a dimensionless interaction parameter

$$\gamma_{\rm bg} = \frac{mg}{\hbar^2\rho_{\rm bg}}, \tag{6.11}$$

that can then serve as a global interaction parameter to characterise the initial state of the system. The weakly interacting regime of the Lieb–Liniger gas corresponds to $\gamma_{\rm bg} \ll 1$; hence any point within the Gaussian bump has $\gamma(x) \ll 1$. The zero-temperature dynamics of the system can be approximated by the GPE:

$$i\hbar\frac{\partial}{\partial t}\Psi(x,t) = \left(-\frac{\hbar^2}{2m}\frac{\partial^2}{\partial x^2} + g|\Psi(x,t)|^2\right)\Psi(x,t). \tag{6.12}$$

In Fig. 6.1, we plot the initial density profile and the dispersive shock waves that formed at some final time t for two systems with $N = 50$ and $N = 2000$ particles (with corresponding interaction parameter $\gamma_{\rm bg} = 0.1$ and $\gamma_{\rm bg} = 0.01$, respectively). In the weakly interacting regime, the interaction between particles introduces a new length-scale that is the healing length of the background density given by

$$l_h = \frac{\hbar}{mg\rho_{\rm bg}}. \tag{6.13}$$

The healing length decreases with increasing interactions, and as soon as it becomes the shortest length-scale in the problem, it overtakes the role of the width σ in determining the characteristic period

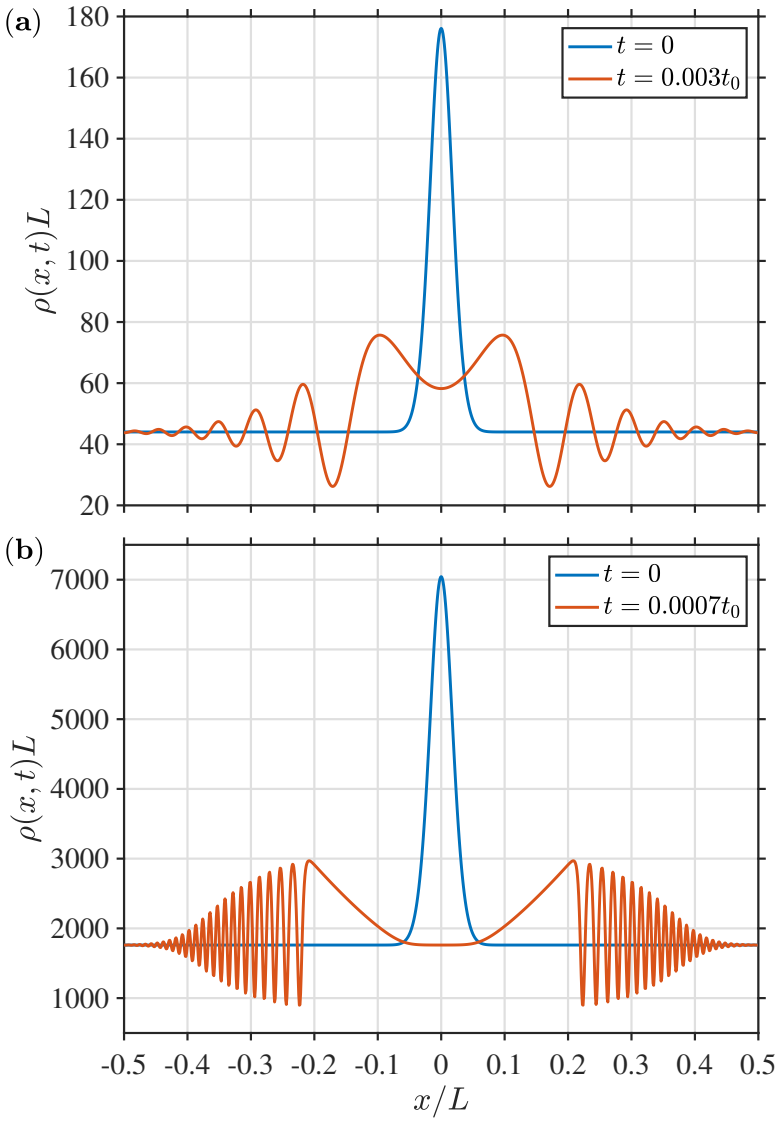

Figure 6.1: Shock waves in a weakly interacting 1D quasicondensate at zero temperature from GPE simulations. Shown are the initial and final-time density profiles for two different numbers of particles with $\beta = 1$ and $\sigma/L = 0.02$. (a) $N = 50$ and $\gamma_{\rm bg} = 0.1$ with corresponding healing length $l_{\rm h}/L =\simeq 0.072$. (b) $N = 2000$ and $\gamma_{\rm bg} = 0.01$ with corresponding healing length $l_{\rm h}/L =\simeq 0.0057$. $t_0 = mL^2/\hbar$ is the dimensionless time scale of the system.

of interference oscillations. For example, in Fig. 6.1, both initial bumps have width $\sigma = 0.02L$. In the $N = 50$ case where the healing length is $l_h = 0.072L > \sigma$, the period of oscillation is approximately 2σ. In the $N = 2000$ case where the healing length is $l_h = 0.0057L < \sigma$, the period of oscillation is now approximately $2l_h$.

To show the origin of dispersion in the GPE, we reformulate it in terms of superfluid hydrodynamics via Madelung's transformation where we represent the complex mean-field amplitude as

$$\Psi(x,t) = \sqrt{\rho(x,t)}\, e^{i\phi(x,t)}, \tag{6.14}$$

where $\rho(x,t)$ and $\phi(x,t)$ are the density and phase, respectively, of the superfluid. The transformation

yields the coupled hydrodynamic equations

$$\frac{\partial}{\partial t}\rho(x,t) = -\frac{\partial}{\partial x}\left[\rho(x,t)v(x,t)\right], \tag{6.15}$$

$$\frac{\partial}{\partial t}v(x,t) = -\frac{\partial}{\partial x}\left[\frac{1}{2}v^2(x,t) + \frac{g}{m}\rho(x,t) - \frac{\hbar^2}{2m^2}\frac{1}{\sqrt{\rho(x,t)}}\frac{\partial^2}{\partial x^2}\sqrt{\rho(x,t)}\right], \tag{6.16}$$

for the density and the velocity field

$$v(x,t) = \frac{\hbar}{m}\frac{\partial}{\partial x}\phi(x,t). \tag{6.17}$$

The last term in Eq. (6.16) is referred to as the quantum pressure term. It represents the dispersion in the system and governs the formation of the oscillatory wave-train in the hydrodynamic approach. This same quantum pressure term arises in the hydrodynamic-like formulation of the single-particle Schrödinger equation after applying Madelung's transformation to the quantum mechanical wavefunction. This means that for a system with noninteracting particles, the quantum pressure term is responsible for producing dispersive shock wave oscillations. Thus, the interaction is not necessary for the formation of the oscillatory shock wave train. As such, these oscillations cannot generally be interpreted as a train of grey solitons [234, 241] that do require the interactions to balance the wave dispersion.

In the following sections, we will consider the effect of both quantum and thermal fluctuations on the propagation of shock waves.

6.3 The effects of thermal fluctuations

We consider the finite temperature quasi-condensate regime of the 1D Bose gas [26, 103, 104, 110, 174, 177] to understand the effect of thermal fluctuations on dispersive shock waves. This regime still corresponds to weak interactions, $\gamma_{bg} \ll 1$, but we focus on temperatures of the initial thermal state lying within $\gamma_{\rm bg} \lesssim \overline{\mathcal{T}} \lesssim \sqrt{\gamma_{\rm bg}}$ [103, 104], where $\overline{\mathcal{T}}$ is the dimensionless temperature given by

$$\overline{\mathcal{T}} = \frac{T}{T_d} = \frac{2mk_{\rm B}}{\hbar^2\rho_{\rm bg}^2}T, \tag{6.18}$$

with T_d being the temperature of quantum degeneracy of the gas at density $\rho_{\rm bg}$, and $k_{\rm B}$ is the Boltzmann constant. In this range of temperatures, which are most readily accessible in ultracold atom experiments [107, 110, 111], the density-density correlations of the gas are dominated by thermal rather than vacuum fluctuations [103, 104]. Accordingly, the shock wave dynamics can be simulated using c-field techniques [123, 138, 242] that involve preparation of the initial thermal equilibrium state using the stochastic projected Gross–Pitaevskii equation (SPGPE) and subsequent real-time evolution according to the GPE.

To generate the initial condition of our system, we numerically solve the SPGPE given by

$$\mathrm{d}\Psi_{\mathbf{C}}(x,t) = \mathcal{P}^{(\mathbf{C})}\left\{-\frac{i}{\hbar}\mathcal{L}_{\mathbf{C}}\Psi_{\mathbf{C}}(x,t)\,\mathrm{d}t + \frac{\Gamma}{k_{\rm B}T}(\mu - \mathcal{L}_{\mathbf{C}})\Psi_{\mathbf{C}}(x,t)\,\mathrm{d}t + dW_{\Gamma}(x,t)\right\}. \tag{6.19}$$

Here, the projection operator $\mathcal{P}^{(\mathbf{C})}\{\cdot\}$ sets up the high-energy cutoff for the classical region, Γ is the growth rate, T is the temperature of the reservoir to which the system is coupled, μ is the chemical

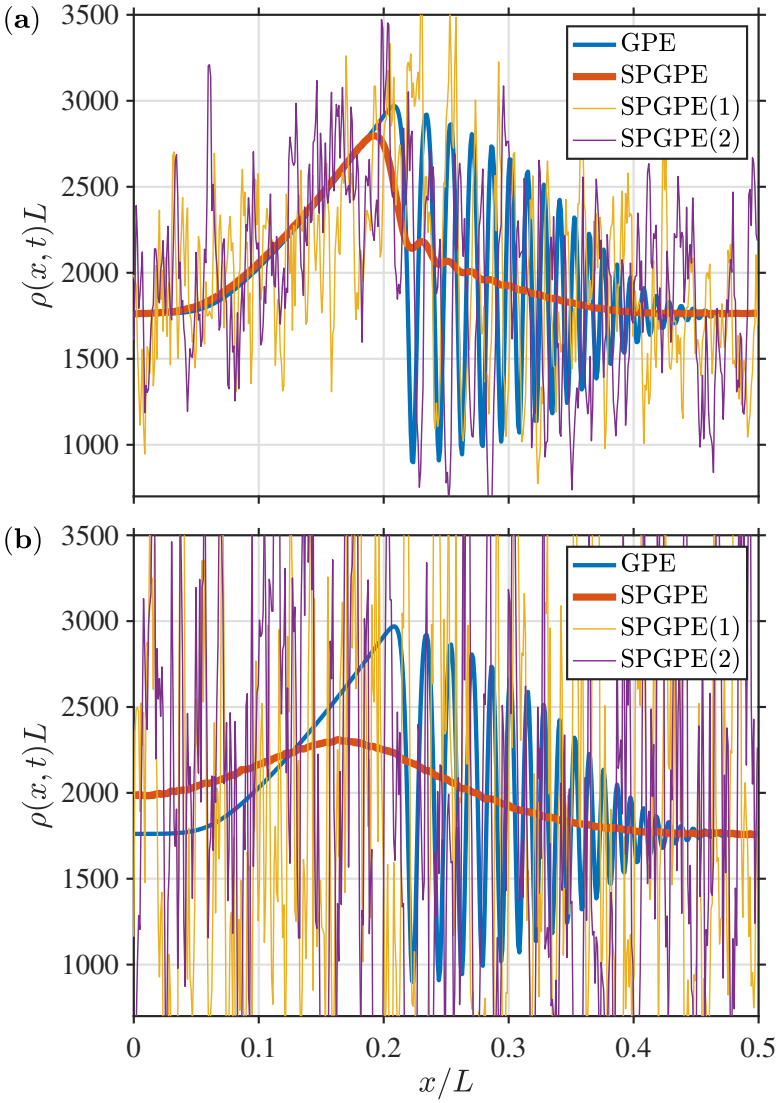

Figure 6.2: Shock waves in a finite-temperature quasicondensate with $N = 2000$ particles from SPGPE simulations (thick red lines). Shown are the final-time ($t = 0.0007t_0$) density distributions for $x > 0$ and two different initial dimensionless temperatures: (a) $\overline{\mathcal{T}} = 0.01$; and (b) $\overline{\mathcal{T}} = 0.1$. Other parameters are as in Fig. 6.1 (c); the GPE results are shown here as blue lines for comparison. The dimensionless thermal phase coherence length here can be expressed as $l_T/L = 2/(\overline{\mathcal{T}} N_{\rm bg})$, giving: (a) $l_T/L \simeq 0.1$; (b) $l_T/L \simeq 0.01$. The SPGPE mean densities are the averages over 100,000 stochastic trajectories, whereas the thin lines show two sample trajectories. $t_0 = mL^2/\hbar$ is the dimensionless time scale of the system.

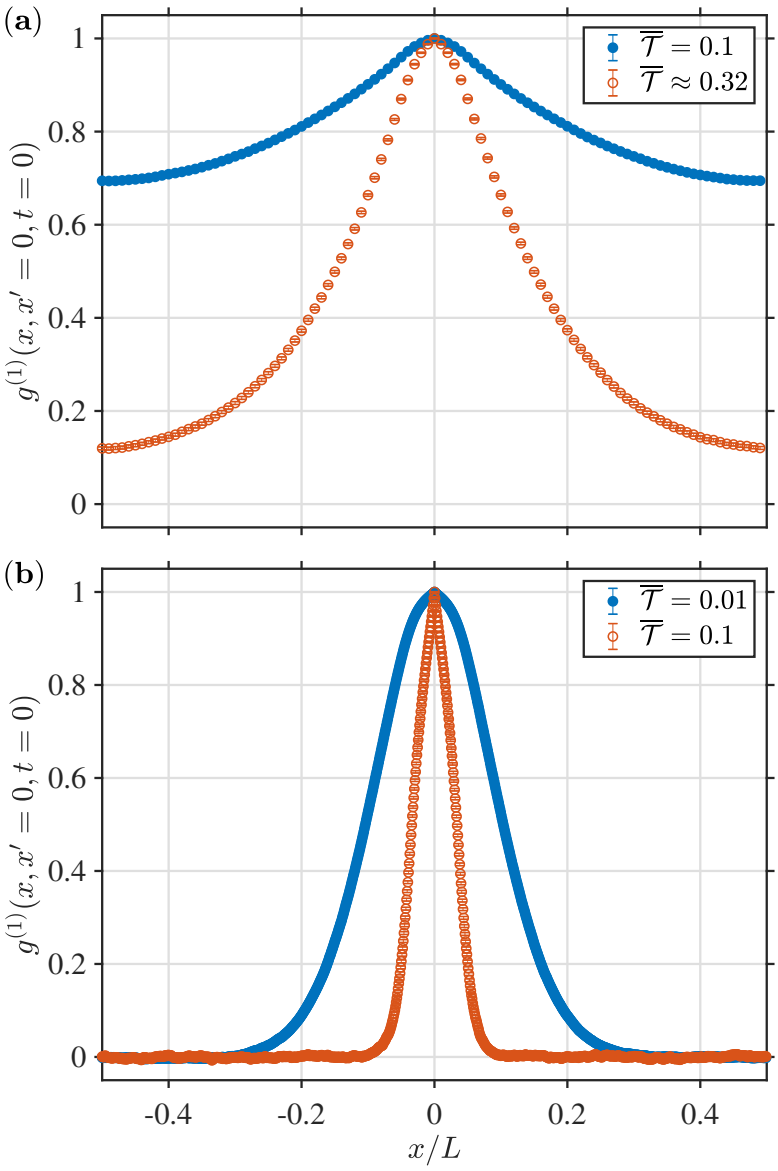

Figure 6.3: Normalised first-order correlation function $g^{(1)}(x, x' = 0, t = 0)$ of the bump on the uniform background. Shown are $g^{(1)}(x, x' = 0, t = 0)$ for (a) the $N = 50$ case for both $\overline{\mathcal{T}} = 0.1$ and $\overline{\mathcal{T}} \approx 0.32$, and for (b) the $N = 2000$ case for both $\overline{\mathcal{T}} = 0.01$ and $\overline{\mathcal{T}} = 0.1$. The dimensionless thermal phase coherence lengths in (a) are $l_T/L \simeq 0.45$ for $\overline{\mathcal{T}} = 0.1$ and $l_T/L \simeq 0.15$ for $\overline{\mathcal{T}} \approx 0.32$. In (b), the dimensionless thermal phase coherence lengths are $l_T/L \simeq 0.1$ for $\overline{\mathcal{T}} = 0.01$ and $l_T/L \simeq 0.01$ for $\overline{\mathcal{T}} = 0.1$. The correlation functions $g^{(1)}(x, x' = 0, t = 0)$ plotted above are the averages over 100,000 stochastic trajectories.

potential that controls the number of particles in the classical region, and $\mathcal{L}_{\mathbf{C}}$ is the Gross–Pitaevskii operator given by

$$\mathcal{L}_{\mathbf{C}}\Psi_{\mathbf{C}}(x,t) = \left[-\frac{\hbar^2}{2m}\frac{\partial^2}{\partial x^2} + V(x) + g|\Psi_{\mathbf{C}}(x,t)|^2\right]\Psi_{\mathbf{C}}(x,t), \tag{6.20}$$

where $V(x)$ is the external potential trap. The last term $dW_\Gamma(x,t)$ in Eq. (6.19) is the associated complex white noise satisfying the following nonzero correlation:

$$\langle dW_\Gamma^*(x,t)dW_\Gamma(x',t)\rangle_{\text{stoch}} = 2\Gamma\delta(x-x')\mathrm{d}t. \tag{6.21}$$

To generate the desired intial Gaussian bump at finite temperature, we use the external potential trap given by [1]

$$V(x) = \frac{\hbar^2}{2m}\frac{\beta^2}{2\sigma^4}\frac{(x^2-\sigma^2)}{e^{x^2/2\sigma^2}+\beta} - g|\Psi(x,0)|^2, \tag{6.22}$$

with the zero-temperature $\Psi(x,0)$ given in Eq. (6.1). The finite-temperature equilibrium temperature configurations are sampled by integrating the SPGPE for sufficiently long time that the memory of the initial trial state (*e.g.* a square wavefunction of unit height and length) is lost.

Once the SPGPE fully evolved to its final thermal equilibrium configuration, we remove the trapping potential and simulate the post-quench dynamics by evolving each stochastic realisation of the c-field in real time according to the GPE:

$$i\hbar\frac{\partial}{\partial t}\Psi_{\mathbf{C}}(x,t) = \left(-\frac{\hbar^2}{2m}\frac{\partial^2}{\partial x^2} + g|\Psi_{\mathbf{C}}(x,t)|^2\right)\Psi_{\mathbf{C}}(x,t). \tag{6.23}$$

Examples of c-field simulations are shown in Fig. 6.2 for the same parameters as in the $N = 2000$ case of Fig. 6.1, but for two nonzero temperatures, $\overline{\mathcal{T}} = 0.01$ and $\overline{\mathcal{T}} = 0.1$. Here, the length $L = 1$ and the growth rate $\hbar\Gamma = 0.01k_{\mathrm{B}}T$ are used in the SPGPE calculations. As expected, the interference contrast is significantly reduced (compared to GPE results) due to thermal fluctuations and the resulting loss of phase coherence. Indeed, for a 1D Bose gas in the quasicondensate regime with uniform density ρ_{bg}, the loss of phase coherence due to thermal fluctuations can be measured by calculating the normalised first-order correlation function

$$g^{(1)}(x,x') = \frac{\langle\Psi_{\mathbf{C}}^*(x)\Psi_{\mathbf{C}}(x')\rangle_{\text{stoch}}}{\sqrt{\rho(x)\rho(x')}}. \tag{6.24}$$

Within the Luttinger liquid approximation, the normalised first-order correlation function computed from the centre of the box ($x' = 0$) can be shown to decay exponentially as [32, 70]

$$g^{(1)}(x) = e^{-|x|/2l_T}, \tag{6.25}$$

where

$$l_T = \frac{\hbar^2\rho_{\mathrm{bg}}}{mk_{\mathrm{B}}T} \tag{6.26}$$

is the thermal phase coherence length of the background density. The thermal phase coherence length l_T describes the length-scale above which randomisation of the phase greatly reduces the phase coherence within the quasicondensate. In Fig. 6.3, we plot the corresponding $g^{(1)}(x,x'=0)$ of the

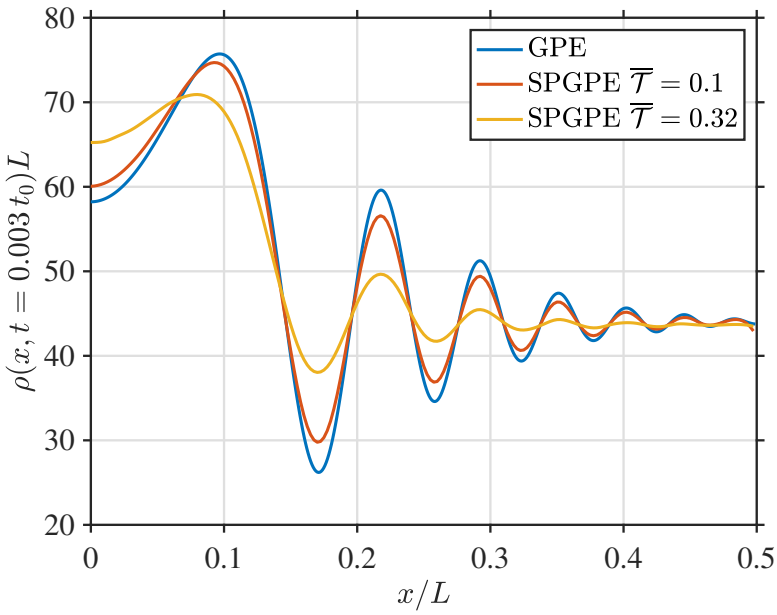

Figure 6.4: Shock waves in a finite-temperature quasicondensate with $N = 50$ particles from SPGPE simulations. Shown are the final-time ($t = 0.003t_0$) density distributions for $x > 0$ and two different initial dimensionless temperatures $\overline{\mathcal{T}} = 0.1$ and $\overline{\mathcal{T}} \approx 0.32$. Other parameters are as in Fig. 6.1; the GPE results are shown here (blue line) for comparison. The dimensionless thermal phase coherence length here can be expressed as $l_T/L = 2/(\overline{\mathcal{T}} N_{\rm bg})$, giving: (a) $l_T/L \simeq 0.45$; (b) $l_T/L \simeq 0.15$. The SPGPE mean densities are the averages over 100,000 stochastic trajectories. $t_0 = mL^2/\hbar$ is the dimensionless time scale of the system.

initial configuration of the $N = 50$ and $N = 2000$ particle cases. We see here that there is a significant loss of coherence for the $N = 2000$ case that leads to the reduction of interference contrast in Fig. 6.2. However, there is still significant phase coherence within the quasicondensate for the $N = 50$ case, especially for temperature $\overline{\mathcal{T}} = 0.1$, and we see less reduction of interference contrast in Fig. 6.4.

Given the thermal phase coherence length of the background density, one can expect that the self-interfering shock wave train would lose its contrast when l_T becomes on the order of or smaller than the width of the bump σ, with oscillations eventually disappearing at sufficiently high temperatures. This is indeed what we see in Fig. 6.2. However, the interference contrast in Fig. 6.2 (a) is essentially lost at temperatures for which l_T is still larger than σ; this can be explained by the shot-to-shot fluctuations in the position of interference fringes due to the same thermal fluctuations. Indeed, even though these individual trajectories show high-contrast interference fringes (albeit with stochastic noise also present), the overall ensemble average over thousands of SPGPE realisations shows much lower interference contrast, as can be seen from samples of individual stochastic SPGPE trajectories (shown as thin lines). This observation is consistent with the interpretation of the individual SPGPE trajectories representing individual experimental runs [123], whereas the mean density corresponds to the ensemble average over many runs.

It is also interesting to consider the normalised second-order correlation function given by

$$g^{(2)}(x, x') = \frac{G^{(2)}(x, x')}{\rho(x)\rho(x')} = \frac{\langle \Psi^*_{\mathbf{C}}(x)\Psi^*_{\mathbf{C}}(x')\Psi_{\mathbf{C}}(x')\Psi_{\mathbf{C}}(x)\rangle_{\rm stoch}}{\langle \Psi^*_{\mathbf{C}}(x)\Psi_{\mathbf{C}}(x)\rangle_{\rm stoch}\langle \Psi^*_{\mathbf{C}}(x')\Psi_{\mathbf{C}}(x')\rangle_{\rm stoch}}. \tag{6.27}$$

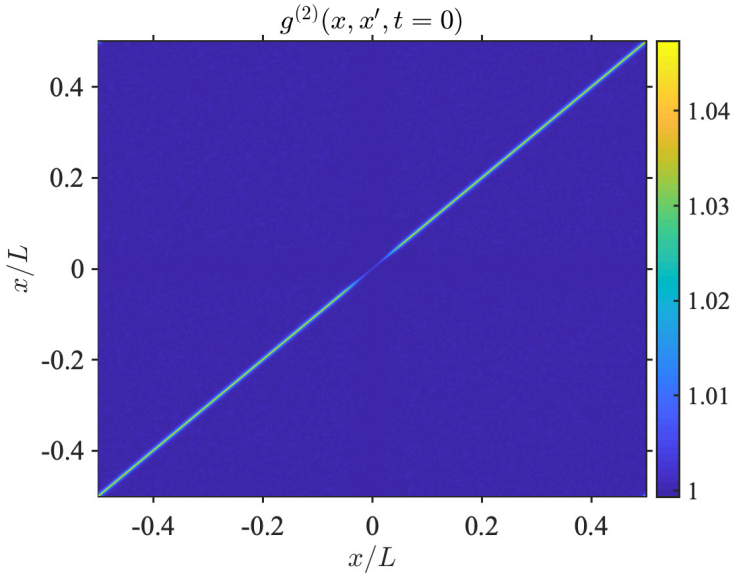

Figure 6.5: Normalised second-order correlation function $g^{(2)}(x, x', t = 0)$ of a Gaussian density bump on top of a uniform background density at finite temperature. The parameters used here are the same as the parameters used in Fig. 6.2 (a). For two points $x \neq x'$, $g^{(2)}(x, x')$ approaches its coherent value of unity, whereas thermal fluctuations yield a local correlation $g^{(2)}(x, x)$ with an intermediate value between unity and the noninteracting limit where $g^{(2)}(x, x) \to 2$.

For weakly interacting 1D Bose gases at zero temperature, the second-order correlation function has the uncorrelated value $g^{(2)}(x, x') = 1$. In contrast, for finite temperature scenarios where thermal fluctuations are present, the local ($x' = x$) second-order correlation function approaches its non-interacting Bose gas value of $g^{(2)}(x, x) \to 2$ [103, 104]. As an example, we plot the second-order correlation function for $N = 2000$ particles with $\gamma_{bg} = 0.01$ at temperature $\overline{\mathcal{T}} = 0.01$ (Fig. 6.2 (a)) in Fig. 6.5. As we can see, the off-diagonal correlations $g^{(2)}(x, x' \neq x)$ are uncorrelated due to thermal fluctuations. On the other hand, the enhanced fluctuations due to temperature give the local correlations $g^{(2)}(x, x)$ intermediate values between the coherent limit $g^{(2)}(x, x) = 1$ and the noninteracting limit $g^{(2)}(x, x) = 2$. In Fig. 6.6, we plot the local second-order correlation function for both the $N = 50$ and $N = 2000$ cases. Here, we see that $g^{(2)}(x, x)$ at points where the gas is uniform are comparable to the analytical predictions of Refs. [103, 104] for temperatures in the limit $\gamma_{\rm bg} \ll \overline{\mathcal{T}} \ll \sqrt{\gamma_{\rm bg}}$:

$$g^{(2)}(x, x) = 1 + \frac{\overline{\mathcal{T}}}{2\sqrt{\gamma_{\rm bg}}}. \tag{6.28}$$

The result from SPGPE is indeed very close to the analytical result, especially at low temperatures.

6.4 The effects of vacuum fluctuations

We use the truncated Wigner approach to study the effects of vacuum fluctuations on the shock wave interference contrast in the weakly interacting regime at $T = 0$ temperature. In this method, the quantum fluctuations are represented in phase space via stochastic distributions of c-field trajectories. Physical observables can be computed by taking ensemble averages over many trajectories. The truncated

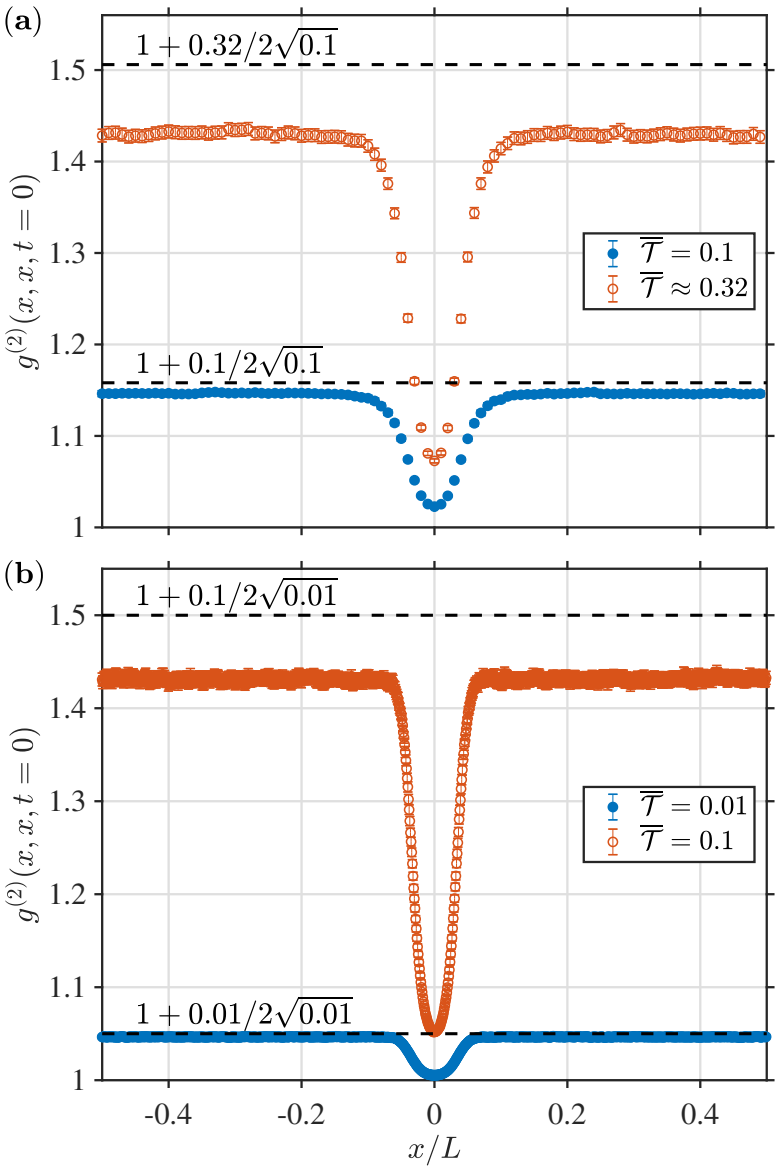

Figure 6.6: Local second-order correlation function $g^{(2)}(x, x' = x, t = 0)$ of a Gaussian density bump on top of a uniform background density at finite temperature. The parameters used here are (a) $N = 50$ for both $\overline{\mathcal{T}} = 0.1$ and $\overline{\mathcal{T}} \approx 0.32$, and (b) $N = 2000$ for both $\overline{\mathcal{T}} = 0.01$ and $\overline{\mathcal{T}} = 0.1$. Thermal fluctuations yield a local correlation with an intermediate value between unity and the noninteracting limit where $g^{(2)}(x, x) \to 2$.

Wigner approach is an approximate phase-space method where the third- and higher-order derivative terms in the evolution equation for the Wigner quasiprobability distribution function are ignored (truncated). Such truncation renders the evolution equation as a true Fokker–Planck equation that can equivalently be formulated in terms of stochastic differential equations for complex c-fields. For the Lieb–Liniger Hamiltonian considered here, with s-wave scattering interactions, these differential equations have the same form as the standard time-dependent GPE. However, the quantum effects are incorporated via noise added to the initial state of the system, which is then sampled stochastically, with each realisation evolving according to the GPE. In this work, we consider zero-temperature initial ground states with vacuum excitations in the Bogoliubov theory. In this case, each realisation of the stochastic Wigner field $\psi_W(x,0)$ is initialised as [123]

$$\psi_W(x,0) = \alpha_0\psi_0(x,0) + \sum_{j=1}^{M_{\mathrm{B}}-1}\left[\alpha_j u_j(x) + \alpha_j^* v_j^*(x)\right] \tag{6.29}$$

where $\psi_0(x,0)$ is the condensate mode wavefunction normalised to unity, with associated complex Gaussian noise α_0 with the following properties:

$$\langle\alpha_0\rangle = \sqrt{N_0}\ , \tag{6.30}$$

$$\langle\alpha_0^2\rangle = N_0, \tag{6.31}$$

$$\langle\alpha_0^*\alpha_0\rangle = N_0 + \frac{1}{2}, \tag{6.32}$$

where N_0 is the number of condensate particles. The functions $u_j(x)$ and $v_j(x)$ are the amplitudes of the j-th Bogoliubov modes obtained by solving the Bogoliubov–de Gennes equations for the initial state of the Gaussian bump, given by

$$\left(-\frac{\hbar^2}{2m}\frac{\partial^2}{\partial x^2} + V(x) + 2g|\Psi_0(x,0)|^2 - \mu\right)u_j(x) + g\Psi_0^2(x,0)v_j(x) = \epsilon_j u_j(x), \tag{6.33}$$

$$\left(-\frac{\hbar^2}{2m}\frac{\partial^2}{\partial x^2} + V(x) + 2g|\Psi_0(x,0)|^2 - \mu\right)v_j(x) + g\left[\Psi_0^*(x,0)\right]^2 u_j(x) = -\epsilon_j v_j(x), \tag{6.34}$$

where $\Psi_0(x,0) = \sqrt{N_0}\ \psi_0(x,0)$ and $V(x)$ is the potential trap given in Eq. (6.22). The associated complex Gaussian noises α_j associated with the Bogoliubov modes has the following mean and correlations:

$$\langle\alpha_j\rangle_{\mathrm{stoch}} = \left\langle\alpha_j^2\right\rangle_{\mathrm{stoch}} = \left\langle(\alpha_j^*)^2\right\rangle_{\mathrm{stoch}} = 0, \tag{6.35}$$

$$\langle\alpha_j^*\alpha_k\rangle_{\mathrm{stoch}} = \frac{1}{2}\delta_{jk}. \tag{6.36}$$

The noise correlations in Eq. (6.36) are the zero-temperature limit of the more general expression

$$\langle\alpha_j^*\alpha_k\rangle_{\mathrm{stoch}} = \left(n_j + \frac{1}{2}\right)\delta_{jk}, \tag{6.37}$$

where

$$n_j = \frac{1}{e^{\epsilon_j/k_{\mathrm{B}}T} - 1} \tag{6.38}$$

are the usual Bose occupation numbers of Bogoliubov modes with energies ϵ_j that vanish at $T = 0$ temperature.

Because even at $T = 0$ temperature we have noncondensate particles due to quantum fluctuations, the condensate complex amplitude $\Psi_0(x, 0)$ is normalised to N_0 such that the total number of particles

$$N = N_0 + N_{\rm nc}, \tag{6.39}$$

is the same as in the pure mean-field approach to which the truncated Wigner results are compared. Here,

$$N_{\rm nc} = \int {\rm d}x \sum_{j=1}^{M_B-1} |v_j(x)|^2, \tag{6.40}$$

is the number of noncondensate particles in the Bogoliubov modes at zero temperature.

We recall that in the Wigner formalism, the averages correspond to expectation values of symmetrically ordered operator products. Thus, the real space density $\rho(x, t)$ is calculated as an average over many stochastic Wigner trajectories using

$$\rho(x, t) = \langle \psi_W^*(x, t)\psi_W(x, t)\rangle_{\rm stoch} - \frac{1}{2}\delta_c(x, x), \tag{6.41}$$

where

$$\frac{1}{2}\int_{-L/2}^{L/2} \delta_c(x, x){\rm d}x = \frac{1}{2}M_B \tag{6.42}$$

represents the half quantum per Bogoliubov mode vacuum noise that is included in the Wigner formalism. On a computational grid of spacing $\Delta x = L/N_{\rm grid}$, the projected delta function $\delta_c(x, x')$ is given by

$$\delta_c(x, x') = \frac{M_B}{N_{\rm grid}\Delta x}\delta_{x,x'}, \tag{6.43}$$

where $N_{\rm grid}$ is the number of grid points, and $\delta_{x,x'}$ is the Kronecker delta function.

In Fig. 6.7, we plot the densities obtained from the truncated Winger approximation and compare them with the densities from mean-field GPE simulations. Here, the length $L = 1$ is used in the TWA calculations. It can be noticed, especially for the $N = 50$ particle case, that the initial density from the Wigner simulations deviates from the mean-field density. In the Wigner simulation, we have the density of noncondensate particles on top of condensate density, whereas we only have the density of the condensate in the mean-field GPE simulation. In Fig. 6.8, we plot the normalised first-order correlation function for the initial state of the $N = 50$ and $N = 2000$ cases. With still-high phase coherence (estimated from the normalised first-order correlation function) throughout the whole length of the box, we expect that there will not be a significant reduction in the interference contrast even with quantum fluctuations. This is indeed the case for $N = 50$ and $\gamma_{bg} = 0.1$ (Fig. 6.7 (a)) – the result from truncated Wigner simulations is very close to the mean-field GPE results. In this regime of very weak interactions, the quantum fluctuations have a negligible effect on the mean density and the interference contrast. However, for $N = 2000$ and $\gamma_{bg} = 0.01$ (Fig. 6.7 (b)), where the interactions are stronger, and the period of shock wave oscillations is determined by the healing length $l_{\rm h}$ instead of the Gaussian width σ, we do not observe the same behaviour of the interference contrast. Here, the quantum fluctuations

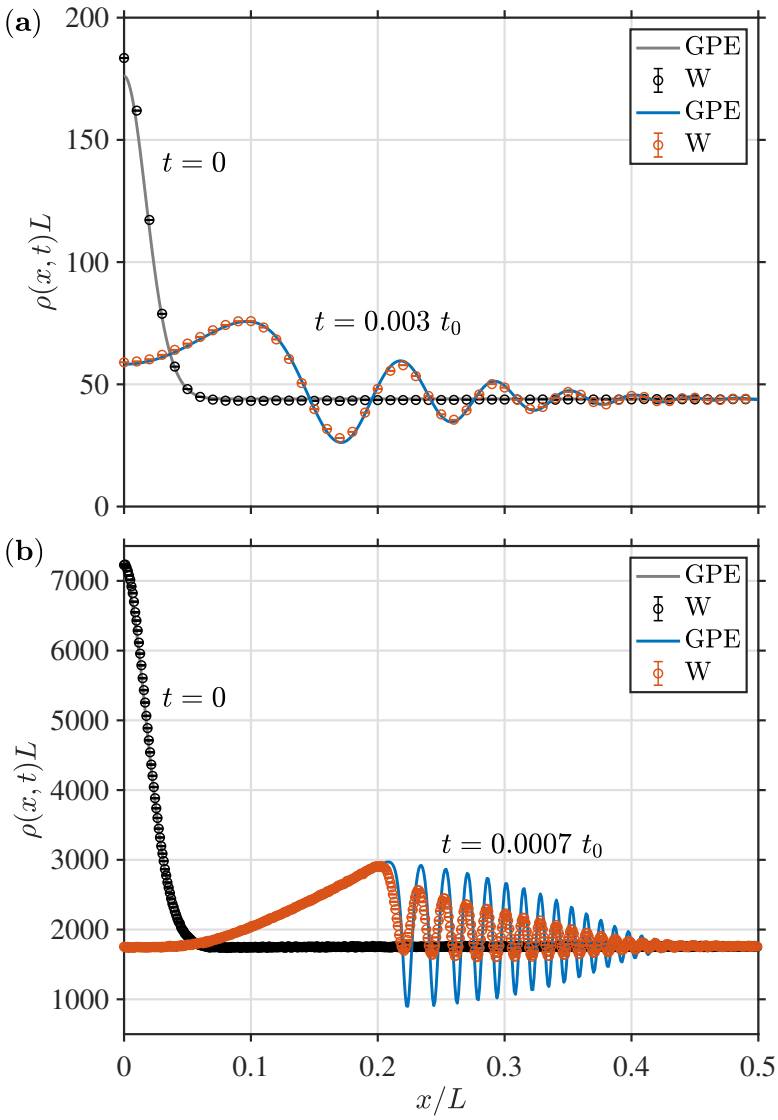

Figure 6.7: Shock waves in a weakly interacting 1D Bose gas at $T = 0$ temperature from TWA simulations. Shown are the initial and final-time density profiles for two different numbers of particles with $\beta = 1$ and $\sigma/L = 0.02$. (a) $N = 50$ and $\gamma_{\rm bg} = 0.1$ with corresponding healing length $l_{\rm h}/L =\simeq 0.072$. (b) $N = 2000$ and $\gamma_{\rm bg} = 0.01$ with corresponding healing length $l_{\rm h}/L =\simeq 0.0057$. The GPE results are shown here as blue lines for comparison. The TWA mean densities are the averages over 100,000 stochastic trajectories. $t_0 = mL^2/\hbar$ is the dimensionless time scale of the system.

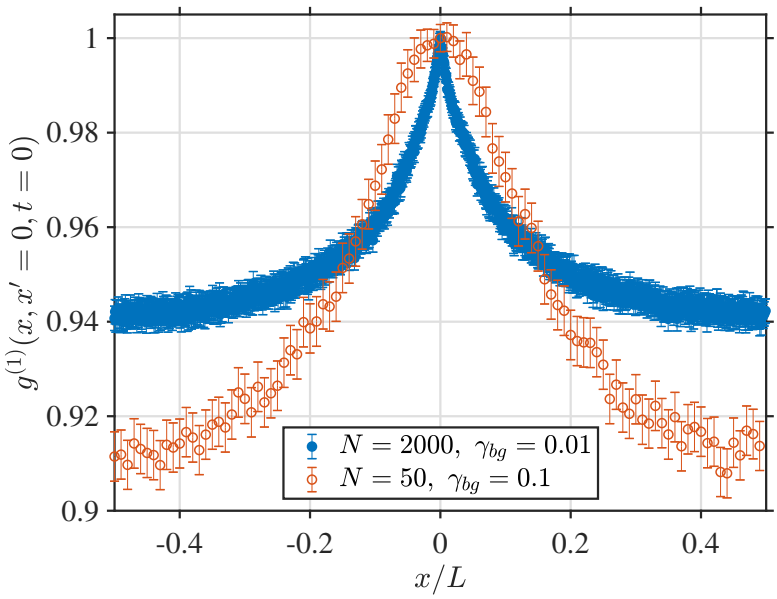

Figure 6.8: Normalised first-order correlation function $g^{(1)}(x, x', t)$ calculated from the centre $x' = 0$ of the box of the initial Gaussian bump. Even with the presence of quantum fluctuations at $T = 0$ temperature, both the $N = 50$ and $N = 2000$ cases still have phase coherence throughout the length of the box given by the large value of $g^{(1)}(x, x' = 0, t = 0)$.

have a more profound effect: the interference contrast is visibly reduced compared to the mean-field GPE results. This is similar to the effect of thermal fluctuations discussed in Section 6.3 and can be attributed to shot-to-shot fluctuations in the position of interference fringes around the mean, where shifting of the shock wave trains with a small period of oscillations (determined by l_{h}) due to quantum fluctuations reduces the contrast in the calculated stochastic average of the density profile.

6.4.1 Second-order correlation function

Now, we look at the signature of the shock wave dynamics in the normalised second-order correlation given by Eq. (6.27) (with the replacement $\Psi_{\mathbf{C}} \to \psi_W$). Again, we recall that the stochastic averages correspond to expected values of symmetrically ordered operator products in the Wigner formalism. Hence, the second-order correlation function $G^{(2)}(x, x')$ is calculated as an average over many stochastic Wigner trajectories using

$$\begin{aligned} G^{(2)}(x, x') = {} & \langle \psi_W^*(x)\psi_W^*(x')\psi_W(x')\psi_W(x)\rangle_{\mathrm{stoch}} \\ & - \frac{1}{2}\delta_c(x, x)\left[\langle \psi_W^*(x)\psi_W(x)\rangle_{\mathrm{stoch}} + \langle \psi_W^*(x')\psi_W(x')\rangle_{\mathrm{stoch}} - \frac{1}{2}\delta_c(x, x)\right] \\ & - \frac{1}{2}\delta_c(x, x')\left[\langle \psi_W^*(x)\psi_W(x')\rangle_{\mathrm{stoch}} + \langle \psi_W^*(x')\psi_W(x)\rangle_{\mathrm{stoch}} - \frac{1}{2}\delta_c(x, x')\right], \end{aligned} \tag{6.44}$$

where the projected delta function $\delta_c(x, x')$ is given in Eq. (6.43). The normalised second-order correlation function $g^{(2)}(x, x', t)$ is then calculated using Eq. (6.44) together with density profile $\rho(x, t)$ calculated according to Eq. (6.41). In Figures 6.9 and 6.10, we plot the local correlation function $g^{(2)}(x, x, t)$ for $N = 50$ and $N = 2000$, respectively. We see a bump in the middle at the initial time

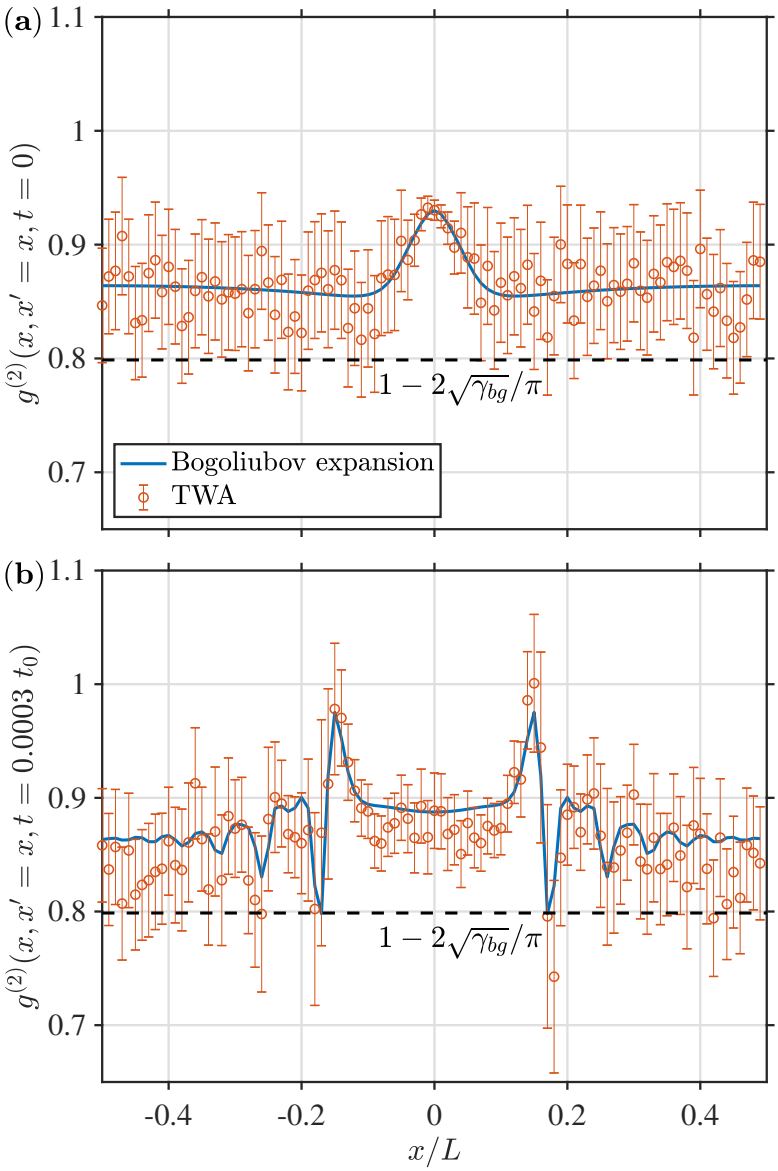

Figure 6.9: Local normalised second-order correlation function $g^{(2)}(x, x' = x, t)$ of the system with $N = 50$ and $\gamma_{bg} = 0.1$ at the initial time $t = 0$ (a) and at a later time $t = 0.0003\ t_0$ (b). Shown here are the correlation function computed from TWA calculations and the correlation function computed by expanding $g^{(2)}(x, x' = x, t)$ in terms of the Bogoliubov modes $u_j(x, t)$ and $v_j(x, t)$ (blue curves). $t_0 = mL^2/\hbar$ is the dimensionless time scale of the system.

$t = 0$ in both plots. This is due to the Gaussian bump over the uniform density we have in our initial state. We also plotted the analytical prediction for $g^{(2)}(x, x)$ in a uniform system [103, 104, 243]. We see here that the analytical prediction is not exactly the same as our result from the TWA. A possible reason behind this discrepancy is the finite-size effects due to our finite box, whereas the analytical results were obtained in the thermodynamic limit. After the systems for $N = 50$ and $N = 2000$ have evolved, we see that there are also shock wave trains in $g^{(2)}(x, x, t)$. Interestingly, we see that in the $N = 2000$ case, the correlation $g^{(2)}(x, x, t)$ is greater than unity at some points. What we observe here is bunching due to the shock wave trains in the density profile.

In Fig. 6.9, we see that calculations of the correlation function $g^{(2)}(x, x, t)$ give a very noisy result.

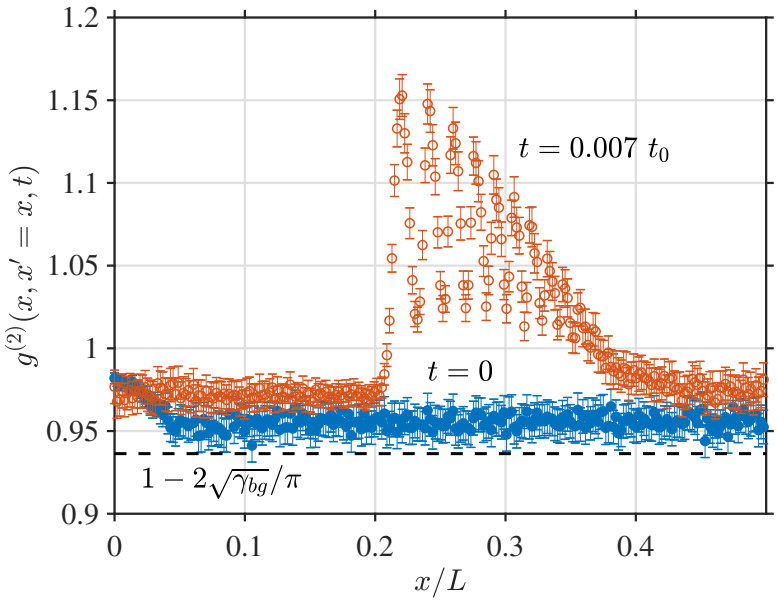

Figure 6.10: Local normalised second-order correlation function $g^{(2)}(x, x' = x, t)$ of the system with $N = 2000$ and $\gamma_{bg} = 0.01$ at the initial time $t = 0$ (blue circles) and at a later time $t = 0.007\ t_0$ (red circles). $t_0 = mL^2/\hbar$ is the dimensionless time scale of the system.

An alternative to calculating the time evolution of the correlation function $g^{(2)}(x, x', t)$ is expanding it in terms of the Bogoliubov modes $u_j(x, t)$ and $v_j(x, t)$ and calculating their time evolutions. With the use of Wick's theorem [116], $g^{(2)}(x, x')$ is expanded in terms of Bogoliubov modes as

$$g^{(2)}(x, x', t) \approx 1 + \frac{1}{\rho_0(x)\rho_0(x')}\Big[2\mathrm{Re}\big[\Psi_0^*(x,t)\Psi_0^*(x',t)\langle\delta\psi(x',t)\delta\psi(x,t)\rangle_{\mathrm{stoch}}\big] + \Psi_0^*(x,t)\Psi_0(x',t)\langle\delta\psi^*(x',t)\delta\psi(x,t)\rangle_{\mathrm{stoch}} + \Psi_0^*(x',t)\Psi_0(x,t)\langle\delta\psi^*(x,t)\delta\psi(x',t)\rangle_{\mathrm{stoch}}\Big], \quad (6.45)$$

where the normal density $\langle\delta\psi^*(x,t)\delta\psi(x',t)\rangle_{\mathrm{stoch}}$ and the anomalous density $\langle\delta\psi(x,t)\delta\psi(x',t)\rangle_{\mathrm{stoch}}$ are given by

$$\langle\delta\psi^*(x,t)\delta\psi(x',t)\rangle_{\mathrm{stoch}} = \sum_{j=1}^{M_B-1} v_j^*(x,t)v_j(x',t), \quad (6.46)$$

$$\langle\delta\psi(x,t)\delta\psi(x',t)\rangle_{\mathrm{stoch}} = \sum_{j=1}^{M_B-1} u_j(x,t)v_j^*(x',t). \quad (6.47)$$

The time evolution of the Bogoliubov modes is obtained by solving the time-dependent Bogoliubov–de Gennes equations

$$i\hbar\frac{\partial}{\partial t}u_j(x,t) = \left(-\frac{\hbar^2}{2m}\frac{\partial^2}{\partial x^2} + V(x) + 2g|\Psi_0(x,t)|^2\right)u_j(x,t) + g\Psi_0^2(x,t)v_j(x,t), \quad (6.48)$$

$$-i\hbar\frac{\partial}{\partial t}v_j(x,t) = \left(-\frac{\hbar^2}{2m}\frac{\partial^2}{\partial x^2} + V(x) + 2g|\Psi_0(x,t)|^2\right)v_j(x,t) + g[(]\Psi_0^*(x,t)]^2u_j(x,t), \quad (6.49)$$

together with the time-dependent Gross–Pitaevskii equation for the condensate mode

$$i\hbar\frac{\partial}{\partial t}\Psi_0(x,t) = \left(-\frac{\hbar^2}{2m}\frac{\partial^2}{\partial x^2} + g|\Psi_0(x,t)|^2\right)\Psi_0(x,t). \quad (6.50)$$

Because the Bogoliubov–de Gennes equations are linear in the Bogoliubov modes $u_j(x,t)$ and $v_j(x,t)$, calculating the time evolution of $g^{(2)}(x,x',t)$ using Eq. (6.45) is only applicable for systems where the effect of nonlinearity is negligible. This is what we see in Fig. 6.9 where the plots of Eq. (6.45) (blue lines) agree well with the result from TWA calculations. However, for systems with stronger interactions where the effect of the nonlinearity of $u_j(x,t)$ and $v_j(x,t)$ becomes more significant, $g^{(2)}(x,x',t)$ calculated using the Bogoliubov–de Gennes equations deviates from calculations using the truncated Wigner simulations. This is indeed the case for the $N = 2000$ system — while the correlation $g^{(2)}(x,x',t)$ at time $t = 0$ calculated using the expansion Eq. (6.45) overlaps with the TWA results, the time evolved $g^{(2)}(x,x',t)$ using the Bogoliubov–de Gennes equations greatly deviates from the TWA results (not plotted in Fig. 6.10).

6.5 Summary

In summary, we have shown the effects of quantum and thermal fluctuations on the dispersive shock wave trains in a 1D quasicondensate. Dispersive shock wave trains are formed due to quantum interference where the local perturbation (in this case, a Gaussian bump) self-interferes with its own background upon expanding into it. The interference contrast is reduced as the local phase coherence of the quasicondensate decreases. At zero temperature, there is phase coherence throughout the length of the quasicondensate. However, the interference contrast is greatly reduced, especially for $N = 2000$, due to shot-shot fluctuations in the position of interference fringes around the mean. At finite temperature, there is a loss of phase coherence that reduces the interference contrast. The interference contrast is reduced when the thermal phase coherence length of the gas is on the order of or lower than the width of the Gaussian bump. In addition, thermal fluctuations also reduce the interference contrast due to shot-to-shot fluctuations similar to the effect of quantum fluctuations.

Chapter 7

Conclusion

In this thesis, we have studied various nonequilibrium dynamics of many-body interacting Bose gases. In particular, we have considered different quenches of one-dimensional (1D) Bose gases and their subsequent dynamics and relaxation. Using the stochastic projected Gross–Pitaevskii equation and the truncated Wigner approximation, we have investigated the effects of thermal and quantum fluctuations on the post-quench dynamics of 1D Bose gases.

In Chapters 3 and 4, we have considered the nonequilibrium dynamics of quenched two tunnel-coupled quasicondensates and observed how they reach their relaxed state after some finite amount of time. We considered in Chapter 3 a system where two initially independent quasicondensates with different chemical potentials and temperatures are instantaneously coupled to initiate Josephson-like oscillations of particles between the two subsystems. We found that after coupling the quasicondensates, the net energy flow in the system is governed by the surplus of the overall number of low energy particles flowing from the colder system to the hotter system, compared to the overall number of high-energy particles flowing in the opposite direction. We also found that the two quasicondensates, though evolving to a state with higher equilibrium temperature (which for the same independent quasicondensates would imply a shorter thermal phase coherence length within each quasicondensate), can have longer thermal phase coherence length than their initial values. This is due to the tunnel coupling that establishes relative phase correlation between the two quasicondensates and is equivalent to an additional degree of freedom in the system, that generally favours establishment of phase coherence over a longer range. However, this increase in coherence length is not proportional to the increase in coupling strength because increasing the latter also increases the temperature of the system.

In the analysis of the phase coherence length in Chapter 3, we have only considered a coupled system in the weakly-interacting regime dominated by thermal fluctuations. It would be interesting in the future to do the same analysis for two coupled systems but in the other low temperature regimes such as the weakly-interacting regime where quantum fluctuations dominate and the strongly-interacting regime. This would contribute to the active research field of quantum thermodynamics where some of the open questions include how quantum correlations, as well as the strength of the coupling between the bath and the system, affect the system dynamics and thermodynamics.

Motivated by the recent experiment in Ref. [53], we have considered the relaxation of a Josephson junction to a phase-locked state in Chapter 4. We have numerically confirmed that c-field simulations could reproduce the same relaxation to a phase-locked state of the system. However, we could not reproduce the fast decay of Josephson oscillations observed in the experiment. A full 3D simulation of the system might be needed to account for the possible effects of 3D geometry on the damping rate of the system. This is indeed what has been done by Mennemann *et al.* in their recent publication [192], where they were able to reproduce the fast decay in the experiment.

In Chapter 5, we have considered the breathing mode dynamics of a 1D Bose gas after a quench of its longitudinal harmonic trap at finite temperature. We find that two breathing mode frequencies with their own distinct damping rates exist during the post-quench dynamics. These two breathing modes are due to two components of the system. The first component is composed of particles with larger local chemical potential that occupy the bulk of the system and have dynamical behaviour closer to the expected breathing dynamics of a quasicondensate at zero temperature, with a breathing mode oscillation frequency of $\omega_B = \sqrt{3}\,\omega$. The other component is composed of particles with smaller local chemical potential that occupy the tails of the trapped Bose gas and have dynamical behaviour close to that of an ideal Bose gas that oscillates at $\omega_B = 2\omega$.

This observation of the presence of two breathing modes with distinct breathing frequencies and damping rate is interesting in the context of 1D Bose gases. The presence of two breathing mode frequencies has long been observed in quenched three-dimensional Bose gases, such as in the experiments of Refs. [198, 244]. In these experiments, the two breathing modes resulted in beating of the breathing mode oscillations. However, the presence of two breathing modes has not been observed yet in experiments with 1D Bose gases. It would be of interest to examine the existence of these two breathing modes in experiments with 1D Bose gases and to check the damping of the breathing modes due to their interactions. Experimental demonstration of the two breathing modes in a quenched 1D quasicondensate would further highlight the significance of the numerical simulations presented in Chapter 5. 1D Bose gases in an atom chip offer an ideal platform for the investigation of these two breathing modes. The authors of Ref. [221] have already observed one of these breathing modes in their experiment, *i.e.* the breathing mode of the low energy particles. By observing the behaviour of high energy particles in the experiment, it should be possible to see the second breathing mode in the system.

We also find in Chapter 5 that the observed damping rate from our c-field simulations is more than twice lower than what is predicted from the theory of Landau damping applied to one dimension. The difference could be due to the assumed equilibrium bath of thermal excitations in Landau theory, whereas the high energy particles that act as the bath of thermal excitations in our system also breathe after the quench of the potential trap. In the future, it would also be of theoretical interest to benchmark the calculated damping rates from our c-field simulations to other numerical techniques, such as a 1D version of the ZNG method of Ref. [198] or the generalised hydrodynamics of Ref. [226], to have further insights on the origin of damping of the breathing mode oscillations.

We have seen in both Chapters 3 and 5 that a single quasicondensate in a harmonic trap can have

two components that behave differently and independently from each other. This difference in behaviour is mainly due to the presence of the longitudinal trapping potential that enables different parts of the gas to locally have their own characteristic and collective motion.

Finally, in Chapter 6, we have studied the effects of quantum and thermal fluctuations on the shock wave trains after a Gaussian bump expands unto a uniform background density and self-interferes with it. Here (and in Ref. [1]), we showed that the quantum shock wave is a result of quantum self-interference which can also be observed in non-interacting systems. This is in contrast to common interpretation of quantum shock waves as grey solitons which require the presence of nonlinear interaction. The effect of thermal fluctuations is to lower the interference contrast of the shock wave trains due to reduced thermal phase coherence and shot-to-shot fluctuations of the position of shock wave fringes around its mean. Similarly, quantum fluctuations reduce the interference contrast due to shot-to-shot fluctuations of the position of the shock wave trains, especially for systems with stronger interactions where the shock wave oscillations are determined by the healing length of the system instead of the width of the initial Gaussian bump. In the future, it would be interesting to extend this analysis to the evolution of a density dip into a uniform background. This is in fact the scenario in which the evolving density depression sheds off actual grey solitons at the mean-field level of description. However, it is not clear how the dynamics of such mean-field grey solitons will modify in the presence of thermal and quantum fluctuations.

Bibliography

[1] S. A. Simmons, F. A. Bayocboc Jr., J. C. Pillay, D. Colas, I. P. McCulloch, and K. V. Kheruntsyan. *What is a quantum shock wave?* Phys. Rev. Lett. **125**, 180401 (2020).

[2] F. A. Bayocboc Jr., M. J. Davis, and K. V. Kheruntsyan. *Dynamics of thermalization of two tunnel-coupled one-dimensional quasicondensates*. arXiv:2108.13095 (2021).

[3] S. N. Bose. *Plancks gesetz und lichtquantenhypothese*. Zeitschrift für Physik **26**(1), 178 (1924).

[4] A. Einstein. *Quantentheorie des einatomigen idealen gases*. Sitzber. Kgl. Preuss. Akad. Wiss. (1924).

[5] A. Einstein. *Quantentheorie des einatomigen idealen gases: Zweite abhandlung*. Sitzber. Kgl. Preuss. Akad. Wiss. (1925).

[6] C. J. Pethick and H. Smith. *Bose–Einstein Condensation in Dilute Gases* (Cambridge University Press, 2008), 2 ed.

[7] T. R. S. A. of Sciences. *Press release of the Nobel Prize in Physics 1997* (1997).

[8] K. B. Davis, M. O. Mewes, M. R. Andrews, N. J. van Druten, D. S. Durfee, D. M. Kurn, and W. Ketterle. *Bose–Einstein condensation in a gas of sodium atoms*. Phys. Rev. Lett. **75**, 3969 (1995).

[9] M. H. Anderson, J. R. Ensher, M. R. Matthews, C. E. Wieman, and E. A. Cornell. *Observation of Bose–Einstein condensation in a dilute atomic vapor*. Science **269**(5221), 198 (1995).

[10] T. R. S. A. of Sciences. *Press release of the Nobel Prize in Physics 2001* (2001).

[11] C. C. Bradley, C. A. Sackett, J. J. Tollett, and R. G. Hulet. *Evidence of Bose–Einstein condensation in an atomic gas with attractive interactions*. Phys. Rev. Lett. **75**, 1687 (1995).

[12] C. C. Bradley, C. A. Sackett, and R. G. Hulet. *Bose–Einstein condensation of lithium: Observation of limited condensate number*. Phys. Rev. Lett. **78**, 985 (1997).

[13] I. Bloch, J. Dalibard, and W. Zwerger. *Many-body physics with ultracold gases*. Rev. Mod. Phys. **80**, 885 (2008).

[14] I. Bloch, J. Dalibard, and S. Nascimbène. *Quantum simulations with ultracold quantum gases*. Nature Physics **8**(4), 267 (2012).

[15] A. Polkovnikov, K. Sengupta, A. Silva, and M. Vengalattore. *Colloquium: Nonequilibrium dynamics of closed interacting quantum systems*. Rev. Mod. Phys. **83**, 863 (2011).

[16] R. Tolman. *The Principles of Statistical Mechanics*. Dover Books on Physics (Dover Publications, 1979).

[17] T. Kinoshita, T. Wenger, and D. S. Weiss. *A quantum Newton's cradle*. Nature **440**(7086), 900 (2006).

[18] S. Hofferberth, I. Lesanovsky, B. Fischer, T. Schumm, and J. Schmiedmayer. *Non-equilibrium coherence dynamics in one-dimensional Bose gases*. Nature **449**(7160), 324 (2007).

[19] M. Gring, M. Kuhnert, T. Langen, T. Kitagawa, B. Rauer, M. Schreitl, I. Mazets, D. A. Smith, E. Demler, and J. Schmiedmayer. *Relaxation and prethermalization in an isolated quantum system*. Science **337**(6100), 1318 (2012).

[20] T. Langen, R. Geiger, M. Kuhnert, B. Rauer, and J. Schmiedmayer. *Local emergence of thermal correlations in an isolated quantum many-body system*. Nature Physics **9**(10), 640 (2013).

[21] T. Langen, S. Erne, R. Geiger, B. Rauer, T. Schweigler, M. Kuhnert, W. Rohringer, I. E. Mazets, T. Gasenzer, and J. Schmiedmayer. *Experimental observation of a generalized Gibbs ensemble*. Science **348**(6231), 207 (2015).

[22] A. Görlitz, J. M. Vogels, A. E. Leanhardt, C. Raman, T. L. Gustavson, J. R. Abo-Shaeer, A. P. Chikkatur, S. Gupta, S. Inouye, T. Rosenband, and W. Ketterle. *Realization of Bose–Einstein condensates in lower dimensions*. Phys. Rev. Lett. **87**, 130402 (2001).

[23] L. Pitaevskii and S. Stringari. *Bose–Einstein condensation and superfluidity*, vol. 164 (Oxford University Press, 2016).

[24] N. D. Mermin and H. Wagner. *Absence of ferromagnetism or antiferromagnetism in one- or two-dimensional isotropic Heisenberg models*. Phys. Rev. Lett. **17**, 1133 (1966).

[25] P. C. Hohenberg. *Existence of long-range order in one and two dimensions*. Phys. Rev. **158**, 383 (1967).

[26] D. S. Petrov, G. V. Shlyapnikov, and J. T. M. Walraven. *Regimes of quantum degeneracy in trapped 1D gases*. Phys. Rev. Lett. **85**, 3745 (2000).

[27] J. W. Kane and L. P. Kadanoff. *Long-range order in superfluid helium*. Phys. Rev. **155**, 80 (1967).

[28] J. W. Kane and L. P. Kadanoff. *Green's functions and superfluid hydrodynamics*. J. Math. Phys. **6**(12), 1902 (1965).

[29] L. Reatto and G. V. Chester. *Phonons and the properties of a Bose system*. Phys. Rev. **155**, 88 (1967).

[30] N. K. Whitlock and I. Bouchoule. *Relative phase fluctuations of two coupled one-dimensional condensates*. Phys. Rev. A **68**, 053609 (2003).

[31] Y. Castin. *Simple theoretical tools for low dimension bose gases*. J. Phys. IV France **116**, 89 (2004).

[32] M. A. Cazalilla. *Bosonizing one-dimensional cold atomic gases*. J. Phys. B **37**(7), S1 (2004).

[33] V. N. Popov. *Functional integrals in quantum field theory and statistical physics*, vol. 8 (Springer Science & Business Media, 2001).

[34] P. Calabrese and J. Cardy. *Evolution of entanglement entropy in one-dimensional systems*. J. Stat. Mech. Theory Exp. **2005**(04), P04010 (2005).

[35] P. Calabrese and J. Cardy. *Time dependence of correlation functions following a quantum quench*. Phys. Rev. Lett. **96**, 136801 (2006).

[36] J. Eisert, M. Friesdorf, and C. Gogolin. *Quantum many-body systems out of equilibrium*. Nature Physics **11**(2), 124 (2015).

[37] A. Posazhennikova, M. Trujillo-Martinez, and J. Kroha. *Thermalization of isolated Bose–Einstein condensates by dynamical heat bath generation*. Annalen der Physik **530**(1), 1700124 (2018).

[38] T. Mori, T. N. Ikeda, E. Kaminishi, and M. Ueda. *Thermalization and prethermalization in isolated quantum systems: a theoretical overview*. Journal of Physics B: Atomic, Molecular and Optical Physics **51**(11), 112001 (2018).

[39] M. Rigol, V. Dunjko, and M. Olshanii. *Thermalization and its mechanism for generic isolated quantum systems*. Nature **452**, 854 EP (2008).

[40] L. D'Alessio, Y. Kafri, A. Polkovnikov, and M. Rigol. *From quantum chaos and eigenstate thermalization to statistical mechanics and thermodynamics*. Advances in Physics **65**(3), 239 (2016).

[41] J. M. Deutsch. *Eigenstate thermalization hypothesis*. Reports on Progress in Physics **81**(8), 082001 (2018).

[42] J. M. Deutsch. *Quantum statistical mechanics in a closed system*. Phys. Rev. A **43**, 2046 (1991).

[43] M. Srednicki. *Chaos and quantum thermalization*. Phys. Rev. E **50**, 888 (1994).

[44] M. Rigol. *Breakdown of thermalization in finite one-dimensional systems*. Phys. Rev. Lett. **103**, 100403 (2009).

[45] M. Rigol, V. Dunjko, V. Yurovsky, and M. Olshanii. *Relaxation in a completely integrable many-body quantum system: An ab initio study of the dynamics of the highly excited states of 1D lattice hard-core bosons*. Phys. Rev. Lett. **98**, 050405 (2007).

[46] E. H. Lieb and W. Liniger. *Exact analysis of an interacting Bose gas. I. the general solution and the ground state*. Phys. Rev. **130**, 1605 (1963).

[47] E. H. Lieb. *Exact analysis of an interacting Bose gas. II. the excitation spectrum*. Phys. Rev. **130**, 1616 (1963).

[48] I. E. Mazets and J. Schmiedmayer. *Dephasing in two decoupled one-dimensional Bose–Einstein condensates and the subexponential decay of the interwell coherence*. Eur. Phys. J. B **68**(3), 335 (2009).

[49] H.-P. Stimming, N. J. Mauser, J. Schmiedmayer, and I. E. Mazets. *Dephasing in coherently split quasicondensates*. Phys. Rev. A **83**, 023618 (2011).

[50] J. Berges, S. Borsányi, and C. Wetterich. *Prethermalization*. Phys. Rev. Lett. **93**, 142002 (2004).

[51] R. Geiger, T. Langen, I. E. Mazets, and J. Schmiedmayer. *Local relaxation and light-cone-like propagation of correlations in a trapped one-dimensional Bose gas*. New J. Phys. **16**(5), 053034 (2014).

[52] T. Langen, T. Schweigler, E. Demler, and J. Schmiedmayer. *Double light-cone dynamics establish thermal states in integrable 1D Bose gases*. New J. Phys. **20**(2), 023034 (2018).

[53] M. Pigneur, T. Berrada, M. Bonneau, T. Schumm, E. Demler, and J. Schmiedmayer. *Relaxation to a phase-locked equilibrium state in a one-dimensional bosonic Josephson junction*. Phys. Rev. Lett. **120**, 173601 (2018).

[54] L. Pitaevskii and S. Stringari. *Bose–Einstein Condensation (International Series of Monographs on Physics)* (Oxford University Press, USA, 2003).

[55] E. P. Gross. *Structure of a quantized vortex in boson systems*. Il Nuovo Cimento (1955-1965) **20**(3), 454 (1961).

[56] L. P. Pitaevskii. *Vortex lines in an imperfect Bose gas*. Sov. Phys. JETP **13**(2), 451 (1961).

[57] N. Bogoliubov. *On the theory of superfluidity*. J. Phys. (USSR) **11**(1), 23 (1947).

[58] F. Dalfovo, S. Giorgini, L. P. Pitaevskii, and S. Stringari. *Theory of Bose–Einstein condensation in trapped gases*. Rev. Mod. Phys. **71**, 463 (1999).

[59] E. Madelung. *Quantentheorie in hydrodynamischer form*. Zeitschrift für Physik **40**(3), 322 (1927).

[60] T. Winiecki, B. Jackson, J. F. McCann, and C. S. Adams. *Vortex shedding and drag in dilute Bose–Einstein condensates*. J. Phys. B **33**(19), 4069 (2000).

[61] C. Barenghi and N. G. Parker. *A Primer on Quantum Fluids* (Springer International Publishing, 2016).

[62] L. D. L. D. Landau and E. M. E. M. Lifshitz. *Fluid mechanics* (London : Pergamon Press ; Reading, Mass. : Addison-Wesley Pub. Co, 1959).

[63] Y. Castin. *Bose–Einstein condensates in atomic gases: Simple theoretical results*. In R. Kaiser, C. Westbrook, and F. David, eds., *Coherent atomic matter waves*, pp. 1–136 (Springer Berlin Heidelberg, Berlin, Heidelberg, 2001).

[64] R. Carretero-González, D. J. Frantzeskakis, and P. G. Kevrekidis. *Nonlinear waves in Bose–Einstein condensates: physical relevance and mathematical techniques*. Nonlinearity **21**(7), R139 (2008).

[65] A. M. Kamchatnov. *Expansion of Bose–Einstein condensates confined in quasi-one-dimensional or quasi-two-dimensional traps*. J. Exp. Theor. Phys. **98**(5), 908 (2004).

[66] M. Ueda. *Fundamentals and New Frontiers of Bose–Einstein Condensation* (World Scientific, 2010).

[67] N. Bogoliubov. *Å JINR Preprint R-1451, Dubna, 1963*. Phys. Abh. SU **6**, 1 (1962).

[68] M. Schwartz. *Off-diagonal long-range behavior of interacting Bose systems*. Phys. Rev. B **15**, 1399 (1977).

[69] F. D. M. Haldane. *Effective harmonic-fluid approach to low-energy properties of one-dimensional quantum fluids*. Phys. Rev. Lett. **47**, 1840 (1981).

[70] C. Mora and Y. Castin. *Extension of Bogoliubov theory to quasicondensates*. Phys. Rev. A **67**, 053615 (2003).

[71] M. J. Davis, S. A. Gardiner, T. M. Hanna, N. Nygaard, N. P. Proukakis, and M. H. Szymańska. *Introduction to theoretical modelling*. In *Quantum Gases*, vol. 1, pp. 63–83 (Imperial College Press, 2011).

[72] K. K. Das. *Bose–Fermi mixtures in one dimension*. Phys. Rev. Lett. **90**, 170403 (2003).

[73] I. Bouchoule, K. V. Kheruntsyan, and G. V. Shlyapnikov. *Interaction-induced crossover versus finite-size condensation in a weakly interacting trapped one-dimensional Bose gas*. Phys. Rev. A **75**, 031606 (2007).

[74] H. Moritz, T. Stöferle, M. Köhl, and T. Esslinger. *Exciting collective oscillations in a trapped 1D gas*. Phys. Rev. Lett. **91**, 250402 (2003).

[75] J. Armijo, T. Jacqmin, K. Kheruntsyan, and I. Bouchoule. *Mapping out the quasicondensate transition through the dimensional crossover from one to three dimensions*. Phys. Rev. A **83**, 021605 (2011).

[76] T. Kinoshita, T. Wenger, and D. S. Weiss. *Observation of a one-dimensional Tonks–Girardeau gas*. Science **305**(5687), 1125 (2004).

[77] T. Kinoshita, T. Wenger, and D. S. Weiss. *All-optical Bose–Einstein condensation using a compressible crossed dipole trap*. Phys. Rev. A **71**, 011602 (2005).

[78] M. Greiner, I. Bloch, O. Mandel, T. W. Hänsch, and T. Esslinger. *Exploring phase coherence in a 2D lattice of Bose–Einstein condensates*. Phys. Rev. Lett. **87**, 160405 (2001).

[79] E. Haller, M. Gustavsson, M. J. Mark, J. G. Danzl, R. Hart, G. Pupillo, and H.-C. Nägerl. *Realization of an excited, strongly correlated quantum gas phase*. Science **325**(5945), 1224 (2009).

[80] E. Haller, R. Hart, M. J. Mark, J. G. Danzl, L. Reichsöllner, M. Gustavsson, M. Dalmonte, G. Pupillo, and H.-C. Nägerl. *Pinning quantum phase transition for a Luttinger liquid of strongly interacting bosons*. Nature **466**(7306), 597 (2010).

[81] N. Fabbri, D. Clément, L. Fallani, C. Fort, and M. Inguscio. *Momentum-resolved study of an array of one-dimensional strongly phase-fluctuating Bose gases*. Phys. Rev. A **83**, 031604 (2011).

[82] I. Bloch. *Ultracold quantum gases in optical lattices*. Nature Physics **1**(1), 23 (2005).

[83] S. Li, S. R. Manmana, A. M. Rey, R. Hipolito, A. Reinhard, J.-F. Riou, L. A. Zundel, and D. S. Weiss. *Self-trapping dynamics in a two-dimensional optical lattice*. Phys. Rev. A **88**, 023419 (2013).

[84] F. Serwane, G. Zürn, T. Lompe, T. B. Ottenstein, A. N. Wenz, and S. Jochim. *Deterministic preparation of a tunable few-fermion system*. Science **332**(6027), 336 (2011).

[85] P. Krüger, S. Hofferberth, I. E. Mazets, I. Lesanovsky, and J. Schmiedmayer. *Weakly interacting Bose gas in the one-dimensional limit*. Phys. Rev. Lett. **105**, 265302 (2010).

[86] van Amerongen, A. H. *One-dimensional Bose gas on an atom chip*. Ann. Phys. Fr. **33**(3), 1 (2009).

[87] J. Reichel and V. Vuletic. *Atom chips* (John Wiley & Sons, 2011).

[88] J. Fortágh and C. Zimmermann. *Toward atom chips*. Science **307**(5711), 860 (2005).

[89] R. Grimm, M. Weidemüller, and Y. B. Ovchinnikov. *Optical dipole traps for neutral atoms*. Advances In Atomic, Molecular, and Optical Physics **42**, 95 (2000).

[90] I. Bouchoule and J. Dubail. *Generalized hydrodynamics in the 1D Bose gas: theory and experiments*. arXiv:2108.02509 (2021).

[91] C. J. Foot *et al.* *Atomic physics*, vol. 7 (Oxford University Press, 2005).

[92] K. B. Davis, M.-O. Mewes, M. A. Joffe, M. R. Andrews, and W. Ketterle. *Evaporative cooling of sodium atoms*. Phys. Rev. Lett. **74**, 5202 (1995).

[93] D. E. Pritchard. *Cooling neutral atoms in a magnetic trap for precision spectroscopy*. Phys. Rev. Lett. **51**, 1336 (1983).

[94] B. Rauer, P. Grišins, I. E. Mazets, T. Schweigler, W. Rohringer, R. Geiger, T. Langen, and J. Schmiedmayer. *Cooling of a one-dimensional Bose gas*. Phys. Rev. Lett. **116**, 030402 (2016).

[95] M. Schemmer and I. Bouchoule. *Cooling a Bose gas by three-body losses*. Phys. Rev. Lett. **121**, 200401 (2018).

[96] I. Bouchoule and M. Schemmer. *Asymptotic temperature of a lossy condensate*. SciPost Phys. **8**, 60 (2020).

[97] P. Krüger, L. M. Andersson, S. Wildermuth, S. Hofferberth, E. Haller, S. Aigner, S. Groth, I. Bar-Joseph, and J. Schmiedmayer. *Potential roughness near lithographically fabricated atom chips*. Phys. Rev. A **76**, 063621 (2007).

[98] M. Girardeau. *Relationship between systems of impenetrable bosons and fermions in one dimension*. Journal of Mathematical Physics **1**(6), 516 (1960).

[99] H. Bethe. *Zur theorie der metalle*. Zeitschrift für Physik **71**(3), 205 (1931).

[100] C. N. Yang and C. P. Yang. *Thermodynamics of a one-dimensional system of bosons with repulsive delta-function interaction*. J. Math. Phys. **10**(7), 1115 (1969).

[101] V. E. Korepin, N. M. Bogoliubov, and A. G. Izergin. *Quantum Inverse Scattering Method and Correlation Functions*. Cambridge Monographs on Mathematical Physics (Cambridge University Press, 1993).

[102] D.S. Petrov, D.M. Gangardt, and G.V. Shlyapnikov. *Low-dimensional trapped gases*. J. Phys. IV France **116**, 5 (2004).

[103] K. V. Kheruntsyan, D. M. Gangardt, P. D. Drummond, and G. V. Shlyapnikov. *Pair correlations in a finite-temperature 1D Bose gas*. Phys. Rev. Lett. **91**, 040403 (2003).

[104] K. V. Kheruntsyan, D. M. Gangardt, P. D. Drummond, and G. V. Shlyapnikov. *Finite-temperature correlations and density profiles of an inhomogeneous interacting one-dimensional Bose gas*. Phys. Rev. A **71**, 053615 (2005).

[105] M. Olshanii. *Atomic scattering in the presence of an external confinement and a gas of impenetrable bosons*. Phys. Rev. Lett. **81**, 938 (1998).

[106] L. Tonks. *The complete equation of state of one, two and three-dimensional gases of hard elastic spheres*. Phys. Rev. **50**, 955 (1936).

[107] I. Bouchoule, N. J. van Druten, and C. I. Westbrook. *Atom chips and one-dimensional Bose gases*. In *Atom Chips*, chap. 11, pp. 331–363 (Wiley-Blackwell, 2011).

[108] B. Paredes, A. Widera, V. Murg, O. Mandel, S. Fölling, I. Cirac, G. V. Shlyapnikov, T. W. Hänsch, and I. Bloch. *Tonks–Girardeau gas of ultracold atoms in an optical lattice*. Nature **429**(6989), 277 (2004).

[109] A. Lenard. *Momentum distribution in the ground state of the one-dimensional system of impenetrable bosons*. Journal of Mathematical Physics **5**(7), 930 (1964).

[110] T. Jacqmin, J. Armijo, T. Berrada, K. V. Kheruntsyan, and I. Bouchoule. *Sub-Poissonian fluctuations in a 1D Bose gas: From the quantum quasicondensate to the strongly interacting regime*. Phys. Rev. Lett. **106**, 230405 (2011).

[111] A. H. van Amerongen, J. J. P. van Es, P. Wicke, K. V. Kheruntsyan, and N. J. van Druten. *Yang–Yang thermodynamics on an atom chip*. Phys. Rev. Lett. **100**, 090402 (2008).

[112] Z. Hadzibabic and M. Köhl. *Low-dimensional atomic Bose gases*. In K. Levin, A. L. Fetter, and D. M. Stamper-Kurn, eds., *Ultracold Bosonic and Fermionic Gases*, vol. 5 of *Contemporary Concepts of Condensed Matter Science*, pp. 95–120 (Elsevier, 2012).

[113] A. E. Feiguin, F. Heidrich-Meisner, G. Orso, and W. Zwerger. *BCS–BEC crossover and unconventional superfluid order in one dimension*. In W. Zwerger, ed., *The BCS-BEC Crossover and the Unitary Fermi Gas*, pp. 503–532 (Springer Berlin Heidelberg, Berlin, Heidelberg, 2012).

[114] T. Kitagawa, A. Imambekov, J. Schmiedmayer, and E. Demler. *The dynamics and prethermalization of one-dimensional quantum systems probed through the full distributions of quantum noise*. New J. Phys. **13**(7), 073018 (2011).

[115] T. Langen. *Non-equilibrium dynamics of one-dimensional Bose gases* (Springer, 2015).

[116] G. C. Wick. *The evaluation of the collision matrix*. Phys. Rev. **80**, 268 (1950).

[117] S. Dettmer, D. Hellweg, P. Ryytty, J. J. Arlt, W. Ertmer, K. Sengstock, D. S. Petrov, G. V. Shlyapnikov, H. Kreutzmann, L. Santos, and M. Lewenstein. *Observation of phase fluctuations in elongated Bose–Einstein condensates*. Phys. Rev. Lett. **87**, 160406 (2001).

[118] D. Hellweg, L. Cacciapuoti, M. Kottke, T. Schulte, K. Sengstock, W. Ertmer, and J. J. Arlt. *Measurement of the spatial correlation function of phase fluctuating Bose–Einstein condensates*. Phys. Rev. Lett. **91**, 010406 (2003).

[119] S. Richard, F. Gerbier, J. H. Thywissen, M. Hugbart, P. Bouyer, and A. Aspect. *Momentum spectroscopy of 1D phase fluctuations in Bose–Einstein condensates*. Phys. Rev. Lett. **91**, 010405 (2003).

[120] I. Shvarchuck, C. Buggle, D. S. Petrov, K. Dieckmann, M. Zielonkowski, M. Kemmann, T. G. Tiecke, W. von Klitzing, G. V. Shlyapnikov, and J. T. M. Walraven. *Bose–Einstein condensation into nonequilibrium states studied by condensate focusing*. Phys. Rev. Lett. **89**, 270404 (2002).

[121] M. Hugbart, J. A. Retter, F. Gerbier, A. F. Varón, S. Richard, J. H. Thywissen, D. Clément, P. Bouyer, and A. Aspect. *Coherence length of an elongated condensate*. The European Physical Journal D - Atomic, Molecular, Optical and Plasma Physics **35**(1), 155 (2005).

[122] D. S. Petrov, G. V. Shlyapnikov, and J. T. M. Walraven. *Phase-fluctuating 3D Bose–Einstein condensates in elongated traps*. Phys. Rev. Lett. **87**, 050404 (2001).

[123] P. Blakie, A. Bradley, M. Davis, R. Ballagh, and C. Gardiner. *Dynamics and statistical mechanics of ultra-cold Bose gases using c-field techniques*. Adv. Phys. **57**(5), 363 (2008).

[124] C. Gardiner and P. Zoller. *The Quantum World of Ultra-Cold Atoms and Light Book I: Foundations of Quantum Optics* (Imperial College Press, 2014).

[125] A. Polkovnikov. *Phase space representation of quantum dynamics*. Annals of Physics **325**(8), 1790 (2010).

[126] A. Sinatra, Y. Castin, and C. Lobo. *A Monte Carlo formulation of the Bogolubov theory*. Journal of Modern Optics **47**(14-15), 2629 (2000).

[127] A. Sinatra, C. Lobo, and Y. Castin. *The truncated Wigner method for Bose-condensed gases: limits of validity and applications*. Journal of Physics B: Atomic, Molecular and Optical Physics **35**(17), 3599 (2002).

[128] C. W. Gardiner. *Quantum Noise* (Springer-Verlag, Berlin, 1991).

[129] M. J. Steel, M. K. Olsen, L. I. Plimak, P. D. Drummond, S. M. Tan, M. J. Collett, D. F. Walls, and R. Graham. *Dynamical quantum noise in trapped Bose–Einstein condensates*. Phys. Rev. A **58**, 4824 (1998).

[130] L. Isella and J. Ruostekoski. *Nonadiabatic dynamics of a Bose–Einstein condensate in an optical lattice*. Phys. Rev. A **72**, 011601 (2005).

[131] L. Isella and J. Ruostekoski. *Quantum dynamics in splitting a harmonically trapped Bose–Einstein condensate by an optical lattice: Truncated Wigner approximation*. Phys. Rev. A **74**, 063625 (2006).

[132] C. Gardiner and P. Zoller. *The Quantum World of Ultra-Cold Atoms and Light Book III: Ultra-Cold Atoms* (World Scientific (Europe), 2017).

[133] J. Ruostekoski and A. D. Martin. *The truncated Wigner method for Bose gases*. In *Quantum Gases*, chap. 13, pp. 203–214 (Imperial College Press, 2013).

[134] M. Brewczyk, M. Gajda, and K. Rzażewski. *Classical fields approximation for bosons at nonzero temperatures*. Journal of Physics B: Atomic, Molecular and Optical Physics **40**(2), R1 (2007).

[135] S. P. Cockburn, A. Negretti, N. P. Proukakis, and C. Henkel. *Comparison between microscopic methods for finite-temperature Bose gases*. Phys. Rev. A **83**, 043619 (2011).

[136] A. A. Abrikosov, L. P. Gorkov, and I. E. Dzyaloshinski. *Methods of Quantum Field Theory in Statistical Physics*. Dover Books on Physics (Dover Publications, 1975), revised ed.

[137] S. A. Morgan. *A gapless theory of Bose-Einstein condensation in dilute gases at finite temperature*. Journal of Physics B: Atomic, Molecular and Optical Physics **33**(19), 3847 (2000).

[138] Y. Castin, R. Dum, E. Mandonnet, A. Minguzzi, and I. Carusotto. *Coherence properties of a continuous atom laser*. Journal of Modern Optics **47**(14-15), 2671 (2000).

[139] C. W. Gardiner, J. R. Anglin, and T. I. A. Fudge. *The stochastic Gross–Pitaevskii equation*. Journal of Physics B, Atomic, Molecular and Optical Physics **35**(6), 1555 (2002).

[140] C. W. Gardiner and M. J. Davis. *The stochastic Gross–Pitaevskii equation: II*. Journal of Physics B, Atomic, Molecular and Optical Physics **36**(23), 4731 (2003).

[141] A. Bradley and C. Gardiner. *The stochastic Gross–Pitaevskii equation: III*. arXiv:0602162 (2006).

[142] A. S. Bradley and P. B. Blakie. *Stochastic projected Gross–Pitaevskii equation for spinor and multicomponent condensates*. Phys. Rev. A **90**, 023631 (2014).

[143] S. J. Rooney, P. B. Blakie, and A. S. Bradley. *Stochastic projected Gross–Pitaevskii equation*. Phys. Rev. A **86**, 053634 (2012).

[144] S. J. Rooney, T. W. Neely, B. P. Anderson, and A. S. Bradley. *Persistent-current formation in a high-temperature Bose–Einstein condensate: An experimental test for classical-field theory*. Phys. Rev. A **88**, 063620 (2013).

[145] A. S. Bradley, P. B. Blakie, and C. W. Gardiner. *Properties of the stochastic Gross–Pitaevskii equation: finite temperature Ehrenfest relations and the optimal plane wave representation*. Journal of Physics B: Atomic, Molecular and Optical Physics **38**(23), 4259 (2005).

[146] G. R. Dennis, J. J. Hope, and M. T. Johnsson. *XMDS2: Fast, scalable simulation of coupled stochastic partial differential equations*. Computer Physics Communications **184**(1), 201 (2013).

[147] O. Penrose and L. Onsager. *Bose–Einstein condensation and liquid helium*. Phys. Rev. **104**, 576 (1956).

[148] J. Gemmer, M. Michel, and G. Mahler. *Quantum thermodynamics: Emergence of thermodynamic behavior within composite quantum systems*, vol. 784 (Springer, 2009).

[149] F. Binder, L. A. Correa, C. Gogolin, J. Anders, and G. Adesso. *Thermodynamics in the quantum regime*, vol. 195 (Springer, 2018).

[150] J. Esteve, J.-B. Trebbia, T. Schumm, A. Aspect, C. I. Westbrook, and I. Bouchoule. *Observations of density fluctuations in an elongated Bose gas: Ideal gas and quasicondensate regimes*. Phys. Rev. Lett. **96**, 130403 (2006).

[151] L. Foini and T. Giamarchi. *Nonequilibrium dynamics of coupled Luttinger liquids*. Phys. Rev. A **91**, 023627 (2015).

[152] L. Foini and T. Giamarchi. *Relaxation dynamics of two coherently coupled one-dimensional bosonic gases*. Eur. Phys. J Spec. Top. **226**(12), 2763 (2017).

[153] Y. M. Bidasyuk, M. Weyrauch, M. Momme, and O. O. Prikhodko. *Finite-temperature dynamics of a bosonic Josephson junction*. Journal of Physics B: Atomic, Molecular and Optical Physics **51**(20), 205301 (2018).

[154] M. R. Momme, Y. M. Bidasyuk, and M. Weyrauch. *Collective excitations and tunneling dynamics in long bosonic Josephson junctions*. Phys. Rev. A **100**, 033601 (2019).

[155] M. R. Momme, O. O. Prikhodko, and Y. M. Bidasyuk. *Dispersion relations and self-localization of quasiparticles in coupled elongated Bose–Einstein condensates*. Phys. Rev. A **102**, 043316 (2020).

[156] Y. D. van Nieuwkerk and F. H. L. Essler. *On the low-energy description for tunnel-coupled one-dimensional Bose gases*. SciPost Phys. **9**, 25 (2020).

[157] T. Betz, S. Manz, R. Bücker, T. Berrada, C. Koller, G. Kazakov, I. E. Mazets, H.-P. Stimming, A. Perrin, T. Schumm, and J. Schmiedmayer. *Two-point phase correlations of a one-dimensional bosonic Josephson junction*. Phys. Rev. Lett. **106**, 020407 (2011).

[158] T. Langen, M. Gring, M. Kuhnert, B. Rauer, R. Geiger, D. A. Smith, I. E. Mazets, and J. Schmiedmayer. *Prethermalization in one-dimensional Bose gases: Description by a stochastic Ornstein–Uhlenbeck process*. Eur. Phys. J Spec. Top. **217**(1), 43 (2013).

[159] T. Schweigler, V. Kasper, S. Erne, I. Mazets, B. Rauer, F. Cataldini, T. Langen, T. Gasenzer, J. Berges, and J. Schmiedmayer. *Experimental characterization of a quantum many-body system via higher-order correlations*. Nature **545**, 323 (2017).

[160] E. G. Dalla Torre, E. Demler, and A. Polkovnikov. *Universal rephasing dynamics after a quantum quench via sudden coupling of two initially independent condensates*. Phys. Rev. Lett. **110**, 090404 (2013).

[161] B. Josephson. *Possible new effects in superconductive tunnelling*. Phys. Lett. **1**(7), 251 (1962).

[162] A. Smerzi, S. Fantoni, S. Giovanazzi, and S. R. Shenoy. *Quantum coherent atomic tunneling between two trapped Bose–Einstein condensates*. Phys. Rev. Lett. **79**, 4950 (1997).

[163] I. Zapata, F. Sols, and A. J. Leggett. *Josephson effect between trapped Bose–Einstein condensates*. Phys. Rev. A **57**, R28 (1998).

[164] S. Raghavan, A. Smerzi, S. Fantoni, and S. R. Shenoy. *Coherent oscillations between two weakly coupled Bose–Einstein condensates: Josephson effects, π oscillations, and macroscopic quantum self-trapping*. Phys. Rev. A **59**, 620 (1999).

[165] I. Marino, S. Raghavan, S. Fantoni, S. Shenoy, and A. Smerzi. *Bose-condensate tunneling dynamics: Momentum-shortened pendulum with damping*. Physical Review A **60**(1), 487 (1999).

[166] S. Giovanazzi, A. Smerzi, and S. Fantoni. *Josephson effects in dilute Bose–Einstein condensates*. Phys. Rev. Lett. **84**, 4521 (2000).

[167] A. Smerzi, A. Trombettoni, T. Lopez-Arias, C. Fort, P. Maddaloni, F. Minardi, and M. Inguscio. *Macroscopic oscillations between two weakly coupled Bose–Einstein condensates*. Eur. Phys. J. B **31**(4), 457 (2003).

[168] P. Grišins and I. E. Mazets. *Coherence and Josephson oscillations between two tunnel-coupled one-dimensional atomic quasicondensates at finite temperature*. Physical Review A **87**(1), 013629 (2013).

[169] G. Spagnolli, G. Semeghini, L. Masi, G. Ferioli, A. Trenkwalder, S. Coop, M. Landini, L. Pezzè, G. Modugno, M. Inguscio, A. Smerzi, and M. Fattori. *Crossing over from attractive to repulsive interactions in a tunneling bosonic Josephson junction*. Phys. Rev. Lett. **118**, 230403 (2017).

[170] M. Pigneur and J. Schmiedmayer. *Analytical pendulum model for a bosonic Josephson junction*. Phys. Rev. A **98**, 063632 (2018).

[171] M. Albiez, R. Gati, J. Fölling, S. Hunsmann, M. Cristiani, and M. K. Oberthaler. *Direct observation of tunneling and nonlinear self-trapping in a single bosonic Josephson junction*. Phys. Rev. Lett. **95**, 010402 (2005).

[172] S. Levy, E. Lahoud, I. Shomroni, and J. Steinhauer. *The a.c. and d.c. Josephson effects in a Bose–Einstein condensate*. Nature **449**, 579 (2007).

[173] L. J. LeBlanc, A. B. Bardon, J. McKeever, M. H. T. Extavour, D. Jervis, J. H. Thywissen, F. Piazza, and A. Smerzi. *Dynamics of a tunable superfluid junction*. Phys. Rev. Lett. **106**, 025302 (2011).

[174] Bouchoule, I. *Modulational instabilities in Josephson oscillations of elongated coupled condensates*. Eur. Phys. J. D **35**(1), 147 (2005).

[175] R. Hipolito and A. Polkovnikov. *Breakdown of macroscopic quantum self-trapping in coupled mesoscopic one-dimensional Bose gases*. Phys. Rev. A **81**, 013621 (2010).

[176] K. F. Thomas, M. J. Davis, and K. V. Kheruntsyan. *Thermalization of a quantum Newton's cradle in a one-dimensional quasicondensate*. Phys. Rev. A **103**, 023315 (2021).

[177] I. Bouchoule, S. S. Szigeti, M. J. Davis, and K. V. Kheruntsyan. *Finite-temperature hydrodynamics for one-dimensional Bose gases: Breathing-mode oscillations as a case study*. Phys. Rev. A **94**, 051602 (2016).

[178] A. Bhattacharyya. *On a measure of divergence between two statistical populations defined by their probability distributions*. Bull. Calcutta Math. Soc. **35**, 99 (1943).

[179] I. Bouchoule, M. Arzamasovs, K. V. Kheruntsyan, and D. M. Gangardt. *Two-body momentum correlations in a weakly interacting one-dimensional Bose gas*. Phys. Rev. A **86**, 033626 (2012).

[180] V. Gritsev, A. Polkovnikov, and E. Demler. *Linear response theory for a pair of coupled one-dimensional condensates of interacting atoms*. Phys. Rev. B **75**, 174511 (2007).

[181] T. Giamarchi. *Quantum Physics in One Dimension*, vol. 121 (Clarendon Press, 2003).

[182] V. Gritsev, E. Demler, M. Lukin, and A. Polkovnikov. *Spectroscopy of collective excitations in interacting low-dimensional many-body systems using quench dynamics*. Phys. Rev. Lett. **99**, 200404 (2007).

[183] T. V. Zache, T. Schweigler, S. Erne, J. Schmiedmayer, and J. Berges. *Extracting the field theory description of a quantum many-body system from experimental data*. Phys. Rev. X **10**, 011020 (2020).

[184] Y. D. van Nieuwkerk and F. H. L. Essler. *Self-consistent time-dependent harmonic approximation for the sine-Gordon model out of equilibrium*. Journal of Statistical Mechanics: Theory and Experiment **2019**(8), 084012 (2019).

[185] D. X. Horváth, I. Lovas, M. Kormos, G. Takács, and G. Zaránd. *Nonequilibrium time evolution and rephasing in the quantum sine-Gordon model*. Phys. Rev. A **100**, 013613 (2019).

[186] M. J. Davis, P. B. Blakie, A. H. van Amerongen, N. J. van Druten, and K. V. Kheruntsyan. *Yang–Yang thermometry and momentum distribution of a trapped one-dimensional Bose gas*. Phys. Rev. A **85**, 031604 (2012).

[187] I. E. Mazets, T. Schumm, and J. Schmiedmayer. *Breakdown of integrability in a quasi-1D ultracold bosonic gas*. Phys. Rev. Lett. **100**, 210403 (2008).

[188] I. Lesanovsky, T. Schumm, S. Hofferberth, L. M. Andersson, P. Krüger, and J. Schmiedmayer. *Adiabatic radio-frequency potentials for the coherent manipulation of matter waves*. Phys. Rev. A **73**, 033619 (2006).

[189] S. Hofferberth, I. Lesanovsky, B. Fischer, J. Verdu, and J. Schmiedmayer. *Radiofrequency-dressed-state potentials for neutral atoms*. Nature Physics **2**(10), 710 (2006).

[190] R. Gati and M. K. Oberthaler. *A bosonic Josephson junction*. Journal of Physics B: Atomic, Molecular and Optical Physics **40**(10), R61 (2007).

[191] A. J. Leggett. *Bose–Einstein condensation in the alkali gases: Some fundamental concepts*. Rev. Mod. Phys. **73**, 307 (2001).

[192] J.-F. Mennemann, I. E. Mazets, M. Pigneur, H. P. Stimming, N. J. Mauser, J. Schmiedmayer, and S. Erne. *Relaxation in an extended bosonic Josephson junction*. Phys. Rev. Research **3**, 023197 (2021).

[193] D. S. Jin, J. R. Ensher, M. R. Matthews, C. E. Wieman, and E. A. Cornell. *Collective excitations of a Bose–Einstein condensate in a dilute gas*. Phys. Rev. Lett. **77**, 420 (1996).

[194] D. S. Jin, M. R. Matthews, J. R. Ensher, C. E. Wieman, and E. A. Cornell. *Temperature-dependent damping and frequency shifts in collective excitations of a dilute Bose–Einstein condensate*. Phys. Rev. Lett. **78**, 764 (1997).

[195] D. M. Stamper-Kurn, H.-J. Miesner, S. Inouye, M. R. Andrews, and W. Ketterle. *Collisionless and hydrodynamic excitations of a Bose–Einstein condensate*. Phys. Rev. Lett. **81**, 500 (1998).

[196] O. Maragò, G. Hechenblaikner, E. Hodby, and C. Foot. *Temperature dependence of damping and frequency shifts of the scissors mode of a trapped Bose–Einstein condensate*. Phys. Rev. Lett. **86**, 3938 (2001).

[197] F. Chevy, V. Bretin, P. Rosenbusch, K. W. Madison, and J. Dalibard. *Transverse breathing mode of an elongated Bose–Einstein condensate*. Phys. Rev. Lett. **88**, 250402 (2002).

[198] C. J. E. Straatsma, V. E. Colussi, M. J. Davis, D. S. Lobser, M. J. Holland, D. Z. Anderson, H. J. Lewandowski, and E. A. Cornell. *Collapse and revival of the monopole mode of a degenerate Bose gas in an isotropic harmonic trap*. Phys. Rev. A **94**, 043640 (2016).

[199] P. O. Fedichev, G. V. Shlyapnikov, and J. T. M. Walraven. *Damping of low-energy excitations of a trapped Bose–Einstein condensate at finite temperatures*. Phys. Rev. Lett. **80**, 2269 (1998).

[200] L. Pitaevskii and S. Stringari. *Landau damping in dilute Bose gases*. Physics Letters A **235**(4), 398 (1997).

[201] L. Pitaevskii and S. Stringari. *Elementary excitations in trapped Bose–Einstein condensed gases beyond the mean-field approximation*. Phys. Rev. Lett. **81**, 4541 (1998).

[202] M. J. Bijlsma and H. T. C. Stoof. *Collisionless modes of a trapped Bose gas*. Phys. Rev. A **60**, 3973 (1999).

[203] U. Al Khawaja and H. T. C. Stoof. *Kinetic theory of collective excitations and damping in Bose–Einstein condensed gases*. Phys. Rev. A **62**, 053602 (2000).

[204] M. Guilleumas and L. P. Pitaevskii. *Temperature-induced resonances and landau damping of collective modes in Bose–Einstein condensed gases in spherical traps*. Phys. Rev. A **61**, 013602 (1999).

[205] B. Jackson and C. S. Adams. *Damping and revivals of collective oscillations in a finite-temperature model of trapped Bose–Einstein condensation*. Phys. Rev. A **63**, 053606 (2001).

[206] B. Jackson and E. Zaremba. *Quadrupole collective modes in trapped finite-temperature Bose–Einstein condensates*. Phys. Rev. Lett. **88**, 180402 (2002).

[207] B. Jackson and E. Zaremba. *Modeling Bose–Einstein condensed gases at finite temperatures with N-body simulations*. Phys. Rev. A **66**, 033606 (2002).

[208] B. Jackson and E. Zaremba. *Accidental suppression of Landau damping of the transverse breathing mode in elongated Bose–Einstein condensates*. Phys. Rev. Lett. **89**, 150402 (2002).

[209] B. Jackson and E. Zaremba. *Landau damping in trapped Bose condensed gases*. New Journal of Physics **5**, 88 (2003).

[210] M. Guilleumas and L. P. Pitaevskii. *Landau damping of transverse quadrupole oscillations of an elongated Bose–Einstein condensate*. Phys. Rev. A **67**, 053607 (2003).

[211] S. A. Morgan, M. Rusch, D. A. W. Hutchinson, and K. Burnett. *Quantitative test of thermal field theory for Bose–Einstein condensates*. Phys. Rev. Lett. **91**, 250403 (2003).

[212] A. Bezett and P. B. Blakie. *Projected Gross–Pitaevskii equation theory of finite-temperature collective modes for a trapped Bose gas*. Phys. Rev. A **79**, 023602 (2009).

[213] T. Karpiuk, M. Brewczyk, M. Gajda, and K. Rzążewski. *Constructing a classical field for a Bose–Einstein condensate in an arbitrary trapping potential: Quadrupole oscillations at nonzero temperatures*. Phys. Rev. A **81**, 013629 (2010).

[214] P. Deuar and J. Pietraszewicz. *A semiclassical field theory that is freed of the ultraviolet catastrophe*. arXiv:1904.06266 (2019).

[215] A. Griffin, T. Nikuni, and E. Zaremba. *Bose-Condensed Gases at Finite Temperatures* (Cambridge University Press, 2009).

[216] S. Beliaev. *Energy spectrum of a non-ideal Bose gas*. Sov. Phys. JETP **34**(2), 299 (1958).

[217] H. B. Thacker. *Exact integrability in quantum field theory and statistical systems*. Rev. Mod. Phys. **53**, 253 (1981).

[218] I. E. Mazets. *Integrability breakdown in longitudinaly trapped, one-dimensional bosonic gases*. The European Physical Journal D **65**(1), 43 (2011).

[219] I. E. Mazets and J. Schmiedmayer. *Thermalization in a quasi-one-dimensional ultracold bosonic gas*. New Journal of Physics **12**(5), 055023 (2010).

[220] S. Tan, M. Pustilnik, and L. I. Glazman. *Relaxation of a high-energy quasiparticle in a one-dimensional Bose gas*. Phys. Rev. Lett. **105**, 090404 (2010).

[221] B. Fang, G. Carleo, A. Johnson, and I. Bouchoule. *Quench-induced breathing mode of one-dimensional Bose gases*. Phys. Rev. Lett. **113**, 035301 (2014).

[222] C. Menotti and S. Stringari. *Collective oscillations of a one-dimensional trapped Bose–Einstein gas*. Phys. Rev. A **66**, 043610 (2002).

[223] P. Pedri, D. Guéry-Odelin, and S. Stringari. *Dynamics of a classical gas including dissipative and mean-field effects*. Phys. Rev. A **68**, 043608 (2003).

[224] E. Zaremba, T. Nikuni, and A. Griffin. *Dynamics of trapped Bose gases at finite temperatures*. Journal of Low Temperature Physics **116**(3), 277 (1999).

[225] Z.-J. Yang, Z.-L. Chai, C.-X. Li, and X.-D. Ma. *Landau damping of collective mode in a quasi-one-dimensional repulsive Bose–Einstein condensate*. Communications in Theoretical Physics **57**(5), 789 (2012).

[226] A. Bastianello, A. De Luca, B. Doyon, and J. De Nardis. *Thermalization of a trapped one-dimensional Bose gas via diffusion*. Phys. Rev. Lett. **125**, 240604 (2020).

[227] O. A. Castro-Alvaredo, B. Doyon, and T. Yoshimura. *Emergent hydrodynamics in integrable quantum systems out of equilibrium*. Phys. Rev. X **6**, 041065 (2016).

[228] B. Bertini, M. Collura, J. De Nardis, and M. Fagotti. *Transport in out-of-equilibrium XXZ chains: Exact profiles of charges and currents*. Phys. Rev. Lett. **117**, 207201 (2016).

[229] G. El and M. Hoefer. *Dispersive shock waves and modulation theory*. Physica D: Nonlinear Phenomena **333**, 11 (2016).

[230] Z. Dutton, M. Budde, C. Slowe, and L. V. Hau. *Observation of quantum shock waves created with ultra-compressed slow light pulses in a Bose–Einstein condensate*. Science **293**(5530), 663 (2001).

[231] B. Damski. *Formation of shock waves in a Bose–Einstein condensate*. Phys. Rev. A **69**, 043610 (2004).

[232] T. P. Simula, P. Engels, I. Coddington, V. Schweikhard, E. A. Cornell, and R. J. Ballagh. *Observations on sound propagation in rapidly rotating Bose–Einstein condensates*. Phys. Rev. Lett. **94**, 080404 (2005).

[233] M. A. Hoefer, M. J. Ablowitz, I. Coddington, E. A. Cornell, P. Engels, and V. Schweikhard. *Dispersive and classical shock waves in Bose–Einstein condensates and gas dynamics*. Phys. Rev. A **74**, 023623 (2006).

[234] J. J. Chang, P. Engels, and M. A. Hoefer. *Formation of dispersive shock waves by merging and splitting Bose–Einstein condensates*. Phys. Rev. Lett. **101**, 170404 (2008).

[235] R. Meppelink, S. B. Koller, J. M. Vogels, P. van der Straten, E. D. van Ooijen, N. R. Heckenberg, H. Rubinsztein-Dunlop, S. A. Haine, and M. J. Davis. *Observation of shock waves in a large Bose–Einstein condensate*. Phys. Rev. A **80**, 043606 (2009).

[236] M. Kulkarni and A. G. Abanov. *Hydrodynamics of cold atomic gases in the limit of weak nonlinearity, dispersion, and dissipation*. Phys. Rev. A **86**, 033614 (2012).

[237] A. Bulgac, Y.-L. Luo, and K. J. Roche. *Quantum shock waves and domain walls in the real-time dynamics of a superfluid unitary Fermi gas*. Phys. Rev. Lett. **108**, 150401 (2012).

[238] S. Peotta and M. D. Ventra. *Quantum shock waves and population inversion in collisions of ultracold atomic clouds*. Phys. Rev. A **89**, 013621 (2014).

[239] N. K. Lowman and M. A. Hoefer. *Fermionic shock waves: Distinguishing dissipative versus dispersive regularizations*. Phys. Rev. A **88**, 013605 (2013).

[240] M. E. Mossman, M. A. Hoefer, K. Julien, P. G. Kevrekidis, and P. Engels. *Dissipative shock waves generated by a quantum-mechanical piston*. Nature Communications **9**(1), 4665 (2018).

[241] M. Hoefer, P. Engels, and J. Chang. *Matter–wave interference in Bose–Einstein condensates: A dispersive hydrodynamic perspective*. Physica D: Nonlinear Phenomena **238**(15), 1311 (2009).

[242] M. J. Davis, S. A. Morgan, and K. Burnett. *Simulations of Bose fields at finite temperature*. Phys. Rev. Lett. **87**, 160402 (2001).

[243] D. M. Gangardt and G. V. Shlyapnikov. *Stability and phase coherence of trapped 1D Bose gases*. Phys. Rev. Lett. **90**, 010401 (2003).

[244] D. S. Lobser, A. E. S. Barentine, E. A. Cornell, and H. J. Lewandowski. *Observation of a persistent non-equilibrium state in cold atoms*. Nature Physics **11**(12), 1009 (2015).

Ex umbris et imaginibus in veritatem.

John Henry Cardinal Newman,
His epitaph